Design and Characterization of Double Dynamic Networks Based on Boronic Ester and Imine Dynamic Covalent Bonds

Larissa Hammer

PSL★
UNIVERSITÉ PARIS

THÈSE DE DOCTORAT
DE L'UNIVERSITÉ PSL

Préparée à ESPCI Paris

Design and Characterization of Double Dynamic Networks Based on Boronic Ester and Imine Dynamic Covalent Bonds

La Conception et Analyse de Réseaux Doubles Dynamiques à Base de Liaisons Covalentes Dynamiques Ester Boronique et Imine

Soutenue par
Larissa Maria HAMMER
Le 10/12/2021

École doctorale n°397
Physique et Chimie des Matériaux

Spécialité
Chimie des Matériaux

Composition du jury :

Costantino CRETON		
Directeur de recherche, ESPCI Paris	*Président du jury*	
Daniel TATON		
Professeur, Université de Bordeaux	*Rapporteur*	
Didier GIGMES		
Directeur de recherche, Aix-Marseille Université	*Rapporteur*	
Evelyne VAN RUYMBEKE		
Professeur, Université catholique de Louvain	*Examinateur*	
Renaud NICOLAŸ		
Professeur, ESPCI Paris	*Directeur de thèse*	

ESPCI ﮮ PARIS ׀ PSL★

Acknowledgments

It is done. This thesis is finally brought to paper and my time in Paris comes to an end. These last 3.5 years would not have been possible without the help, support and guidance of many people.

First, I would like to thank my supervisor Renaud Nicolaÿ. I'm enormously grateful for all the mentoring and guidance over the last years. Thank you for the trust, the council and the inspiration and for giving me the liberty to thrive and learn. I would also like to thank Evelyne van Ruymbeke for her always open ear and the help she offered conquering my rheology problems.

I would like to thank for the help in the laboratory and during my time at ESPCI:

- Adrien Smith, who was a reliable and ambitious intern. Thank you for your work and stamina when it came to the synthetic work for Chapter 3.

- Mickaël Pomes-Hadda for the help with the DSC, TGA and DMA experiments.

- Gaëlle Carré De Lusancay, Isabelle Marlart and Aroul Radja for the technical and administrative support.

- Nathan Van Zee for the always competent council and for the co-authorship and all the improvements of my literature review.

- Amandine Guerinot for the fruitful discussions during the mini group meetings.

My time in Paris would not have been the same without the company of my unique colleagues:

- Antoine, who had the desk next to me and helped me with all my struggles, no matter if it was about boronic esters or the French language

- Sélène, who was always up for a girls night out in la Perla, Café de la Presse, le Baron Rouge (etc.) and of course to get "un truc bon" in Rue Mouffetard

- Alexis and Thomas, who had always good council regarding everything scientific and beyond

- Phuong-Anh, who made the best pâtisseries

- Clément, my office mate, who always greeted me with a smile and never got tired explaining French politics and culture to me

- Maddalena. Maïssa and Sarah, who supported me especially in the beginning of my time here in France

- Jakob (my fellow German), Imed, Mohammad, Noushin and Alvaro, who were always helpful inside and outside the lab

- George, who always has an open ear and a lot of patience (especially when it comes to complaints about the GPC ;))

- Maïlie and Violette, who were always kind and friendly

- Maxime, who is always up for a joke and made the lab socializing legendary

- Henrique, who always makes me laugh! Thank you for your friendship

- Oliva, who was always up for a party. Thank you for the girl talks, the twerking in the office, and all the adventures we had together in Paris

- Diego, whose openness and kindness are an inspiration and have often saved my day

- Chiara, Alexi, Quentin, Camille, Pierre and Arnaud, who always convinced me to take another verre in Rue du Pot de Fer

- Bruno, who cooks the best pasta e patate and gives good health advice (which I ignore always and deliberately)

- Quentin, who carried my suitcase through whole Napoli and woke up to make me coffee every morning in Capri. It was much appreciated

- Stefania, my sister in arms, who shared many of my challenges in the beginning here in Paris

- Ibrahim, who had many questions. Thank you for making me your unofficial supervisor ;) and for running my NMRs always on priority

- Marta Abellan-Flos, who worked with me on the project of Chapter 3. Thank you for the excellent collaboration and the friendly and warm discussions

List of Abbreviations

ADH	adipic acid dihydrazide
AIBN	azobisisobutyronitrile
AFM	atomic force microscopy
ARGET	activators regenerated by electron transfer
ATRP	atom-transfer radical polymerization
BMS	borane dimethylsulfide
CAN	covalent adaptable network
CC	column chromatography
CPDT	2-cyano-2-propyl dodecyl trithiocarbonate
CTA	chain transfer agent
$Đ$	dispersity
DA	Diels-Alder
DCB	dynamic covalent bond
DCM	dichloromethane
DDD	1,2-dodecandiol
DDN	dual dynamic network
DMA	dynamic mechanical analysis
DMAP	4-dimethylaminopyridine
DMF	dimethylformamide
DMSO	dimethyl sulfoxide
DN	double network
DP_n	number-average degree of polymerization
DSC	differential scanning calorimetry
E_a	activation energy
ENR	epoxidized natural rubber
eq	equivalent(s)
Et_2O	diethyl ether
EtOAc	ethyl acetate
FPT	freeze-pump-thaw
FRP	free radical polymerization
FTIR	fourier-transform infrared

hex	hexane
IPN	interpenetrating network
IR	infrared
KWW	Kohlrausch-Williams-Watts
LCE	liquid-crystal elastomers
M_n	number average molar mass
M_w	weight average molar mass
MBP	methyl 2-bromopropionate
MeCN	acetonitrile
MeOH	methanol
Me$_6$TREN	tris[2-(dimethylamino)ethyl]amine
N_{CL}	number of cross-links per chain
N_f	number of functional groups
*n*BA	*n*-butyl acrylate
NCB	non-covalent bond
NEt$_3$	triethylamine
NMR	nuclear magnetic resonance
PBA	phenylboronic acid
PEG	poly(ethylene glycol)
PHU	polyhydroxyurethane
P*n*BA	poly(*n*-butyl acrylate)
PNIPAM	poly(*N*-isopropylacrylamide)
ppm	parts per million
PS	polystyrene
PUR	polyurethane
ρ**(CL)**	crosslinking density
R_f	retention factor
RAFT	reversible addition - fragmentation chain transfer
rDA	retro Diels-Alder
RDRP	reversible deactivation radical polymerization
RILN	reversibly interlocking network
SEC	size exclusion chromatography
SMP	shape memory polymer
SN	single network
T_i	isotropic transition temperature
T_m	melting temperature
T_g	glass transition temperature

T_V	topology freezing temperature
TBAB	tetra-*n*-butylammonium bromide
TCEP	tris-(2-carboxyethyl)-phosphine
TFA	trifluoroacetic acid
TGA	thermal gravimetric analysis
THF	tetrahydrofuran
TP	thermoplastic precursor
TPE	thermoplastic elastomer
TsOH	p-toluenesulfonic acid
TTS	time temperature superposition
UPy	2-ureido-4[1H]-pyrimidinone
UV	ultraviolet
v/v	volume per unit volume (volume-to-volume ratio)
Vis	visible
w/w	weight per unit weight (weight-to-weight ratio)

Contents

General Introduction

Polymer networks, systems consisting of crosslinked polymer chains, are ubiquitous in our daily life. Covalent adaptable networks (CANs) are polymeric networks containing covalent crosslinks that are dynamic under specific conditions. CANs feature a unique combination of physical properties, including adaptability, self-healing, shape-memory, stimuli-responsiveness, and enhanced recyclability. The physical properties and the service conditions of CANs are defined by the nature of their constituent dynamic covalent bonds (DCBs). When the DCBs are dynamic, CANs can present the malleability of thermoplastics, while they display the dimensional stability of thermosets when their network is not dynamic. CANs that contain DCBs that proceed via a degenerate mechanism are named vitrimers. Their bond exchange typically involves an associative addition/elimination pathway, which essentially maintains constant the connectivity of the system at all times and temperatures. The flow properties of vitrimers are thus mainly dictated by the rate of exchange of the DCBs, and the evolution of the viscosity as a function of temperature obeys the Arrhenius law.

The use of a single crosslinker within vitrimers sometimes does not allow designing materials with a set of properties appropriate for a given application. In response to the increasing demand for more sophisticated and adaptable materials, the scientific community has identified dual dynamic networks (DDNs) as a promising new class of polymeric materials that combine two (or more) distinct crosslinkers in one system. The different crosslinks can be chosen from a vast variety of static covalent, dynamic covalent, and physical bonds. By combining different crosslinking strategies, a precisely tailored material can be designed. The choice of complementary chemistries provides access to diversified material properties and can give rise to synergistic effects. The main challenge in the design and characterization of such DDNs is to identify the adequate combination of crosslinkers. Furthermore, simple and scalable synthetic strategies still need to be developed to allow flexibility in combining different kinds of dynamic crosslinkers. The characterization of DDNs is not trivial in regard to the differentiation between the individual responses of the subnetworks.

Recently, a variety of DDNs have been reported in the literature, a few of them containing vitrimers further crosslinked with supramolecular or static covalent bonds. There are very

few studies that investigate the combination of two different and orthogonal degenerate exchange chemistries in one single system. The purpose of this thesis is to design and characterize such elastomeric DDNs. More precisely, the targeted DDNs will consist of two interpenetrated soft subnetworks, each crosslinked by a different dynamic chemistry. The employed crosslinking strategies must be orthogonal and should allow a facile implementation into the system. The orthogonality of the two bonds warrants that the two networks interpenetrate each other, without being chemically connected. Boronic ester metathesis and imine-aldehyde transimination have been identified as a combination of exchange reactions that could fulfill these criteria. The two subnetworks were envisioned so that they feature distinct properties in order to fulfill specific tasks. The boronic ester network should present fast exchange reactions between the dynamic bonds in order to dissipate energy and relax stress under service conditions. Previous studies have shown that by introducing sacrificial bonds into a network, stiffness and toughness can be enhanced and material failure can be postponed. Elastomers that are dynamic at application temperature show poor to no creep resistance. The imine-aldehyde network was designed to act at the structural component. It is supposed to compensate this shortcoming by holding the dynamic network in place and imparting elasticity to the DDN thanks to its slow dynamics.

The DDN was synthesized from functional thermoplastic precursors (TPs), which were crosslinked simultaneously with the corresponding difunctional molecular crosslinkers. To characterize the properties of this new material and uncover synergistic effects, an intensive comparative study was conducted, which focused on the DDN as well as its constituting single networks (SNs). The study encompasses the swelling and solubility properties, the thermal properties (stability and thermal transitions), the mechanical properties (mechanical strength and stretchability), and the rheological behavior (stress relaxation, creep, modulus) of the different networks. The ability of the vitrimeric DDN to be recycled mechanically and chemically was also assessed.

In Chapter 1, an extensive literature review is given on dually crosslinked polymer networks incorporating DCBs. It includes an overview about the nature and the properties of DCBs and the CANs they form. Subsequently, representative CANs featuring at least two different dynamic modes are discussed. In the Chapters 2 to 4, the respective SNs are synthesized and characterized. The SNs were tailored individually to fulfill their specific needs in terms of dynamic behavior, processability and dimensional stability. These properties were adjusted by changing the molar mass of the TPs, their degree of functionality, their crosslinking density, or the lifetime of the dynamic bonds. In Chapter 5, the components were tested for orthogonality and united to form the DDN. The results of

the comparative study of the DDN with the SNs are presented and discussed. In the end, the DDN is tested for mechanical and chemical recyclability.

1 | Literature Review

Chapter Contents

Introductory Remarks

The content of this chapter is an adapted version of the literature review "Dually Crosslinked Polymer Networks Incorporating Dynamic Covalent Bonds" by Larissa Hammer, Nathan J. Van Zee and Renaud Nicolaÿ (Reference [1]) published in *Polymers* in **2021**. Author Contributions: Writing-original draft preparation, L.H. Writing-review and editing, L.H., N.J.V.Z., and R.N.

Abstract

CANs are polymeric networks containing covalent crosslinks that are dynamic under specific conditions. In addition to possessing the malleability of thermoplastics and the dimensional stability of thermosets, CANs exhibit a unique combination of physical properties, including adaptability, self-healing, shape-memory, stimuli-responsiveness, and enhanced recyclability. The physical properties and the service conditions (such as temperature, pH, and humidity) of CANs are defined by the nature of their constituent dynamic covalent bonds DCBs. In response to the increasing demand for more sophisticated and adaptable materials, the scientific community has identified DDNs as a promising new class of polymeric materials. By combining two (or more) distinct crosslinkers in one system, a material with tailored thermal, rheological, and mechanical properties can be designed. One remarkable ability of DDNs is their capacity to combine dimensional stability, bond dynamicity, and multi-responsiveness. This review aims to give an overview of the advances in the emerging field of DDNs with a special emphasis on their design, structure-property relationships, and applications. This review illustrates how DDNs offer many prospects that single (dynamic) networks cannot provide and highlights the challenges associated with their synthesis and characterization.

1.1 Introduction

Synthetic organic polymers have found use in an incredibly broad range of applications, spanning single-use packaging materials to specialized medical devices. This versatility is realized at a global scale of production, which is a testament to the capabilities of modern polymer chemistry. In discussing such a diverse body of materials, a practical approach is to categorize polymers as either thermoplastics or thermosets,

which essentially distinguishes polymers on the basis of their temperature-dependent flow properties. Thermoplastics are characterized by a thermal phase transition that results in a viscoelastic fluid. Amorphous thermoplastics behave like brittle solids at temperatures below the glass transition temperature (T_g) and, like viscoelastic liquids, upon heating above the melting temperature (T_m). Semi-crystalline thermoplastics are like ductile solids between the T_g and the T_m, and heating above the T_m causes the crystalline domains to melt and the material to flow. Typical commercial amorphous and semi-crystalline thermoplastics have an average molecular weight that is significantly larger than the associated entanglement molecular weight, but these transient physical crosslinks are weak and do not prevent viscous flow. Thus, upon heating to a suitably high temperature (and excluding the impact of side reactions), thermoplastics can be processed and reprocessed by industrial techniques, such as extrusion, injection molding, melt spinning, and 3D-printing. For these reasons, thermoplastics represent about 80 % of global polymer consumption.[2] In contrast, thermosets do not flow at any temperature owing to the presence of chemical crosslinks that are permanent and static. When an amorphous thermoset is heated above its T_g, it becomes rubbery and behaves like a viscoelastic solid. Narrow-meshed networks that are glassy solids at service temperature are typically called structural thermosets, while wide-meshed thermosets that exhibit a rubbery elastic behavior at low temperatures (i.e., below 0 °C) are elastomers. In contrast to structural thermosets, elastomers undergo large deformation at service temperatures because of the segmental movement of the chains between the sparsely-distributed crosslinking points. Although thermosets tend to exhibit thermomechanical properties, chemical resistance, and dimensional stability superior to those of their thermoplastic counterparts, they cannot be reprocessed nor recycled because of the permanent and static nature of the crosslinks.

Beginning over 30 years ago,[3] researchers have targeted materials with physical properties that are in between those of thermoplastics and thermosets. One prominent strategy is to introduce exchangeable dynamic bonds into polymer networks. Under certain conditions, the crosslinks are able to shuffle, which permits the topology of the network to respond to external stimuli. In addition to possessing the malleability of thermoplastics and the dimensional stability of thermosets, the resulting materials exhibit a unique combination of physical properties, including adaptability, self-healing, shape-memory, stimuli-responsiveness, and enhanced recyclability. Dynamic bonds are commonly categorized based on the interaction responsible for the bond's strength. Non-covalent bonds (NCBs) are those formed by supramolecular interactions such as hydrogen bonding, π-π stacking, dipole-dipole interactions, and van der Waals forces.

For the purposes of this discussion, we consider metal-ligand bonds as a form of NCB as well. The strength of NCBs varies widely. For example, the free dissociation energy of neutral hydrogen bonds is on the order of a few kJ·mol^{-1}.[4] The strength of a given metal-ligand bond depends on many factors, such as the identity and oxidation state of the metal, the denticity of the ligand, and the electronic properties of proximal chemical species (e.g., other ligands coordinated to the metal). Metal-ligand bonds can range from tens to hundreds of kJ·mol^{-1}.[5] Most NCBs exhibit a short lifetime, imparting a highly dynamic character to the materials, in which they are implemented. The reversible nature of NCBs gives rise to the dynamic character of supramolecular systems,[6] which has been exploited to design self-healing and stimuli-responsive materials.[7–13] However, an undesirable consequence of this design is that these systems tend to creep, thus, limiting the material's dimensional stability. In contrast, DCBs are covalent bonds that can undergo exchange reactions, typically in response to an external stimulus, such as heat, light, and changes in pH. Due to the covalent nature of the interaction, the bond strength of DCBs is significantly larger than that of NCBs. DCBs typically have a bond dissociation energy on the order of several 100 kJ·mol^{-1}. Polymer networks that incorporate such bonds are called CANs.[14–16] Thanks to the covalent nature of their interaction, DCBs tend to impart greater creep resistance to dynamically crosslinked materials when compared to NCBs. The physical properties of dynamic materials that incorporate just one kind of NCB or DCB strongly depend on the nature and kinetics of the bond exchanges within the polymer network. The choice of a single crosslinker restricts the material to a relatively narrow window of properties, which limits the user's ability to design a material for a desired application. In response to increasing demand for more sophisticated and adaptable materials, the scientific community has identified DDNs as a promising new class of polymeric materials that combine two (or more) distinct crosslinkers in one system. The different crosslinks can be chosen from a vast variety of static covalent, dynamic covalent, and physical bonds. By combining different crosslinking strategies, a precisely tailored material can be designed. The choice of complementary chemistries can provide easy access to diversified material properties and give rise to synergistic effects.

A remarkably large number of DDNs have already been reported. DCBs have been exploited in nearly all kinds of polymer materials by now, ranging from bulk materials, like polyurethane (PUR) thermoplastic elastomers (TPEs) and vitrimers to hydrogels. Although it is difficult to form generalized principles for such a diverse field, it is clear that the thoughtful and creative combination of two kinds of crosslinks can lead to materials with unique combinations of properties. In this review, we aim to give the reader a

comprehensive view of the design and properties of dual networks that include at least one type of DCB. In the opening section, a brief overview presents the nature and the properties of DCBs as well as the CANs in which they are integrated. After a brief discussion of the historical context of DDNs, we highlight a variety of materials in the fields of polyurethane elastomers, shape memory materials, vitrimers, hydrogels, and interpenetrated polymer networks.

1.2 DCBs in Polymer Networks

The introduction of a sufficiently large number of DCBs into polymer networks yield CANs that have the ability to change their topology by shuffling the DCBs. The first CANs were reported only 20 years ago, consisting of crosslinked polymer materials that contain reversible covalent bonds based on the Diels-Alder (DA) reaction.[17] Subsequent CANs have been developed that extend the scope of dynamic covalent reactions and polymeric matrices. CANs can be divided into two subgroups on the basis of how the exchange reaction proceeds: dissociative and degenerate mechanisms (Figure 1.1).
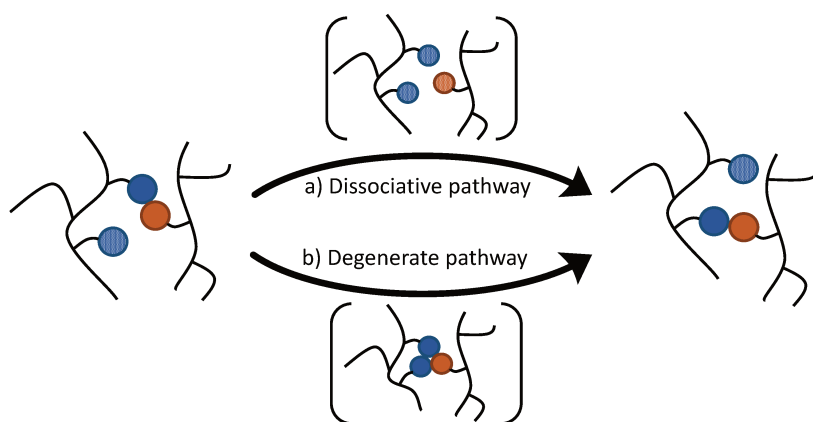
Figure 1.1: Dynamic bond exchange can proceed via two distinct mechanisms. (a) Dissociative exchange: the dynamic bond dissociates before a new one is formed. (b) Associative or degenerate exchange: the reaction proceeds via an intermediate (or transition) state in which the entities involved in the exchange are chemically linked together.

These different mechanisms have important consequences on how polymer networks behave. A detailed discussion can be found in a recent review by Winne, Leibler, and Du

Prez,[18] and a brief overview is provided in the present section. A dissociative exchange mechanism is comprised of a stepwise elimination/addition pathway in which the chemical bond is first broken before it is formed again with another exchange partner. Dissociative exchange reactions take place via an endothermic intermediate step that leads to de-crosslinking and free reactive chain ends. At all times, there is a dynamic equilibrium between associated and dissociated crosslinks. The equilibrium constant and, thus, the crosslinking density are dependent on the temperature. When the equilibrium is significantly shifted to the endothermic side, the connectivity decreases considerably, compromising the network structure. As a result, the viscosity drops significantly and the material behaves more like a thermoplastic (Figure 1.2, left).

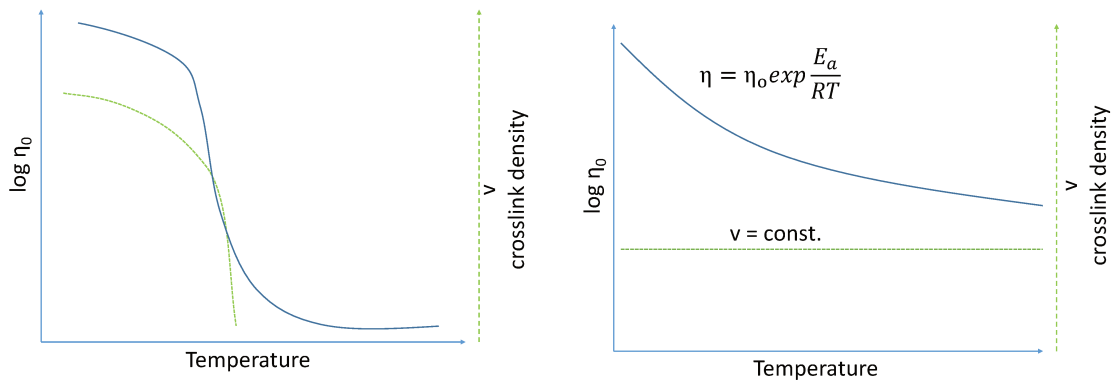$$\eta = \eta_0 exp \frac{E_a}{RT}$$

$v = const.$

Figure 1.2: Development of viscosity and the crosslinking density with temperature. Left: for systems following a dissociative exchange mechanism. Right: for systems following a degenerate exchange mechanism.

Upon cooling in the absence of side reactions, the crosslinks reform and the physical properties of the network are restored. In solution, materials that solely rely on dissociative exchange reactions undergo a gel-sol transition when the equilibrium is shifted to the dissociated side as a result of the de-crosslinking of the matrix. In contrast, exchange reactions that follow a degenerate mechanism are characterized by chemical entities on both sides of the equilibrium that are thermodynamically identical. Thus, the reaction equilibrium constant is equal to unity, and it is independent of temperature. Degenerate exchange reactions typically involve an associative addition/elimination pathway. In polymer networks relying on such exchanges, one of the chemical entities involved in the exchange process, which can be a free chain-end, a pendant functional group, or even functional groups within the backbone or crosslinks, adds onto another dynamic covalent linkage. The resulting intermediate (or transition state) is characterized by a higher degree of connectivity. The subsequent fragmentation of this species releases the

two chemical partners involved in the degenerate process. In general, the lifetime of the species exhibiting a higher order of connectivity is negligible. Thus, systems proceeding via degenerate exchanges exhibit an essentially constant number of crosslinks at all temperatures (Figure 1.2, right). The ability to maintain a constant connectivity while undergoing topological changes results in a gradual viscosity decrease that follows an Arrhenius relationship, which which is a property previously found only in vitreous silica. Polymer networks containing DCBs that follow a degenerate exchange mechanism are called vitrimers, a term coined by Leibler and co-workers in 2011.[19] Like other polymer networks, vitrimers have a T_g that defines the transition between the glassy and rubbery states. Additionally, vitrimers often possess a second characteristic transition temperature called the topology freezing temperature (T_V), which is deriving from the exchange reactions taking place between the DCBs. The T_V is defined as the temperature at which the melt viscosity is equal to 10^{12} Pa·s.[19,20] However, when the T_g of the matrix (or the T_m in the case of semi-crystalline vitrimers) is higher than the theoretical T_V predicted based on the lifetime of the dynamic bonds, vitrimers do not display a T_V. In these cases, the topology of the network is frozen because of the restricted mobility of the polymer chains associated to the T_g (or T_m) and not because of the dynamicity of the DCBs present in the network.

The flow properties of vitrimers are mainly dictated by the rate of exchange of the DCBs, and the evolution of the viscosity as a function of temperature obeys the Arrhenius law. The rate of exchange of the DCBs within vitrimers can be limited by the rate constant of the degenerate process in which case the activation energy (E_a) of the viscous flow is comparable to that of a model exchange reaction between small molecules.[19,21] However, when the concentration of the DCBs is sufficiently low or if the mobility of the DCBs in the matrix is sufficiently restricted, the E_a of viscous flow may be significantly larger than that of the degenerate exchange between the analogous small molecules.[21–23] Although Arrhenius temperature-dependence of the viscosity was initially identified as a hallmark of vitrimers, several CANs with DCBs that follow a dissociative exchange mechanism are reported to also exhibit Arrhenius viscosity profiles.[24–27] In fact, when the enthalpy for the bond breaking reaction of a dissociative exchange is sufficiently large, the temperature to shift the equilibrium to the de-crosslinked state may exceed the degradation temperature of the material. For such systems, the fraction of dissociated linkages is negligible at processing temperatures, and the network will present an apparent constant crosslinking density despite the dissociative nature of the CAN. The insolubility of vitrimers in non-reactive solvents regardless of the temperature, which is another characteristic that has long been considered to be an intrinsic property of vitrimers,[18,28] was experimentally con-

tradicted. Recent studies suggest that some vitrimers can partially or completely dissolve depending on the network topology, integrated functionality, dynamics of exchange, and time scale of the dissolution test.[23,29] The dissolution of the vitrimers does not reflect a loss of connectivity but rather the formation of soluble branched and cyclic structures during the reorganization of the network.[30,31]

Numerous DCBs have been successfully incorporated into polymer matrices to obtain CANs. Several reviews provide an overview about the state-of-the-art systems in this field.[16,18,21,28,32–35] We advise readers to take caution when interpreting the use of the term "vitrimer" in the literature. Some systems have been introduced as vitrimers,[36] even though they ultimately were found to undergo exchange reactions through a dissociative mechanism.[24] Many of the chemistries found in supramolecular polymer networks and CANs have been exploited and extended to create DDNs. An overview over dynamic covalent bonds found in DDNs is provided in Table 1.1, and a detailed overview about dual CANs comprising supramolecular bonds can be found in Table 1.2.

1.3 Origin of Dual Dynamic Networks: Supramolecular Networks

Perhaps the most prominent early example of a DDN is ionomers developed by DuPont in the 1960s.[102] R. W. Rees, working within a team interested in copolymerizing ethylene with functional comonomers, discovered that the sodium salt of ethylene methacrylic acid copolymers has peculiar physical properties. It exhibits unusually high optical clarity, yet it is processable like polyethylene. This early DDN features two different forms of supramolecular crosslinking: the crystallized polyethylene segments of the matrix and the clustering between the sodium carboxylate groups. The combination of these two crosslinks results in a material that is strikingly different compared to virgin polyethylene. Aside from its enhanced optical clarity, the polyethylene ionomers exhibit higher melt strength, higher solid-state toughness, and enhanced oil resistance compared to polyethylene. This finding ultimately led to the commercialization of such materials under the tradename Surlyn, which continues to be sold today. The group of J.-M. Lehn was the first to combine dynamic covalent chemistry with explicit supramolecular units in dynamic polymers.[47] They designed molecular components that simultaneously generate non-covalent, high-affinity sextuple hydrogen bonds and acylhydrazone links, with both types of bonds featuring dynamic behavior. The resulting DDNs undergo assembly, disassembly, and exchange processes, foreshadowing the great potential of this new

Table 1.1: DCBs used in DDNs: dynamic bonds, stimuli triggering the exchange, polymer systems developed (first example reported in this review), and imparted functions.

Dynamic Bonds	Triggers	Polymeric systems	Imparted functions
Diels-Alder	T	PURs,[37] SMPs,[38] hydrogels,[39] IPNs,[40] combined networks[41]	reshapeability, enhanced mechanical properties, self-healing ability, facilitated synthesis, structural stability, shape memory
Disulfide	redox, light, T, pH	PURs,[42] SMPs,[43] vitrimers,[44] hydrogels,[45] IPNs[46]	reshapeability, self-healing ability, enhanced mechanical properties, responsiveness, facilitated synthesis, shape memory
Acylhydrazone	pH	supramolecular polymers,[47] hydrogels,[45] IPNs[48]	reshapeability, self-healing ability, responsiveness, facilitated synthesis, injectability
Oxime	T, pH, addition of molecules	hydrogels[49]	structural stability, self-healing ability, enhanced mechanical properties
Imine/Schiffs base	T, pH, addition of molecules	SMPs,[50] vitrimers,[51] combined networks[52]	reshapeability, self-healing ability, enhanced mechanical properties, facilated synthesis
Urethane/Urea	T, catalysts	SMPs,[53] vitrimers[54]	reshapeability, enhanced mechanical properties, facilated synthesis
Ester	T, catalysts	SMPs,[55] vitrimers[55]	reshapeability, facilated synthesis, shape memory
Boronic ester	pH, addition of molecules	SMPs,[56] vitrimers,[57] hydrogels,[49] IPNs,[48] combined networks,[52]	reshapeability, self-healing ability, enhanced mechanical properties, responsiveness, facilitated synthesis
C-C (scission)	mechanical force, T	PURs[58]	self-healing ability, responsiveness, enhanced mechanical properties
Photoreversible [2+2] cycloaddition	light	SMPs[59]	shape memory
Allyl sulfide and trithiocarbonate	T, radical source	SMPs,[60] vitrimers[30]	reshapeability, self-healing ability, facilitated synthesis

class of adaptable materials. Later, the same group combined acylhydrazone chemistry with hydrogen bonds between urea-type groups in siloxane-based linear polymers.[61] The resulting material forms an elastic film that shows self-healing properties. The observed pH-independent time scale of the self-healing process indicates that the healing mechanism predominantly relies on hydrogen bonding. The dynamic exchange of the acylhydrazone units was exploited to perform post-polymerization modification reactions that allowed for the incorporation of new compounds into the polymer.[61]

1.4 Polyurethane Elastomers

The most prevalent example of physical networks formed by linear polymers are TPEs. They typically consist of block copolymers that combine two or more incompatible seg-

Table 1.2: Supramolecular systems found in DDNs: Physical systems, combined DCBs, polymeric systems developed, and imparted functions.

Physical systems	Combined DCBs	Polymeric systems	Imparted functions
Hydrogen bonds	acylhydrazone,[47,61] C-C,[58,62] DA cycloadduct,[37,40,63,64] disulfide,[42,65–67] imine,[50] olefine,[68] ester[69]	supramolecular polymers, PURs, SMPs, vitrimers, hydrogels, IPNs	self healing ability, enhanced mechanical properties
Ionic interactions	boronic ester,[70] imine,[71] oxime[72], ester[73]	SMPs, vitrimers, hydrogels	structural stability, enhanced mechanical properties, creep, solvent, and acid resistance
Liquid crystals	allyl sulfide,[60] boronic ester,[56] disulfide,[74–76] carbamate,[77] ester,[55,78–83]	SMPs	shape memory
MPS	anhydride,[84] DA cycloadducts,[38,85–89] imine,[50] disulfide,[90–92] urethane/urea,[53,93,94] ester,[73,78,95–97], boronic esters[98,99]	SMPs, vitrimers	shape memory, self-healing ability
Self-assemblies	acylhydrazone,[100] ester[101]	vitrimers, hydrogels	self healing ability, enhanced mechanical properties

ments that phase separate. One phase is most commonly composed of a high-T_g or high-T_m polymer and acts as crosslinking nodules of the continuous, soft, elastomeric phase, which typically consists of a low T_g amorphous polymer. This composition makes TPEs outstanding materials that not only exhibit the processability of thermoplastics but also the elasticity of vulcanized rubber.[103–106] One of the most commercially important classes of TPEs is PUR elastomers. In addition to phase separation, intermolecular hydrogen bonding takes place between the urethane groups of the individual chains.[107,108] Several approaches have been reported for upgrading the physical properties of PUR systems through the addition of DCBs. The addition of a second form of dynamic crosslinking is mainly focused on enhancing the self-healing ability of these materials.[42,65–67] Other approaches aim to make PUR systems responsive to additional stimuli,[58,62,67,109] or impart a new function like damage reporting.[58] Rekondo et al.,[42] for example, incorporated dynamic aromatic disulfides crosslinkers into poly(urea-urethane) elastomers, which impart excellent self-healing abilities under ambient conditions. The authors discovered that the self-healing behavior was largely due to the H-bonds in the urea-urethane backbone of the elastomer, as opposed to only the disulfide exchange. This behavior is in contrast to that reported for systems based on aliphatic disulfides, which require an external stimulus and show dynamic behavior through a combination of metathesis reactions and the equilibrium of the thiol-disulfide bonds.[110,111] A later study by Jian et al.[65] on similar systems (Scheme 1.1a) confirms the important role of H-bonds in the self-healing process. Liu and colleagues extended this concept by introducing a self-healing PUR based on

ditelluride bonds, which have a lower dissociation energy than disulfide bonds and, thus, exhibit faster dynamics of exchange.[66] For example, exchanges between ditellurides can take place at room temperature in the absence of light. The H-bond interactions between the polymer chains also played an important auxiliary role in the healing process of this system.
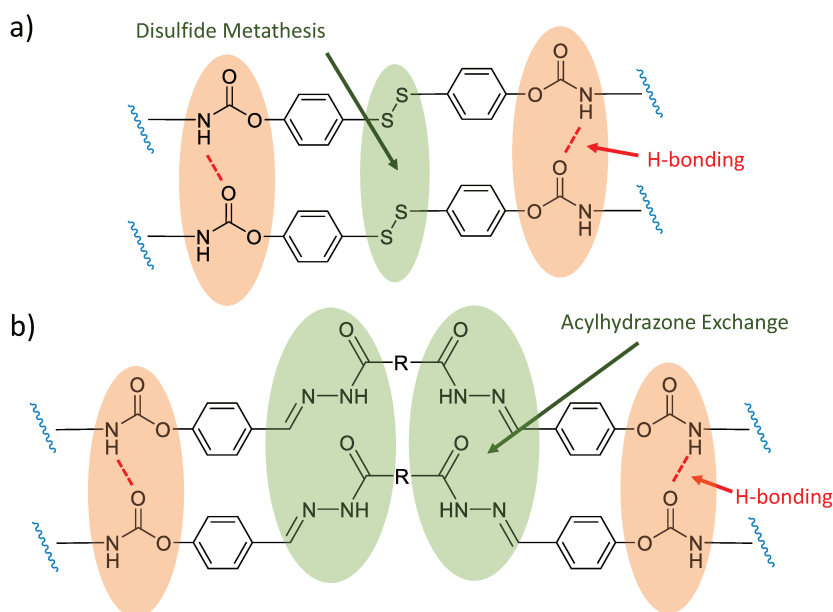
Scheme 1.1: Dual dynamic self-healing PUR elastomers. (a) PUR elastomer containing aromatic disulfides.[65] (b) PUR elastomer containing acylhydrazone units.[109]

Xu et al.[67] took advantage of the interplay of H-bonding and disulfide dynamic chemistry to design a self-healing PUR. The ability of aliphatic disulfides to undergo dynamic exchange reactions when subjected to sunlight, as well as the mobility of the polymer chains of the colorless transparent matrix, are all pivotal to obtain materials that display light-triggered self-healing properties at room temperature. Furthermore, the hydrogen bonds throughout the PUR matrix are believed to enhance the healing efficiency. When the material presents fractures or cracks, H-bonds favor intimate contact of the damaged surfaces and promote disulfide exchanges between dangling chain ends. Consequently, the healing process results from the rapid closure of the fracture driven by hydrogen bonds, which was followed by a gradual restoration of the mechanical properties thanks to the progressive reformation of the disulfide bonds. The group of Y. Bai[109] reported the design of two PUR elastomers with one containing dynamic acylhydrazone bonds (Scheme 1.1b) and a second one containing both acylhydrazone and disulfide DCBs.

Both kinds of elastomers exhibit self-healing abilities. However, the system containing additional disulfide bonds has a higher healing efficiency. This feature is proposed to result from the ability of the disulfide bonds to exchange faster than the acylhydrazone bonds. Furthermore, the addition of disulfide bonds presumably allows the system to undergo self-healing under neutral conditions at room temperature thanks to the sensitivity of the S-S bond to visible light. In a distinctly biomimetic approach, the group of P. Sun designed a linear segmented PUR that features H-bonded hard segments that are linked by thermally reversible DA cycloadducts.[37] This design is intended to mimic the hierarchical structures and H-bonding assemblies found in spider silk. The addition of DCBs imparts enhanced mechanical properties to the system, including high strength, stiffness, and toughness, as well as good solvent and heat resistance. In a recent study, Xu et al. designed a PUR with three complementary dynamic bonds.[112] In addition to the intrinsic hydrogen bonding ability of the urethane groups, the polymer backbone is equipped with thermo-responsive disulfide bonds, and the system was further chemically crosslinked with boronic esters. The goal of this approach was to design a system that shows good mechanical properties, thanks to a certain crosslinking density, while maintaining sufficient mobility of the polymer chains to allow fast and efficient self-healing. This efficiency relies on the different chemical pathways the two exchange reactions offer. Self-healing can be enhanced by the capacity of the boronic esters to undergo hydrolysis, thereby providing a temporal de-crosslinking. At the same time, the crosslinking via the boronic ester endows good mechanical properties and structural stability to the system.

Imato et al. incorporated diarylbibenzofuranone as a dynamic linker into the soft segments of a PUR elastomer.[58] The mechanism of elongation was thoroughly investigated via tensile tests. Under the action of mechanical stress, the soft segments elongate to full extension, and then the diarylbibenzofuranone mechanophores begin to dissociate into stable radicals via C-C scission (Figure 1.3). The aggregated hard domains serve as physical crosslinks, and they impart high dimensional stability to the material during this process. When the stress is removed, the extended chains relax and the dissociated radicals recombine. The blue color of the free radicals serves to signal emerging damage. Another PUR network based on C-C scission, which relied on benzopinacol moieties as DCBs, was introduced by Zhang et al.[62] Originally used as initiators for free radical polymerization, these aromatic pinacol derivatives form stable radicals upon application of moderate heat or UV irradiation. The dissociation of the benzopinacol units and the rapid recombination of the formed carbon radicals was found to become active at approximately 80 °C, and this behavior allows the bulk material to completely relax stress at this temperature. The network not only shows excellent self-healing and

reprocessing characteristics but also high solubility in common solvents when heated above the onset dissociation temperature of the benzopinacol units. These PUR networks can be used as macro-initiators to polymerize methyl methacrylate (MMA) or styrene in solution. In this process, semi-interpenetrating polymer networks are created, and polymer side chains are grafted onto the network. The grafted polymers are capable of reinitiating a polymerization, providing a reversible deactivation radical polymerization (RDRP) character to the process. This feature endows this material with attractive polymer engineering possibilities, such as extrinsic self-healing, selective functionalization, or possible re-growing abilities.
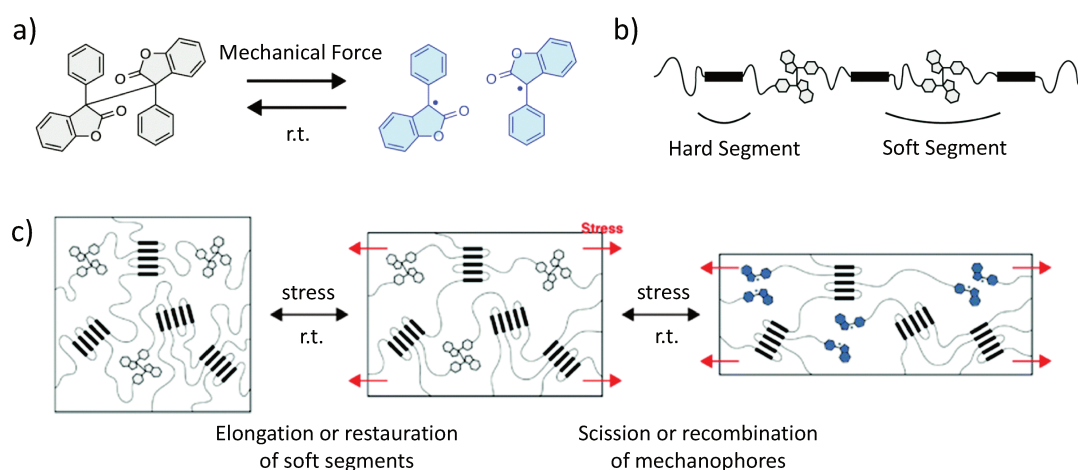
Figure 1.3: PUR elastomer incorporating diarylbibenzofuranone mechanophores designed by Imato et al.[58] (a) Diarylbibenzofuranone dissociates into stable radicals through C-C scission. (b) Structure of the PUR elastomer: the mechanophores are incorporated in the soft segments. (c) Mechanism of the uniaxial stretching of the dual PUR elastomer: under the action of stress, the soft segments elongate to full extension at which point the mechanophores dissociate and emit blue light. Adapted from Reference [58]. Published by The Royal Society of Chemistry 2016.

1.5 Shape Memory Polymers

Shape memory polymers (SMPs) constitute a class of polymers that intrinsically require a

dual crosslinking strategy. As polymeric actuators, SMPs are stimuli-responsive materials able to change their shape to produce motions and forces when subjected to an external trigger.[113–118] In general, the polymer is processed by conventional means to obtain its original, permanent shape. In the case of thermo-responsive SMPs, a temporary shape is programmed by heating the material and then shaping it to the desired temporary form, which is then fixed by rapid cooling. Upon a specific trigger signal, the original form can be recovered. The shape recovery takes place when the SMP is heated above a specific transition temperature, most commonly the T_g or the T_m. The permanent shape of many SMPs is fixed by covalent permanent crosslinks. Thus, the shape memory process only works in one direction. As soon as the permanent shape is recovered, the temporary shape is lost and the material must be programmed again. Recently, materials that can alternate between two different programmed shapes without the need to be reprogrammed between cycles have been developed and coined as reversible shape memory polymers. This multi-shape memory effect is made possible by the implementation of additional reversible phase transitions, such as those of aligned liquid crystalline phases.[119–122]

In early exemplifications, the original shape of the material is still defined by the network structure composed of static permanent crosslinks. The reprocessing of such materials is, thus, impossible, limiting the scope of industrial applications and precluding recycling. Incorporating DCBs not only provides a means to change the original form of the SMPs but also imparts properties like self-healing, re-processability (reshaping the polymer in its fluidic state), and solid-state plasticity (reshaping polymers permanently without macroscopic melting), while maintaining the mechanical robustness of the materials.[123–125] Various dynamic covalent chemistries, such as DA cycloadditions,[38,85–88] photoreversible [2+2] cycloadditions,[59,126] imine exchange,[50] anhydride exchange,[84] trans-esterification,[73,78,95–97,126] transcarbamoylation,[53,93,94,126] hindered urea bond exchange,[93] and disulfide exchange,[43,90,91] have been explored to produce adaptable SMPs. Very recently, a comprehensive review about CANs in polymer actuators, such as SMPs and liquid-crystal elastomerss (LCEs), has been published by Ji et al.[124]

As an interesting representative example, Xu et al. designed a self-healing PUR SMP based on poly(tetramethylene ether glycol), which comprises dynamic disulfide bonds.[92] In this case, the shape memory behavior was utilized to support the self-healing ability of the material. According to the theory of Wool and Conner,[127] surface rearrangement and chain diffusion are essential for efficient crack healing in polymeric materials. In the PUR SMP, the reversible glass transition of the PUR's soft segments leads to accelerated chain mobility, which significantly promotes the exchange reaction and, thus, the self-healing

ability of the material. DCBs have also been utilized to act as the switch units for programming the temporary shape.[43,59,73,89] Kuang et al. developed a triple shape memory strategy based on reversible and irreversible dual crosslinking of epoxy polymers.[89] The permanent shape of the material was fixed by the static covalent epoxy linkages, while two temporary shapes are programmed by exploiting the glass transition of the epoxy polymer and the presence of thermally reversible DA units. The temporary shape was obtained by heating the material to the temperature at which the retro Diels-Alder (rDA) reaction prevails. The shape was then fixed by cooling down the system and reforming the DA cycloadduct crosslinks. The original form could be recovered by heating to the temperature at which the DA cycloadducts dissociate. The triple shape-memory effect was achieved thanks to the T_g of the epoxy matrix, which is significantly lower than the temperature of the DA unit dissociation. Lendlein et al. prepared a photo-responsive SMP using cinnamic acid and cinnamylidene acetic acid derivatives as switching units.[59] The efficient photoreversible [2 + 2] cycloaddition of the chromophores made it possible to program to temporary shapes and, subsequently, recover the original shape at ambient temperature by ultraviolet (UV) light illumination. Other switches depend on the redox-dependent thiol-disulfide equilibrium.[43] The group of Xie combined thermally induced transesterification and transcarbamoylation with photo-responsive dimerizable cinnamate groups to create a single-component soft robot.[126] The thermo-reversible bonds provide plasticity to the material, while the photo-reversible bonds serve as a shape switch.

The group of A.-C. Shi reported an innovative SMP that utilizes the properties of vitrimers to create a triple-shape memory material (Figure 1.4).[73] This system is based on the combination of β-hydroxy ester transesterification and metal-ligand interactions of Zn^{2+} and carboxylate groups. The Zn^{2+} ions not only catalyze the transesterification in vitrimers, as reported by Leibler and co-workers,[19] but also act as crosslinking points. The permanent shape is set by the metal-ligand interactions, as they form exceptionally strong physical crosslinks. The authors further exploited the T_g and T_V to realize the triple shape memory behavior. The first temporary shape is fixed by the T_V, which is the topology freezing temperature associated to the ester-based DCBs, and the second temporary shape is fixed using the T_g. This system displays high dimensional recovery across programming cycles. Furthermore, the SMP is reprocessable and shows self-healing abilities as a result of transesterification reactions between the hydroxyl and ester groups. Ji, Terentjev and co-workers used β-hydroxy transesterifications to revolutionize the concept of LCEs, which are actuators that change their shape due to mesogen alignments caused by liquid crystal phase transitions.[55] This transition can be induced by heating above the isotropic transition temperature (T_i) of the liquid crystalline
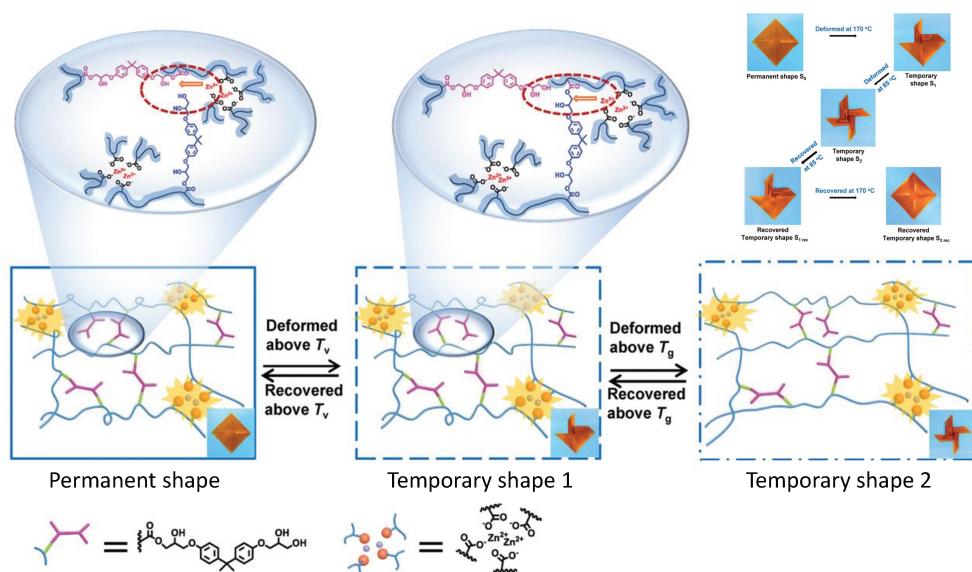
Figure 1.4: Example of a SMP based on the specific properties of vitrimers. The permanent shape is set by strong ionic interactions. Two temporary shapes can be programmed using the T_V (temporary shape 1) and the T_g of the material (temporary shape 2). Adapted from Reference [73]. Published by John Wiley and Sons 2019.

phase. The problem with earlier designs of LCEs was the need to align the liquid crystals before crosslinking, constraining how LCEs can be practically processed because of the risk of inducing disorder to the liquid crystalline phase upon crosslinking. Terentjev and Ji proposed a new vitrimer-based strategy in which the mesogens are aligned after the formation of the network by heating the system above its T_V under uniaxial stress (Figure 1.5).[55] For these systems to behave as actuators, the transition temperatures must be carefully balanced such that the T_i is well below the T_V. An added benefit of this design is that the material can be reprogrammed by simply heating the system above its T_V. The introduction of DCBs in LCEs, which were coined xLCEs,[55] paved the way for simpler fabrication protocols and gave access to complex 3D shapes, making xLCEs eligible for sophisticated high-tech applications like Braille displays.[79] Following this initial report on xLCEs, several studies have adapted and improved the process.[78–82,128] In addition, other dynamic covalent chemistries have been tested, and new xLCEs incorporating disulfide,[74–76] boronic ester,[56] and urethane DCBs,[77] as well as radical-mediated addition-fragmentation chain transfer functionalities,[60] have been developed.
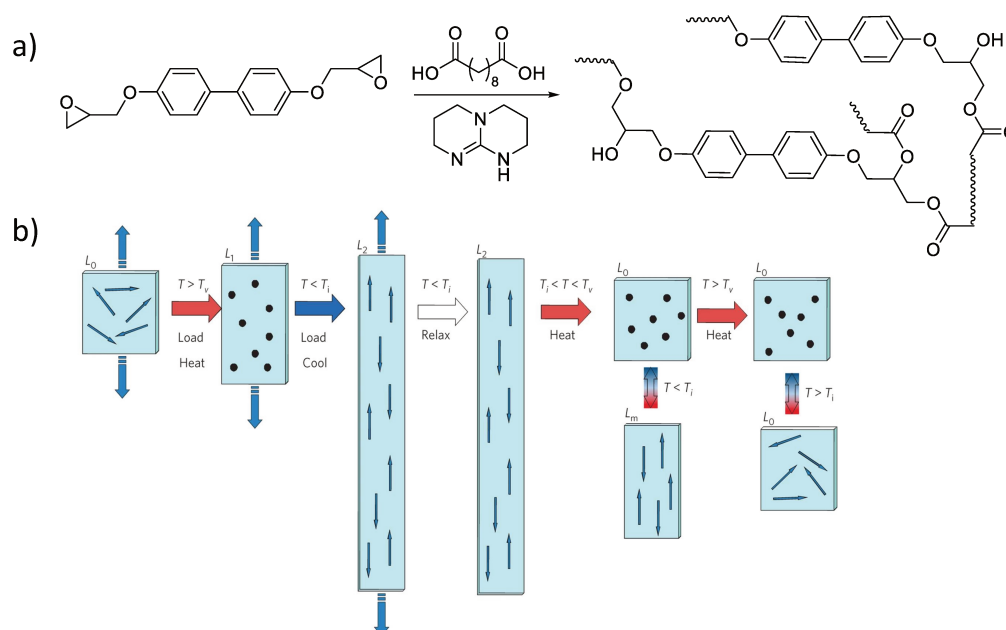
Figure 1.5: (a) Synthesis of an xLCE based on β-hydroxy ester DCBs. (b) Uniaxial align-
ment process of the xLCE. The reshuffling of the network topology, through
transesterification reactions, leads to the reversibility of the monodomain
alignmet. Adapted from Reference [55]. Published by the Nature Publishing
Group 2014.

1.6 Dual Dynamics in Vitrimers and Related CANs

1.6.1 Vitrimers and CANs with Two Covalent Dynamic Crosslinking Strategies

As highlighted in the context of SMPs and xLCEs, the concept of DDNs has been recently
applied to vitrimers. For example, the Zhang group combined transesterification and
disulfide metathesis in an epoxy vitrimer.[129] The synergistic combination of these two
degenerate exchanges allows the material to undergo topological changes more readily.
This feature not only accelerates stress relaxation but also decreases the temperature
at which the vitrimer is malleable. As a result, this vitrimer can be reprocessed at
100 °C in 1 h, and the resulting material exhibits complete recovery of mechanical
strength. Model networks comprising only one type of exchange chemistry, i.e., disulfide
metathesis or transesterification, were synthesized for comparing to the corresponding
DDN.[129] It must be stated that the respective single dynamic material has the same
concentration of disulfide or ester groups as the double network. Therefore, the overall

concentration of exchangeable groups is lower in the model single dynamic networks compared to the DDN. At a temperature of 180 °C, the relaxation rate of the dual dynamic vitrimer is approximately 28 times higher than that of the single-disulfide material and 122 times higher than that of the single-ester vitrimer. The synergy of the exchange reactions is also evident in the T_V of the materials. The experimentally-determined T_V of the DDN is 6.3 °C, while the T_V values of the single disulfide and ester vitrimers are 31.0 °C and 71.3 °C, respectively. The malleability at low temperature makes these materials appealing for applications that require self-healing and recyclability. For instance, electronic encapsulation could be a new application of interest. Common vitrimers are not suitable because they tend to exhibit T_V values that are too large.

In 2015, Dichtel and colleagues introduced a new vitrimer system based on the transcarbamoylation of polyhydroxyurethane (PHU) (Scheme 1.2a).[130,131] PHUs are a promising alternative to common PURs due to their nontoxic and ecologically-friendly starting materials. In contrast to conventional PUR thermosets, which are not effectively reprocessed, the PHU vitrimers show dynamic behavior and can be reprocessed without the addition of a catalyst. The material exhibits excellent mechanical properties, although stress relaxation and reprocessing took place only at high temperatures and under pressure (160 °C, 8 h, 4 MPa). A subsequent study tackled this downside by incorporating a second dynamic mode into the PHU vitrimers in the form of disulfide DCBs (Scheme 1.2b).[132] Using cystamine as a comonomer, PHU networks with the same excellent thermal stability and mechanical properties as the single dynamic PHU vitrimers are obtained. The introduction of the second DCB results in an increase in dynamicity, making processing possible under milder conditions (150 °C, 30 min). In contrast, a control material containing no disulfide bonds gave only highly inhomogeneous materials in reprocessing experiments, which is consistent with the slower dynamics observed when decreasing the disulfide content in the matrix. However, it should be noted that an increase of the disulfide content is accompanied by a decrease of the crosslinking density, which is a consequence of the different functionality between the bifunctional cystamine and the trifunctional tris(2-aminoethyl)amine (Scheme 1.2b). This change of average crosslinking density is expected to impact both the dynamics and thermo-mechanical properties of the vitrimers.

a)

b)

c)
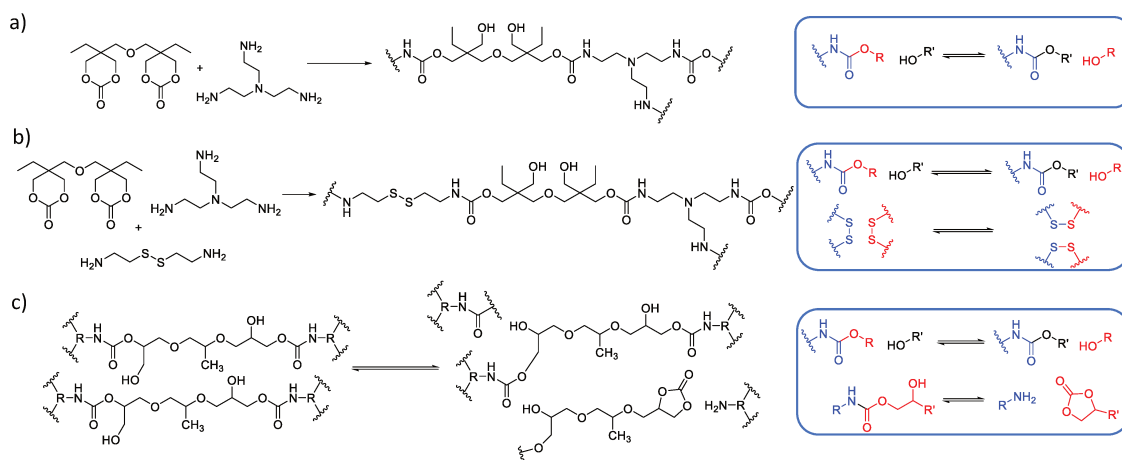
Scheme 1.2: PHU vitrimers. (a) PHU vitrimer structure introduced by Dichtel and co-workers.[130] Transcarbamoylation takes place between the urethane groups present in the backbone and the pendant primary hydroxyl groups. (b) DDN incorporating hydroxyurethane and disulfide DCBs.[132] (c) PHU networks displaying both intermolecular and intramolecular transcarbamoylation as introduced by the Torkelson group.[54] The intramolecular transcarbamoylation leads to the depolymerization of the system.

1.6.2 Vitrimers and CANs with One DCB That Follows Two Different Exchange Mechanisms

Using crosslinks with dual exchange mechanisms represents an elegant approach for achieving the characteristic physical properties of DDNs in a network that contains only one type of DCB. Torkelson and co-workers developed recyclable PHU networks in which both intermolecular and intramolecular transcarbamoylation play an important role (Scheme 1.2c).[54] These networks are obtained using five-membered cyclic carbonates instead of the six-membered cyclic carbonate employed by Dichtel et al.[130,131] They contain the catalyst 4-dimethylaminopyridine (DMAP). Intramolecular transcarbamoylation restores the monomeric functions, i.e., a cyclic carbonate and an amino group. Even though the intramolecular trans-carbonylation is not a dissociative reaction from a mechanistic point of view, this reaction functionally results in the depolymerization of the network and decrease in its overall connectivity. Both the intramolecular and the intermolecular transcarbamoylation contribute significantly to the network rearrangement with no prevalence of either pathway. This dual process results in a decrease of both the temperature and duration of reprocessing, going from 8 h at 160 °C to 2 h at 140 °C. However, the position of the equilibrium is temperature-dependent because the reversible

ring-opening and ring-closing of the cyclic carbonates are not degenerate processes. Thus, depolymerization should be favored above a certain temperature unless the system undergoes degradation. In 2019, Torkelson and colleagues reported reprocessable polymer networks relying on thiourethane exchange reactions.[128] A dual exchange mechanism was also proposed for this system. Alongside the associative thiol-thiourethane exchange, the system dissociates to its starting products at moderate temperatures. Bowman and co-workers investigated the mechanism of thiourethane exchange as a function of the catalyst.[133] They confirmed the dual mechanism proposed by Torkelson and colleagues, and they showed that it can be altered by the nature of the catalyst. Sumerlin and co-workers used boronic esters to further exemplify this strategy.[57] Boronic ester exchange reactions proceed either by a dissociative (i.e., hydrolysis and esterification) or degenerate (i.e., transesterification or metathesis) mechanism depending on the environment (Scheme 1.3).
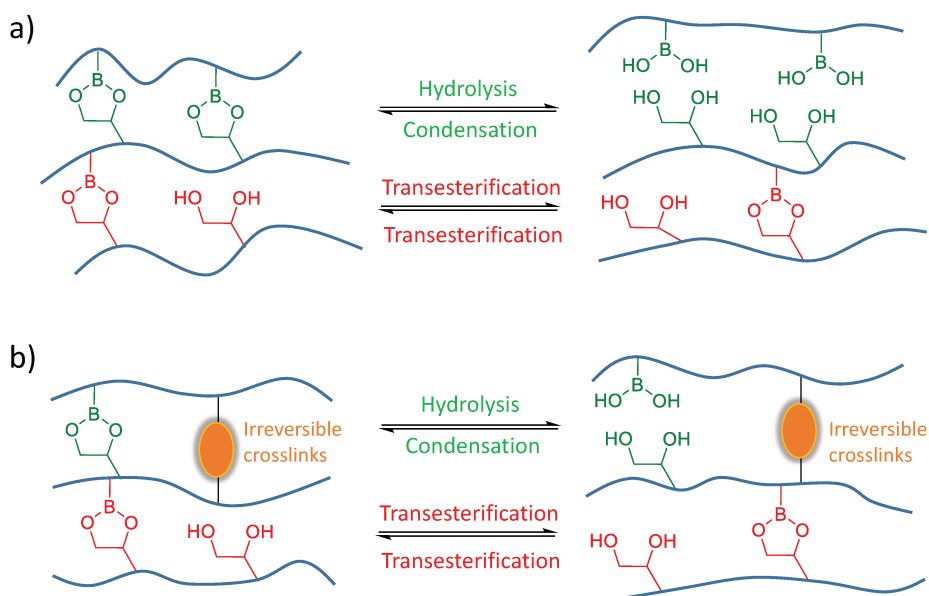
Scheme 1.3: DDNs relying on boronic ester DCBs.[57] (a) Boronic esters undergo two distinct exchange mechanisms under these conditions. In the presence of moisture, boronic esters undergo reversible hydrolysis and condensation reactions. In the presence of free diols, boronic esters undergo rapid transesterification-based degenerate exchange. (b) When the DDN is reinforced with additional static crosslinks, its dimensional stability is enhanced and properties like creep resistance are improved.

Due to the hydrolytic sensitivity of boronic esters, dissociation and transesterification are

the dominant reactions in humid environments. The transesterification between free diols and boronic esters takes place significantly faster than the metathesis between boronic esters.[98,134] Experiments reveal that the exchange pathway can be easily controlled by simply changing parameters like humidity and diol content, representing another useful tool to tailor material properties.

Guerre, Winne, Du Prez et al. introduced a vitrimer based on vinylogous urethane bonds that comprises two coexisting yet competing bond exchange mechanisms.[135] This study focuses on fluorinated vitrimers relying on vinylogous urethane degenerate exchange.[136,137] While studying the dynamics of these systems through stress relaxation experiments, two different activation energies are observed for the same material depending on the temperature window (Figure 1.6).
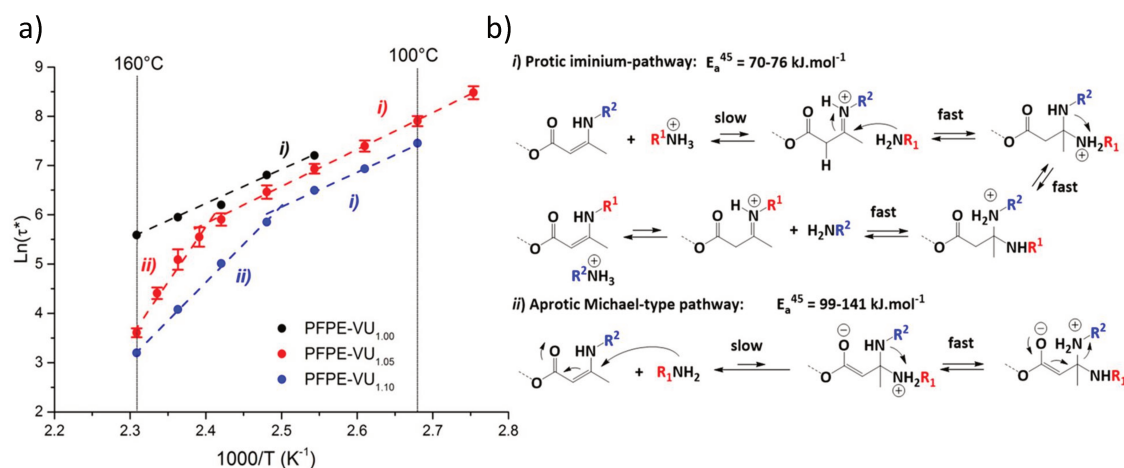
Figure 1.6: (a) Arrhenius plots of fluorinated vinylogous urethane vitrimers.[135] Materials comprising an excess of free amines (PFPE-VU1.05, red, and PFPE-VU1.10, blue) show two distinct temperature dependencies. The material prepared using a stoichiometric amount of amines (PFPE-VU1.00, black) only shows one exchange pathway. (b) Two competitive mechanisms: (i) a protic iminium pathway, which prevails at lower temperatures, (ii) an aprotic Michael-type pathway, which requires higher thermal activation and the presence of free amines. Reprinted (adapted) with permission from Reference [135]. Copyright (2018) American Chemical Society.

This result differs significantly from the values obtained with model small molecules as well as previous materials based on catalyst-free vinylogous urethane exchange.[136] This behavior is rationalized on the basis of two distinct exchange mechanisms with varying activation barriers. The exchange mechanism that prevails at lower temperature proceeds via a protic iminium species (Figure 1.6b, part i). The dominant pathway at

higher temperature involves a direct Michael-type addition of a neutral amine (Figure 1.6b, part ii). In polymers that do not contain free amine species, the Michael-type exchange does not take place. Further investigations revealed that the appearance of the second pathway is related to the network structure of the material. Only materials with larger non-dynamic segments show this kind of behavior, regardless of the presence of fluorinated components. The approach of using DCBs with dual mechanisms is a promising way to access new materials with varying rheology profiles that can be adjusted to meet specific processing demands. However, it must be emphasized that the variation of some key parameters, such as polymer architecture and composition, can give rise to unexpected behavior even for DCBs seemingly well-known in the community. New reaction pathways may occur that significantly change the behavior of the material, but if they are undetected or if a dual response is misinterpreted as a single response, incorrect conclusions may be drawn.

1.6.3 Reinforcement by Supramolecular Interactions

Another strategy to manipulate vitrimer properties is to introduce supramolecular bonds that reinforce the network.[68,69,71,101,138] Guan and colleagues introduced H-bonding secondary amide side groups into covalently-crosslinked dynamic polymer networks relying on olefin cross-metathesis as an exchange reaction.[68] The resulting materials show improved mechanical properties, such as elongation and stress at break, compared to materials that do not contain hydrogen bonding units. Tang, Guo, and colleagues presented an H-bond reinforced vitrimer obtained through concurrent crosslinking and grafting of epoxidized natural rubber (ENR) with sebacic acid and N-acetylglycine, respectively (Figure 1.7).[69] At a high temperature, the rubber network rearranges its topology through degenerate transesterification reactions. The N-acetyglycine grafts provide amide functions that form hydrogen bonds. The dynamic breaking and reformation of the H-bonds are able to dissipate energy. Tensile tests demonstrate that the addition of the sacrificial H-bonds leads to a significant improvement to the modulus, ultimate strength, and toughness of the material without sacrificing extensibility. Loading-unloading experiments exemplify the ability of these elastomers to dissipate a large amount of energy through the breaking and reformation of the sacrificial H-bonds. The reformation of the hydrogen bonds during the loading-unloading experiment is time-dependent and accelerated with an increasing temperature. At low strain rates, due to their finite lifetime, the H-bonds have more time to relax and, thus, contribute less to the modulus of the system than at higher strain rates. Creep and stress relaxation experiments at high

temperatures indicate that the network relaxes faster with the increase of the hydrogen units. The grafting of N-acetylglycine introduces β-hydroxyl esters into the material, thereby, increasing both the number of hydrogen bonding units and the concentration of DCBs. An increase in the concentration of exchangeable groups leads an increase in the rate of exchange and, thus, a decrease in the lifetime of the dynamic ester bonds at a given temperature.
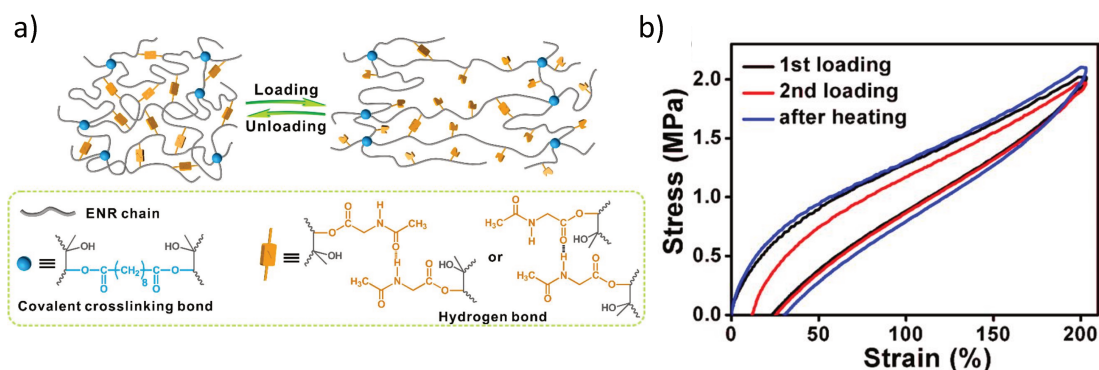
Figure 1.7: Vitrimer based on dynamic covalent β-hydroxyl ester linkages and supramolecular H-bonds.[69] (a) When the material is strained, the H-bonds dissociate. They re-associate when the load is removed. (b) Loading-unloading curves illustrating energy dissipation through H-bonds dissociation and reformation. The H-bond reformation is time-dependent and can be accelerated by increasing the temperature. Reprinted (adapted) with permission from Reference [69]. Copyright (2019) American Chemical Society.

In a subsequent paper, the same group presented a DDN vitrimer based on epoxidized ENR.[138] Boronic esters are introduced into the system as dynamic crosslinks through the ring-opening of epoxides by a dithiol bis(dioxaborolane) crosslinker. In addition, the system is reinforced with metal-ligand coordination bonds by introducing zinc salts that react with pendant hydroxyl groups along the ENR backbone. At service temperature, the vitrimer with the additional coordination bonds exhibits a higher modulus and stiffness compared to the singly crosslinked network. The DDN still has self-healing capability and reprocessability because the metal-ligand bonds are dynamic at higher temperatures. A comparable system based on styrene-butadiene rubber is reinforced in a similar way via the complexation of Zn^{2+} salts and pendant imidazole groups.[70] In a recent paper, Wang et al. incorporated up to three different metal complexes into vitrimers relying on imine exchange.[71] The additional metal-ligand bonds give rise to enhanced creep resistance. The study shows that the extent of creep suppression depends on the stability of the complex formed between the metal ions and the imine-based ligands, revealing

another interesting strategy to control material dynamics. Another approach to reinforce vitrimers with supramolecular bonds combines epoxy vitrimers with the self-assembly of long alkyl chains.[101] The initial relaxation modulus is increased by the non-covalent interactions of the octyl, dodecyl, or hexadecyl side-chains. The strength of the physical interactions is modulated by selecting the length of the alkyl side chains. Looking beyond explicitly-integrated pendant functionality, supramolecular crosslinking in vitrimers can also be derived from interactions originating from the polymer matrix. For example, the crystalline domains of a semi-crystalline vitrimer essentially act as supramolecular crosslinks. This point is analogous to the one made in Section 1.3 with respect to polyethylene ionomers. A variety of polyethylene vitrimers have already been reported to exhibit novel properties because of the combination of DCBs and the crystallinity of the polyethylene backbone.[98,99,139–146] Along these same lines, microphase separation can also be combined with DCBs to make DDN vitrimers. Sumerlin and colleagues recently exemplified this principle with the synthesis of block copolymer vitrimers, which exhibit distinct viscoelastic properties compared to the statistical copolymer control vitrimer.[147]

1.6.4 Reinforcement by Static Covalent Bonds

To achieve efficient responsiveness, self-healing, and reprocessing at service temperature, bond exchange in a vitrimer needs to operate at an acceptably fast rate. A network possessing DCBs with a short lifetime fulfills these criteria, but the downside is that such materials exhibit continuous and permanent deformation when subjected to mechanical stress. Creep and stress relaxation at service temperatures limit the practical utility of such vitrimers. Numerous elastomeric vitrimers display this undesired behavior at service temperatures.[20,23,135,148] This challenge has recently been tackled by complementing dynamic covalent bonds with static covalent crosslinks. Sumerlin and co-workers showed that the incorporation of static covalent crosslinks in a boronic ester-based vitrimer improves the creep resistance such that it is comparable to that of a conventional thermoset (Scheme 1.3b).[57] This DDN still displays self-healing ability, even though bond reformation is slower and less efficient compared to networks containing solely dynamic crosslinks. Using epoxy-based vitrimers, Torkelson and colleagues further studied the consequences of introducing static crosslinks to vitrimers, trying to find the optimal balance between creep resistance and processability.[149] The authors used the Flory-Stockmayer gelation theory to predict the critical content of permanent static crosslinks that a vitrimer should not exceed in order to remain processable. The authors postulate that, for a polymer

network to be fully reprocessable, the static crosslinks should be present at a level that is insufficient to form a percolated static network in the material.

In order to experimentally validate this model, thiol-epoxy networks comprising both static and dynamic covalent bonds were prepared. The latter undergo transesterification reactions catalyzed by DMAP. Networks containing either fewer (40 %) or more (60 %) static crosslinks than the calculated critical value of 50 % were prepared. The stress relaxation, creep behavior, and reprocessability of both materials were then compared (Figure 1.8).
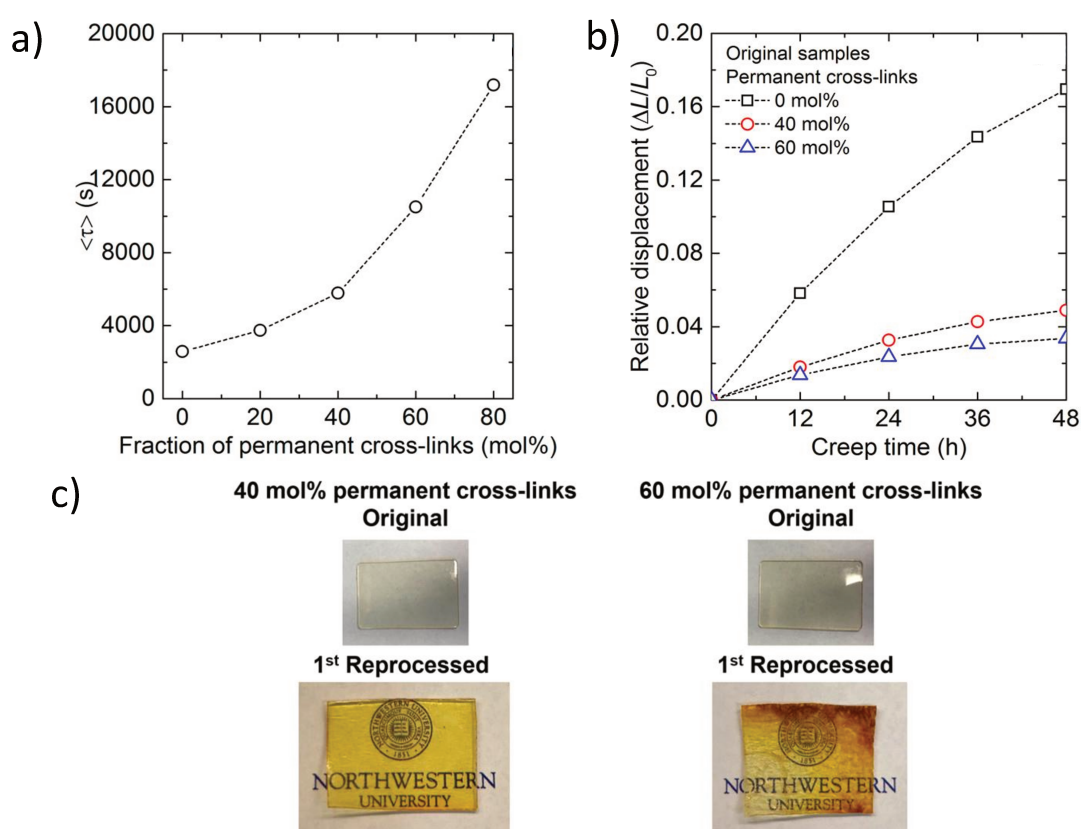
Figure 1.8: Vitrimers with varying fractions of static crosslinks.[149] (a) Average stress relaxation time <τ> as a function of the fraction of static crosslinks. When the proportion of static crosslinks increases, the material requires more time to relax stress. (b) Relative displacement as a function of creep time. The incorporation of static crosslinks significantly reduces the displacement. (c) Photographic images of samples with 40 % and 60 % of static crosslinks. The samples comprising 60 % of static crosslinks cannot be reprocessed without deterioration of the material. Reprinted (adapted) with permission from Reference [149]. Copyright (2018) American Chemical Society.

Stress relaxation experiments show that increasing the fraction of static bonds in the material results in an increase in the time necessary to relax stress. In addition, the material with 60 % static crosslinks shows only limited reprocessability. This sample loses its structural integrity upon heating and deformation, while the sample with 40 % static crosslinks retains its shape and shows full recovery of its mechanical properties. In contrast to materials with exclusively dynamic bonds, the network containing 40 % of static crosslinks shows 70 % less creep. This study convincingly demonstrates that increasing the fraction of static crosslinks in a vitrimer can significantly improve its creep resistance without suppressing its ability to be reprocessed. Defining a universal criterion regarding the fraction of static crosslinks that can be incorporated into a vitrimer without deteriorating reprocessability is a challenging task. Depending on the structure and functionality of the (macro)molecules used to synthesize the DDN, the weight fraction of the hypothetical static percolated network can vary significantly, as well as the consequential flow properties and processability of the material. The requirements for the flow properties of the polymer melt depend on the desired processing technique (e.g., blow molding, injection molding, extrusion molding, or compression molding). Thus, a dynamic polymer network that contains a secondary percolated static network can be sufficiently processable in certain cases, such as when reprocessing is performed by compression molding after a step of mechanical grinding. Indeed, it has been demonstrated that very strong adhesion can be created between polymer networks incorporating DCBs.[150–153] This point was experimentally confirmed by our group in the context of polybutadiene networks incorporating both static and dynamic dioxaborolane-based crosslinks.[23] For example, a DDN containing static crosslinks such that it has an insoluble fraction of 60 wt % (after the selective cleavage of all the dioxaborolane crosslinks) was efficiently recycled multiple times by compression molding. Moreover, dynamic mechanical analysis (DMA) and mechanical testing indicate that, even after three cycles of recycling (by mechanical grinding and compression molding), the material displays the same crosslinking density and exhibits full recovery of its mechanical properties. As expected based on the observed recyclability, strong adhesion is generated between macroscopic objects made of the dual networks containing both static and dynamic crosslinks. Saed et al. also reported DDNs combining static and dynamic bonds in which the static bonds are incorporated into boronic ester-based liquid crystalline vitrimers to enhance the dimensional stability of the material during actuation.[56]

Besides improving creep resistance, the incorporation of static bonds can be used to tune the dynamics and topological rearrangement of CANs. Nicolaÿ, Matyjaszewski et al. reported one of the first associative CANs, later coined vitrimers, when they

designed gels that can be welded in solution thanks to the presence of dynamic covalent trithiocarbonate crosslinks that exchange via an addition-fragmentation mechanism.[30] The introduction of a fraction of static crosslinks to the system permits tuning of the swelling properties of the gels while keeping the overall crosslinking density constant. The higher the amount of dynamic crosslinks, the greater the degree to which the gels can reorganize and adapt to the chemical environment. As a result, some of the mechanical stress generated by the diffusion of the solvent within the polymer network is relaxed, and gels presenting a higher swelling ratio are, thus, obtained. The Matyjaszewski group also used a combination of static and dynamic crosslinks to develop self-healing coatings.[154] The coatings are constituted of multiarm star polymers that carry dynamic covalent bonds at the periphery, which are used to generate dynamic disulfide crosslinks. This peculiar branched architecture features specific flow properties and distribution of the functionality that enhance the self-healing ability by providing a better accessibility and mobility to the reactive groups. This concept, initially modeled by Matyjaszewski, Balazs, and colleagues through computational simulations,[155] was confirmed experimentally by a combination of the atomic force microscopy (AFM) micromachining technique, continuous AFM imaging, and optical microscopy. In this case, static crosslinks are used to precisely control the topology of the polymers, which results in coatings with superior self-healing properties. Another approach to design DDNs is to integrate dynamic bonds into well-known thermoset systems, such as epoxy resins. This was recently achieved by incorporating disulfide,[44,156] imine,[51] or vinylogous urethane moieties[157] into common epoxy or diene networks. By integrating DCBs, properties like recyclability and reprocessability can be imparted to typical thermosetting materials.

1.7 Hydrogels

Hydrogels are polymeric networks that absorb and retain large amounts of water. They are generally designed to be biocompatible, stimuli responsive, self-healable, and injectable. Their unique soft rubbery consistency, which is very close to that of living tissues, makes them ideal candidates for a wide range of applications[158,159] especially cell cultures,[160,161] cosmetics,[162] sensors,[163] drug delivery devices,[164,165] and tissue engineering.[166–168] In recent years, much work has focused on the design of hydrogels based on biopolymers and bio-sourced polymers, like collagen, chitosan, hyaluronic acid, and other polysaccharides in order to develop bio-compatible eco-friendly materials.[169–171] However, the limited mechanical properties of common hydrogels have precluded their

use in applications that call for enhanced mechanical performances. Introducing dual crosslinking is a promising strategy for expanding the scope of applications.

1.7.1 Hydrogels Combining DCBs and Supramolecular Interactions

Sacrificial bonds are commonly employed to improve the mechanical properties of hydrogels. Crosslinks based on NCBs are useful sacrificial bonds because they have short lifetimes under service conditions, which causes the hydrogels to be highly dissipative. Even though the toughness of hydrogels is enhanced, the use of NCBs does not significantly improve the structural stability of the materials because their dynamic nature makes them prone to creep. Most examples of such DDNs rely on either a combination of NCBs and static covalent bonds,[172–176] which suppresses the dynamics of the system, or on a combination of different NCBs,[177–181] which enhances structural stability only to a limited extent. Combining NCBs with DCBs provides the optimal possibility to improve the structural stability while maintaining adaptability and energy dissipation. For example, Guo et al. married acylhydrazone chemistry with transient hydrogen bonds to design tough injectable hydrogels.[182] The gels were synthesized by free radical copolymerization of acrylamide and diacetoneacrylamide in the presence of adipic acid dihydrazide (ADH) and polyvinylpyrrolidone. The dihydrazide of the ADH reacts with the ketone groups of the polyamides to form dynamic covalent acylhydrazone bonds, while the polyvinylpyrrolidone forms hydrogen bonds with the amide units of the polyacrylamides, as already demonstrated in physical hydrogels.[183] Previous studies conducted by the authors show that similar hydrogels relying only on acylhydrazone bonds show very poor mechanical properties.[184] The addition of intermolecular hydrogen bonds provides the hydrogels with higher toughness, stretchability, and ductility thanks to synergistic effects. The hydrogels exhibit superior fatigue resistance and self-recovery comparable to that of materials crosslinked with static covalent bonds. They feature self-healing properties at ambient conditions without external stimuli. In addition, the sol-gel transition of these hydrogels is easily controlled through the pH-dependent dissociation of the acylhydrozone bonds. In strongly acidic environments, the acylhydrazone bonds hydrolyze, and the hydrogels turn into injectable viscous solutions. By adding a base, the equilibrium shifts back to the associated form, and tough hydrogels are obtained after ca. 2 h. This feature makes it possible to inject the hydrogels to any desired form. The good cytocompatibility and the excellent mechanical strength of these hydrogels are highly desirable attributes for various biomedical applications, such as artificial tissue engineering. Chen and co-workers reported a DDN based on the crosslinking of telechelic amphiphilic triblock copolymers.[100]

As presented in Figure 1.9, the aldehyde-terminated polymers form micelles in water, and these structures are crosslinked with a three-arm acylhydrazine linker. Thanks to the combination of the chemical stability of the acylhydrazone DCBs and the dissipative nature of the physical crosslinks, a tough, ultra-stretchable, self-healing hydrogel is obtained.
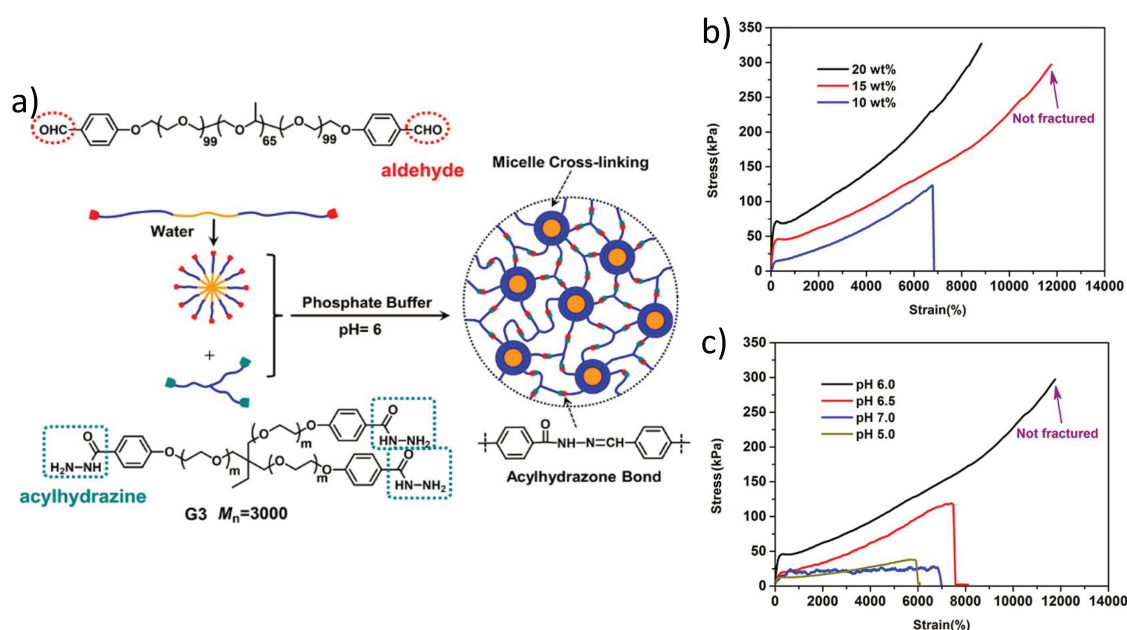
Figure 1.9: Hydrogels comprising acylhydrazone and micellar crosslinks.[100] (a) Synthetic strategy: Homotelechelic aldehyde functionalized triblock copolymers are crosslinked at a pH = 6 with a three-arm acylhydrazine. (b) Uniaxial tensile test of the dual dynamic hydrogel and a hydrogel comprising solely acylhydrazone crosslinks. (c) Uniaxial tensile tests of the dual network at different pH values. The gel shows the highest stability at pH = 6.0. Reprinted (adapted) with permission from Reference [100]. Copyright (2017) American Chemical Society.

The DDN hydrogel was compared to a similar gel that contained acylhydrazone bonds but no physical interactions, and was also compared to a hydrogel with the same triblock copolymer micellization but with static covalent bonds instead of DCBs. The dual dynamic hydrogel shows superior stretchability and mechanical properties than the reference

systems, indicating that both dynamic interactions contribute to the ultra-stretchability and high toughness of the material. The hydrogel exhibits the highest stretchability and mechanical strength at pH 6, which is the pH at which the acylhydrazone bond features the fastest dynamics. At a higher pH, the lifetime of the acylhydrazone bonds increases, while the bonds dissociate at a lower pH, leading to a lower crosslinking density. Cyclic loading-unloading experiments on the different hydrogels indicate that both dynamic interactions contribute to energy dissipation. The dislocation and decomposition of the micelles, in conjunction with the simultaneous chain sliding enabled by the dissociation-reformation equilibria of the acylhydrazone bonds, lead to a pronounced hysteresis in the cyclic experiments, which is proposed as the origin of the material's excellent mechanical properties. Polysaccharide-based hydrogels incorporating dynamic oxime crosslinks were also developed by Roh and co-workers.[72] In these systems, the natural ability of alginates to form complexes with divalent cations such as Ca^{2+} was used to create a DDN. The oxime crosslinking permits the formation of viscoelastic hydrogels in microbead or micro-thread geometries. The beads were used to encapsulate and culture 2PK-3 cells. The ability to form biomimetic viscoelastic microenvironments in a defined geometry is a highly desirable feature in biomedical applications.

1.7.2 Hydrogels with Dynamic Covalent Crosslinks of Different Natures

Incorporating two different types of DCBs is an appealing strategy for realizing hydrogels that are strong yet dynamic. For example, one DCB with a short lifetime can be used to impart a dynamic character to the system, and another DCB with a long lifetime can be used as a tunable structural component. Chen and co-workers exemplified this approach by combining acylhydrazone exchange with DA cycloaddition.[39] The cycloadduct-based crosslinks are not dynamic at room temperature, thereby, providing dimensional stability and mechanical strength to the network. The acylhydrazone bonds are highly dynamic under service conditions, conferring self-healing ability to the network. Thanks to the presence of free aldehyde groups involved in the dissociative equilibrium of the acylhydrazone units, the hydrogel shows excellent adhesive properties through the formation of imines with primary amines, rendering the material a promising candidate for tissue engineering applications. Collins et al. developed a dynamic hydrogel based on oxime groups, which undergo reversible degradation and reformation.[49] The degradation is achieved by transoximination with an excess of both butyraldehyde and trifluoroacetic acid (TFA) at 60 °C. Alternatively, the authors demonstrate a reversible gel-sol transition by treating the oxime-based gel with TFA in dichloromethane (DCM) at room temperature.

After rapid degradation of the gel, the TFA (and DCM) evaporates over time, allowing the equilibrium to shift back to network formation. Boronic acid moieties can also be introduced as side-groups. After crosslinking with the polyphenol tannic acid, the resulting material is a dynamic hydrogel with two distinct and orthogonal DCBs. The flexibility of design of DDNs has revealed new opportunities for making materials that respond to multiple external stimuli. The group of Zhang combined several dynamic covalent chemistries in multi-responsive hydrogels that display quadruple-stimuli sensitiveness (Figure 1.10).[185,186]
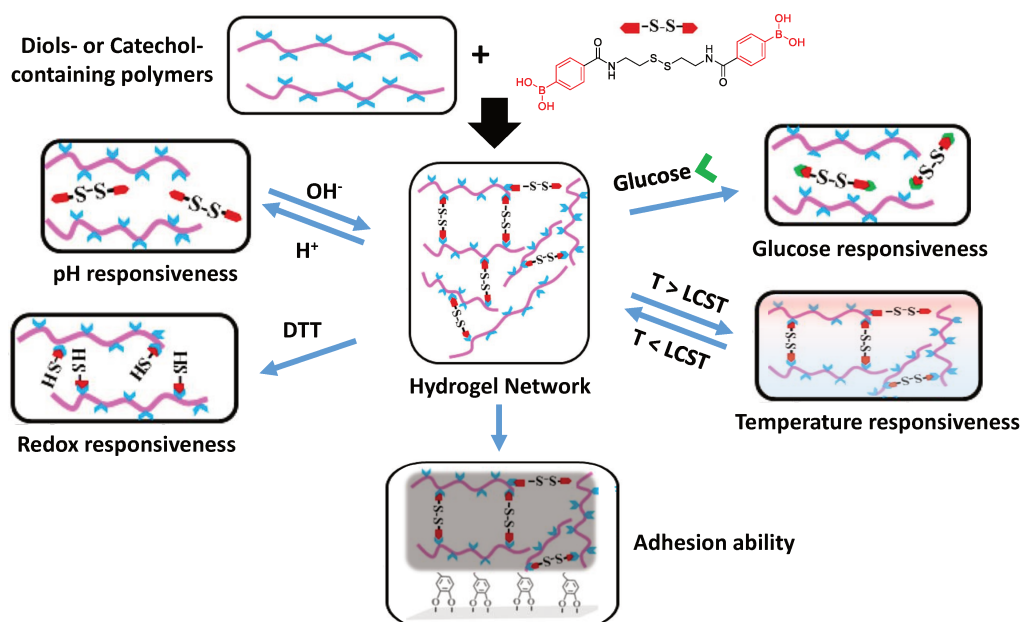
Figure 1.10: Multi-responsive hydrogel.[186] A pH-, redox-, glucose-, and temperature-responsive hydrogel is obtained through the crosslinking of catechol-functionalized poly(*N*-isopropylacrylamide) (PNIPAM) with a disulfide di-boronic acid. The resulting hydrogel additionally presents self-healing and adhesion abilities. Adapted from Reference [186]. Published by WILEY-VCH Verlag GmbH in 2017.

In their studies, diol-containing and catechol-containing polymers were crosslinked with a disulfide diboronic acid crosslinker. The final hydrogels feature not only pH, sugar, redox, and thermal responsiveness, but also enhanced self-healing abilities. The boronic ester bonds are susceptible to hydrolysis in the presence of an acid, but the crosslinks can be reformed under basic conditions. The boronic esters can also be dissociated by the addition of a competitive monofunctional molecule, such as glucose. The disulfide bonds give access to a redox-induced cleavage of the crosslinks. However, the use of glucose

or redox reactions lead to irreversible disassembly of the system. Only the pH-dependent hydrolysis-condensation equilibrium of the boronic ester bonds is reversible in this case, which enables the material to exhibit self-healing. When the multi-responsive crosslinker is used to create a network with a catechol-functionalized PNIPAM, the hydrogel shows an additional thermo-responsiveness originating from the lower critical solution temperature of PNIPAM. Furthermore, the hydrogels display advanced adhesive features that stem from the catechol units, which are responsible for the mussel-like adhesive properties. Dual systems can also be used to expand the window of operation within which a stimulus is effective. For example, Deng et al. used two different covalent crosslinkers in responsive hydrogels to extend the self-healing properties to a broader pH spectrum (Figure 1.11).[45]
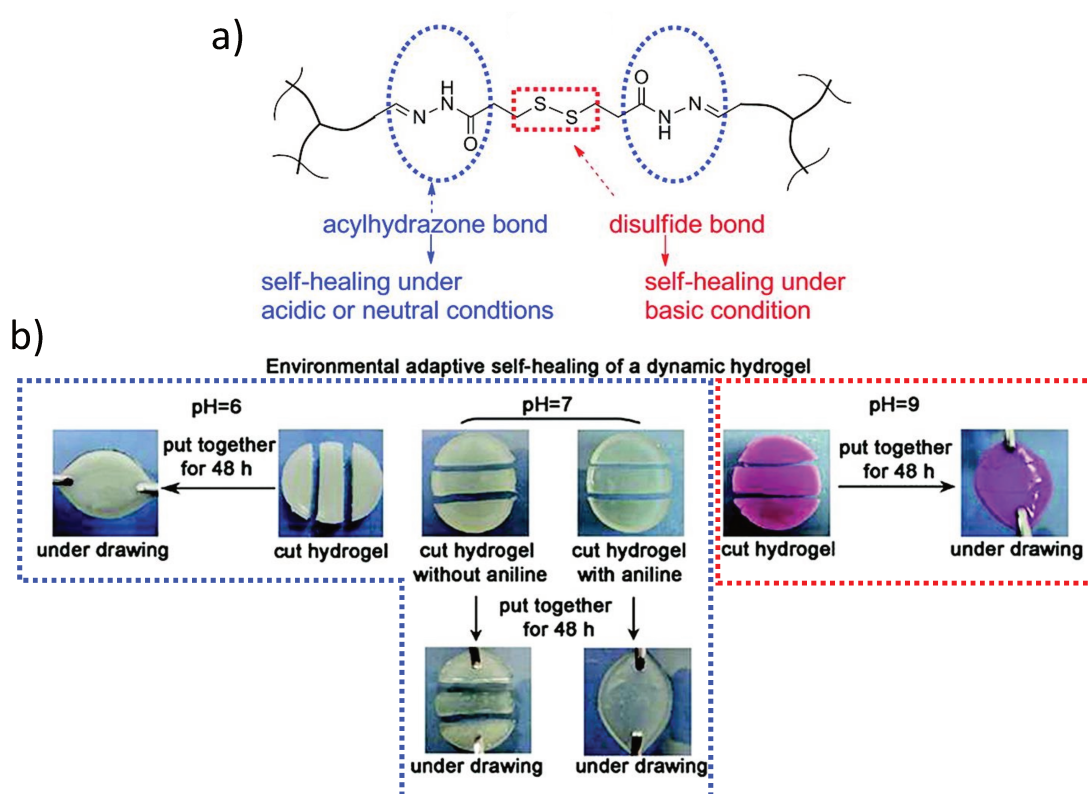
Figure 1.11: (a) Dual dynamic hydrogel based on a combination of acylhydrazone and disulfide DCBs.[45] (b) Self-healing of the hydrogel under acidic, basic, and neutral conditions. Reprinted (adapted) with permission from Reference [45]. Copyright (2012) American Chemical Society.

DCBs, such as acylhydrazone and disulfide bonds, show dynamic behaviors within pH

windows that do not overlap. These two chemistries were successfully combined within a single system to obtain hydrogels with self-healing properties under both acidic and basic conditions, thanks to the dynamic nature of acylhydrazone and disulfide bonds, respectively. Self-healing is also possible under neutral conditions in the presence of aniline. Furthermore, these hydrogels undergo pH-induced and redox-induced reversible gel-sol transitions through the selective cleavage of the acylhydrazone or disulfide bonds, respectively.

1.8 Networks Combining Two Different Structures

The combination of two types of dynamic covalent crosslinkers provides the possibility to intimately blend different polymer structures into one material. Many variations are possible, as the polymer structures might differ with respect to the chemical nature of the matrix, crosslinking chemistry, and crosslinking density. In this section, we focus on interpenetrating networks (IPNs) as well as networks that are chemically connected to each other, which we call "combined networks" for the purposes of this discussion.

1.8.1 Interpenetrated Networks

IPNs are a class of polymer alloys in which two or more networks are at least partially intermeshed at a molecular level but not covalently bonded to each other.[187,188] Such a structure is achieved by polymerizing a monomer that has been pre-swollen within an orthogonal polymer network. The objective of this approach is to realize enhanced mechanical features that cannot be achieved with simple blends of the constituent subnetworks (or with either of the individual subnetworks). In the early 2000s, the Gong group reported outstanding tough hydrogels featuring mechanical properties that arise from the synergy of two interpenetrated networks: a loosely (statically) crosslinked network interwoven with a densely (statically) crosslinked network. The superior mechanical properties stem from the sacrificial breaking of the highly crosslinked network on extension, which leads to energy dissipation. The work of Gong was taken up by Creton and colleagues,[189] who adapted this concept to elastomers. The interplay between both networks leads to a more uniform stress distribution that delays crack propagation. A potential drawback of these systems is the irreversible breakage of bonds, and, thus, the significant weakening of the material after the first high-stress loading. A recent approach to address this issue is the addition of dynamic links. Most examples, thus far, feature

NCBs.[190–195] The introduction of DCBs to IPNs is a new topic of research, and the few examples that exist nicely exemplify the potential of dynamic covalent chemistry, both in terms of versatility and control of the performances. The combination of reversible acylhydrazone and boronic ester crosslinks allowed Yang, Zhang, and colleagues to prepare a multi-functional, self-healing, injectable IPN.[48] The network was synthesized from four functional poly(*N,N*-dimethylacrylamide) prepolymers equipped with either aldehyde, hydrazone, boronic acid, or catechol side-groups. When these prepolymers are mixed together, the aldehyde groups selectively react with the hydrazide to form acylhydrazide linkages, while the boronic acid and the catechol moieties form boronic esters. The orthogonality of the reactions leads to the formation of two interlocking yet independent subnetworks. The innovative synthetic strategy of mixing components together that feature a fast-gelation behavior makes this hydrogel an ideal candidate for 3D-printing solutions. The two bonds display dynamic behavior in different pH ranges. The acylhydazone bonds are stable in mildly acidic environments but dissociate under basic conditions, whereas the boronic ester bonds only form under basic conditions. As a result, the hydrogel self-repairs under both acidic and basic conditions, but it shows chemical stability under neutral conditions. Thus, by varying the pH to acidic (or basic) conditions, one subnetwork undergoes a gel-sol transition while the other one maintains its gel state. This reversible transition from an IPN to a network penetrated by a linear or branched polymer allows for the pH-dependent tuning of the mechanical properties and average pore size of the hydrogel. Another approach for combining two DCBs in an IPN was reported by Rong, Zhang, and co-workers.[46] A bulk IPN was prepared from two single PUR elastomer networks, with one comprising boronic esters and the other comprising disulfides (Figure 1.12). These materials are used to make a reversibly interlocking network (RILN) through the simultaneous and orthogonal exchange of the boronic esters and disulfides present in the respective single networks. The exchange of the DCBs over time leads to the formation of an interlocking topology architecture. In combination with the formation of intermolecular hydrogen bonds between the urethane groups of the two polymer networks, this dynamic interlocking process resulted in the formation of a homogenous material. The RILN shows superior non-linear mechanical properties when compared to the individual subnetworks. This improvement is explained by synergistic effects between structures that lead to improved load bearing capability and more homogeneous stress distribution. The two exchange reactions can be triggered selectively by orthogonal external stimuli. The boronic ester bonds are thermally stable, but they can be cleaved by adding water and reformed when the latter is removed. In contrast, the disulfide bonds are hydrolytically stable and are cleaved homolytically at elevated temperatures. Hence, through the selective hydrolysis of the boronic esters, the

IPN can be disassembled and the original single networks can be recovered.
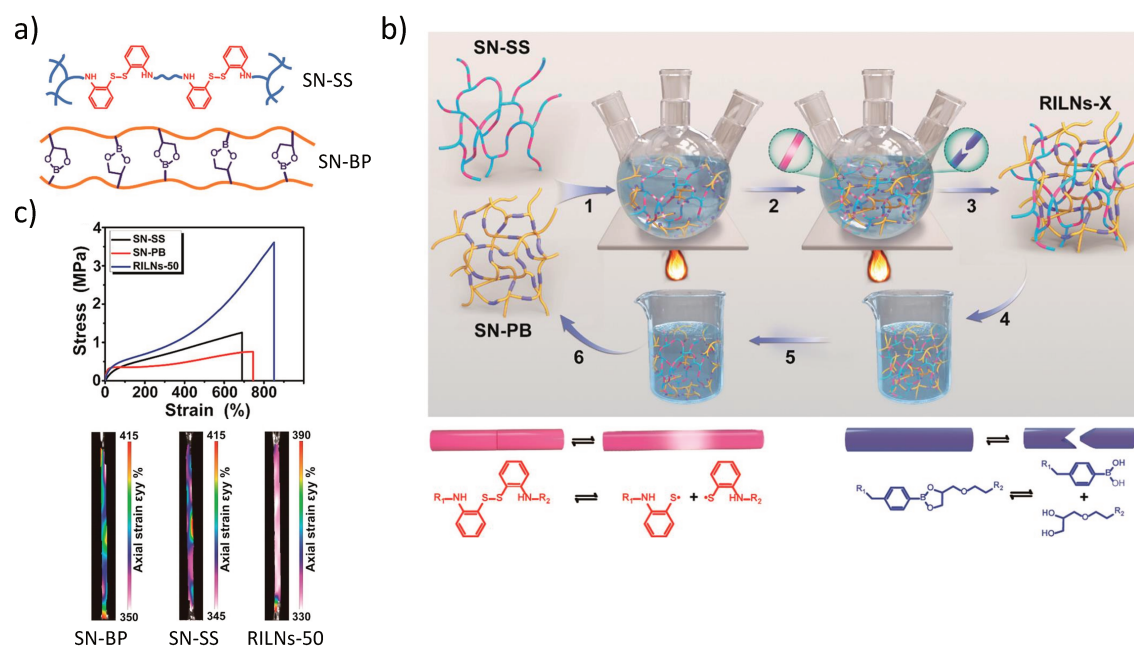
Figure 1.12: Dual dynamic bulk IPN comprising disulfide and boronic ester DCBs.[46] (a) Structure of the disulfide (SN-SS) and the boronic ester (SN-PB) single networks. (b) Synthesis of the IPN. The single networks are mixed (1) and the dynamic bonds dissociate under the influence of heat and moisture (2) and interlock (3) when heating is stopped and moisture removed. The process is reversible through the specific hydrolysis of the boronic ester crosslinks in the presence of water (4 and 5). The individual networks can, thus, be separated (6). (c) Tensile properties of the single networks and the IPN. Due to the synergistic effects of the two interwoven networks, the strain is better distributed in the IPN, which leads to improved mechanical properties. Reprinted (adapted) with permission from Reference [46]. Copyright (2020) American Chemical Society.

Inspired by the groundbreaking work of the Gong group,[196–199] Konkolewicz and co-workers designed dual dynamic IPNs in which the sacrificial bonds are H-bonds formed between pendant 2-ureido-4[1H]-pyrimidinone (UPy) moieties.[40,63,64] The second crosslinker relies on long lifetime DA cycloadducts. Thanks to the high dynamicity of the sacrificial bonds, the network of covalent bonds is conserved, postponing the weakening of the material. The combination of dynamic bonds with two significantly different lifetimes allows for the preparation of IPNs that exhibit improved stress at break and fracture toughness, as well as self-healing and reprocessability, while presenting good creep resistance at room temperature. In one of their studies, Konkolewicz and colleagues

compared the properties of an IPN and a SN, which are both crosslinked with UPy units and DA cycloadducts (Figure 1.13).[40]
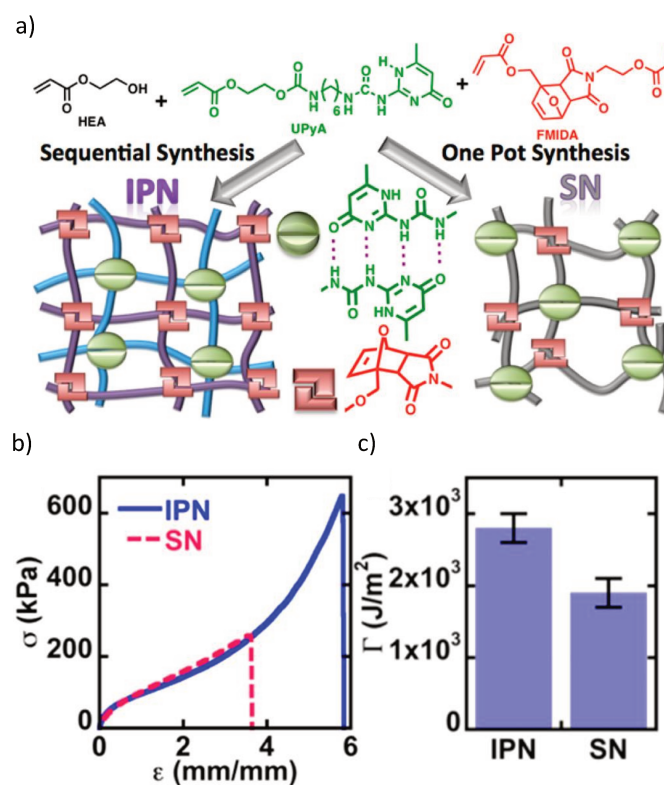
Figure 1.13: DDN incorporating DA cycloadducts and UPy units as dynamic crosslinkers.[40] (a) Synthesis of a dual dynamic IPN through sequential polymerization. Each subnetwork contains solely one type of crosslinker (left). Synthesis of a SN containing both types of crosslinkers via a single step copolymerization (right). (b) Tensile properties of the IPN and the SN. (c) Fracture energies of both networks. The IPN generally displays superior mechanical properties than the SN. Reprinted (adapted) with permission from Reference [40]. Copyright (2017) American Chemical Society.

The IPN features superior mechanical properties, as it exhibits improved peak stress, strain at break, and fracture energy. The IPN also displays strain hardening behavior. The separation of both crosslinkers facilitates the energy dissipation, which is also evident in loading-unloading experiments. The SN shows less creep and longer stress-relaxation. The ability of the IPN to partially relax stress faster at room temperature and

to deform faster during creep experiments likely reflects the capacity of the subnetworks to move independently in combination with the fast dynamics of the UPy subnetwork. However, both networks show complete creep recovery, which is induced by the DA bonds that display a static behavior under the conditions of the creep experiment. With respect to self-healing and malleability, the IPN also outperforms the SN. The decoupling of the networks gives the IPN more degrees of freedom, at least with respect to the subnetwork crosslinked with short lifetime dynamic bonds, thus, facilitating the dynamic bond exchange. The studies of the Konkolewicz group are a striking example on how molecular architecture can influence the macroscopic properties of a DDN.

1.8.2 Combined Networks

In contrast to IPNs, so-called combined networks are constituted of two different network structures that are not necessarily interlaced but are chemically connected. For example, Tao and colleagues used this strategy to design a multi-responsive hydrogel consisting of two different networks crosslinked with dynamic imine and boronic ester moieties.[52] Using the Ugi reaction, a tetrafunctional poly(ethylene glycol) (PEG) with a benzaldehyde group and phenylboronic acid group at each chain-end was prepared from a dicarboxy-homotelechelic PEG. This tetrafunctional PEG was used to generate a combined network by selective crosslinking of the benzaldehyde moieties with glycol chitosan and crosslinking the phenyl boronic acid groups with poly(vinyl alcohol). The combined network shows superior self-healing abilities and good mechanical strength. The synergy between the different network structures also provides the material with enhanced muco-adhesive abilities. Furthermore, the hydrogel shows excellent biocompatibility, and it was injectable thanks to the short lifetime of the dynamic crosslinks. This DDN hydrogel was, thus, used as a drug-delivery carrier to transport the anti-cancer drug doxorubicin to a tumor. The slow and gradual release of the drug associated with the hydrolysis of the crosslinkers shows significant advantages over the direct delivery to the tumor. The Bowman group reported a unique combination of two different polymer networks relying on dynamic and static covalent crosslinks to create an adaptable solid-state photoresist via stereolithography (Figure 1.14).[41] In a typical stereolithography process, a liquid monomer is selectively photo-irradiated to generate an insoluble chemical network where the resin is exposed to light. The unreacted resin is later removed during the development process, typically through dissolution in suitable solvents. However, the creation of 3D objects often requires a physical support to hold the structures during their formation to prevent collapse, sedimentation, or loss of resolution. To address this

challenge, Bowman and colleagues developed a double network photoresist, which is synthesized via a dual-cure process. In the first step, a scaffold network composed of reversible DA adducts is synthesized.
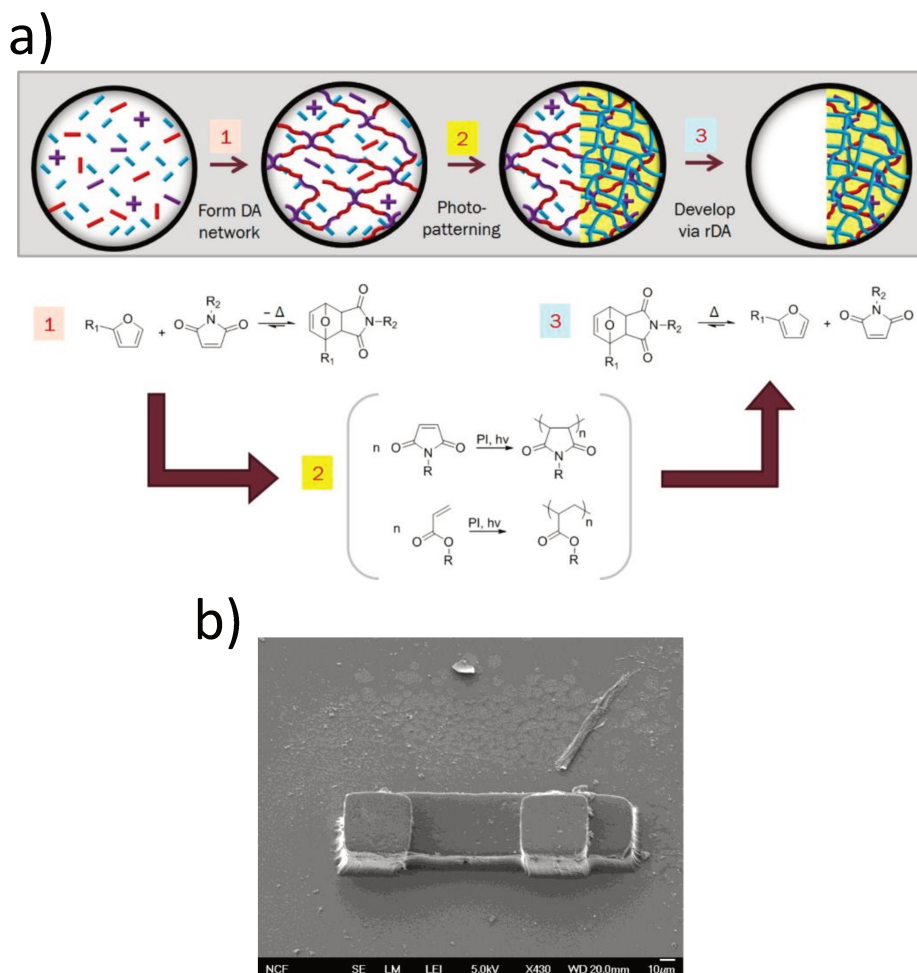
Figure 1.14: Dual cure system based on DA cycloadducts and static covalent bonds.[41] (a) In the first step, the support network is formed via DA cycloaddition (1). During the photopatterning, a static permanent network is created within the DA network (2). In the development step, the support network is removed through thermo-activated rDA depolymerization (3). (b) The scanning electron microscopy image of two-layer structures created with the dual cure photoresist process. Reprinted (adapted) with permission from Reference [41]. Copyright (2014) American Chemical Society.

The "click" nature of this reaction allows for an efficient synthesis of the support network, while the rDA reaction at an elevated temperature imparts thermo-reversibility to the

network. The second step of the curing process consists of the photopolymerization of acrylate monomers present in the supporting network. This strategy allows for the spatial and temporal control over the formation of the second network within the first one. Using a multifunctional crosslinker bearing furan and acrylate functions allows for the covalent connection between the two networks. In the development step, the DA network not involved in the second curing step (i.e., the material that had not been exposed to light irradiation) is removed by thermal depolymerization. The use of an easily-removable scaffold network based on a CAN offers new possibilities for layer-by-layer stereolithography applications, as it addresses the challenging removal of the support material from complex or microscale objects.

1.9 Conclusions and Outlook

This review provides an overview of the development of a new class of CANs that incorporates multiple crosslinkers featuring different degrees of dynamicity. The elaboration of new crosslinking strategies in recent years, combined with the demand for more sophisticated materials, has motivated the design of DDNs, resulting in materials that feature unprecedented properties. By combining DCBs with static covalent, supramolecular, and other kinds of dynamic covalent bonds, materials can exhibit significant advantages over those relying solely on just one kind of dynamic crosslinking. Whereas, in singly crosslinked materials, there are always trade-offs between structural stability, dynamicity, adaptability, and responsiveness, DDNs offer the possibility to combine seemingly contradictory features. The diverse examples presented in this review illustrate how DDNs have already become an indispensable strategy in polymer science with applications already ranging from actuating robots[126] to adaptable bio-materials.[185,186] As the field of CANs continues to mature, more dynamic crosslinkers will be combined in increasingly diverse matrices. A key challenge in this context is that it is not trivial a priori to identify the adequate combination of crosslinkers to realize a targeted set of properties. Moreover, simple and scalable synthetic strategies will need to be developed to allow flexibility in combining different kinds of dynamic crosslinkers. The characterization of DDNs must also be advanced to address the difficulty in differentiating between the individual responses of the different dynamic modes.[135] Although many DDNs are directly compared to their respective single networks, a precise and meaningful comparison is not always achievable in this way. Minor changes in the chemical nature, topology, crosslinking density, and functionality can strongly influence how a given dynamic bond behaves in a

given DDN. The productive future of this field will rely on the simultaneous advancement of modeling, synthesis, characterization, dynamics, and material development. Many intriguing DDNs have already been reported, but even more fascinating paths forward remain open for exploration.

Bibliography

(1) Hammer, L.; Van Zee, N. J.; Nicolaÿ, R. *Polymers (Basel).* **2021**, *13*, DOI: `10.3390/polym13030396`.

(2) Michel Biron, *Thermoplastics and Thermoplastic Composites*, 3rd ed.; Elsevier: Amsterdam, 2018, p 944.

(3) Fouquey, C.; Lehn, J.-M. *Adv. Mater.* **1990**, *2*, 254–257.

(4) Biedermann, F.; Schneider, H. J. *Chem. Rev.* **2016**, *116*, 5216–5300.

(5) Luo, Y.-R., *Comprehensive Handbook of Chemical Bond Energies*, 1st ed.; CRC Press: Boca Raton, FL, USA, 2007.

(6) Lehn, J. M. *Chem. Soc. Rev.* **2007**, *36*, 151–160.

(7) Lehn, J. M. *Polym. Int.* **2002**, *51*, 825–839.

(8) Noro, A.; Hayashi, M.; Matsushita, Y. *Soft Matter* **2012**, *8*, 6416–6429.

(9) Yan, X.; Wang, F.; Zheng, B.; Huang, F. *Chem. Soc. Rev.* **2012**, *41*, 6042–6065.

(10) Aida, T.; Meijer, E. W.; Stupp, S. I. *Science.* **2012**, *335*, 813–817.

(11) Seiffert, S., *Supramolecular Polymer Networks and Gels*; Springer: Berlin/Heidelberg, Germany, 2015; Vol. 268, p 288.

(12) Voorhaar, L.; Hoogenboom, R. *Chem. Soc. Rev.* **2016**, *45*, 4013–4031.

(13) Lehn, J. M. *Chem. Soc. Rev.* **2017**, *46*, 2378–2379.

(14) Kloxin, C. J.; Scott, T. F.; Adzima, B. J.; Bowman, C. N. *Macromolecules* **2010**, *43*, 2643–2653.

(15) Bowman, C. N.; Kloxin, C. J. *Angew. Chemie - Int. Ed.* **2012**, *51*, 4272–4274.

(16) Kloxin, C. J.; Bowman, C. N. *Chem. Soc. Rev.* **2013**, *42*, 7161–7173.

(17) Chen, X.; Dam, M. a.; Ono, K.; Mal, A.; Shen, H.; Nutt, S. R.; Sheran, K.; Wudl, F. *Science.* **2002**, *295*, 1698–1702.

(18) Winne, J. M.; Leibler, L.; Du Prez, F. E. *Polym. Chem.* **2019**, *10*, 6091–6108.

(19) Montarnal, D.; Capelot, M.; Tournilhac, F.; Leibler, L. *Science.* **2011**, *334*, 965–968.

(20) Capelot, M.; Unterlass, M. M.; Tournilhac, F.; Leibler, L. *ACS Macro Lett.* **2012**, *1*, 789–792.

(21)   Van Zee, N. J.; Nicolaÿ, R. *Prog. Polym. Sci.* **2020**, *104*, 101233.

(22)   Brutman, J. P.; Delgado, P. A.; Hillmyer, M. A. *ACS Macro Lett.* **2014**, *3*, 607–610.

(23)   Breuillac, A.; Kassalias, A.; Nicolaÿ, R. *Macromolecules* **2019**, *52*, 7102–7113.

(24)   Obadia, M. M.; Jourdain, A.; Cassagnau, P.; Montarnal, D.; Drockenmuller, E. *Adv. Funct. Mater.* **2017**, *27*, 1703258.

(25)   Delahaye, M.; Winne, J. M.; Du Prez, F. E. *J. Am. Chem. Soc.* **2019**, *141*, 15277–15287.

(26)   Jourdain, A.; Asbai, R.; Anaya, O.; Chehimi, M. M.; Drockenmuller, E.; Montarnal, D. *ACS Appl. Mater. Interfaces* **2020**, *53*, 1884–1900.

(27)   Chakma, P.; Morley, C. N.; Sparks, J. L.; Konkolewicz, D. *Macromolecules* **2020**, *53*, 1233–1244.

(28)   Denissen, W.; Winne, J. M.; Du Prez, F. E. *Chem. Sci.* **2016**, *7*, 30–38.

(29)   Hajj, R.; Duval, A.; Dhers, S.; Avérous, L. *Macromolecules* **2020**, *53*, 3796–3805.

(30)   Nicolaÿ, R.; Kamada, J.; Van Wassen, A.; Matyjaszewski, K. *Macromolecules* **2010**, *43*, 4355–4361.

(31)   Sun, H.; Kabb, C. P.; Sims, M. B.; Sumerlin, B. S. *Prog. Polym. Sci.* **2019**, *89*, 61–75.

(32)   Jiang, Z.; Bhaskaran, A.; Aitken, H. M.; Shackleford, I. C.; Connal, L. A. *Macromol. Rapid Commun.* **2019**, *40*, 1900038.

(33)   Chakma, P.; Konkolewicz, D. *Angew. Chemie - Int. Ed.* **2019**, *58*, 9682–9695.

(34)   Scheutz, G. M.; Lessard, J. J.; Sims, M. B.; Sumerlin, B. S. *J. Am. Chem. Soc.* **2019**, 16181–16196.

(35)   Guerre, M.; Taplan, C.; Winne, J. M.; Du Prez, F. E. *Chem. Sci.* **2020**, 4855–4870.

(36)   Obadia, M. M.; Mudraboyina, B. P.; Serghei, A.; Montarnal, D.; Drockenmuller, E. *J. Am. Chem. Soc.* **2015**, *137*, 6078–6083.

(37)   Yu, S.; Zhang, R.; Wu, Q.; Chen, T.; Sun, P. *Adv. Mater.* **2013**, *25*, 4912–4917.

(38)   Inoue, K.; Yamashiro, M.; Iji, M. *J. Appl. Polym. Sci.* **2009**, *112*, 876–885.

(39)   Yu, F.; Cao, X.; Du, J.; Wang, G.; Chen, X. *ACS Appl. Mater. Interfaces* **2015**, *7*, 24023–24031.

(40)   Foster, E. M.; Lensmeyer, E. E.; Zhang, B.; Chakma, P.; Flum, J. A.; Via, J. J.; Sparks, J. L.; Konkolewicz, D. *ACS Macro Lett.* **2017**, *6*, 495–499.

(41) Berg, G. J.; Gong, T.; Fenoli, C. R.; Bowman, C. N. *Macromolecules* **2014**, *47*, 3473–3482.

(42) Rekondo, A.; Martin, R.; Ruiz De Luzuriaga, A.; Cabañero, G.; Grande, H. J.; Odriozola, I. *Mater. Horizons* **2014**, *1*, 237–240.

(43) Aoki, D.; Teramoto, Y.; Nishio, Y. *Biomacromolecules* **2007**, *8*, 3749–3757.

(44) Ruiz De Luzuriaga, A.; Martin, R.; Markaide, N.; Rekondo, A.; Cabañero, G.; Rodríguez, J.; Odriozola, I. *Mater. Horizons* **2016**, *3*, 241–247.

(45) Deng, G.; Li, F.; Yu, H.; Liu, F.; Liu, C.; Sun, W.; Jiang, H.; Chen, Y. *ACS Macro Lett.* **2012**, *1*, 275–279.

(46) Peng, W. L.; You, Y.; Xie, P.; Rong, M. Z.; Zhang, M. Q. *Macromolecules* **2020**, *53*, 584–593.

(47) Kolomiets, E.; Lehn, J. M. *Chem. Commun.* **2005**, 1519–1521.

(48) Wang, Y.; Yu, H.; Yang, H.; Hao, X.; Tang, Q.; Zhang, X. *Macromol. Chem. Phys.* **2017**, *218*, 1700348.

(49) Collins, J.; Nadgorny, M.; Xiao, Z.; Connal, L. A. *Macromol. Rapid Commun.* **2017**, *38*, 1600760.

(50) Song, F.; Li, Z.; Jia, P.; Zhang, M.; Bo, C.; Feng, G.; Hu, L.; Zhou, Y. *J. Mater. Chem. A* **2019**, *7*, 13400–13410.

(51) Liu, H.; Zhang, H.; Wang, H.; Huang, X.; Huang, G.; Wu, J. *Chem. Eng. J.* **2019**, *368*, 61–70.

(52) Li, Y.; Yang, L.; Zeng, Y.; Wu, Y.; Wei, Y.; Tao, L. *Chem. Mater.* **2019**, *31*, 5576–5583.

(53) Zheng, N.; Fang, Z.; Zou, W.; Zhao, Q.; Xie, T. *Angew. Chemie - Int. Ed.* **2016**, *55*, 11421–11425.

(54) Chen, X.; Li, L.; Jin, K.; Torkelson, J. M. *Polym. Chem.* **2017**, *8*, 6349–6355.

(55) Pei, Z.; Yang, Y.; Chen, Q.; Terentjev, E. M.; Wei, Y.; Ji, Y. *Nat. Mater.* **2014**, *13*, 36–41.

(56) Saed, M. O.; Gablier, A.; Terentejv, E. M. *Adv. Funct. Mater.* **2020**, *30*, 1906458.

(57) Cash, J. J.; Kubo, T.; Dobbins, D. J.; Sumerlin, B. S. *Polym. Chem.* **2018**, *9*, 2011–2020.

(58) Imato, K.; Kanehara, T.; Nojima, S.; Ohishi, T.; Higaki, Y.; Takahara, A.; Otsuka, H. *Chem. Commun.* **2016**, *52*, 10482–10485.

(59)   Lendlein, A.; Jiang, H.; Jünger, O.; Langer, R. *Nature* **2005**, *434*, 879–882.

(60)   McBride, M. K.; Martinez, A. M.; Cox, L.; Alim, M.; Childress, K.; Beiswinger, M.; Podgorski, M.; Worrell, B. T.; Killgore, J.; Bowman, C. N. *Sci. Adv.* **2018**, *4*, DOI: `10.1126/sciadv.aat4634`.

(61)   Roy, N.; Buhler, E.; Lehn, J. M. *Polym. Int.* **2014**, *63*, 1400–1405.

(62)   Zhang, Z. P.; Rong, M. Z.; Zhang, M. Q. *Adv. Funct. Mater.* **2018**, *28*, 1706050.

(63)   Zhang, B.; Digby, Z. A.; Flum, J. A.; Foster, E. M.; Sparks, J. L.; Konkolewicz, D. *Polym. Chem.* **2015**, *6*, 7368–7372.

(64)   Zhang, B.; Ke, J.; Vakil, J. R.; Cummings, S. C.; Digby, Z. A.; Sparks, J. L.; Ye, Z.; Zanjani, M. B.; Konkolewicz, D. *Polym. Chem.* **2019**, *10*, 6290–6304.

(65)   Jian, X.; Hu, Y.; Zhou, W.; Xiao, L. *Polym. Adv. Technol.* **2018**, *29*, 463–469.

(66)   Liu, J.; Ma, X.; Tong, Y.; Lang, M. *Appl. Surf. Sci.* **2018**, *455*, 318–325.

(67)   Xu, W. M.; Rong, M. Z.; Zhang, M. Q. *J. Mater. Chem. A* **2016**, *4*, 10683–10690.

(68)   Neal, J. A.; Mozhdehi, D.; Guan, Z. *J. Am. Chem. Soc.* **2015**, *137*, 4846–4850.

(69)   Liu, Y.; Tang, Z.; Wu, S.; Guo, B. *ACS Macro Lett.* **2019**, *8*, 193–199.

(70)   Liu, Y.; Tang, Z.; Wang, D.; Wu, S.; Guo, B. *J. Mater. Chem. A* **2019**, *7*, 26867–26876.

(71)   Wang, S.; Ma, S.; Li, Q.; Xu, X.; Wang, B.; Huang, K.; Liu, Y.; Zhu, J. *Macromolecules* **2020**, *53*, 2919–2931.

(72)   Sánchez-Morán, H.; Ahmadi, A.; Vogler, B.; Roh, K. H. *Biomacromolecules* **2019**, *20*, 4419–4429.

(73)   Niu, X.; Wang, F.; Kui, X.; Zhang, R.; Wang, X.; Li, X.; Chen, T.; Sun, P.; Shi, A. C. *Macromol. Rapid Commun.* **2019**, *40*, 1900313.

(74)   Wang, Z.; Tian, H.; He, Q.; Cai, S. *ACS Appl. Mater. Interfaces* **2017**, *9*, 33119–33128.

(75)   Li, Y.; Zhang, Y.; Rios, O.; Keum, J. K.; Kessler, M. R. *Soft Matter* **2017**, *13*, 5021–5027.

(76)   Li, Y.; Zhang, Y.; Rios, O.; Keum, J. K.; Kessler, M. R. *RSC Adv.* **2017**, *7*, 37248–37254.

(77)   Wen, Z.; McBride, M. K.; Zhang, X.; Han, X.; Martinez, A. M.; Shao, R.; Zhu, C.; Visvanathan, R.; Clark, N. A.; Wang, Y.; Yang, K.; Bowman, C. N. *Macromolecules* **2018**, *51*, 5812–5819.

(78) Yang, Y.; Pei, Z.; Li, Z.; Wei, Y.; Ji, Y. *J. Am. Chem. Soc.* **2016**, *138*, 2118–2121.

(79) Yang, Y.; Terentjev, E. M.; Zhang, Y.; Chen, Q.; Zhao, Y.; Wei, Y.; Ji, Y. *Angew. Chemie - Int. Ed.* **2019**, *58*, 17474–17479.

(80) Pei, Z.; Yang, Y.; Chen, Q.; Wei, Y.; Ji, Y. *Adv. Mater.* **2016**, *28*, 156–160.

(81) Li, Y.; Rios, O.; Keum, J. K.; Chen, J.; Kessler, M. R. *ACS Appl. Mater. Interfaces* **2016**, *8*, 15750–15757.

(82) Lu, X.; Guo, S.; Tong, X.; Xia, H.; Zhao, Y. *Adv. Mater.* **2017**, *29*, 1606467.

(83) Chen, Q.; Li, Y.; Yang, Y.; Xu, Y.; Qian, X.; Wei, Y.; Ji, Y. *Chem. Sci.* **2019**, *10*, 3025–3030.

(84) Lawton, M. I.; Tillman, K. R.; Mohammed, H. S.; Kuang, W.; Shipp, D. A.; Mather, P. T. *ACS Macro Lett.* **2016**, *5*, 203–207.

(85) Defize, T.; Riva, R.; Thomassin, J. M.; Alexandre, M.; Van Herck, N.; Du Prez, F.; Jérôme, C. *Macromol. Rapid Commun.* **2017**, *38*, 1600517.

(86) Zhang, J.; Niu, Y.; Huang, C.; Xiao, L.; Chen, Z.; Yang, K.; Wang, Y. *Polym. Chem.* **2012**, *3*, 1390–1393.

(87) Defize, T.; Riva, R.; Raquez, J. M.; Dubois, P.; Jérôme, C.; Alexandre, M. *Macromol. Rapid Commun.* **2011**, *32*, 1264–1269.

(88) Zhang, G.; Zhao, Q.; Yang, L.; Zou, W.; Xi, X.; Xie, T. *ACS Macro Lett.* **2016**, *5*, 805–808.

(89) Kuang, X.; Liu, G.; Dong, X.; Wang, D. *Polymer (Guildf).* **2016**, *84*, 1–9.

(90) Michal, B. T.; Jaye, C. A.; Spencer, E. J.; Rowan, S. J. *ACS Macro Lett.* **2013**, *2*, 694–699.

(91) Zhang, S.; Pan, L.; Xia, L.; Sun, Y.; Liu, X. *React. Funct. Polym.* **2017**, *121*, 8–14.

(92) Xu, Y.; Chen, D. *Macromol. Chem. Phys.* **2016**, *217*, 1191–1196.

(93) Fang, Z.; Zheng, N.; Zhao, Q.; Xie, T. *ACS Appl. Mater. Interfaces* **2017**, *9*, 22077–22082.

(94) Zheng, N.; Hou, J.; Xu, Y.; Fang, Z.; Zou, W.; Zhao, Q.; Xie, T. *ACS Macro Lett.* **2017**, *6*, 326–330.

(95) Zhao, Q.; Zou, W.; Luo, Y.; Xie, T. *Sci. Adv.* **2016**, *2*, e1501297.

(96) Gao, Y.; Liu, W.; Zhu, S. *Macromolecules* **2018**, *51*, 8956–8963.

(97) Liu, T.; Hao, C.; Wang, L.; Li, Y.; Liu, W.; Xin, J.; Zhang, J. *Macromolecules* **2017**, *50*, 8588–8597.

(98) Röttger, M.; Domenech, T.; Van Der Weegen, R.; Breuillac, A.; Nicolaÿ, R.; Leibler, L. *Science.* **2017**, *356*, 62–65.

(99) Ricarte, R. G.; Tournilhac, F.; Leibler, L. *Macromolecules* **2019**, *52*, 432–443.

(100) Wang, P.; Deng, G.; Zhou, L.; Li, Z.; Chen, Y. *ACS Macro Lett.* **2017**, *6*, 881–886.

(101) Altuna, F. I.; Casado, U.; Dell'Erba, I. E.; Luna, L.; Hoppe, C. E.; Williams, R. J. *Polym. Chem.* **2020**, *11*, 1337–1347.

(102) R. J. Statz In *Seymour R.B., Cheng T. Hist. Polyolefins*, 7th ed.; Springer: Dordrecht, 1989; Vol. 7, pp 172–192.

(103) Legge, N. R. *Rubber Chem. Technol.* **1989**, *62*, 529–547.

(104) Spontak, R. J.; Patel, N. P. *Curr. Opin. Colloid Interface Sci.* **2000**, *5*, 333–340.

(105) Amin, S.; Amin, M. *Rev. Adv. Mater. Sci.* **2011**, *29*, 15–30.

(106) Fazli, A.; Rodrigue, D. *Materials (Basel).* **2020**, *13*, 782.

(107) Ishihara, H.; Kimura, I.; Saito, K.; Ono, H. *J. Macromol. Sci. Part B Phys.* **1974**, *10*, 591–618.

(108) Petrovic, Z. S.; Ferguson, J. *Prog. Polym. Sci.* **1991**, *16*, 695–836.

(109) Wang, X.; Wei, Y.; Chen, D.; Bai, Y. *J. Macromol. Sci. Part A Pure Appl. Chem.* **2017**, *54*, 956–966.

(110) Otsuka, H.; Nagano, S.; Kobashi, Y.; Maeda, T.; Takahara, A. *Chem. Commun.* **2010**, *46*, 1150–1152.

(111) Canadell, J.; Goossens, H.; Klumperman, B. *Macromolecules* **2011**, *44*, 2536–2541.

(112) Xu, M.; Cheng, B.; Sheng, Y.; Zhou, J.; Wang, M.; Jiang, X.; Lu, X. *ACS Appl. Polym. Mater.* **2020**, *2*, 2228–2237.

(113) Lendlein, A.; Kelch, S. *Angew. Chem. Int. Ed. Engl.* **2002**, *41*, 2034–2057.

(114) Liu, C.; Qin, H.; Mather, P. T. *J. Mater. Chem.* **2007**, *17*, 1543–1558.

(115) Behl, M.; Razzaq, M. Y.; Lendlein, A. *Adv. Mater.* **2010**, *22*, 3388–3410.

(116) Leng, J.; Lan, X.; Liu, Y.; Du, S. *Prog. Mater. Sci.* **2011**, *56*, 1077–1135.

(117) Hu, J.; Zhu, Y.; Huang, H.; Lu, J. *Prog. Polym. Sci.* **2012**, *37*, 1720–1763.

(118) Hager, M. D.; Bode, S.; Weber, C.; Schubert, U. S. *Prog. Polym. Sci.* **2015**, *49-50*, 3–33.

(119) Davis, F. J. *J. Mater. Chem.* **1993**, *3*, 551–562.

(120) Finkelmann, H.; Nishikawa, E.; Pereira, G. G.; Warner, M. *Phys. Rev. Lett.* **2001**, *87*, 015501/1–015501/4.

(121) Mayer, S.; Zentel, R. *Curr. Opin. Solid State Mater. Sci.* **2002**, *6*, 545–551.

(122) Warner, M.; Terentjev, E. M., *Liquid crystal elastomers*; Oxford University Press: Oxford, UK, 2003, 424p.

(123) Lewis, C. L.; Dell, E. M. *J. Polym. Sci. Part B Polym. Phys.* **2016**, *54*, 1340–1364.

(124) Wu, Y.; Wei, Y.; Ji, Y. *Polym. Chem.* **2020**, *11*, 5297–5320.

(125) Hoekstra, D. C.; Schenning, A. P.; Debije, M. G. *Soft Matter* **2020**, *16*, 5106–5119.

(126) Jin, B.; Song, H.; Jiang, R.; Song, J.; Zhao, Q.; Xie, T. *Sci. Adv.* **2018**, *4*, eaao3865.

(127) Wool, R. P.; O'Connor, K. M. *J. Appl. Phys* **1981**, *52*, 5953.

(128) Li, L.; Chen, X.; Torkelson, J. M. *Macromolecules* **2019**, *52*, 8207–8216.

(129) Chen, M.; Zhou, L.; Wu, Y.; Zhao, X.; Zhang, Y. *ACS Macro Lett.* **2019**, *8*, 255–260.

(130) Fortman, D. J.; Brutman, J. P.; Cramer, C. J.; Hillmyer, M. A.; Dichtel, W. R. *J. Am. Chem. Soc.* **2015**, *137*, 14019–14022.

(131) Fortman, D. J.; Brutman, J. P.; Hillmyer, M. A.; Dichtel, W. R. *J. Appl. Polym. Sci.* **2017**, *134*, 44984.

(132) Fortman, D. J.; Snyder, R. L.; Sheppard, D. T.; Dichtel, W. R. *ACS Macro Lett.* **2018**, *7*, 1226–1231.

(133) Wen, Z.; Han, X.; Fairbanks, B. D.; Yang, K.; Bowman, C. N. *Polymer (Guildf).* **2020**, *202*, 122715.

(134) Roy, C. D.; Brown, H. C. *J. Organomet. Chem.* **2007**, *692*, 784–790.

(135) Guerre, M.; Taplan, C.; Nicolaÿ, R.; Winne, J. M.; Du Prez, F. E. *J. Am. Chem. Soc.* **2018**, *140*, 13272–13284.

(136) Denissen, W.; Rivero, G.; Nicolaÿ, R.; Leibler, L.; Winne, J. M.; Du Prez, F. E. *Adv. Funct. Mater.* **2015**, *25*, 2451–2457.

(137) Denissen, W.; Droesbeke, M.; Nicola, R.; Leibler, L.; Winne, J. M.; Du Prez, F. E. *Nat. Commun.* **2017**, *8*, 14857.

(138) Chen, Y.; Tang, Z.; Liu, Y.; Wu, S.; Guo, B. *Macromolecules* **2019**, *52*, 3805–3812.

(139) Ji, F.; Liu, X.; Lin, C.; Zhou, Y.; Dong, L.; Xu, S.; Sheng, D.; Yang, Y. *Macromol. Mater. Eng.* **2019**, *304*, 1800528.

(140) Tanaka, R.; Tonoko, N.; Kihara, S.-I.; Nakayama, Y.; Shiono, T. *Polym. Chem* **2018**, *9*, 3774.

(141) Caffy, F.; Nicolaÿ, R. *Polym. Chem.* **2019**, *10*, 3107–3115.

(142) Tellers, J.; Pinalli, R.; Soliman, M.; Vachon, J.; Dalcanale, E. *Polym. Chem* **2019**, *10*, 5534.

(143) Prasanna Kar, G.; Osman Saed, M.; Michael Terentjev, E. *J. Mater. Chem. A* **2020**, *8*, 24137.

(144) Ricarte, R. G.; Ois Tournilhac, F.; Cloître, M.; Leibler, L. *Macromolecules* **2020**, *53*, 1852–1866.

(145) Yang, F.; Pan, L.; Ma, Z.; Lou, Y.; Li, Y.; Li, Y. *Polym. Chem* **2020**, *11*, 3285.

(146) Zych, A.; Pinalli, R.; Soliman, M.; Jerome Vachon; Dalcanale, E. *Polymer (Guildf).* **2020**, *199*, 122567.

(147) Lessard, J. J.; Garcia, L. F.; Easterling, C. P.; Sims, M. B.; Bentz, K. C.; Arencibia, S.; Savin, D. A.; Sumerlin, B. S. *Macromolecules* **2019**, *52*, 2105–2111.

(148) Zhang, H.; Wang, D.; Liu, W.; Li, P.; Liu, J.; Liu, C.; Zhang, J.; Zhao, N.; Xu, J. *J. Polym. Sci. Part A Polym. Chem.* **2017**, *55*, 2011–2018.

(149) Li, L.; Chen, X.; Jin, K.; Torkelson, J. M. *Macromolecules* **2018**, *51*, 5537–5546.

(150) Capelot, M.; Montarnal, D.; Ois Tournilhac, F.; Leibler, L. *J. Am. Chem. Soc* **2012**, *134*, 7664–7667.

(151) Lu, Y.-X.; Guan, Z. *J. Am. Chem. Soc* **2012**, *134*, 14226–14231.

(152) Legrand, A.; Soulié-, C.; Ziakovic, S. *Macromolecules* **2016**, *49*, 5893–5902.

(153) Chabert, E.; Vial, J.; Cauchois, J. P.; Mihaluta, M.; Tournilhac, F. *Soft Matter* **2016**, *12*, 4838–4845.

(154) Yoon, J. A.; Kamada, J.; Koynov, K.; Mohin, J.; Nicolaÿ, R.; Zhang, Y.; Balazs, A. C.; Kowalewski, T.; Matyjaszewski, K. *Macromolecules* **2012**, *45*, 142–149.

(155) Kolmakov, G. V.; Matyjaszewski, K.; Balazs, A. C. *ACS Nano* **2009**, *3*, 885–892.

(156) Imbernon, L.; Oikonomou, E. K.; Norvez, S.; Leibler, L. *Polym. Chem.* **2015**, *6*, 4271–4278.

(157) Spiesschaert, Y.; Guerre, M.; De Baere, I.; Van Paepegem, W.; Winne, J. M.; Du Prez, F. E. *Macromolecules* **2020**, *53*, 2485–2495.

(158) Peppas, N. A.; Hilt, J. Z.; Khademhosseini, A.; Langer, R. *Adv. Mater.* **2006**, *18*, 1345–1360.

(159) Ullah, F.; Othman, M. B. H.; Javed, F.; Ahmad, Z.; Akil, H. M. *Mater. Sci. Eng. C* **2015**, *57*, 414–433.

(160) Jayawarna, V.; Ali, M.; Jowitt, T. A.; Miller, A. F.; Saiani, A.; Gough, J. E.; Ulijn, R. V. *Adv. Mater.* **2006**, *18*, 611–614.

(161) Tibbitt, M. W.; Anseth, K. S. *Biotechnol. Bioeng.* **2009**, *103*, 655–663.

(162) Parente, M. E.; Ochoa Andrade, A.; Ares, G.; Russo, F.; Jiménez-Kairuz, A. *Int. J. Cosmet. Sci.* **2015**, *37*, 511–518.

(163) Bashir, R.; Hilt, J. Z.; Elibol, O.; Gupta, A.; Peppas, N. A. *Appl. Phys. Lett.* **2002**, *81*, 3091–3093.

(164) Lin, C.; Gitsov, I. *Macromolecules* **2010**, *43*, 10017–10030.

(165) Vermonden, T.; Censi, R.; Hennink, W. E. *Chem. Rev.* **2012**, *112*, 2853–2888.

(166) Lee, K. Y.; Mooney, D. J. *Chem. Rev.* **2001**, *101*, 1869–1879.

(167) Nguyen, K. T.; West, J. L. *Biomaterials* **2002**, *23*, 4307–4314.

(168) Zhu, J.; Marchant, R. E. *Expert Rev.Med.Devices* **2011**, *8*, 607–626.

(169) Mohammadinejad, R. et al. *Appl. Mater. Today* **2019**, *16*, 213–246.

(170) Mitura, S.; Sionkowska, A.; Jaiswal, A. *J. Mater. Sci. Mater. Med.* **2020**, *31*, 50.

(171) Klein, M.; Poverenov, E. *J. Sci. Food Agric.* **2020**, *100*, 2337–2347.

(172) Hao, J.; Weiss, R. A. *Polymer (Guildf).* **2013**, *54*, 2174–2182.

(173) Li, J.; Suo, Z.; Vlassak, J. J. *J. Mater. Chem. B* **2014**, *2*, 6708–6713.

(174) Li, J.; Illeperuma, W. R. K.; Suo, Z.; Vlassak, J. J. *ACS Macro Lett* **2014**, *3*, 520–523.

(175) Zhou, H.; Xu, G.; Li, J.; Zeng, S.; Zhang, X.; Zheng, Z.; Ding, X.; Chen, W.; Wang, Q.; Zhang, W. *Macromol. Res.* **2015**, *23*, 1098–1102.

(176) Hu, X.; Vatankhah-Varnoosfaderani, M.; Zhou, J.; Li, Q.; Sheiko, S. S. *Adv. Mater.* **2015**, *27*, 6899–6905.

(177) Hackelbusch, S.; Rossow, T.; Becker, H.; Seiffert, S. *Macromolecules* **2014**, *47*, 4028–4036.

(178) Chen, Q.; Yan, X.; Zhu, L.; Chen, H.; Jiang, B.; Wei, D.; Huang, L.; Yang, J.; Liu, B.; Zheng, J. *Chem. Mater.* **2016**, *28*, 5710–5720.

(179) Jia, H.; Huang, Z.; Fei, Z.; Dyson, P. J.; Zheng, Z.; Wang, X. *ACS Appl. Mater. Interfaces* **2016**, *8*, 31339–31347.

(180) Brassinne, J.; Gohy, J. F.; Fustin, C. A. *ACS Macro Lett.* **2016**, *5*, 1364–1368.

(181) Qin, Z.; Niu, R.; Tang, C.; Xia, J.; Ji, F.; Dong, D.; Zhang, H.; Zhang, S.; Li, J.; Yao, F. *Macromol. Mater. Eng.* **2018**, *303*, 1700396.

(182) Guo, Z.; Gu, H.; He, Y.; Zhang, Y.; Xu, W.; Zhang, J.; Liu, Y.; Xiong, L.; Chen, A.; Feng, Y. *Chem. Eng. J.* **2020**, *388*, 124282.

(183) Li, Z.; Zhou, F.; Li, Z.; Lin, S.; Chen, L.; Liu, L.; Chen, Y. *ACS Appl. Mater. Interfaces* **2018**, *10*, 25194–25202.

(184) Guo, Z.; Ma, W.; Gu, H.; Feng, Y.; He, Z.; Chen, Q.; Mao, X.; Zhang, J.; Zheng, L. *Soft Matter* **2017**, *13*, 7371–7380.

(185) Guo, R.; Su, Q.; Zhang, J.; Dong, A.; Lin, C.; Zhang, J. *Biomacromolecules* **2017**, *18*, 1356–1364.

(186) Chen, J.; Su, Q.; Guo, R.; Zhang, J.; Dong, A.; Lin, C.; Zhang, J. *Macromol. Chem. Phys.* **2017**, *218*, 1700166.

(187) Alemán, J.; Chadwick, A. V.; He, J.; Hess, M.; Horie, K.; Jones, R. G.; Kratochvíl, P.; Meisel, I.; Mita, I.; Moad, G.; Penczek, S.; Stepto, R. F. *Pure Appl. Chem.* **2007**, *79*, 1801–1829.

(188) Dragan, E. S. *Chem. Eng. J.* **2014**, *243*, 572–590.

(189) Ducrot, E.; Chen, Y.; Bulters, M.; Sijbesma, R. P.; Creton, C. *Science.* **2014**, *344*, 186–189.

(190) Asmarandei, I.; Fundueanu, G.; Cristea, M.; Harabagiu, V.; Constantin, M. *J. Polym. Res.* **2013**, *20*, 700487.

(191) Yang, J.; Ma, M.; Zhang, X.; Xu, F. *Macromolecules* **2016**, *49*, 4340–4348.

(192) Zhang, Y.; Wu, F.; Li, M.; Wang, E. *Polymer (Guildf).* **2005**, *46*, 7695–7700.

(193) Wu, W.; Wang, D. S. *React. Funct. Polym.* **2010**, *70*, 684–691.

(194) Xing, Z.; Wang, C.; Yan, J.; Zhang, L.; Li, L.; Zha, L. *Soft Matter* **2011**, *7*, 7992–7997.

(195) Wu, Y.; Hu, J.; Han, J.; Zhu, Y.; Huang, H.; Li, J.; Tang, B. *J. Mater. Chem. A* **2014**, *2*, 18816–18822.

(196) Gong, J. P.; Katsuyama, Y.; Kurokawa, T.; Osada, Y. *Adv. Mater.* **2003**, *15*, 1155–1158.

(197) Gong, J. P. *Soft Matter* **2010**, *6*, 2583–2590.

(198) Haque, M. A.; Kurokawa, T.; Gong, J. P. *Polymer (Guildf).* **2012**, *53*, 1805–1822.

(199) Gong, J. P. *Science.* **2014**, *344*, 161–162.

2 | P*n*BA Vitrimers Based on Dioxaborolane Exchange

Chapter Contents

2.1 Introduction

Boronic acids are boron-containing trivalent structures that possess one carbon-based substituent and two hydroxyl groups. The boron atom is sp^2-hybridized with six valence electrons and a vacant p-orbital. Boronic acids are not found in nature but can be prepared synthetically from primary sources of boron such as boric acid.[1] The first boronic acid was prepared in the 1860s by Sir Edward Frankland.[2] Since then, boronic acids and their esters have found application in multiple fields such as organic[3–6] and medical chemistry[7,8]. One outstanding application is their use as coupling agents in Suzuki coupling reactions,[9–11] which awarded Professor Akira Suzuki the Nobel Prize in chemistry in 2010.[12] In general, organoboron compounds are easy to synthesize and handle and show no serious hazards regarding their reactivity, toxicity or impact on the environment.[1,3] Boronic acids can form a variety of DCBs. The dehydration of boronic acids leads to boroxines that can reversibly be retransformed into boronic acids by hydrolysis. Boronic acids can also be transformed into esters by condensation with alcohol groups. Boronic ester formations generally occur with 1,2- or 1,3-diol groups, yielding conformationally favored 5- or 6-membered rings like shown in Scheme 2.1. The formation of cyclic boronic esters was firstly reported more than 60 years ago.[13] Under neutral or acidic conditions, boronic esters are prone to hydrolysis. The equilibrium can be readily controlled by the addition or removal of water or Lewis bases.
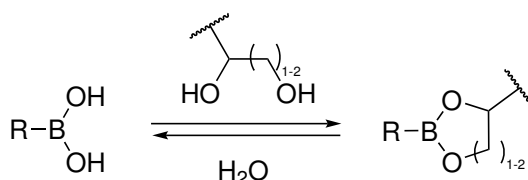
Scheme 2.1: Boronic acids undergo condensation reactions with 1,2- or 1,3-diol groups to form 5- or 6-membered cyclic boronic esters.

Boronic acids and esters have been widely applied in polymers. Their reversibility and response to moisture, pH and competitive molecules allow to design dynamic materials that can self-heal[14–20] or self-assemble[21–23]. Boronic esters can undergo transesterifications with diols like shown in Scheme 2.2. The rate of the transesterification is dependent on the structure of the boronic ester. It has been found[24] that alkyl substituents on the α-position of the diols slow down the transesterification but yield thermodynamically more stable boronic esters. It was also observed that 6-membered boronic ester rings are more stable than their 5-membered counter parts.[24,25] The exchange rate can also be tuned by neighboring groups adjacent to the boronic ester group.[26]
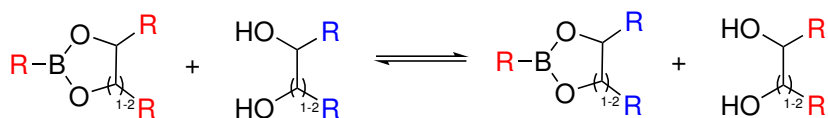
Scheme 2.2: Transesterification between a boronic ester and a 1,2- or 1,3-diol.

In 2017 Nicolaÿ, Leibler and co-workers reported that boronic esters can undergo metathesis reactions like displayed in Scheme 2.3 without the addition of a catalyst.[27] The boronic ester metathesis showed to have an E_a of 15.9 kJ/mol in small molecules that show rapid metathesis reaction at moderate temperatures.[27] During the reaction no intermediate water or diol products could be detected, indicating a degenerate exchange mechanism. The boronic ester metathesis was applied to create vitrimers from polymers like poly(methyl methacrylate) (PMMA), polystyrene (PS) or high-density polyethylene (HDPE).[27] It was found that transesterifications between boronic esters and diols occur in general much faster than the respective metathesis reaction.[28] Also humidity can play a significant role in the exchange process: the cleavage of the crosslinks via hydrolysis leads to an accelerated crosslink exchange.[28]
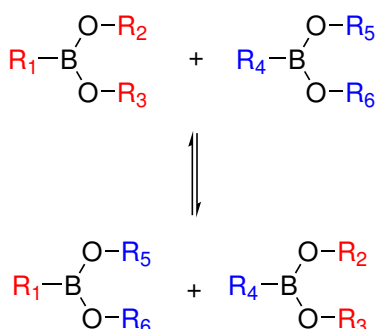
Scheme 2.3: Boronic esters can undergo metathesis reactions with other boronic esters via a degenerate pathway.

Since then, boronic ester exchanges have been applied to form a variety of vitrimers.[29–35] Their high tolerance for other functional groups makes them ideal candidates to be incorporated into DDNs. Systems have been developed where boronic ester exchanges were combined with permanent static bonds,[29,34] liquid crystalline domains,[34] coordination bonds,[32] or metal-ligand coordinations.[30]

The goal of this project is to create an interpenetrated DDN in which one of the subnetworks relies on an exchange via boronic ester metathesis. This network should show dynamic properties like rapid stress relaxation, and fast reshuffling. The tolerance towards other functional groups makes boronic esters a good candidate to be the base

of one of the subnetworks. It has to be evaluated, if a boronic ester based material would form a dynamic enough material. The boronic ester network should represent a sacrificial network, the fast exchange of the boronic ester bonds is supposed to dissipate energy. In this chapter, the synthesis and the characterization of the boronic ester based subnetwork is described. A functional monomer was synthesized and copolymerized with *n*-butyl acrylate (*n*BA). The resulting polymer was further functionalized to yield a TP with pendent boronic ester moieties. A bifunctional boronic ester crosslinker was synthesized and the thermoplastic precursor was crosslinked to yield the boronic ester network that was processed by compression molding. The network was characterized to determine if it fulfills the requirements to be used as the dynamic subnetwork in the double network system. Characterizations included swelling and solubility tests, infrared (IR) spectrometry, DMA, differential scanning calorimetry (DSC), thermal gravimetric analysis (TGA), tensile tests and rheometry (stress relaxation, creep resistance). The properties of the subnetwork are compared to those of the double network in the Chapter 5.

2.2 Monomer Synthesis

To synthesize the thermoplastic that forms the boronic ester subnetwork (hereinafter referred to as **Network 1**) an acrylate monomer with a corresponding pendent functionality has to be synthesized. In this case, this could either be a monomer with a diol function or a monomer carrying a phenylboronic ester. A very straight forward way to synthesize the latter one is to start with the esterification of 1,2,6-hexanetriol with phenylboronic acid (PBA) followed by the condensation of the remaining alcohol function with acryloyl chloride like depicted in Scheme 2.4.

The first step of this reaction worked well and compound **2** was obtained in high yields. However, the PBA moiety is very sensitive to hydrolysis. The second step, the condensation of acryloyl chloride with **2**, is accompanied with the formation of HCl. To drive the reaction equilibrium to the product side, the HCl has to be continuously removed from the reaction mixture. A possible method is to add a base, e.g., triethylamine (NEt$_3$), to neutralize the HCl. This bears the disadvantage that the base (or the respective formed salt) has to be removed after the reaction to purify the product, which involves aqueous washing, risking a loss of yield and unwanted side products due to hydrolysis. As a result, an alternative reaction method was attempted to avoid the use of a base: it was tried to remove the HCl by venting the formed gas through washing bottles equipped with NaOH. However, this attempt was unsuccessful. The formed HCl presumably stayed in
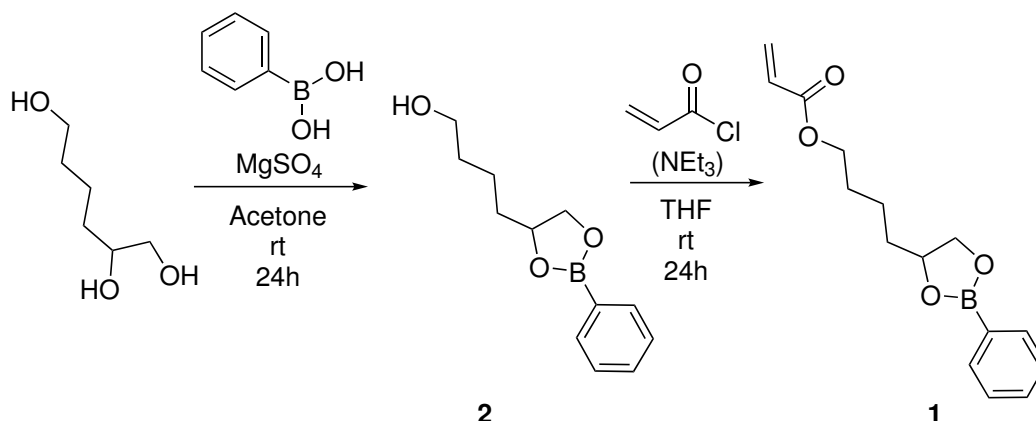
Scheme 2.4: Synthesis of a monomer with a pendent boronic ester functionality **1**.

the reaction mixture and prevented the equilibrium to drive to the product side. As can be seen in the nuclear magnetic resonance (NMR) spectrum (Figure 2.1), only a part of the reactant **2** was converted.
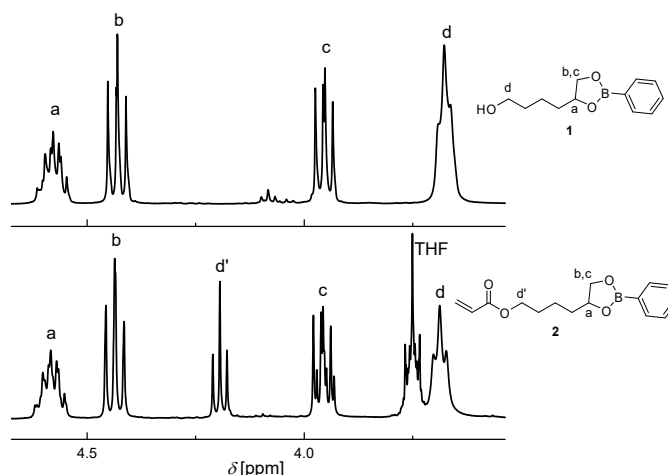
Figure 2.1: Characteristic peaks of the ^{1}H NMR spectrum (in CDCl$_3$, at 400 MHz, zoomed in the 4.7-3.5 ppm region) of **2** and **1**. A successful esterification is indicated by the shift of peak **d** → **d'** to the downfield. As can be seen, the reaction was not complete.

Hence, the driving force of the reaction was too low. An alternative procedure would be the acrylation in presence of the base and a subsequent separation of the product via column chromatography (CC). However, the silica gel used as stationary phase turned out to be acidic enough to cause a de novo cleavage of the boronic ester group. The monomer could therefore not be purified. As an alternative reaction route, 1,2,6-hexanetriol can be

protected via an acetal, a protecting group significantly more stable towards hydrolysis than PBA, to yield compound **3**. The protection was conducted by a reaction of the triol with acetone, which is additionally also cheaper than PBA. After the protection of the diol, the remaining hydroxyl group was esterified with acryloyl chloride. The resulting acrylic monomer **4** (Scheme 2.5) could be easily purified by several aqueous washing steps and is obtained in acceptable yields (44 % overall yield over two steps).
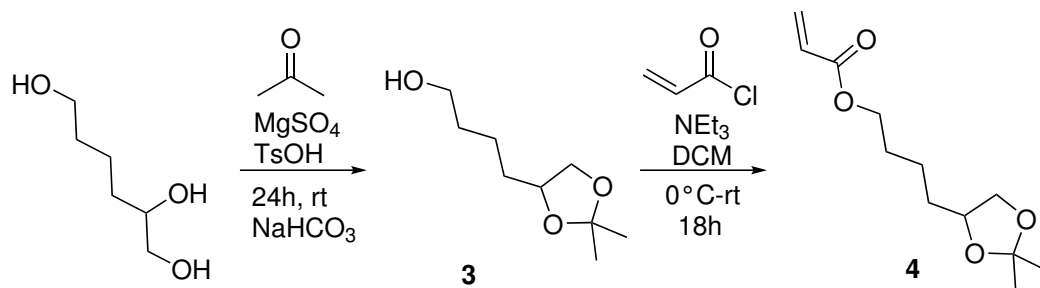
Scheme 2.5: Synthesis of monomer **4** with a diol protected by an acetal group.

It was attempted to subsequently exchange the protecting group with the boronic ester one as depicted in Scheme 2.6.
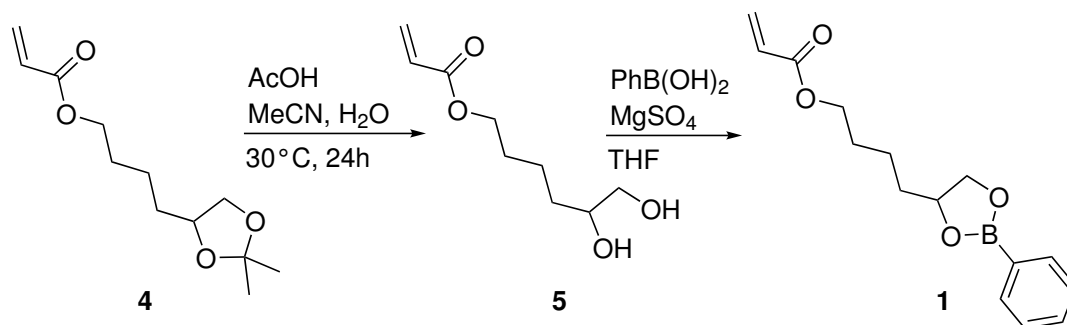
Scheme 2.6: Attempted exchange of the acetal protecting group with a boronic ester on the monomer.

The acetal protecting group was removed in acidic medium utilizing acetic acid to obtain the diol monomer **5**. However, as a consequence, a significant amount of the product remained in the aqueous phase during the washing step. Due to its polarity, the product **5** could only be isolated in poor yields (<50 %). When dried, compound **5** had a strong tendency of self-polymerization. As a consequence, it was decided to polymerize the acetal protected monomer **4** first, before the protecting group was exchanged on the polymer to avoid aforementioned problems.

2.3 Copolymerization and Post-Polymerization Functionalization

2.3.1 RAFT Copolymerization of the Acetal Protected Monomer

To obtain a copolymer, the functional monomer **4** was copolymerized with *n*BA by reversible addition - fragmentation chain transfer (RAFT) polymerization employing 2-cyano-2-propyl dodecyl trithiocarbonate (CPDT) as a chain transfer agent (CTA) and azobisisobutyronitrile (AIBN) as initiator (Scheme 2.7). RAFT is a RDRP method, which provides control over the size, dispersity ($Đ$), and structure of the polymer chains, while having the additional advantage of relatively facile and non-demanding reaction conditions. The reactant ratios were set to $[nBA]_0 : [\mathbf{4}]_0 : [CPDT]_0 : [AIBN]_0 = 1000 : 115 : 1 : 0.2$, for a target number average molar mass (M_n) of 100 kDa and a functional group ratio of 10 %. 1,4-Dioxane was chosen as a solvent and was added in a 1 : 1 ratio (v/v) in respect to the monomers.
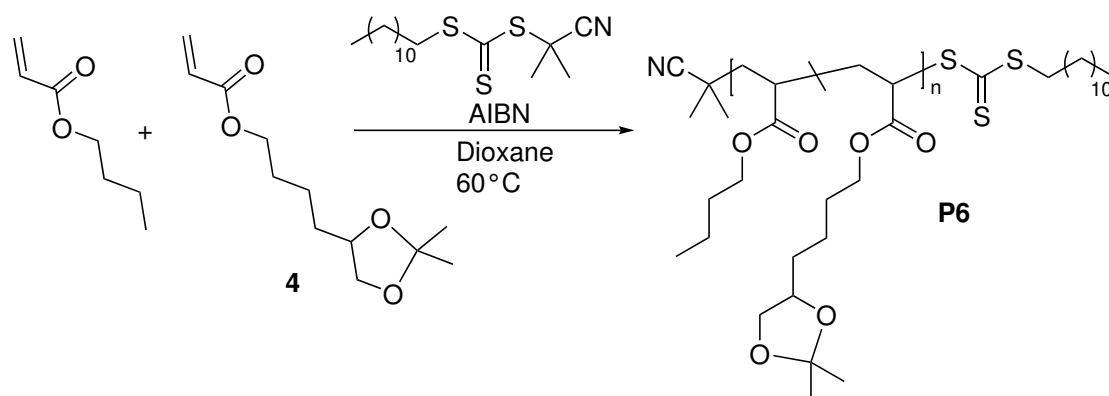
Scheme 2.7: RAFT copolymerization of *n*BA and the protected diol functional monomer **4** to yield the precursor **P6** of the thermoplastic of **Network 1**.

2.3.1.1 Polymerization Kinetics

A kinetic study was conducted to follow the RAFT polymerization. During the polymerization samples were taken after 0, 2, 4, 5.5, 7, 22, and 24 h and analyzed via ^{1}H NMR and size exclusion chromatography (SEC). During the NMR analysis, the monomer conversion was tracked via the integration of the acrylic peaks between 5.7 and 6.5 ppm in comparison with the integral of the dioxane peak at 3.71 ppm (see Figure 2.2).
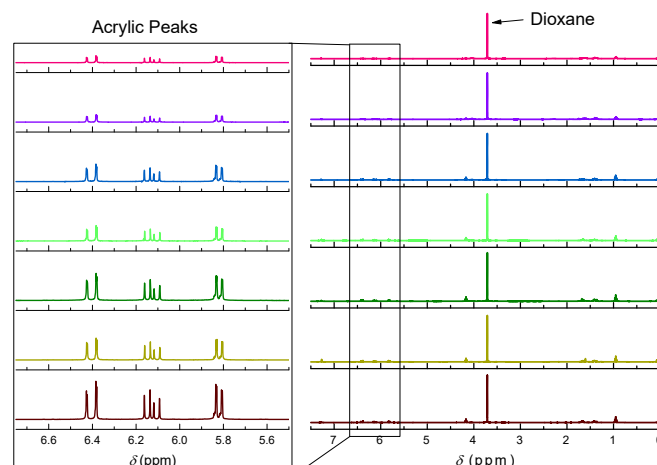
Figure 2.2: ^{1}H NMR spectra (in CDCl$_3$, at 400 MHz) of the polymerization mixture after 0, 2, 4, 5.5, 7, 22, and 24 h (bottom to top).

The theoretical M_n was calculated by Equation 2.1 under the assumption that the termination took place exclusively via recombination. $[\mathrm{M}]_0$ is the initial total monomer concentration ($[n\mathrm{BA}]_0 + [\mathbf{4}]_0$), X(t) is the monomer conversion at time t, $[\mathrm{RAFT}]_0$ is the initial CTA concentration, f is the initiator efficiency (taken as 0.5), $[\mathrm{I}_2]_0$ is the initial initiator concentration, $[\mathrm{I}_2]_t$ is the estimated initiator concentration at time t, M(M_{Av}) is the average molar mass of the monomers (calculated with Equation 2.2), and M_RAFT is the molar mass of the CTA. $[\mathrm{I}_2]_t$ was calculated with Equations 2.3 and 2.4 with ln(A) = 36.3 and E_a = 132.4 kJ mol^{-1} K^{-1} (supplier information[36]).

$$M_{\mathrm{n, theo}} = \frac{[\mathrm{M}]_0 \cdot X(t)}{[\mathrm{RAFT}]_0 + \mathrm{f} \cdot ([\mathrm{I}_2]_0 - [\mathrm{I}_2]_t)} \cdot M(M_{Av}) + M_\mathrm{RAFT} \qquad (2.1)$$

$$M(M_{Av}) = \frac{[n\mathrm{BA}]_0 \cdot M(n\mathrm{BA}) + [\mathbf{4}]_0 \cdot M(\mathbf{4})}{[\mathrm{M}]_0} \qquad (2.2)$$

$$[\mathrm{I}_2]_t = [\mathrm{I}_2]_0 \cdot e^{-k_d t} \qquad (2.3)$$

$$k_d = A \cdot e^{\frac{-E_a}{RT}} \qquad (2.4)$$

The results have been compared with the M_n determined via SEC (see Figure 2.3, right). The theoretical M_n and the values obtained by SEC are compared in Figure 2.3, left. In

the beginning the values are in good accordance with each other. At higher yields the M_n determined by SEC is somewhat lower than the theoretical value. When the overall concentration of available monomer decreases the polymerization slows down. The Đ remains stable at around 1.2-1.3, the higher values at low conversions might be due to the susceptibility of this value to fluctuations at low M_n and the detection limit of the SEC.
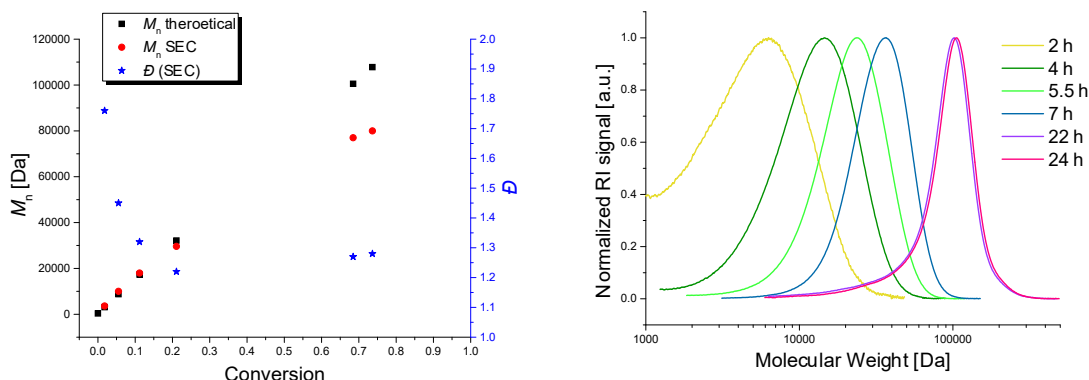
Figure 2.3: Kinetic study of the the RAFT polymerization of **4** and *n*BA ($[nBA]_0$: $[4]_0$: $[CPDT]_0$: $[AIBN]_0$ = 1000 : 115 : 1 : 0.2, 1 : 1 (v/v) dioxane : monomers, 60 °C). Left: Comparison of the theoretical M_n and the values obtained by SEC. Development of the M_n and Đ with increasing conversion. Right: SEC traces in THF (PS calibration) after 2, 4, 5.5, 7, 22, and 24 h.

2.3.2 Functionalization of the Thermoplastic Precursor

The copolymer **P6** was intended to be further functionalized like displayed in Scheme 2.8. First the RAFT end-group is removed (**P7**), in a second step the diol is deprotected (**P8**) and finally reprotected with a boronic ester moiety to get **P9**.

2.3.2.1 RAFT End-Group Removal

The RAFT end-group of the resulting polymer causes the material to have a strong yellow color. Depending on the application field it would be more preferable to have a colorless polymer. In addition, the RAFT end-group might cause some unwanted side reactions in the following reaction steps. Therefore, it is preferable to remove the RAFT end-group. The most efficient way to do this would be in a one-pot synthesis right after the RAFT
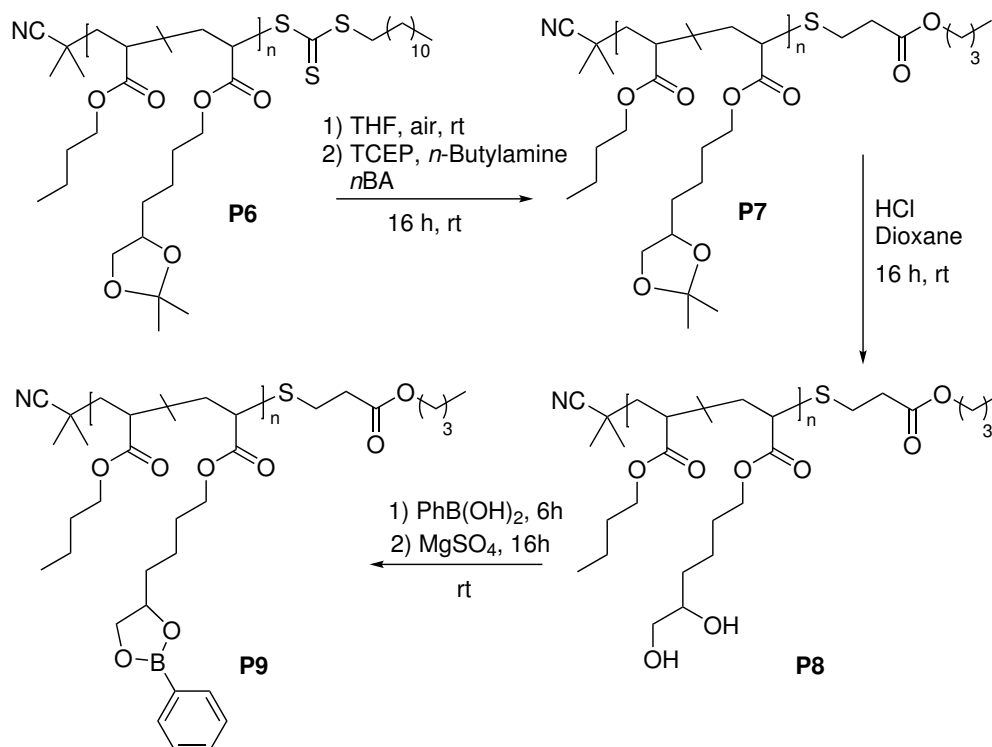
Scheme 2.8: Further functionalization of precursor **P6** to yield the thermoplastic precursor **P9**.

polymerization without any further purification of the polymer. The RAFT end-group removal was thus conducted via aminolysis with a subsequent Michael-addition according to a literature procedure.[37,38] A detailed pathway is depicted in Scheme 2.9.
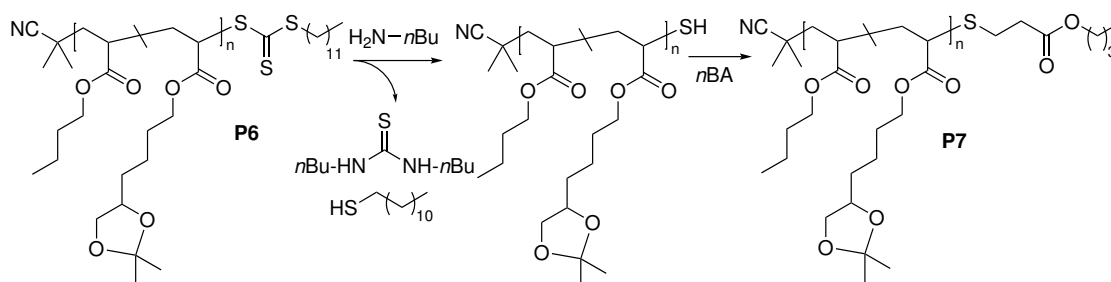
Scheme 2.9: Synthetic pathway for the transformation of the polymer end-groups. In the first step, the RAFT end-group is transformed into a thiol. Subsequently, the thiol reacts in a Michael-addition with the α, β-unsaturated *n*BA still present in the reaction medium.

First, the RAFT polymerization was stopped and it was made sure that no further radicals

could be active in the solution. In order to do so, the reaction mixture was cooled down, exposed to air and tetrahydrofuran (THF) was added. The aminolysis was then carried out using an excess of *n*-butylamine and tris-(2-carboxyethyl)-phosphine (TCEP) as a reducing agent to suppress interpolymeric oxidative coupling of the thiol end-groups into disulfides. The excess of amine catalyzes the subsequent Michael-addition of the thiols with the unreacted monomer in the reaction mixture. The small molecule side products of the aminolysis were separated from the polymer during precipitation. The concentration of the end-group in the polymer is too low to be detected by NMR spectroscopy. The termination of the reaction was thus assessed via the color change. In Figure 2.4, photos of the polymer before (yellow color) and after (colorless) the removed RAFT end-group is shown. In the same Figure, the ^{1}H NMR spectra of the polymer before and after the removed RAFT end-group are presented. Since the RAFT end-group is not detectable in the NMR spectrum, the spectra are identical. Yet, this indicates that the aminolysis does not impact the functional groups of the polymer. The RAFT agent CPDT has a strong
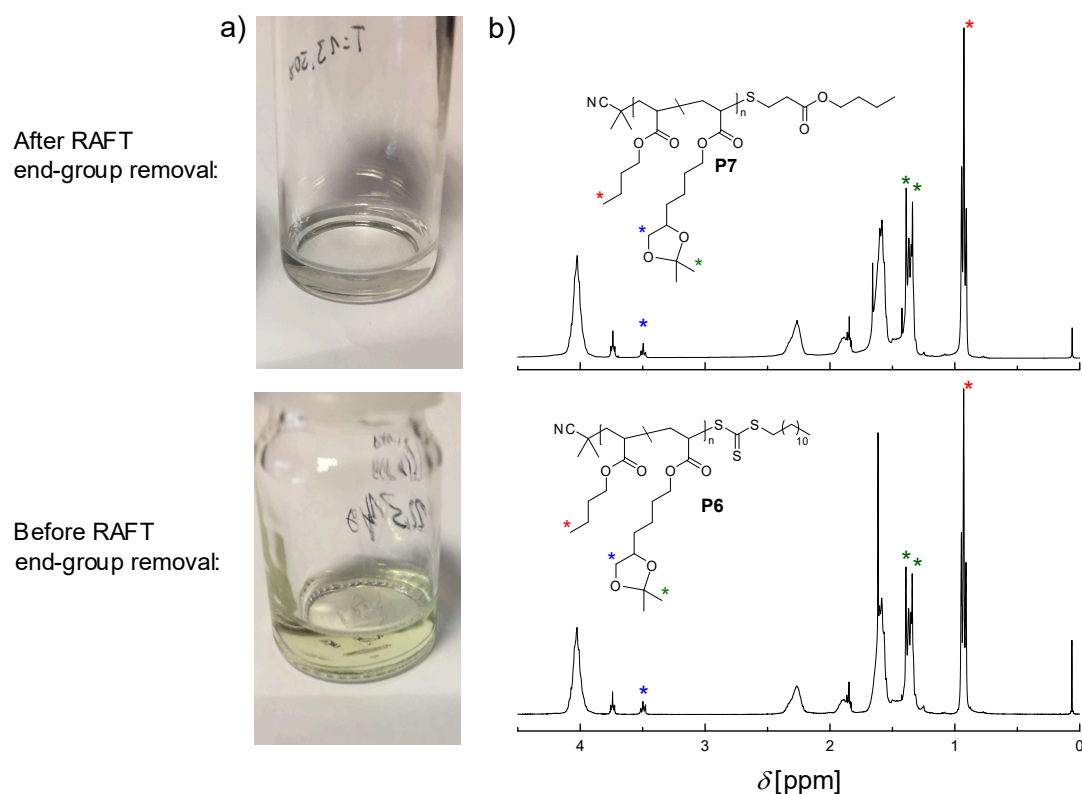
Figure 2.4: Raft end-group removal. a) Photos of the copolymer before (**P6**, bottom), and after (**P7**, top) the RAFT end-group was removed. b) ^{1}H NMR spectra in CDCl$_3$ at 400 MHz of copolymers **P6** and **P7**. The significant functional groups are annotated.

yellow color, thus absorbs light in the blue region of the spectrum (around 450 nm). It was attempted to detect the removal of the RAFT end-group via UV-visible (Vis) spectroscopy. However, the RAFT end-group was too diluted in the polymer to be detected. In the pure polymer (assumed M_n = 100 kDa, ρ = 1.087 g mL^{-1} (supplier information[39])) the concentration of the RAFT end-group would be at $1.09 \cdot 10^{-2}$ mmol L^{-1}. The detection limit of the UV-Vis spectrometer was already reached when going to concentrations below 0.7 mmol L^{-1}, as can be seen in Figure 2.5.
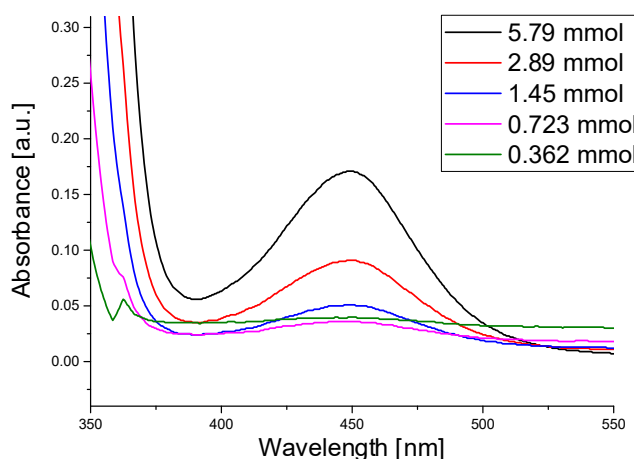
Figure 2.5: UV-Vis spectra of the RAFT agent CPDT in THF at different concentrations in the visible range between 350 and 750 nm. The concentration was halved by dilution after each measurement. At 0.362 mmol, no absorbance in the visible region could be detected anymore.

2.3.2.2 Deprotection of the Acetal Group

The deprotection was attempted employing acetic acid (Scheme 2.10). However, to make the deprotection work a certain amount of water is necessary in the reaction mixture. Yet, the polymer is so hydrophobic that in all attempted solvents (acetonitrile (MeCN), dioxane, THF) phase separation occurred when a certain amount of water was added. In consequence, no deprotection took place. When the deprotection was attempted employing diluted or concentrated HCl in dioxane (Scheme 2.11), and the polymer was subsequently purified by precipitation in hexane, **P8** crosslinked to an insoluble gel probably due to traces of acid still present within the polymer. To avoid that, a way had to be found to remove the acid. Apparently, precipitation in cold hexane was not sufficient to achieve this goal. Other more polar solvents (toluene, xylene, diethyl ether (Et$_2$O), dichloroethane, methanol (MeOH), ethanol (EtOH)) dissolved the polymer completely

due to its enhanced polarity originating from the free hydroxy groups. The polymer could be precipitated in H_2O/MeOH (2 : 1 v/v) mixtures. The remaining hydrochloric acid could thus be removed and the polymer **P8** did not gel during solvent evaporation. It was obtained as a colorless, transparent viscous liquid.
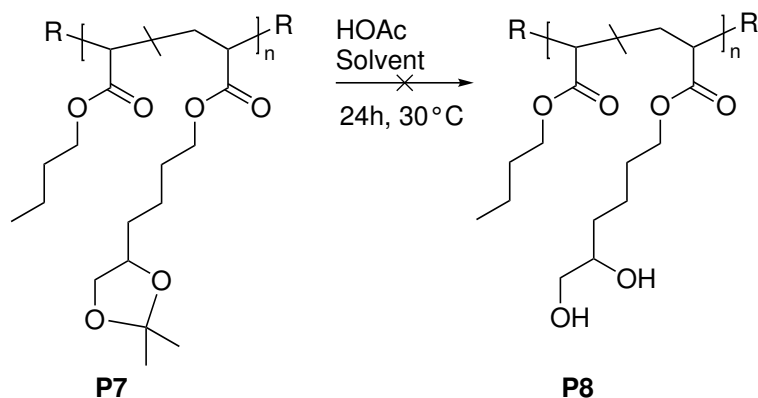
Scheme 2.10: Attempt of deprotecting copolymer **P7** using HOAc.
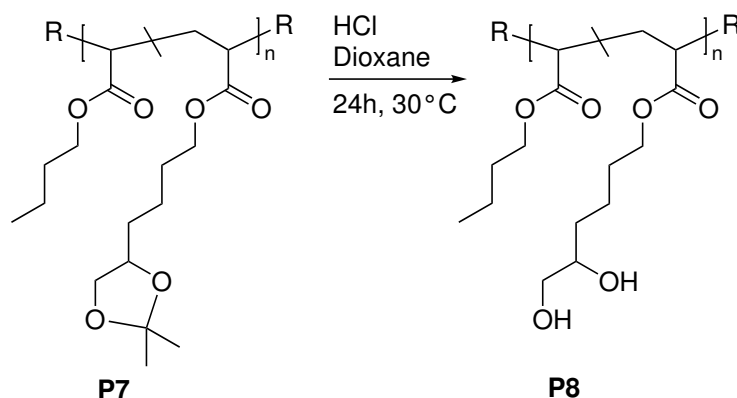
Scheme 2.11: Attempt of deprotecting copolymer **P7** using HCl in dioxane to yield **P8**.

The successful formation of the targeted polymer was confirmed via NMR spectroscopy. In Figure 2.6, the ^{1}H NMR spectra of **P8** and its precursor **P7** are compared. The successful deprotection is indicated by the disappearance of the signals originating from the protection group (signal d') and the shift of the adjacent peaks of the (protected) diol (a'-c' → a-c). In the same graph, the spectrum of the deprotected copolymer is compared with the one of the deprotected monomer. The location of the signals adjacent to the free diol of the polymer (a, b, c) is in accordance with the respective signals from the monomer (a", b", c").
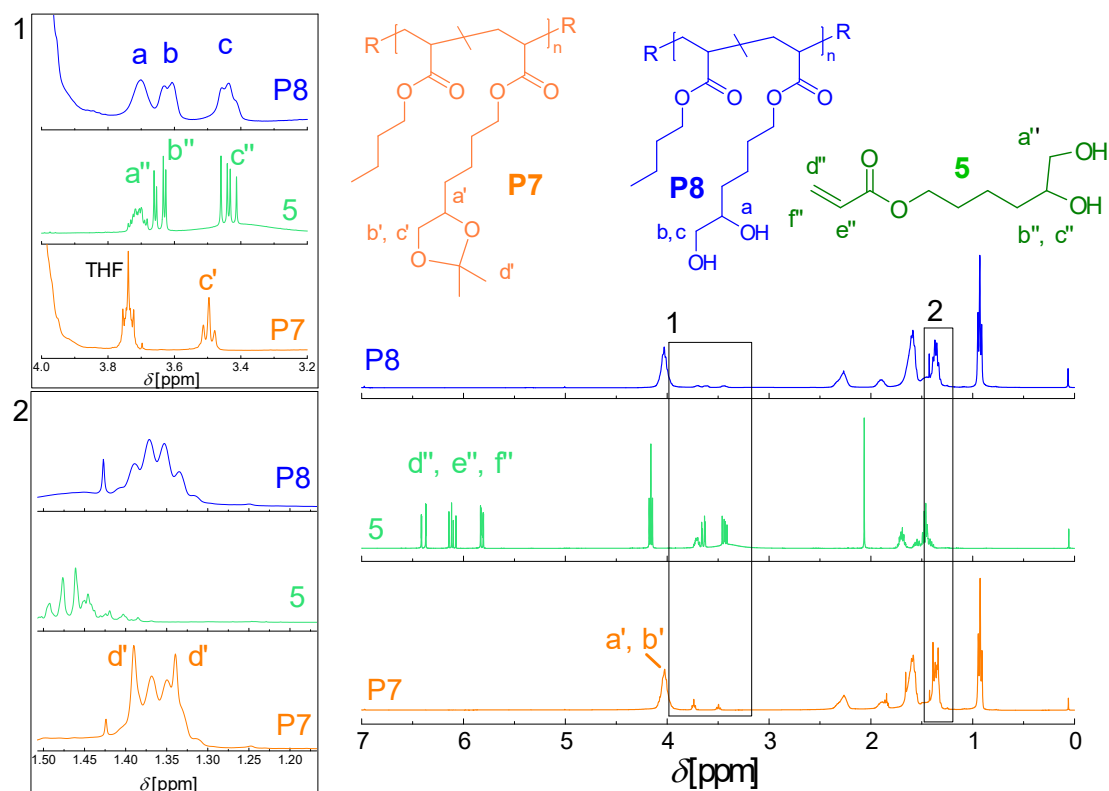
Figure 2.6: ^{1}H NMR spectra in CDCl$_3$ at 400 MHz of copolymer **P8** (blue, top), its precursor **P7** (orange, bottom) and monomer **5** (green, center). The successful deprotection of the copolymer is indicated by the disappearance of the signals originating from the protection group (signal d') and the shift of the adjacent peaks of the protected diol (a', b', c' $\rightarrow$ a, b, c). The location of the proton peaks of the copolymer **P8** adjacent to the diol group (a-c) are in accordance to the ones of the monomer **5** (a"-c").

2.3.2.3 Esterification with a Boronic Acid

The next step is the esterification of the polymer **P8** with PBA to yield **P9** (Scheme 2.12). Subsequent to the condensation reaction, the polymer was precipitated in cold hexane. The hexane could not dissolve the PBA though, which remained as an impurity inside the polymer. Protic solvents could not be used for precipitation, since they could cleave the boronic ester bonds.
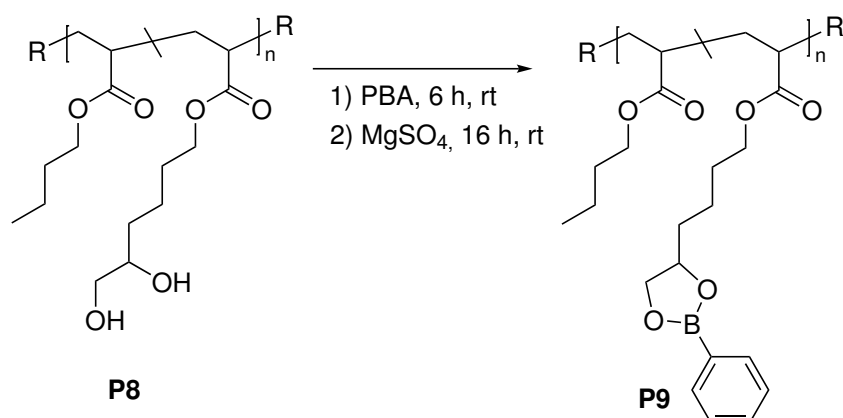
Scheme 2.12: Reprotectiong copolymer **P8** with a boronic acid to yield **P9**.

The non-protic solvents DCM, ethyl acetate (EtOAc), Et$_2$O, and acetone dissolved the polymer. The only other available solvent other than alkanes that did not fully dissolve the polymer was MeCN. The polymer was partly soluble in MeCN though. To avoid yield loss, the precipitation was conducted close to the freezing temperature of MeCN. The PBA could be removed during this purification step and the polymer was obtained as a colorless, transparent viscous liquid. The successful esterification was confirmed via ^{1}H NMR spectroscopy by comparing the spectra of the precursor and of the formed polymer (Figure 2.7). The aromatic protons of the PBA appear (signals d-f) and the signals of the adjacent protons of the diol shift to the downfield (a-c → a'-c').

2.4 Crosslinker Synthesis

For the crosslinking of the subnetwork carrying boronic ester moieties a crosslinker containing two boronic ester groups is needed . The crosslinker forms a network by an exchange reaction, thereby releasing a (volatile) small molecule. 1,4-Benzenediboronic acid esterified with 1,2-propanediol like shown in Scheme 2.13 fulfills this criterion. When the crosslinker participates in a metathesis reaction with another boronic ester group, a small phenyl boronic ester derivative is set free, which can easily be removed from the reaction mixture (compare Scheme 2.14). The reaction worked well to almost complete conversion and the product is obtained pure.
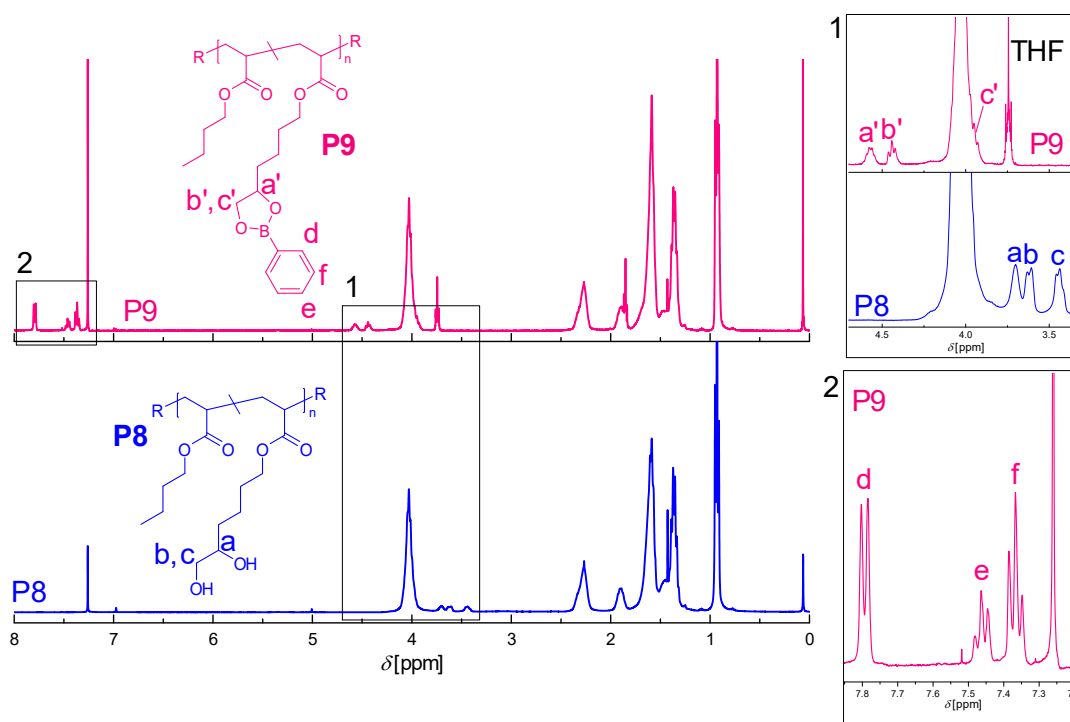
Figure 2.7: ^{1}H NMR spectra in CDCl$_3$ at 400 MHz of copolymer **P9** (top) and its precursor **P8** (bottom). The successful esterification with PBA is indicated by the appearance of the aromatic proton signal of PBA (signals d-f) and the shift of the adjacent peaks of the diol (a-c → a'-c').
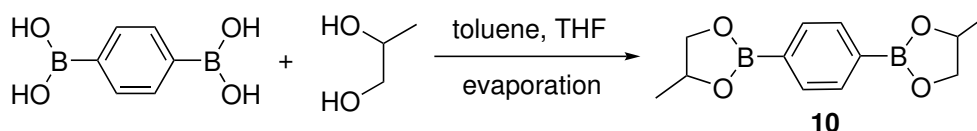
Scheme 2.13: Esterification of 1,4-benzenediboronic acid with 1,2-propanediol yielding compound **10**.

2.5 Crosslinking of the Boronic Ester Thermoplastic

The TP **P9** was crosslinked with the bis(boronic ester) **10** to create **Network 1** (see Scheme 2.14). A crosslinking density (ρ(CL)) of 2 % was targeted. The amount of substance of crosslinker n(CL) was calculated employing Equations 2.5 to 2.8, with

eq(CL)/chain as the equivalents of crosslinker per chain, n(P) as the amount of substance of the polymer, N_f(chain) as the number of functional groups per chain, f(P) as the functionality of the polymer, m(P) as the mass of the **P9** sample, and M(P) as the molecular mass of **P9**. The number of functional groups of the crosslinker (N_f(CL)) is 2 for it has two reactive boronic ester groups. The functionality of the polymer is around 0.10, the actual value was calculated via the NMR integration areas of the respective monomers. To reach the aimed 2 % crosslinking density, 20 % of the functional groups are to be crosslinked (f_{CL} = 20 %). These equations are only valid under the assumption of a complete crosslinking reaction. An overview about typical properties of the TP **P9** and the formed **Network 1** is given in Table 2.1, N_{CL} is the number of crosslinks per chain.
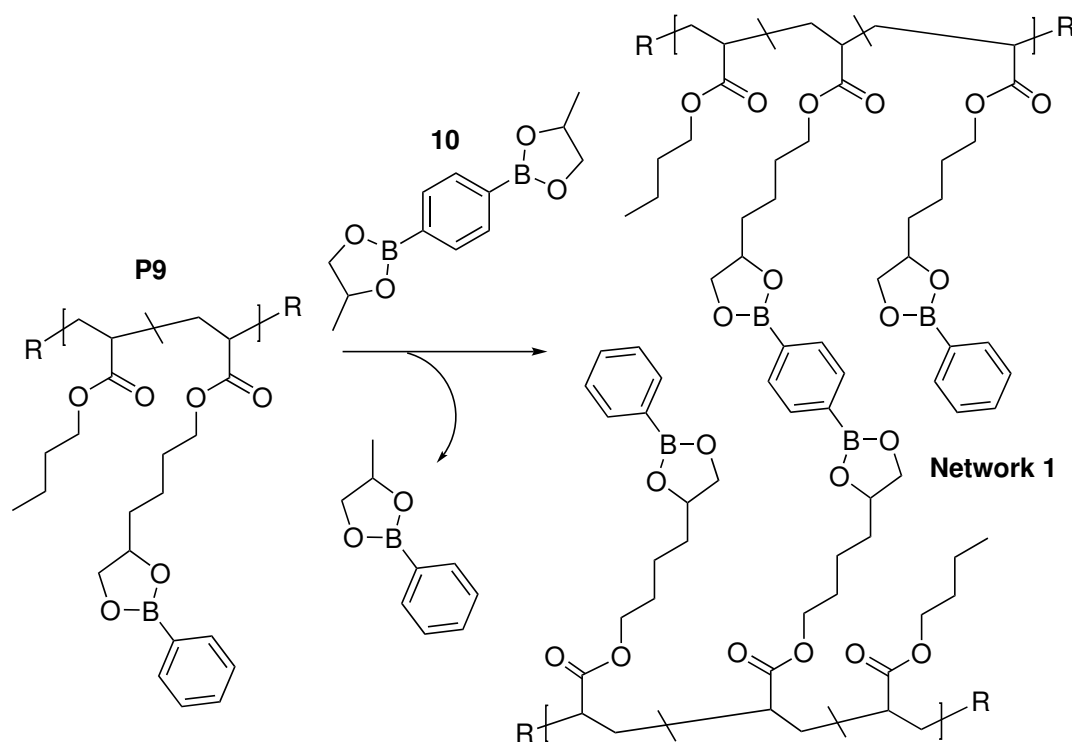
Scheme 2.14: Synthesis of Network 1 by crosslinking of TP **P9** with **10**.

Table 2.1: Overview over the properties of TP **P9** and **Network 1**.

M_n[1] [kDa]	DP_n[1]	Đ	f [%]	N_f(chain)	f_{CL} [%]	N_{CL}(chain)	ρ(CL) [%]
90	650	1.3	10	65	20	13	2

1: determined via SEC with a standard PS calibration.

$$n(CL) = \frac{eq(CL)}{chain} \cdot n(P) \tag{2.5}$$

$$\frac{eq(CL)}{chain} = \frac{N_f(chain) \cdot f_{CL}}{N_f(CL)} \tag{2.6}$$

$$N_f(chain) = DP_n \cdot f(P) \tag{2.7}$$

$$n(P) = \frac{m(P)}{M(P)} \tag{2.8}$$

The DP_n is dependent of the molecular mass of the polymer. Therefore, to calculate the amount of crosslinker in the end only the functionality and the mass of the thermoplastic precursor is necessary, while using the average mass of the employed monomers $M(M_{Av})$ (Equation 2.10 with M(nBA) as the molar mass of nBA and M(FM) as the molar mass of the boronic ester functional monomer). Therefore, the amount of crosslinker can be calculated with Equation 2.9.

$$n(CL) = \frac{f_{CL} \cdot m(P) \cdot f(P)}{N_f(CL) \cdot M(M_{Av})} \tag{2.9}$$

$$M(M_{Av}) = f(P) \cdot M(FM) + (1 - f(P)) \cdot M(nBA) \tag{2.10}$$

The thermoplastic precursor **P9** was dissolved in THF and the respective amount of the bis(boronic ester) crosslinker **10** in THF solution was added. The mixture was stirred rapidly. After 2-3 minutes the mixture gelified. The solvent was slowly evaporated at ambient conditions for 24 h, before it was cured under vacuum for 16 h at 80 °C. The network was obtained as a colorless elastomer foam as can be seen in Figure 2.8, left.

2.6 Compression Molding

Pieces of **Network 1** were introduced into a metal mold with the desired shape and pressed at 110 °C for 20-30 min with a force equivalent to 3 tons. The material was obtained as a homogenous, transparent, colorless elastomer as depicted in Figure 2.8,

right. The network is thus well processable by compression molding, exhibiting short processing times at moderate temperatures.

Figure 2.8: Pictures of **Network 1**. Left: after crosslinking, before compression molding. Right: after compression molding.

2.7 IR Measurements

Fourier-transform infrared (FTIR) spectra were recorded of the TP **P9**, of **Network 1** after crosslinking and compression molding and of **Network 1** after removal of soluble fraction (see Figure 2.9). The peaks of the aromatic C=C stretch of the grafted boronic esters can be found at 1499 and 1603 cm^{-1} in all materials. After the crosslinking, the peak of the aromatic C=C stretch of the crosslinker appears at 1518 cm^{-1}.[40] This peak remains even after the soluble fraction is removed, which confirms the covalent connection of the crosslinker to the polymer backbone.

2.8 Swelling and Solubility Tests

To determine the swelling ratio and the soluble fraction of **Network 1** swelling tests were performed. Three circular samples (m(dry)) prepared by compression molding were immersed for 24 h in anhydrous THF. The THF was removed, the samples weighted (m(swollen)) and subsequently dried under vacuum at 80 °C for 16 h, before they were weighted again (m(dried)). The swelling ratio and insoluble fraction were calculated with Equations 2.11 and 2.12, respectively. The results are summarized in Table 2.2. In all
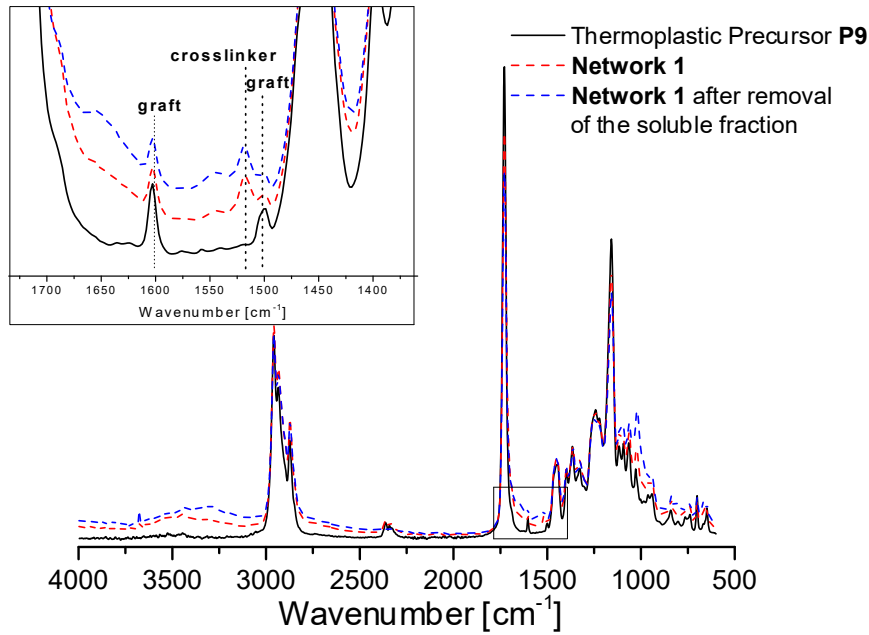
Figure 2.9: FTIR spectra of the TP **P9**, of **Network 1** after crosslinking and compression molding and of **Network 1** after the soluble fraction was removed.

samples the soluble fraction is low exhibiting an average insoluble fraction of 98 ± 1.3 %. This indicates a good connectivity of the network.

$$\text{Swelling ratio} = \frac{m(\text{swollen}) - m(\text{dried})}{m(\text{dried})} \tag{2.11}$$

$$\text{Insoluble fraction} = \frac{m(\text{dried})}{m(\text{dry})} \tag{2.12}$$

Table 2.2: Results of swelling test of **Network 1** in THF.

Sample	m(dry) [mg]	m(swollen) [mg]	m(dried) [mg]	Swelling ratio	Insoluble fraction [%]
1	319	1840	315	4.84	98.7
2	271	1855	263	6.05	97.0
3	318	1837	317	4.79	99.7
Average				5.22 ± 0.71	98.5 ± 1.3

2.9 Solvolyses

2.9.1 Diolysis

Network 1 is dynamic and can react to external trigger signals. One of its desired properties is to react to competitive small molecules, which can be used for chemical recycling. Boronic ester bonds are known to exchange rapidly with diols. Hence, when an excess of free diol is added to the network, it should be cleaved into diol functionalized TPs like depicted in Scheme 2.15.
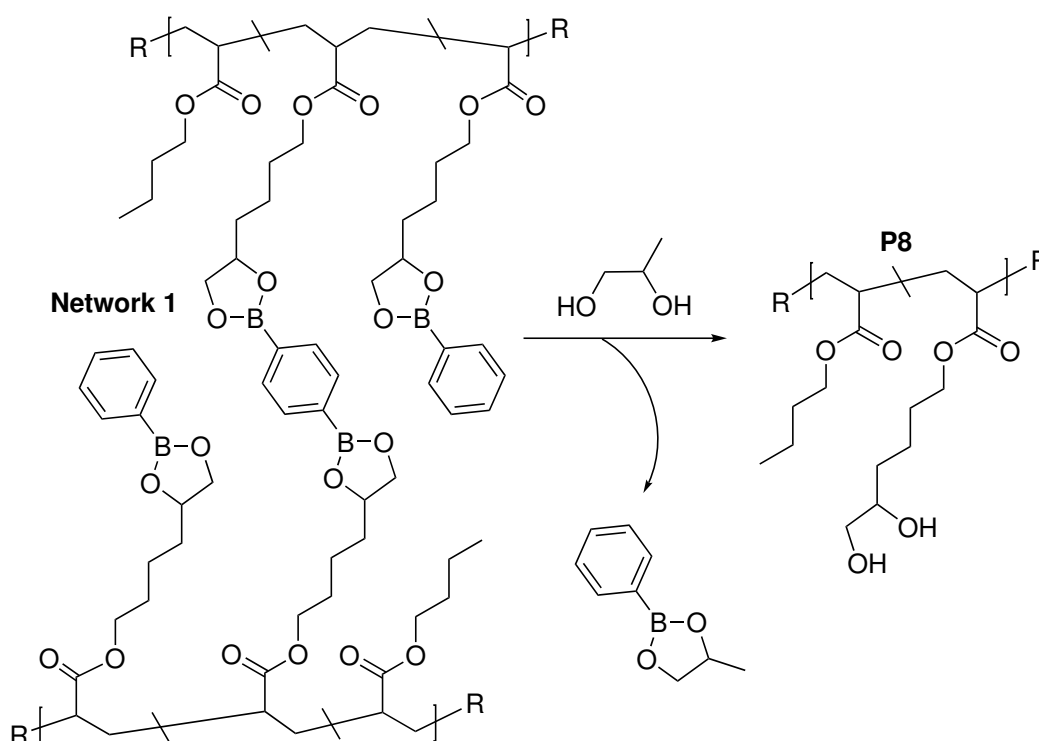
Scheme 2.15: Diolysis of **Network 1** to the TP **P8**.

During this process, the network loses its 3D-structure and becomes soluble. A piece of **Network 1** was immersed in THF and an excess (500 eq/CL) of 1,2-propanediol was added. After 48 h, the network was completely dissolved. The sample was purified by precipitation and an SEC was conducted. The thermoplastic hence obtained was compared to the pristine diol functionalized TP **P8**. As can be seen in Figure 2.10 the curves overlap very well, and the diolysed TP and the TP **P8** present very similar M_n and

Đ. Hence, diolysis is a powerful tool to de-crosslink the formed network and recover the diol functionalized TP. **Network 1** has thus the ability to be recycled chemically.
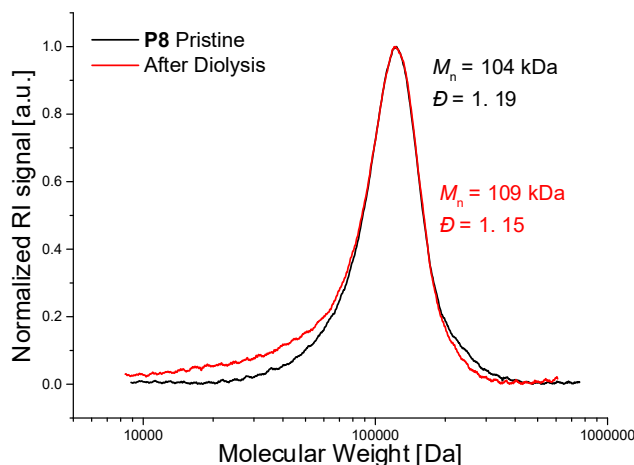
Figure 2.10: SEC trace in THF (PS calibration) of **Network 1** after the diolysis (red) in comparison with the SEC trace of the pristine diol TP **P8** (black).

2.9.2 Long Term THF Stability

The boronic ester network showed a good short-term stability in THF. When immersed in the solvent for 24 h, the soluble fraction was lower than 3 %. The test was repeated over a longer time period. After 7 days, the solvent was removed and the samples were dried. In Table 2.3 the values for the initial entry (m(dry)), the remaining polymer (m(dried)) and the resulting soluble fraction calculated with Equation 2.12 are listed.

Table 2.3: Results of long term solubility test of **Network 1** in THF.

Sample	m(dry) [mg]	m(dried) [mg]	Insoluble fraction [%]
1	255.9	4.1	1.6
2	305.3	8.7	2.8
3	345.9	10.6	3.1

It can be seen that most of the network dissolved during that time. This is not necessarily due to a loss in connectivity. It was shown in recent studies that some vitrimers can partially or completely dissolve in suitable solvents depending on the network topology, integrated functionality, dynamics of exchange, and time scale of the dissolution test.[29,41]

This dissolution is linked to the formation of soluble species like branched and cyclic structures during the reorganization of the network. These are no longer connected to the rest of the network and thus able to diffuse into the solvent. This theory was confirmed by evaporating the solvent. Once dried, a swellable network was reobtained. By removing the solvent the chains come in proximity with each other and intermolecular exchange takes place again, reforming a network.

This behavior has to be taking into account, when considering the chemical recycling of the double network. It might be challenging to separate the imine-aldehyde network from the boronic ester one, when parts of the boronic ester network are diffusing into the solution with time. It should also be considered that these tests are also temperature dependent. At higher temperatures the sample might lose its structural integrity sooner.

2.9.3 Hydrolytic Stability

Boronic ester bonds are prone to hydrolysis. Depending on their chemical nature, functionality and crosslinking density, boronic ester based networks can lose their crosslinked nature when placed in contact with water. In our case, the material is hydrophobic due to the poly(n-butyl acrylate) (PnBA) backbone. Immersion into water does not dissolve the material. Water diffuses into the structure only slowly and to a limited extend, as it is not a solvent of the polymer matrix. To bypass this hydrophobia, the polymer was immersed into a THF/water (3 : 1 v/v) mixture. The network dissolved within several hours. The polymer was precipitated in hexane and dried. The NMR spectrum of the resulting polymer can be seen in Figure 2.11. A comparison with the boronic ester TP **P9** and the unprotected diol TP **P8** shows that only a part of the boronic ester groups have been cleaved by hydrolysis. The ratio between the remaining pendent boronic ester groups and diol groups is 1 : 2, enough to dissolve the network structure. The SEC curve of the polymer is shown in Figure 2.12. Even though part of the boronic ester groups have been cleaved off, it matches very well the curve of the original thermoplastic with 75 kDa and 1.27 for the pristine **P8** vs. 75 kDa and 1.28 after the hydrolysis.
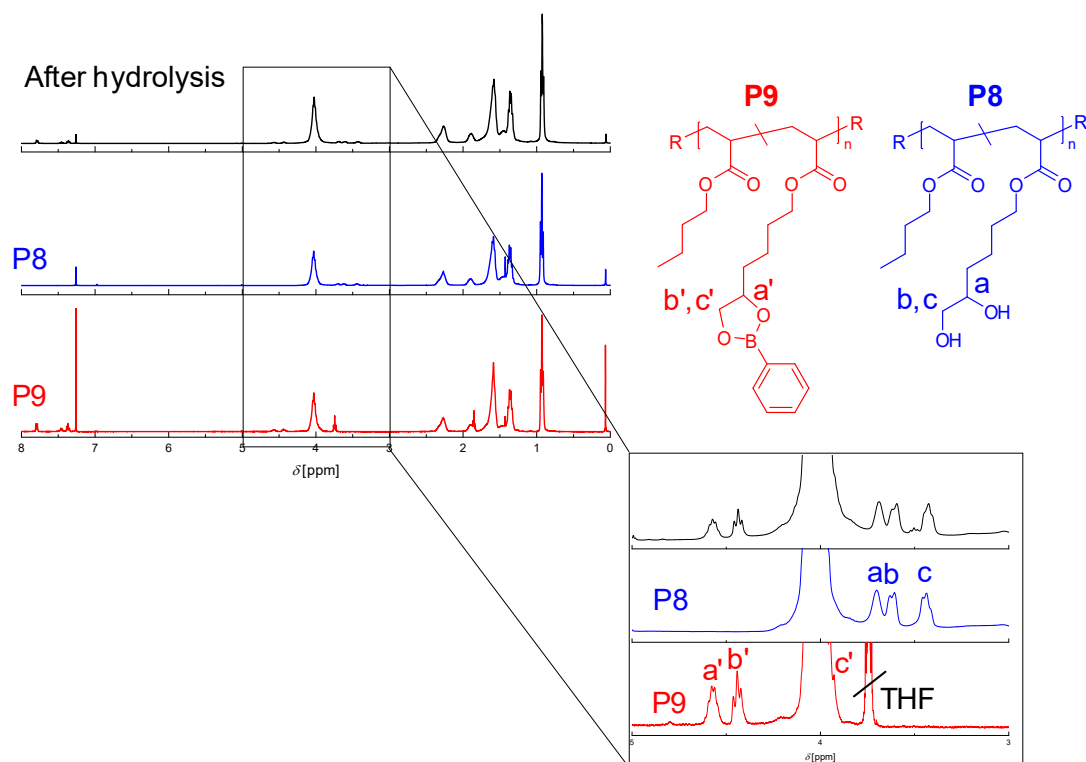
Figure 2.11: ¹H NMR spectra in CDCl₃ at 400 MHz of **Network 1** after hydrolysis (black). Below the spectra of the unprotected TP **P8** (blue) and the boronic ester protected TP **P9** (red) are shown.
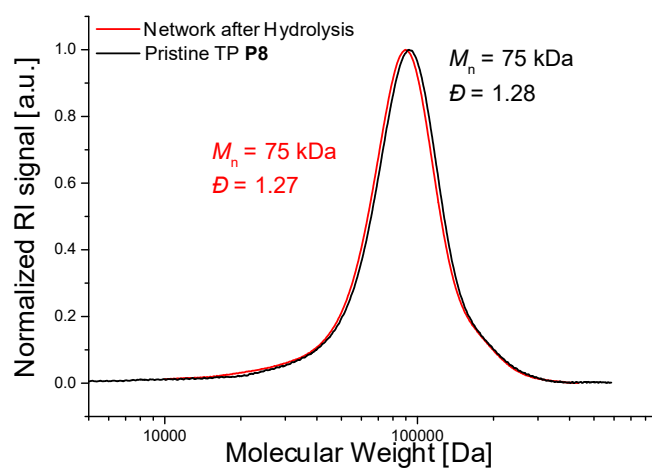
Figure 2.12: SEC curves in THF (PS calibration) of the pristine **P8** and **Network 1** after hydrolysis.

2.10 Thermal Characterization

2.10.1 TGA

The TGA of **Network 1** was conducted by applying a 10 K/min temperature ramp between 25 and 600 °C under nitrogen. The results are show in Figure 2.13a. The first drop in the beginning is due to an instrument artifact. The sample maintained 98 % of its mass up to 264 °C.
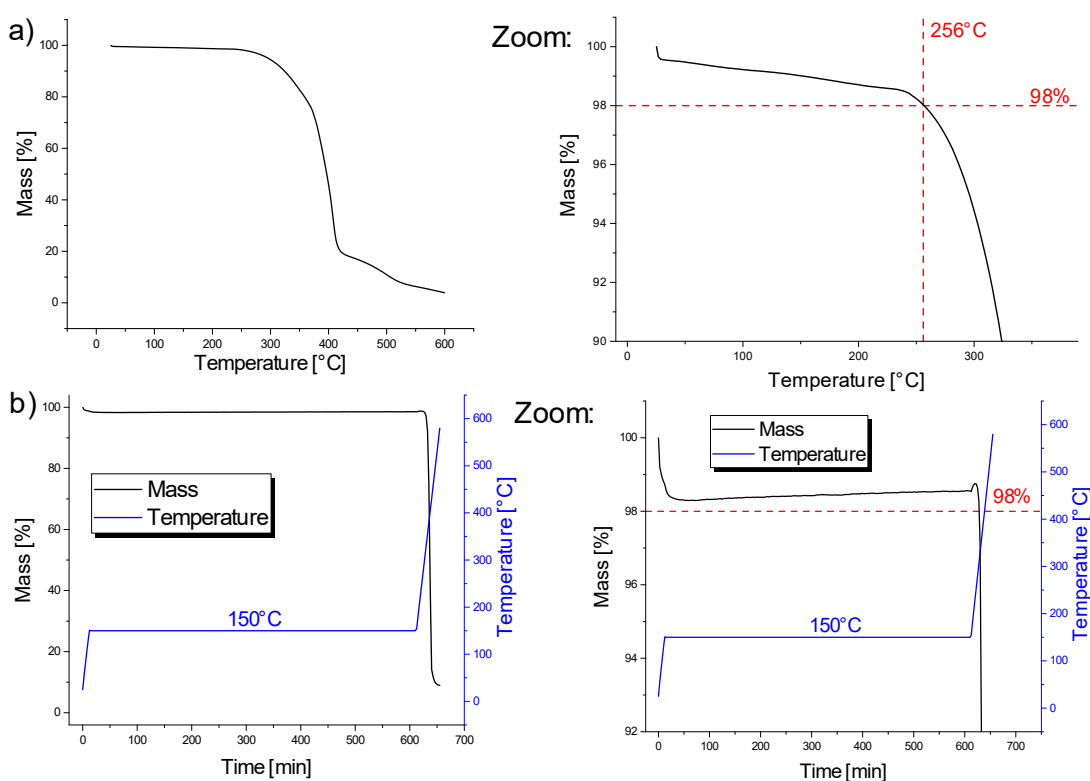
Figure 2.13: TGA of **Network 1**. a) 10 K/min temperature ramp between 25 and 600 °C under nitrogen. b) Isothermal at 150 °C under nitrogen during 10 h.

Since many tests are to be conducted at elevated temperatures, the long term stability of the network was tested with an isothermal measurement during 10 h at 150 °C. As the results in Figure 2.13b show, the network features excellent stability at 150 °C during the entire measurement period.

2.10.2 DSC

To determine the T_g of the sample, DSC measurements have been conducted. It can be seen that the T_g of the **Network 1** (Figure 2.14) was determined at -39.4 °C, which is slightly higher than the T_g of pure P*n*BA (-49 °C[39]), but significantly below room temperature. No other transition than the glass transition could be observed.
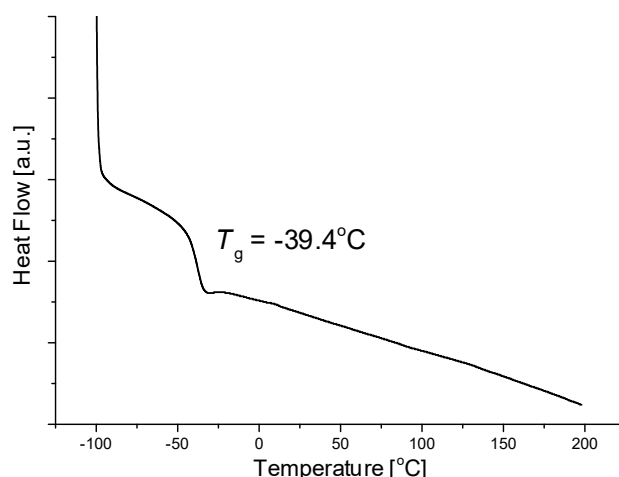
Figure 2.14: DSC analysis of the **Network 1**, second heating cycle.

2.10.3 DMA

In Figure 2.15, the DMA measurement of **Network 1** is shown. Below T_g there is a plateau of the storage modulus around 1600 MPa. The T_g is determined at the maximum of the loss modulus function, located at -25.0 °C. The T_g determined via DMA is in general a little higher than the one obtained via DSC. This is due to the time temperature superposition (TTS) principle: during the DMA measurement a frequency is applied to the sample, while in DSC the behavior is measured in static conditions. After the glass transition, E' decreases and reaches a plateau around 490 kPa at 25 °C and increases then slightly with increasing temperature. This is a clear sign that the network structure is maintained over the applied temperature window. The increase in modulus with temperature is due to entropic effects linked to the rubber elasticity.[42] When the chains are extended on the stretching of the network, the number of available rotational isomeric states and with them the entropy decreases. Since $\Delta Q = T\Delta S$, it requires a higher force to change the entropy at higher absolute temperatures, the material becomes stiffer.
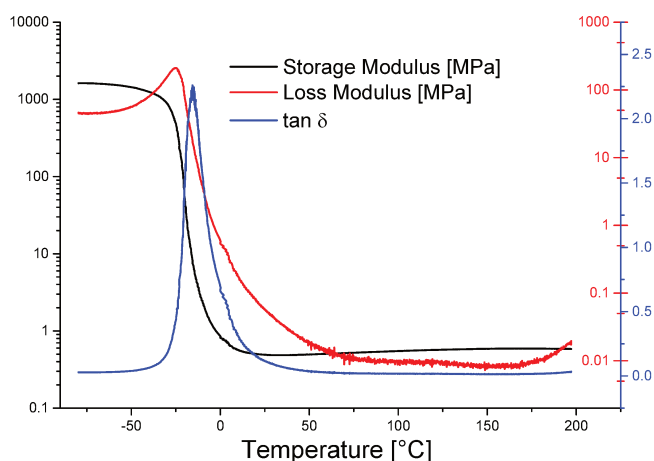
Figure 2.15: DMA of **Network 1**.

2.11 Tensile Tests

Network 1 was pressed into dumbbell shape specimen and tensile tests were conducted at a strain rate of 10 mm/s. A first test was run using a 5 kN transducer (see specimen #1). However, the resolution was not sufficient and the set-up was changed to a 100 N transducer. The strain/stress curves are exhibited in Figure 2.16, the values for specimen #1 have been smoothed by averaging over 30 data points. The Young's modulus was calculated by determining the slope in the linear regime at the beginning of the measurement. Due to instabilities in the signal at the very beginning, the slope was determined between 2-5 % strain. The values determined for all specimen can be found in Table 2.4.
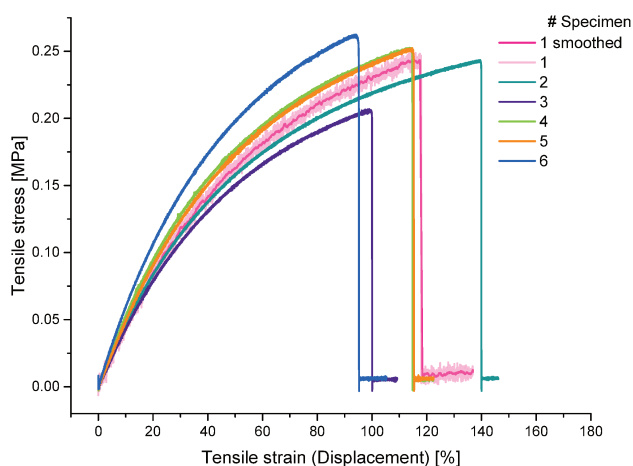
Figure 2.16: Stress/strain curves of **Network 1** in uniaxial tensile tests.

Table 2.4: Results of the uniaxial tensile test of **Network 1**.

Specimen #	1	2	3	4	5	6	Average
Tensile Strain at Break [%]	118	140	100	115	115	95	114 ± 16
Tensile Stress at Break [kPa]	242	245	206	252	252	205	234 ± 22
Young's Modulus [kPa]	417	484	452	551	509	618	505 ± 72

2.12 Rheometry: Conditioning

In order to characterize **Network 1** via rheometry, the material was compression molded into disks of 25 mm diameter and a thickness of around 1.5 mm. The disks had a mass of around 900 mg. Rheological measurements were conducted on an Anton Paar MCR 501 rheometer with parallel plate geometry of 25 mm. The sample could not be installed manually. Due to the brittleness of the material a too high normal force led to destruction of the sample, as shown in Figure 2.17. Since the measuring gap could not be set manually, a constant normal force of 0.4 N was applied, so the measuring gap was set automatically by the machine. In this fashion no destruction occurred.

Figure 2.17: Sample of **Network 1** after failed manual installation into the rheometer.

First experiments gave inconsistent results regarding both the initial modulus and the relaxation time. In fact, the sample showed anti-thixotropic behavior. The initial modulus increased with time, indicating that the sample was not in equilibrium when the actual experiment was started. It was thus decided to include an equilibration step before each

experiment. The equilibration was conducted first at 110 °C for several hours. It can be seen in Figure 2.18 that the storage modulus increases during this time, while the loss modulus decreases. The change of modulus decelerates with time and approaches an equilibrium modulus.
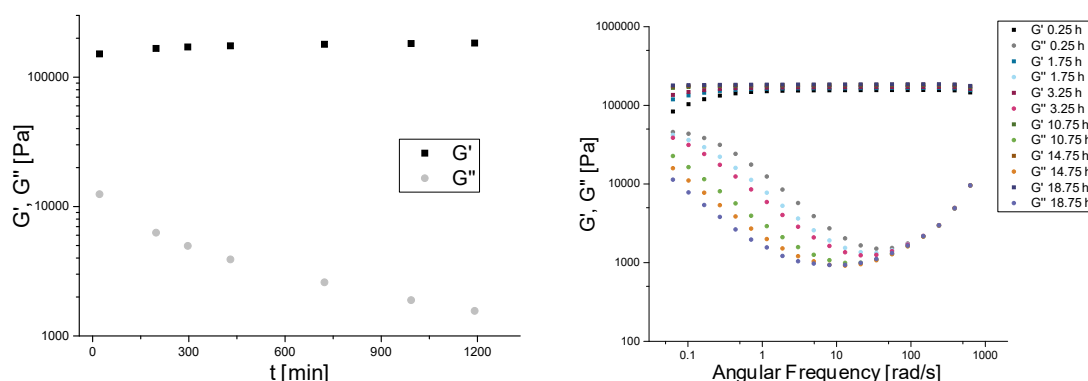
Figure 2.18: Development of G' and G" during the equilibration of **Network 1** at 110 °C. Left: Values at 1.15 rad/s with time. Right: Frequency sweeps after the indicated equilibration periods.

The equilibration step was shortened by conducting it at 150 °C. In Figure 2.19, it can be seen that also during this equilibration G' is increasing while G" is decreasing. The change in the moduli decelerates with time and approaches an equilibrium modulus. 4-5 h at this temperature was sufficient to reach equilibrium.
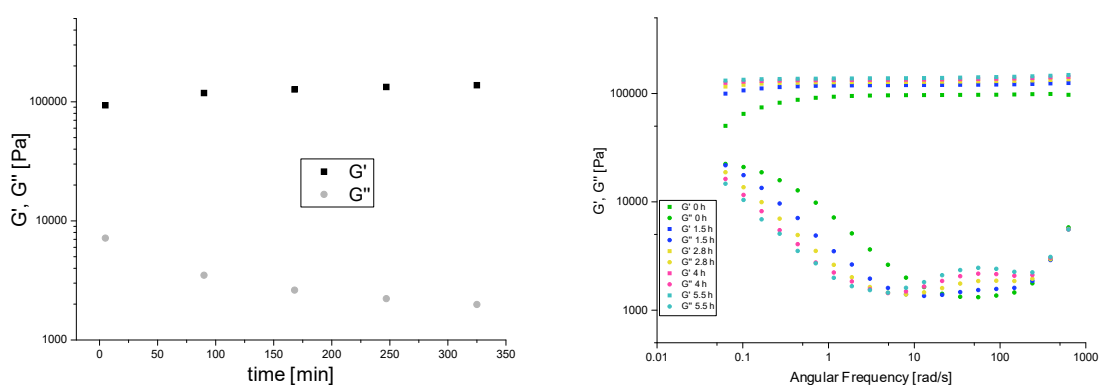
Figure 2.19: Development of G' and G" during the equilibration of **Network 1** at 150 °C. Left: Values at 1.15 rad/s with time. Right: Frequency sweeps after the indicated equilibration periods.

2.12.1 Thermal Stability of the Thermoplastic Precursor

The increase of the modulus could potentially be caused by irreversible crosslinking reactions occuring at elevated temperature. In case free diols would be present in the sample, transesterifications could take place and lead to static bonds as depicted in Scheme 2.16.
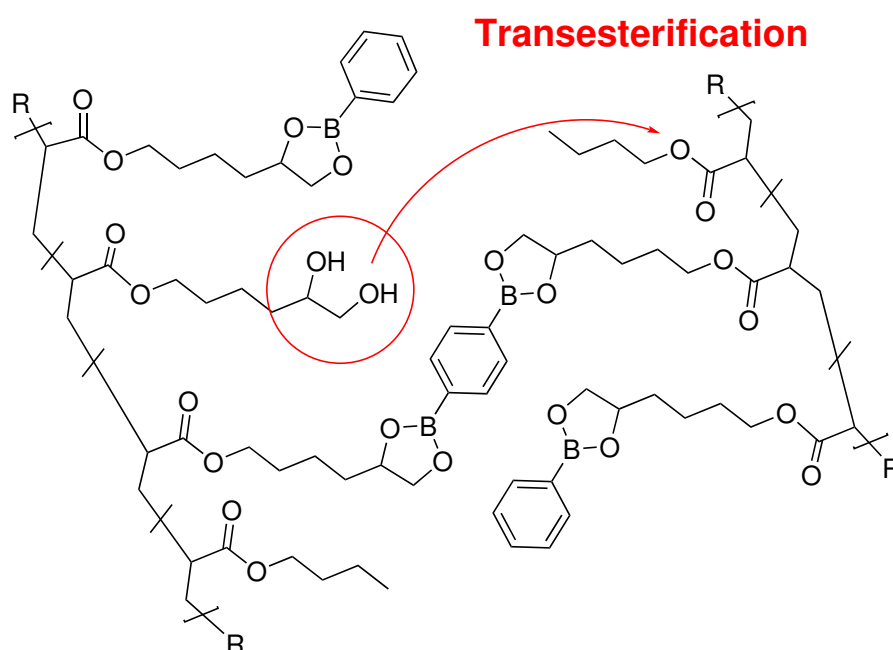
Scheme 2.16: Irreversible/static crosslinking through transesterification between traces of pendent diols and ester moieties.

It must be stated that no diol was detected either by ^{1}H NMR and IR spectroscopy. In NMR (Figure 2.20), the adjacent proton peaks of the diol (a, b, c; Figure 2.20) can be easily differentiated from the boronic ester adjacent proton peaks (d, e, f; Figure 2.20).
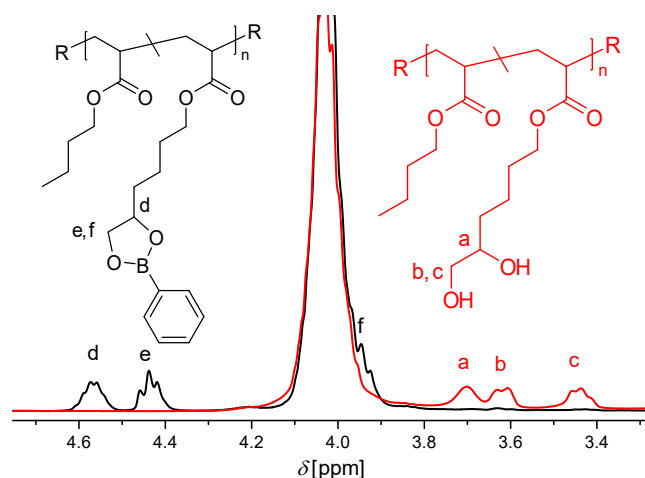
Figure 2.20: ^{1}H NMR spectra in CDCl$_3$ at 400 MHz of the TPs **P8** and **P9**, carrrying diol and boronic ester moieties, respectively.

In the IR spectrum (Figure 2.21), the signals associated with the hydroxy groups can be found between 3100-3600 cm^{-1}.
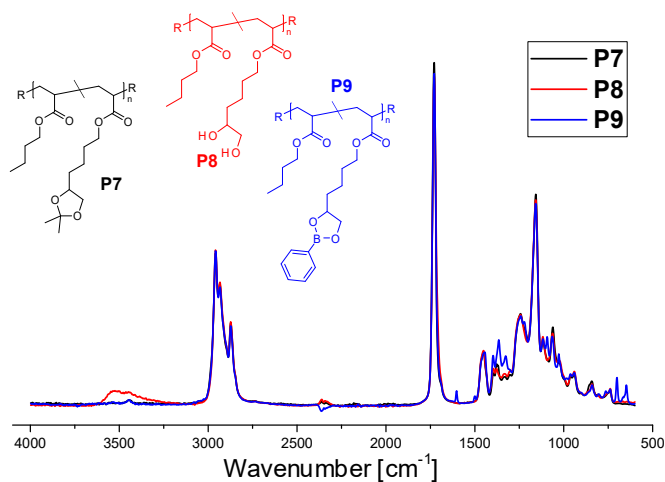
Figure 2.21: IR spectra of the TPs comprising the acetal protection group (**P7**), unprotected diols (**P8**), and the boronic esters (**P9**).

For the boronic ester and the acetal protected thermoplastic only an artifact can be found there, which might stem from air moisture. The concentration of free diols is hence below the detection limit of NMR and IR spectroscopy. The conversion of the protection of **P8** with the boronic acid is high, but it must be assumed that it is not 100 %. Therefore, a small number of diols are always present in the polymer of which already very small

amounts can cause the material to change its rheological properties. The effect of temperature on the rheological behavior of the TP **P9** was studied first. Figure 2.22 presents the TTS master curve. In Figure 2.23, the frequency sweeps of the sample at 150 °C over time are displayed. As can be seen, G' and G" increase and after 12 h there is a crossover that proceeds to lower frequencies with time. After 15 h at 150 °C, the crossover occurs at 90 rad/s. With time, the sample shows to becomes more "solid", a sign that the number of crosslinks in the sample is increasing.
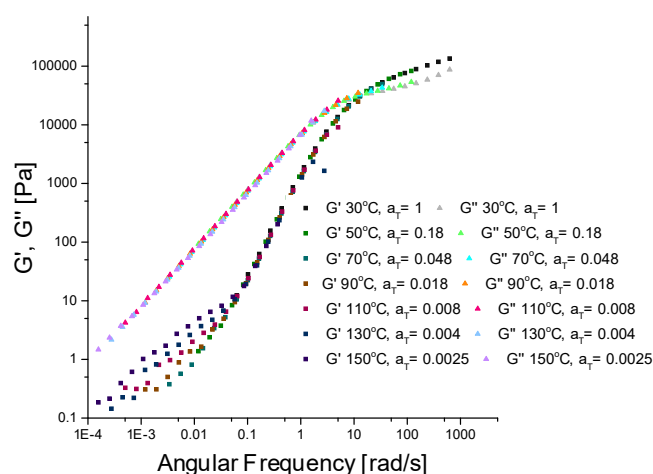
Figure 2.22: TTS mastercurve for the TP **P9** carrying boronic ester moieties.
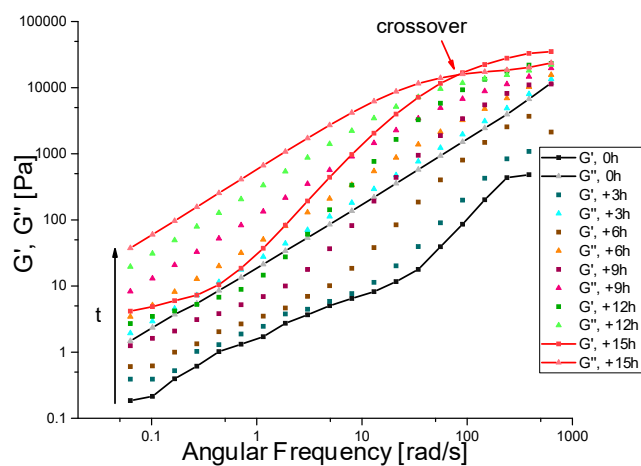
Figure 2.23: Frequency sweeps of the thermoplastic **P9** over the course of 15 h at 150 °C.

After the experiment, SEC was performed to assess the possible outcome of crosslinking reactions or degradation of the chains. As can be seen in Figure 2.24, a slight shoulder

appeared after the rheological test. This could indicate some branching. However, the sample was still well soluble and the M_n and $Đ$ were only slightly modified: 111 kDa and 1.19 for **P9** before the treatment vs. 116 kDa and 1.35 after 15 h at 150 °C.
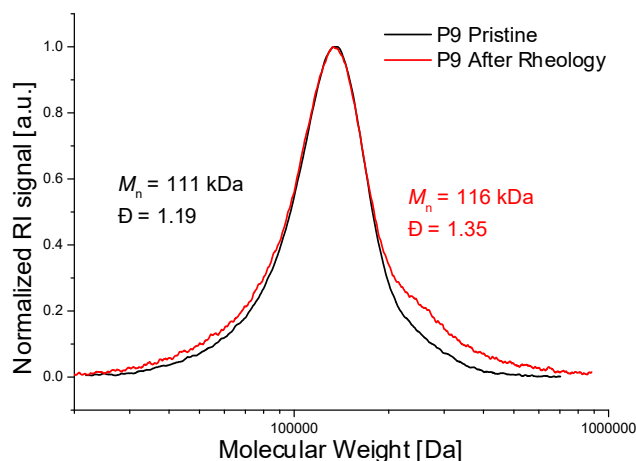
Figure 2.24: SEC analysis in THF (PS calibration) of **P9** before and after the rheology.

These experiments indicate that after a significant time at high temperature free diols in the polymer very likely generate inter-chain coupling. However, even after 15 h at 150 °C, the gel point was not reached and the sample was still well soluble. These experiments were conducted on the TP. The final network will presumably not show as much side reactions due to the more limited mobility of the chains, which circumvents unwanted diol transesterifications kinetically. However, irreversible crosslinking at high temperatures is a factor, which has to be considered in the design and interpretation of the following experiments.

2.13 Frequency Sweeps

Frequency sweeps have been conducted to evaluate the viscoelastic behavior of **Network 1**. Figure 2.25 presents the frequency sweep experiment performed at the lowest, 25 °C, and the highest, 150 °C, measured temperature on the **Network 1**. The sample shows a rubbery plateau of the storage modulus at all frequencies, with a G' of around 100-140 kDa. The fluctuations of the modulus at 25 °C at high frequencies might be due to slippage. The sample shows no sign of flow or relaxation under the applied conditions for no crossover of the moduli towards lower frequencies is observed. The change of

modulus with temperature is in accordance with the rubber elasticity theory (compare Subsection 2.10.3).
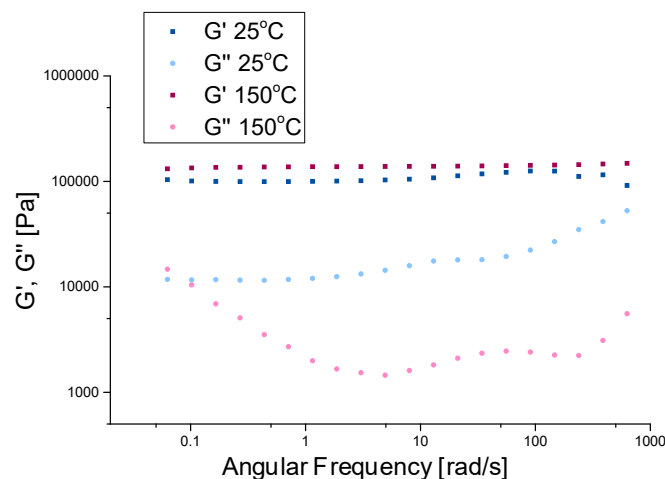
Figure 2.25: Frequency sweeps of **Network 1** at the lowest measured temperature 25 °C and the highest measured temperature 150 °C.

2.14 Stress Relaxation

2.14.1 Theory

The dynamics of the network can be assessed by stress relaxation experiments via rheometry. When an instant strain is applied to an ideal elastic solid, it will respond with a constant level of stress. In case of a viscoelastic solid the initial stress will be proportional to the applied strain and will decrease with time at a rate that can be described by the characteristic relaxation time τ.[42] The viscoelastic behavior in the boronic ester network is expected to be, like typically in vitrimer materials,[43] essentially controlled by the exchange reactions. Consequently, the thermal viscosity decrease should follow the Arrhenius law. The relaxation time and the viscosity are linearly connected like shown in Equation 2.13 according to the Maxwell model. Therefore, the characteristic stress relaxation times plotted in an Arrhenius plot as a function of 1/T exhibit a linear progression. The slope reflects the E_a for macroscopic flow like expressed in Equation 2.14, in which $\tau(T)$ represents the characteristic relaxation time at the temperature T, τ_0 is the Arrhenius prefactor, R the gas constant, and E_a is the activation energy of the viscous flow.

$$\eta = G \cdot \tau \tag{2.13}$$

$$\tau(T) = \tau_0 exp\left(\frac{E_a}{R \cdot T}\right) \tag{2.14}$$

The characteristic relaxation time can be calculated via different models. One is the calculation of the viscosity via the integration of the relaxation modulus G(t) over time according to the Equations 2.15 and 2.16. The accuracy of the rheometer has a significant influence using this method. There are fluctuations of the relaxation modulus at very short time periods in the beginning of the measurement as well as in the end of the measurement, when the relaxation modulus is low and the detection limit of the rheometer is reached. In addition, the integration area influences the value to an extent that the result is significantly determined by the experiment time, especially when the material does not relax stress to absolute zero.

$$\eta_0 = \int_0^\infty G(t)\mathrm{d}t \tag{2.15}$$

$$\tau = \frac{\int_0^\infty tG(t)\mathrm{d}t}{\int_0^\infty G(t)\mathrm{d}t} \tag{2.16}$$

One alternative method that has been used often in literature[44–49] is to approximately estimate the relaxation time by measuring how long it takes for a system to relax to $1/e$ (approx. 36.7 %) of its initial stress. This happens under the assumption that the system follows the Maxwell model for a single-exponential decay response, i.e., it relaxes via only one mode. For the boronic ester network, however, we must assume that it relaxes via several modes, and that next to the covalent exchange reactions other relaxation mechanisms caused e.g. by entanglements have to be taken into account. A more suitable model would be the Kohlrausch-Williams-Watts (KWW) stretched exponential decay described by Equation 2.17, where G(t) signifies the relaxation modulus at time t, G_0 the initial relaxation modulus, G_{rest} the residual stress that cannot be relaxed with time, τ the characteristic relaxation time, and β ($0 < \beta \leq 1$) the exponent that reflects the broadness of the relaxation distribution.[50,51] Since the system shows complete stress relaxation within the experimental error, G_{rest} can be set to 0. The equation hence simplifies to Equation 2.18.

$$\frac{G(t)}{G_0} = \frac{G_{rest}}{G_0} + \left(1 - \frac{G_{rest}}{G_0}\right) exp\left\{-\left(\frac{t}{\tau}\right)^{\beta}\right\} \tag{2.17}$$

$$\frac{G(t)}{G_0} = exp\left\{-\left(\frac{t}{\tau}\right)^{\beta}\right\} \tag{2.18}$$

Also in this method, fluctuations in the beginning of the measurement have to be considered. Modeling has been conducted only after the values of the relaxation modulus have reached a stable level (after approx. 0.07 s measuring time).

2.14.2 Experiments with Equilibration at 110 °C

For the stress relaxation a measuring protocol has been elaborated that considers the following premises:

- The sample needs a significant time at elevated temperatures to equilibrate;

- The sample might undergo side reactions when kept long times at high temperatures;

- Slippage events are more likely to occur at low temperatures;

- The sample relaxes stress slowly at low temperatures, which requires very long experiment times.

Consequently, the sample was allowed to equilibrate at 110 °C for 24 h, before the experiments were conducted. Before every experiment a frequency sweep was done. Stress relaxation was performed from 110 °C downwards in 10 °C steps to avoid side reactions. The lowest temperature was 70 °C to avoid too long experiment times. After 70 °C the rheometer was reprogrammed and stress relaxation was conducted from 110 °C upwards in 10 °C steps to 150 °C. The results were interpreted with precaution due to the possible diol transesterifications at these temperatures.

The relaxation curves of this experiment are shown in Figure 2.26 (left). A repetition of the experiment with another specimen of the same batch gave almost identical results. The curves were used to obtain the characteristic relaxation times τ using the KWW model after Equation 2.18 with β values around 0.5-0.6. The so calculated relaxation times were plotted in an Arrhenius plot (see Figure 2.26, right), whose slope was used

to determine the E_a using Equation 2.14. When going down from 110 °C to 70 °C an Arrhenius behavior with a linear dependance of the characteristic relaxation times in relation to the inverse of the temperature could be observed. This resulted in an E_a of 56.6 ± 1.5 kJ/mol and a $\ln(\tau_0)$ of -10.6 ± 0.5. When going back to 110 °C and doing stress relaxation going in 10 °C steps up until 150 °C, an Arrhenius dependance was also observed, but this time with a much higher slope. In this case E_a was 120.2 ± 6.0 kJ/mol and $\ln(\tau_0)$ -30.6 ± 1.8, the sample relaxes stress much faster.
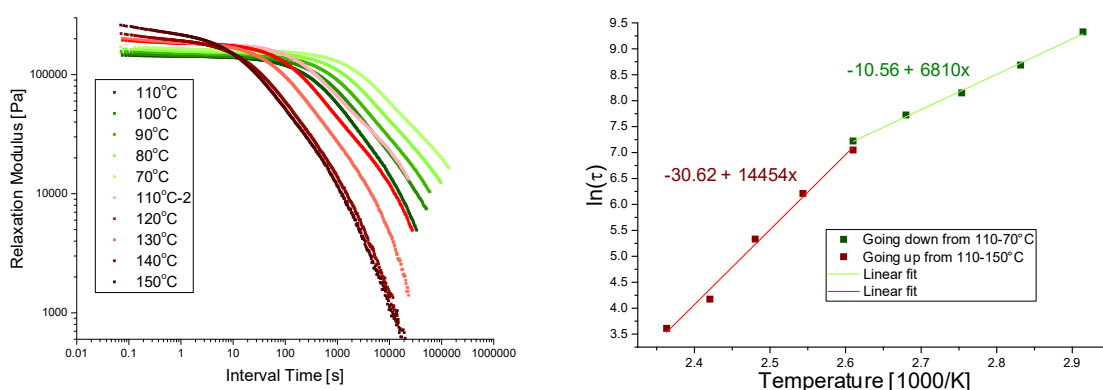
Figure 2.26: Left: Stress relaxation curves of **Network 1** when going down from 110 to 70 °C (green) and then up from 110 to 150 °C (red). Right: Arrhenius plot of the characteristic relaxation times of **Network 1**.

It seems that several relaxation mechanisms play a role in the overall relaxation process, which might be temperature and/or time dependent. When the curves from 110 °C to 70 °C are shifted using the TTS principle (Figure 2.27) one can see that a second relaxation mechanism takes over. The first relaxtion can be attributed to the boronic ester exchanges. With lower temperatures (or longer experiment time) a second relaxation at longer time scales becomes prominent. It seems that this second relaxation is not anymore observed during the relaxations at 140 and 150 °C. To get more insight into the behavior of the sample, stress relaxation experiments were started at 150 °C, going down from there. Before the experiment, the sample was equilibrated for 24 h at 110 °C, to get better comparability with the previous experiment. After these 24 h, the material was heated to 150 °C and was kept at this temperature for 60 min, before a frequency sweep was conducted. After the frequency sweep, stress relaxation was tested. After the stress was relaxed, the sample was cooled down 10 °C, equilibrated for another hour, before the procedure was repeated.
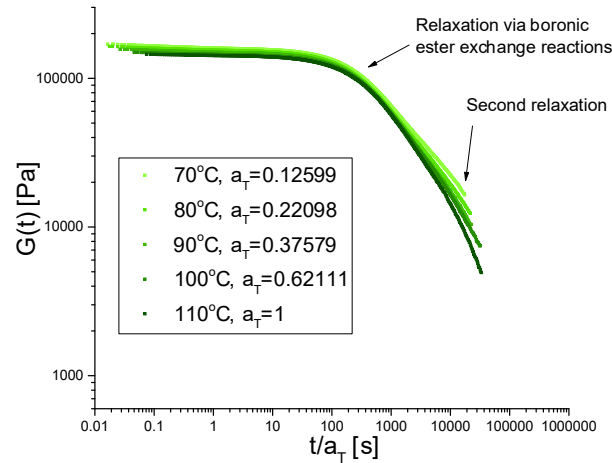
Figure 2.27: Stress relaxation curves of **Network 1** when going down from 110 to 70 °C shifted after the TTS principle.

The stress relaxation curves are displayed in Figure 2.28 (left). From 150 to 120 °C the stress relaxation curves are very similar, starting from 110 °C, the relaxation process is slowing down with the decrease of the temperature, as expected for vitrimers. The Arrhenius plot of this experiment next to the one of the previous experiment is shown in Figure 2.28 (right). The question rises why there is no linear decrease in relaxation time at the higher temperatures. One explanation might be that during the equilibration clusters between the boronic ester groups have formed and it takes time to break them up again. In the first measurements after the equilibration they slow down the relaxation process. 110 °C might hence be a too low temperature to equilibrate the samples. To avoid this possible cluster formation, equilibration was conducted at a higher temperature.
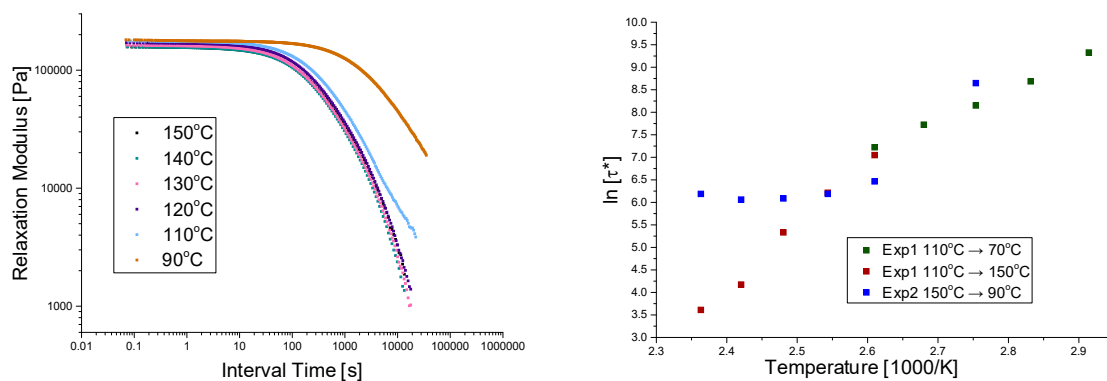
Figure 2.28: Left: Stress relaxation curves of **Network 1** when going down from 150 to 90 °C after an equilibration step. Right: Arrhenius plot of the characteristic relaxation times.

2.14.3 Experiments with Equilibration at 150 °C

The stress relaxation was repeated skipping the equilibration step at 110 °C. The first stress relaxation was conducted directly at 150 °C. The relaxation curves and the respective Arrhenius plot of this experiment are displayed in Figure 2.29. The first relaxation at 150 °C is out of equilibrium, as indicated by the lower initial relaxation modulus and the very fast relaxation time. This was expected, since no equilibration step was conducted. In fact, the first relaxation at 150 °C during 5 h can be seen as the equilibration step in this case. The stress relaxations that followed were at equilibrium G_0 and followed an Arrhenius behavior.
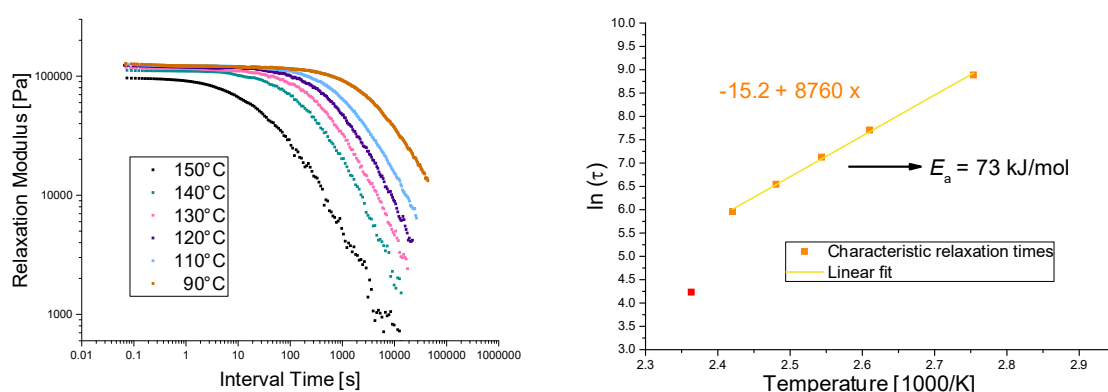
Figure 2.29: Left: Stress relaxation curves of **Network 1** when going down directly from 150 to 90 °C. Right: Arrhenius plot of the characteristic relaxation times. The first value at 150 °C was excluded from the fit.

The activation energy is with 72.8 $\pm$ 1.6 kJ/mol and a ln(τ_0) of -15.2 $\pm$ 0.5 in between the values obtained in the first experiment (see Figure 2.30, left). When the curves are shifted after the TTS principle one can see that they overlap (Figure 2.30, right). In comparison to the relaxation curves of the first experiment (green), no second relaxation can be observed. This could be a sign that cluster formation is avoided conducting the experiment in this manner.

2.14.4 Conclusion

Stress relaxation experiments showed that the thermal history of the sample has a significant influence on its behavior. Initial equilibration is essential to reach the equilibrium modulus. Several relaxation processes seem to play a role in the network. One is
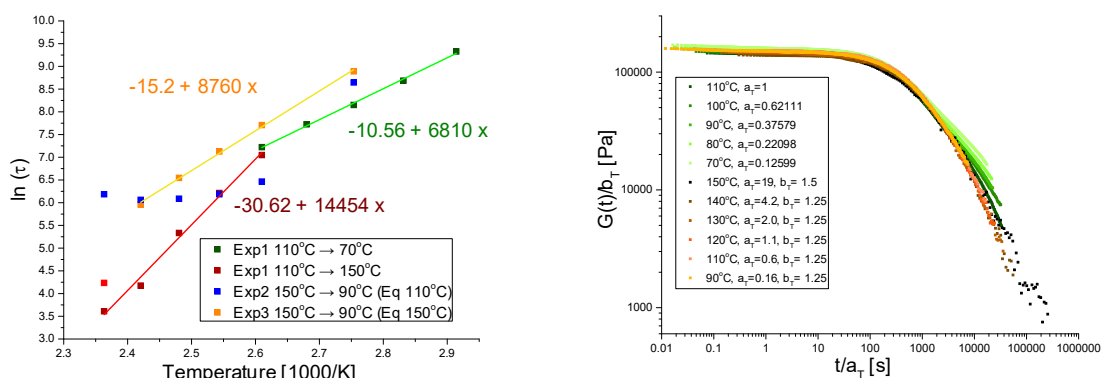
Figure 2.30: Left: Comparison of the Arrhenius plot with the values from the previous experiments. Right: Stress relaxation curves of **Network 1** when going down from 150 to 90 °C (orange) directly compared to the ones when going down from 110 to 70 °C (green). The curves were shifted for comparability. The curves when going down from 150 to 90 °C indicate that no cluster relaxation took place.

the exchange reaction between the boronic ester bonds. Other possible relaxation mechanisms would be cluster formation between the functional groups potentially resulting from Lewis acid/base interactions between dioxaborolane units, π-π interactions between the phenyl rings of boronic ester and Van-der-Waals interactions. In addition to these temperature dependant interactions, irreversible crosslinking induced by traces of free diol might also impact the relaxation behavior of the complex. Entanglements between the polymer chains are also a factor that has to be taken into account. To assess the relaxation behavior of the boroic ester exchange in this network, the results obtained when going from very high temperature to low temperature seem to give the most reliable results, since clustering and physical interactions are suppressed or play a rather ancillary role. Thus the obtained values of E_a = 72.8 $\pm$ 1.6 kJ/mol and $\ln(\tau_0)$ = -15.2 $\pm$ 0.5 will be used for further discussion. More experiments can be conducted to further investigate the relaxation mechanisms of **Network 1**. Techniques, such as steady state NMR spectroscopy, X-ray diffraction, or AFM, might give further insight into the structural composition of the material.

2.15 Creep

It is of interest to see, how the dynamics of the bonds affect the dimensional stability of the network. To evaluate this aspect, a creep and recovery experiment was conducted.

Creep is defined as the time-dependent change in strain following a step change in stress.[42] A typical viscoelastic solid will respond with an immediate elastic deformation, followed by a delayed elastic deformation and the Newtonian flow, which represents the viscous part of the material and obeys Newton's law of viscosity.[42] In case the sample shows full relaxation, the increase of the strain becomes linearly proportional to time. This steady state flow indicates the material has reached terminal relaxation.[52] The creep compliance (J(t)) is a mean to quantify the capacity of a material to flow in response to a sudden applied stress. J(t) and the creep recovery compliance (J_r(t)) were determined via Equations 2.19 and 2.20, respectively. γ(t) is the strain at time t, σ is the applied shear stress, and γ_f is the value of the strain when the stress was removed. In order to eliminate the parasitic drift from the creep recovery compliance, the true creep recovery compliance (J_r^{true}(t)) was estimated utilizing Equation 2.21.[52]

$$J(t) = \gamma(t)/\sigma \tag{2.19}$$

$$J_r(t) = (\gamma_f - \gamma(t))/\sigma \tag{2.20}$$

$$J_r^{true}(t) = J_r(t) - \frac{dJ_r}{dt_r}t_r \tag{2.21}$$

Beforehand, a strain sweep was conducted at 50 °C. As can be seen in Figure 2.31, the sample remains in the linear regime up to 10 % strain and 8000 Pa.
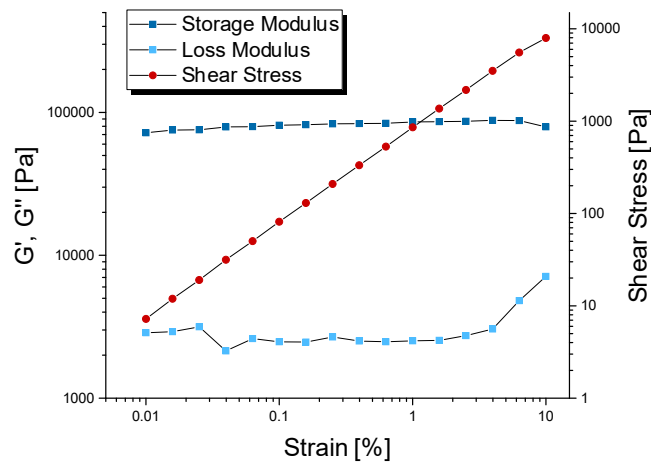
Figure 2.31: Strain Sweep of **Network 1**. The sample remains in the linear regime.

The creep experiment was conducted by applying a shear stress of 2500 Pa for 24 h at 25 °C, before the sample was allowed to recover another 24 h. In Figure 2.32, left, it can be seen that the sample only shows limited deformation during the elastic response. 5 min after the stress was applied, the sample showed a deformation of 4.6 %. During the next 24 h it crept to 5.3 %. When the stress was taken away, the sample recovered to 1.9 % strain. After 24 h of relaxation, 1.7 % residual strain remained. The strain rate during the creep experiment can be used to determine the viscosity of the sample by using Equation 2.22. The strain rate was calculated by determining the slope of the strain plotted vs. interval time and was calculated for all times over 30 data points and is displayed in Figure 2.32, right, as a function of time. The last value was taken to determine the viscosity, which was calculated to be $4.02 \cdot 10^{10}$ Pa·s at 25 °C. It shows in Figure 2.32 (right) that the strain rate decreases with time, leading to an increase in viscosity. The absence of a steady state flow indicates that the sample has not (yet) reached terminal relaxation.

$$\eta = \frac{\sigma_0}{\dot{\gamma}} \tag{2.22}$$
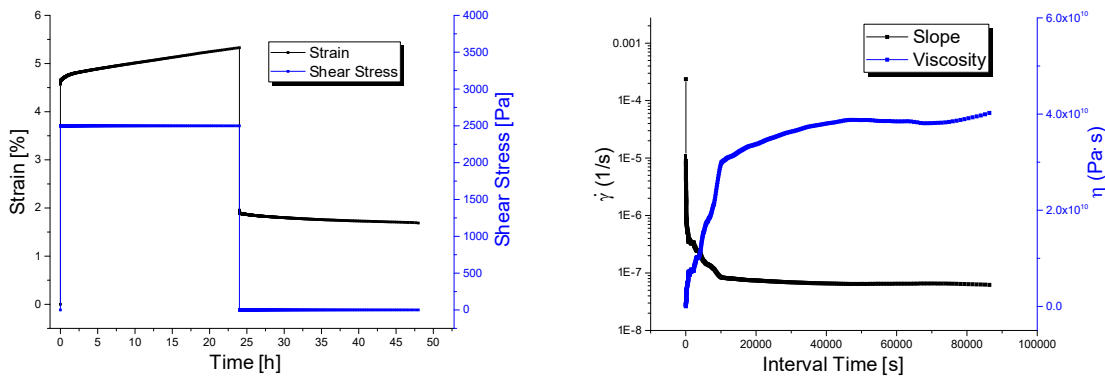
Figure 2.32: Creep behavior of **Network 1**. A shear stress of 2500 Pa was applied for 24 h, before the sample was allowed to recover for another 24 h. Left: Strain and shear stress in function of the creep experiment time. Right: $\dot{\gamma}$ and the viscosity in function of the creep experiment time.

In Figure 2.33 the creep compliance and the creep recovery compliance with time are displayed. It can be seen clearly that J(t) does not reach the steady-state flow scaling of 1 during the time of the experiment. It does not reach terminal relaxation.[52]
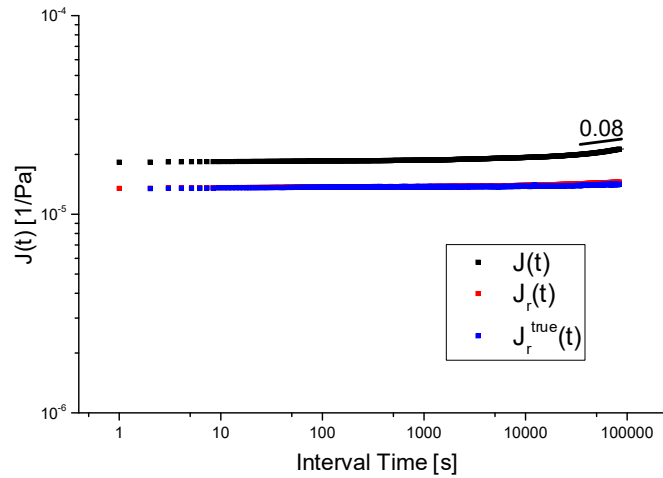
Figure 2.33: J(t), J_r(t), and J_r^{true}(t) of **Network 1** in function of the creep experiment time.

2.16 Viscosity and Topology Freezing Temperature

Since the viscosity and the relaxation time are linked with Equation 2.13 after the Maxwell model, the results of the creep experiment can be compared with the viscosity extrapolated by the stress relaxation experiment. The relation between relaxation time and temperature can be expressed via the Arrhenius relationship in Equation 2.14. With the values obtained by the linear fit of the Arrhenius plot (Figure 2.29) of the stress relaxation experiment, this equation becomes Equation 2.23. This leads to a theoretical relaxation time of $1.45 \cdot 10^6$ s at 25 °C.

$$In(\tau(T)) = -15.193 + \frac{8759.55}{T} \tag{2.23}$$

To calculate the respective viscosity Equation 2.13 with G as the shear modulus can be applied. G was estimated from the tensile modulus determined by the DMA measurements. In general, the relation between the shear modulus and the tensile modulus can be expressed with Equation 2.24, which can be simplified by assuming that the Poisson's ratio is $\nu = 0.5$ as usually for rubber systems.[44,53] E' was taken as a temperature dependent value (see Figure 2.15) and with Equation 2.25 the theoretical viscosity of the network for this temperature range was calculated and is shown in Figure 2.34.

$$G = \frac{E'}{(2(1 + \nu))} \approx \frac{E'}{3} \tag{2.24}$$

$$\eta(T) = \left[\tau_0 * exp\left(\frac{E_a}{R \cdot T}\right)\right] * \frac{E'}{3} \tag{2.25}$$
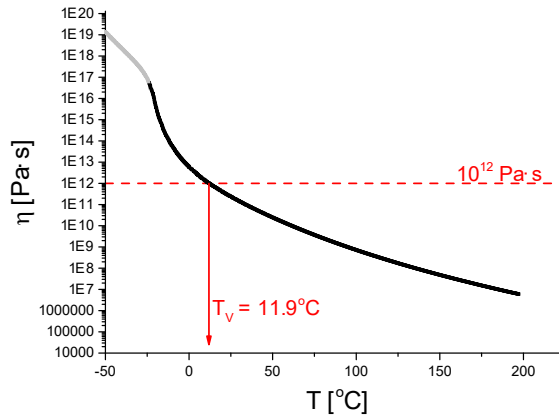
Figure 2.34: Calculated development of the viscosity of **Network 1** with temperature based on data obtained via stress relaxation and DMA. The T_V is defined as the temperature where the melt viscosity becomes higher than 10^{12} Pa·s. Below the T_g (grey points) the viscous flow is restricted due to the frozen motion of the polymer chains.

At 25 °C, the calculated viscosity of the sample is around $2.28 \cdot 10^{11}$ Pa·s, somewhat higher than the one obtained from the creep experiment ($4.02 \cdot 10^{10}$ Pa·s). It has to be taken into account that there is a certain error margin for τ_0, E_a and E', as well as for the values obtained via the creep measurement. In addition, this can be explained by the fact that the two values are obtained at different temperature ranges. The sample showed to relax stress via different relaxation modes. Next to the exchange reactions, cluster formation, π-π stacking, permanent crosslink formation due to side reactions or other dynamic modes can influence the behavior of the sample. These modes become and stay active in different temperature and/or time windows. The stress relaxation was conducted at rather high temperature, the creep experiment at room temperature. Also the DMA measurement is influenced by the thermal history of the sample. Yet, the two values agree very well.

The Arrhenius dependance of the relaxation time with the temperature gives also the possibility to calculate the T_V of the system. T_V represents the characteristic transition temperature of a vitrimer system starting from which the degenerate reactions between the DCBs are proceeding. T_V only becomes relevant though if it is above the T_g.

Otherwise, the viscous flow would be restricted by the frozen motion of the polymer chains. T_V is defined as the temperature at which the melt viscosity becomes higher than 10^{12} Pa·s.[54–56] Using the obtained data, the sample has a T_V around 11.9 °C. This value is close to room temperature and this might be an explanation why the sample showed only limited creep and no terminal relaxation during the creep experiment at 25 °C.

2.17 Tailoring the Dynamics of the Network

The rheometry experiments show that the network features only limited dynamics at room temperature. The exchange is not fast enough to let the sample relax stress at acceptable time scales. Usually it is not desirable for a material to relax stress at room temperature, since this leads to a lack of dimensional stability and creep. For the DDN, however, a subnetwork is needed that is able to dissipate energy (fast). Therefore, it is desirable that the boronic ester network relaxes stress rapidly at ambient conditions. One relatively simple way to accelerate the exchange reaction is to add free diols into the system, as a study by the group of Sumerlin suggested.[28] A straight forward way would be to leave some or all diol groups on the thermoplastic **P8** unprotected. However, experiments indicated that free diols in the system might lead to esterifications with the polymer backbone and thus to irreversible crosslinking, which might alter the system properties significantly (compare Subsection 2.12.1). A way to avoid side reactions on a large scale is to add a monofunctional diol as a free molecule like shown in Scheme 2.17. In case the diol reacts with the backbone, no additional crosslink is formed. However, the amount of diol that can be added to the system is limited. The diol reduces the crosslinking density by reacting with the crosslinking boronic ester moieties. In addition, when the diol engages in transesterifications with the pendent boronic ester groups, these are transformed into free diols, which are prone to undergo side reactions that lead to irreversible crosslinking. The diol has to stay in the system at high temperatures, because of its low volatility 1,2-dodecandiol (DDD) was chosen as small molecule.
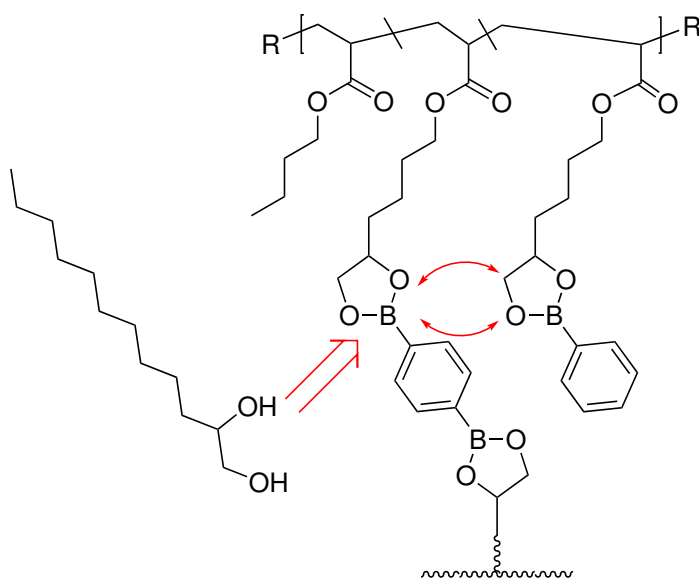
Scheme 2.17: A free diol, such as 1,2-dodecandiol (DDD), can accelerate the exchange reaction between boronic esters.

For a first test, it was envisioned to add 5 % DDD in respect to boronic ester functions to the material. To assess how much this would affect the crosslinking density, the probability of the following events were calculated:

- P_x: Probability that a crosslinker is linked on both ends to a polymer chain

- P_p: Probability that a crosslinker is linked on one end only to a polymer chain, it is pendant

- P_f: Probability that a crosslinker is not linked to a polymer chain on both ends, it diffuses freely

The probabilities were calculated with the Equations 2.26-2.28, where x is the ratio of crosslinker and y the ratio of DDD per chain, when 20 % of the pendent boronic esters are crosslinked and 5 % of DDD is added with respect to the total amount of boronic ester functions. The values are P_x = 95.2 %, P_p = 4.8 % and P_f < 0.1 %. Practically seen, the addition of 5 % DDD affects the crosslinking density to only an insignificant amount.

$$P_x = \left(\frac{2x}{2x + y} \right)^2 \tag{2.26}$$

$$P_p = \frac{2 \cdot (2x) \cdot y}{(2x + y)^2} \tag{2.27}$$

$$P_f = \left(\frac{y}{2x + y} \right)^2 \tag{2.28}$$

After the crosslinking of the network, the material was swollen in THF and a solution of the respective amount of DDD was added. The sample was dried and then processed like before to yield **Network 1a**. To evaluate the dynamics of the system, stress relaxation experiments were performed. As can be seen in Figure 2.35, the sample with the DDD relaxes stress much faster than the sample, where no diol was added.
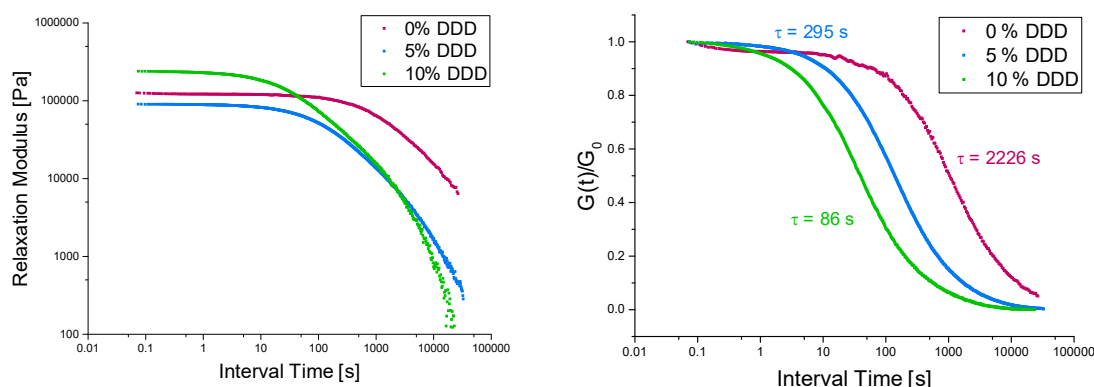
Figure 2.35: Left: Stress relaxation curves of **Network 1** (containing no DDD, red), **Network 1a** (containing 5 % DDD, blue), and **Network 1b** (containing 10 % DDD, green) at 110 °C. Right: normalized to G_0.

The sample without the DDD has a relaxation time of $\tau = 2226$ s at 110 °C, whereas the sample with the 5 % DDD takes 295 s to relax at the same temperature. However, the absolute modulus of the **Network 1a** is somewhat lower, which is in accordance with the lower crosslinking density. To determine, if this relaxation time can be even more decreased, a second network (**Network 1b**) containing 10 % DDD was prepared. As can be seen in Figure 2.35, with the higher amount of DDD, the stress relaxation time further decreases to only 86 s. Employing Equations 2.26-2.28, P_x decreases to 90.7 %, and P_p increases to 9.1 % with $P_f = 1.6$ %. However, **Network 1b** exhibited a much higher relaxation modulus than the other two networks, which have in fact a higher theoretical crosslinking density, which is contradictory. These results confirm that by the addition of a free diol the dynamics of the exchange reactions can be altered significantly. However, to show energy dissipation at application temperature a fast exchange at lower temperatures

is necessary. When the stress relaxation was conducted at room temperature, one can see that the system still requires a significant amount of time to relax stress (Figure 2.36). At 25 °C the relaxation time is about 7000 s for **Network 1a** and 2700 s for **Network 1b**.
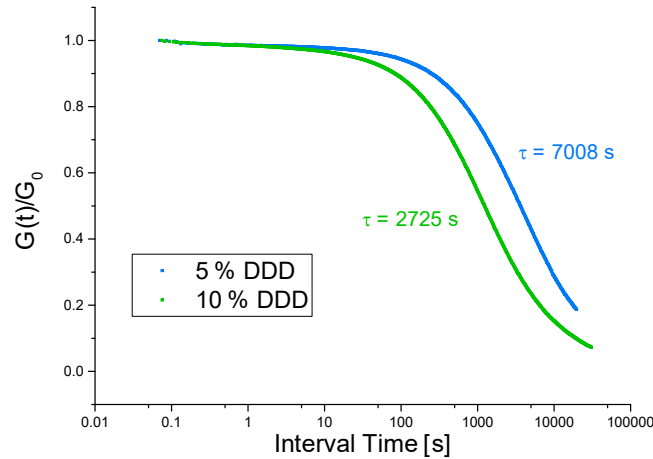
Figure 2.36: Stress relaxation curves of **Network 1a** (containing 5 % DDD, blue), and **Network 1b** (containing 10 % DDD, green) at 25 °C.

Figure 2.37 presents frequency sweep experiments on the networks conducted at 25 °C (left) and 110 °C (right). It shows that at ambient conditions all three networks exhibit
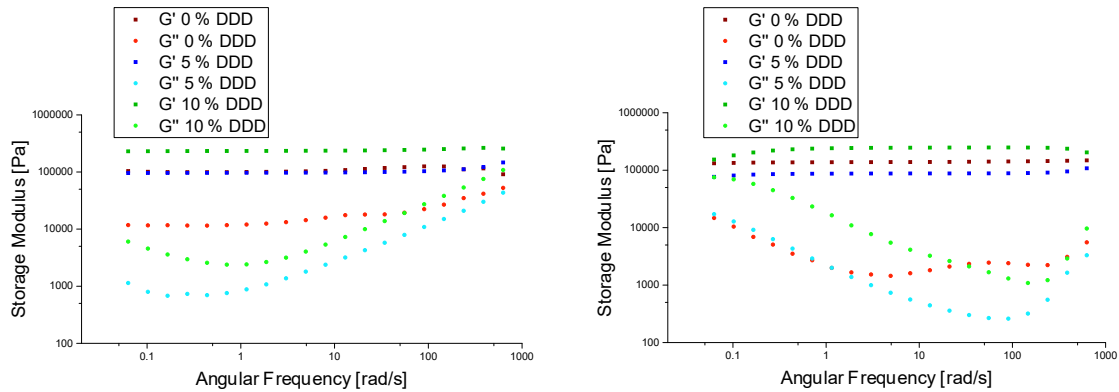
Figure 2.37: Frequency sweeps of **Network 1** (containing no DDD, red), **Network 1a** (containing 5 % DDD, blue), and **Network 1b** (containing 10 % DDD, green). Left: at 25 °C. Right: at 110 °C.

a plateau of the storage modulus over the entire frequency range. No crossover of the moduli can be detected, indicating no transition to the terminal flow regime takes place. At 110 °C **Network 1b** exhibits an increase of the loss modulus as well as a decrease of

the storage modulus at lower frequencies, approaching the crossover point. The sample with the highest amount of DDD showed the highest modulus, which is contradictory to its lowest theoretical crosslinking density. Since there is no trend in value of the modulus with decreasing crosslinking density, one can suppose the discrepancy in the moduli has its origin in the experimental setup (differences in gap and normal force).

The addition of DDD has a strong effect on the dynamics of the exchange reaction and the rheological properties of **Network 1**. It could be shown that the characteristic relaxation times of the sample could be significantly decreased with increasing amount of added diol. At high temperatures and low frequencies the sample featured more viscous behavior with increasing amount of DDD. However, at ambient conditions the relaxation times were still in the range of several thousand seconds and no transfer to the viscous regime could be detected during frequency sweeps. It must therefore be evaluated if the change of dynamicity is sufficient to impart properties like energy dissipation at room temperature.

2.18 Conclusion

In this chapter it was described how the boronic ester subnetwork was prepared and analyzed. A protected diol functionalized acrylate monomer was synthesized over two steps and copolymerized with *n*BA via RAFT polymerization. The resulting well defined polymer was further treated to yield the TP with pendent boronic ester functions. This procedure would allow to create thermoplastic precursors of various molecular weights and functional densities, if needed. A bifunctional boronic ester crosslinking agent was synthesized in one step and the TP was crosslinked to a network. The network could be processed via compression molding in short times at moderate temperature into a transparent, colorless material. A relatively brittle elastomer with a Young's Modulus of 0.50 MPa and a T_g of around -40 °C was obtained. The material showed good thermal stability up to 250 °C and an excellent long term stability at 150 °C. The material maintained its network structure up to high temperatures in DMA measurements with a tensile storage modulus around 0.5 MPa above the T_g. The network structure showed a stable integrity in THF over short term. When the sample is immersed into THF over a longer period, the material completely dissolves, likely due to the formation of soluble branched and cyclic structures. This characteristic will have to be taken into account for the chemical recycling for the double network. The network can be de-crosslinked in a controlled manner by adding free small molecule diols. The crosslinks in the network are

sensitive to hydrolysis. A direct contact with water does not harm the material due to the hydrophobic character of the polymer matrix. When immersed into a water/THF solution, the material de-crosslinks completely.

The sample was thoroughly characterized via rheometry. During frequency sweeps, the sample showed a rubbery plateau with a storage modulus of 100-150 kPa with no sign of relaxation at all tested temperatures (25-150 °C) and frequencies (0.01-100 Hz). Its rheological behavior is strongly dependent of the thermal history of the sample. Presumptively, this is due to the formation of clusters between the functional groups at lower temperatures with time, which leads to additional relaxation modes. To avoid this cluster formation, equilibration steps at high temperatures before the experiments have been implemented. During stress relaxation experiments, complete stress relaxation could be observed. Employing the characteristic relaxation times at various temperatures, an activation energy of 73 kJ/mol could be determined. However, the relaxation times were relatively high with e.g. 2200 s at 110 °C. At ambient temperatures, the sample showed only very slow dynamics. This could also been seen during creep experiments, where the sample showed hardly creep and no terminal relaxation at room temperature even after 24 h. With the data obtained via stress relaxation and DMA, the T_V was extrapolated to be around 12 °C, which is very close to ambient conditions and a possible explanation for the limited dynamics at low temperatures. One of the goals of the double network project was to combine a more dynamic with a more static network. However, the boronic ester network did not show the desired dynamic behavior under the applied conditions.

In order to make the material more dynamic, free diols have been added to the sample. In theory, the diols do not affect the crosslinking density significantly. Stress relaxation experiments indicated that the characteristic relaxation time of the material can be lowered via this method by a factor of 25. However, the material still needs several thousands of seconds to relax stress at application temperature. Further experiments, such as cyclic loading/unloading tensile tests, will show, if the reaction can be accelerated enough to make the system show fast enough dynamics for energy dissipation at room temperature.

2.19 Experimental Part

2.19.1 Materials

All chemicals were purchased from Sigma Aldrich, Alfa Aesar, TCI, Acros Organics and Fischer. All starting materials and reagents were of analytic grade and used without further purification, if not stated otherwise. AIBN was recrystallized from methanol prior to use. 1,4-Dioxane and *n*BA were passed through a short column of basic alumina to remove inhibitors or antioxidants.

2.19.2 Instrumental Data

NMR Spectroscopy

^{1}H NMR and ^{13}C NMR spectroscopy measurements were performed in oven dried NMR tubes on a Bruker Ultra Shield machine (400 MHz for ^{1}H NMR, 100 MHz for ^{13}C NMR) at ambient temperature. If not stated otherwise, samples of 10 mg for ^{1}H NMR and 30 mg for ^{13}C NMR were analyzed. CDCl$_3$ was employed as deuterated solvent. Chemical shifts are expressed in parts per million (ppm) and calibrated on characteristic solvent signals as internal standards (^{1}H NMR: CDCl$_3$: 7.26 ppm; ^{13}C NMR: CDCl$_3$: 77.16 ppm).

Size Exclusion Chromatography

The samples for SEC chromatography were prepared by dissolving the respective polymer in anhydrous THF to obtain a concentration of 1.0-1.2 mg/mL. A drop of toluene was added and the sample was passed through a 0.20 μm PTFE filter and placed in a Malvern GPC vial. SEC was performed on a Viscotek GPCmax/VE2001 connected to a Triple detection array (TDA 305) from Malvern. Obtained raw data were treated with a PS calibration.

FTIR Spectroscopy

FTIR spectroscopy was conducted on a Tensor 37 spectrometer from Bruker in the solid or liquid state and recorded in attenuated total reflection (ATR) mode.

DSC

DSC analyses were performed on TA DSC 250 apparatus. Two heating cycles, from -100 to 200 °C, were performed employing a heating rate of 10 °C min^{-1}. The values of T_g were determined with the data obtained on the second heating cycle.

TGA

TGA measurements were performed on a TG 209 F1 Libra from Netzsch under a nitrogen flow. The samples were heated constantly with a rate of 10 °C min^{-1} from 30 to 600 °C. Isothermal analyses were conducted by heating samples constantly with a rate of 10 °C min^{-1} from 30 to 150 °C, and keeping the sample at 150 °C for 10 h.

DMA

DMA measurements were conducted on a TA Instruments Q800 in tension mode. Heating ramps were performed from -80 to 200 °C at a constant rate of 3 °C min^{-1} with a fixed frequency of 1 Hz and a maximum strain amplitude of 1 %. The T_g of the sample was determined at the maximum of the loss modulus function E".

Compression Molding

Compression molding was conducted using a hydraulic press applying a pressure equivalent to 3 tons. Dry samples were placed into a metal mold and pressed at 110 °C for 20-30 min.

Tensile Tests

Uniaxial tensile tests were performed on dumbbell-shaped specimens (l x w x h = 13 x 1.6 x 2.1 mm) using an Instron 5564 tensile machine mounted with a 100 N transducer cell. The specimens were tested at a fixed cross-head speed of 10 mm/min. Testing was carried out at room temperature for all materials. Engineering stress-strain curves were obtained through measurements of the tensile force F and cross-head displacement Δl by defining the engineering stress as $\sigma = F/S_0$ and the strain as $\gamma = \Delta l/l_0$, where S_0 and l_0

are the initial cross section and gauge length of the specimens, respectively. The Young's modulus E was determined as the slope of the engineering stress-strain curves between 2-5 % strain.

Swelling and Solubility Experiments

The network was compression molded into disk like shapes and cut into parts of 200-300 mg (m(dry)). 20 mL of THF were added and the sample was allowed to swell for 24 h or 7 days. Subsequently, the excess of THF was removed with a syringe. The swelled samples were weighted (m(swollen)). The samples were dried under vacuum at elevated temperatures to remove the THF that was taken up. In the end the mass of the dried sample was evaluated (m(dried)). The swelling ratio was determined via Equation 2.29, the insoluble fraction via Equation 2.30.

$$\text{Swelling ratio} = \frac{m(\text{swollen}) - m(\text{dried})}{m(\text{dried})} \tag{2.29}$$

$$\text{Insoluble fraction} = \frac{m(\text{dried})}{m(\text{dry})} \tag{2.30}$$

Solvolysis

-Diolysis

227 mg of **Network 1** was immersed into a mix of THF (10 mL) and 1,2-propanediol (500 eq/CL: 8.20 mmol, 624 mg, 0.6 mL). After 48 h a part of the mixture was concentrated and precipitated in MeOH, the precipitate was dissolved in THF and subjected to SEC analysis.

-Hydrolysis

Around 250 mg of **Network 1** was immersed into a mix of THF and water (3 : 1, 20 mL). After 24 h, a part of the mixture was concentrated and precipitated in hexane, the precipitate was dissolved in THF and subjected to SEC analysis.

Rheological Characterizations

All rheological characterizations were conducted on a Anton Paar MCR 501 rotational rheometer with a parallel plate geometry with a diameter of 25 mm. If not otherwise stated, the experiments were run in a convection oven under nitrogen. For solid samples, a normal force of 0.4 N was employed. For liquid samples, a constant gap was set, which was adjusted as a function of the volume of the sample. Before the experiment, samples were allowed to equilibrate for 24 h at 110 °C or for 5-6 h at 150 °C, if not stated otherwise.

Frequency sweeps were conducted at 1 % strain between 0.01 and 100 Hz on a logarithmic ramp with 5 measuring points per decade (if not stated otherwise).

Stress relaxations were conducted with an applied strain of 1 % A frequency sweep was conducted, before every stress relaxation experiment. The relaxation time τ was calculated from the obtained data using the KWW model after Equation 2.31.

$$\frac{G(t)}{G_0} = exp\left\{-\left(\frac{t}{\tau}\right)^{\beta}\right\} \tag{2.31}$$

Table 2.5: Relaxation times τ and β determined via the modeling employing Equation 2.31 during the stress relaxation experiments of **Network 1** in the relaxation experiment when going down from 110 to 70 °C and then up from 110 to 150 °C (Figure 2.26).

T [°C]	τ [s]	β
110	1369	0.57
100	2261	0.54
90	3463	0.51
80	5917	0.48
70	11236	0.46
110-2	1151	0.48
120	499	0.50
130	207	0.50
140	65	0.47
150	37	0.45

Table 2.6: Relaxation times τ and β determined via the modeling employing Equation 2.31 during the stress relaxation experiments of **Network 1** in the experiment with the equilibration step (Exp2, Figure 2.28) and without the equilibration step (Exp3, Figure 2.29) going down from 150 to 90 °C.

T [°C]	τ [s] Exp2	β Exp2	τ [s] Exp3	β Exp3
150	486	0.63	69	0.55
140	429	0.64	387	0.60
130	440	0.64	696	0.59
120	486	0.64	1245	0.58
110	642	0.64	2226	0.57
90	5690	0.58	7254	0.53

Amplitude sweeps were conducted between 0.01-10 % strain on a logarithmic ramp with 5 measuring points per decade at a frequency of 1 rad/s at 50 °C.

Creep experiments were conducted at 25 °C with a constant shear stress of σ = 2.5 kPa for 24 h. Subsequently, the sample rested at 0 shear stress at the same temperature for another 24 h. Before the experiment a frequency sweep was conducted.

The slope of the strain as a function of time was calculated for all times using the LINEST Excel command over 30 points. The value of the last 30 points were taken to calculate $\dot{\gamma}$.

2.19.3 Synthesis

2.19.3.1 Synthesis of the Boronic Ester Monomer
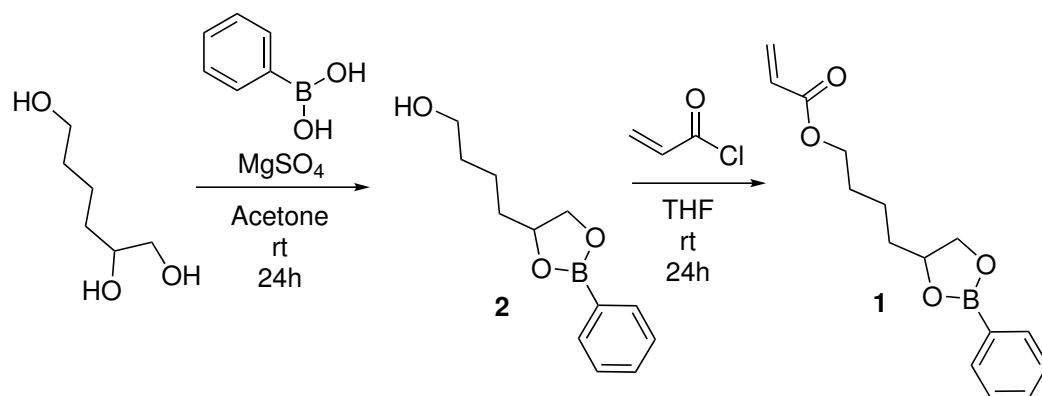
Scheme 2.18: Synthesis of the boronic ester monomer **1**.

Synthesis of 4-(2-Phenyl-1,3,2-dioxaborolan-4-yl)butan-1-ol (2)
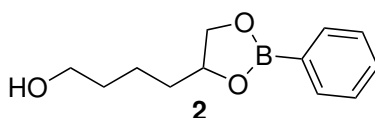
Scheme 2.19: 4-(2-Phenyl-1,3,2-dioxaborolan-4-yl)butan-1-ol (**2**).

10.0 g of 1,2,6-hexanetriol (9.01 mL, 74.5 mmol, 1.00 eq) were dissolved in 80 mL of acetone. 9.55 g of PBA (78.3 mmol, 1.05 eq) and 0.2 mL of deionized water were added. Subsequently, 20.0 g (164 mmol, 2.00 eq) of MgSO$_4$ were added, before the dispersion was stirred for 24 h at room temperature. The mixture was filtered, the filtrate was dried over MgSO$_4$ and concentrated under reduced pressure to obtain 14.4 g of a colorless viscous liquid (65.4 mmol, 88 % yield).

[1]**H NMR** (400 MHz, CDCl$_3$, 298 K): δ [ppm] = 7.81 (m, 2H, **H$_{Ar}$**), 7.47 (m, 1H, **H$_{Ar}$**), 7.36 (m, 2H, **H$_{Ar}$**), 4.58 (m, 1H, O-C**H**), 4.43 (dd, *J* = 8.9, 7.9 Hz, 1H, O-C**H$_2$**), 3.96 (dd, *J* = 8.9, 7.1 Hz, 1H, O-C**H$_2$**), 3.68 (t, *J* = 5.5 Hz, 2H, HO-C**H$_2$**), 1.80-1.43 (m, 6H, C**H$_2$**).

[13]**C NMR** (100 MHz, CDCl$_3$, 298 K): δ [ppm] = 134.94 (B-**C$_{Ar}$**), 131.57 (H-**C$_{Ar}$**), 127.95 (H-**C$_{Ar}$**), 77.56 (O-**C**H), 71.27 (O-**C**H$_2$), 62.83 (HO-**C**H$_2$), 36.01 (**C**H$_2$), 32.61 (**C**H$_2$), 21.46 (**C**H$_2$).
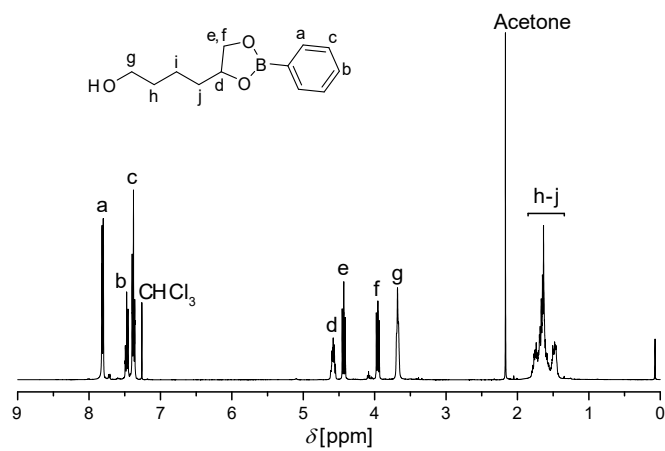
Figure 2.38: ^{1}H NMR spectrum of **2** in CDCl$_3$.
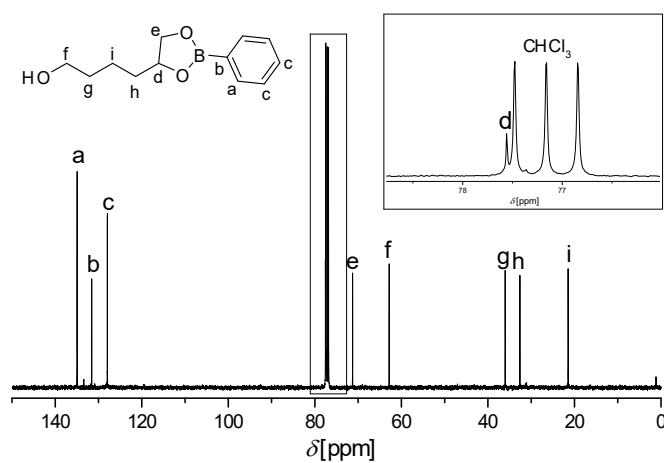
Figure 2.39: ^{13}C NMR spectrum of **2** in CDCl$_3$.

4-(2-Phenyl-1,3,2-dioxaborolan-4-yl)butyl acrylate 1
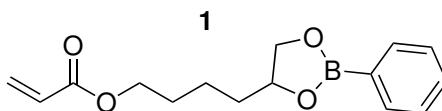
Scheme 2.20: 4-(2-Phenyl-1,3,2-dioxaborolan-4-yl)butyl acrylate **1**.

2.08 g of **2** (9.09 mmol, 1.00 eq) were dissolved in 250 ml of anhydrous THF. The reaction mixture was cooled down to 0 °C and 0.78 mL of acryloyl chloride (9.63 mmol, 1.06 eq) were added slowly. Simultaneously, a constant stream of air was bubbled through the reaction mixture and the off-gas was led through a washing flask equipped with concentrated NaOH to remove the formed HCl. After 24 h of constant stirring and bubbling at ambient temperature, 0.5 mL of MeOH were added and the reaction mixture was allowed to stir another 7 h. Subsequently, the solvent was removed under reduced pressure. Analytic revealed an incomplete reaction.
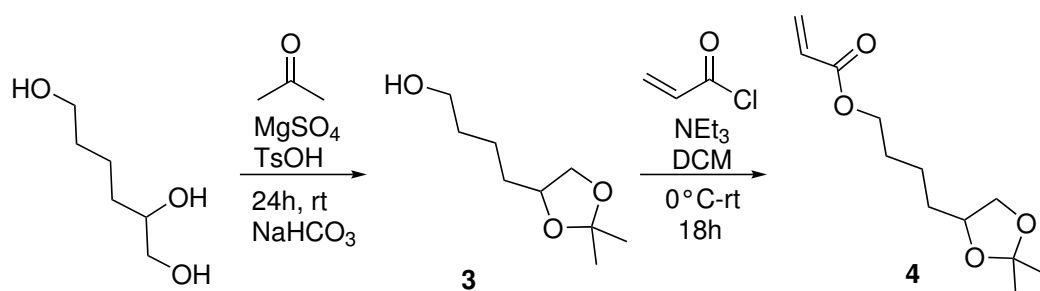
Scheme 2.21: Synthesis of the protected diol monomer **4**.

4-(2,2-dimethyl-1,3-dioxolan-4-yl)butan-1-ol (3)
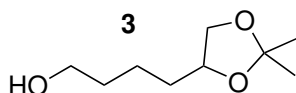
Scheme 2.22: 4-(2,2-dimethyl-1,3-dioxolan-4-yl)butan-1-ol **3**.

50.0 g of 1,2,6-hexanetriol (45.1 mL, 373 mmol, 1.00 eq) were added to a dispersion of 89.7 g of $MgSO_4$ (745 mmol, 2.00 eq) in 600 mL of acetone. 6.34 g of p-toluenesulfonic acid (TsOH) (33.5 mmol, 0.09 eq) were added slowly and the mixture was stirred for 24 h at room temperature. Then, 5.63 g of $NaHCO_3$ (67.1 mmol, 0.18 eq) were added and the mixture was stirred another 5 h before filtration. The filtrate was concentrated under reduced pressure at ambient temperature to obtain a white slurry. Deionized water was added and the organic phase was extracted 4 times with 150 mL of DCM. The organic phase was dried over $MgSO_4$, filtrated and the solvent was removed under reduced pressure at ambient temperature. The product was obtained as 46.7 g of a colorless oil (268 mmol, 72% yield).

^{1}H NMR (400 MHz, CDCl$_3$, 298 K): δ [ppm] = 4.07 (m, 1H, O-C**H**), 4.03 (t, 1H, O-C**H**$_2$), 3.64 (t, *J* = 6.4 Hz, 1H, HO-C**H**$_2$), 3.50 (t, *J* = 7.3 Hz, 1H, O-C**H**$_2$), 1.75-1.35 (m, 6H, C**H**$_2$), 1.40 (s, 3H, C**H**$_3$), 1.35 (s, 3H, C**H**$_3$).

^{13}C NMR (100 MHz, CDCl$_3$, 298 K): δ [ppm] = 108.79 (O-**C**), 76.09(O-**C**H), 69.50 (O-**C**H$_2$), 62.59, (HO-**C**H$_2$), 33.32 (**C**H$_2$), 32.66 (**C**H$_2$), 27.00 (**C**H$_3$), 25.80 (**C**H$_3$), 22.12 (**C**H$_2$).
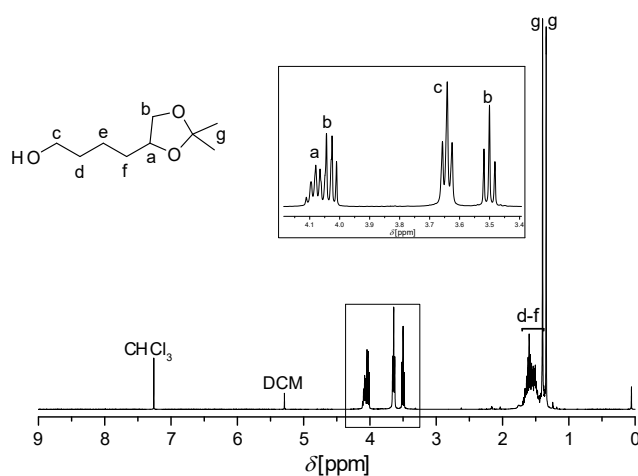
Figure 2.40: ^{1}H NMR spectrum of **3** in CDCl$_3$.
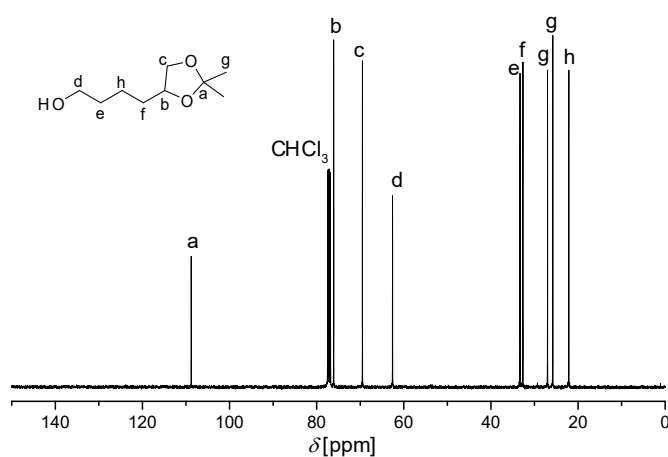
Figure 2.41: ^{13}C NMR spectrum of **3** in CDCl$_3$.

4-(2,2-dimethyl-1,3-dioxolan-4-yl)butyl acrylate (4)
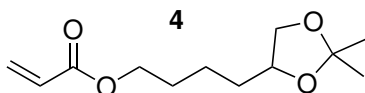
Scheme 2.23: 4-(2,2-dimethyl-1,3-dioxolan-4-yl)butyl acrylate **4**.

10.0 g of **3** (57.5 mmol, 1.00 eq) were dissolved in 100 mL of DCM. 11.2 mL of NEt_3 (8.14 g, 80.4 mmol, 1.40 eq) were added and the mixture was bubbled with nitrogen for 20 min, before it was cooled down to 0 °C with an ice bath. Subsequently, 6.07 mL of acryoyl chloride (6.70 g, 74.7 mmol, 1.30 eq) were added slowly over a period of 20 min. The mixture was stirred at 0 °C for 2 h, then the ice bath was removed and the mixture was stirred for another 18 h. 1.0 mL of MeOH was added and the solution was stirred at ambient temperature for 5 h, before it was washed 3 times with 100 mL of 1M HCl_{aq}, 3 times with 100 mL of saturated $NaHCO_3$ solution, and 2 times with 100 mL of brine. The organic layer was then dried over $MgSO_4$ and filtered. The solvent was removed under reduced pressure to yield the crude product as an orange oil. The oil was passed through a column of basic aluminum oxide using DCM as eluent to obtain the product as 7.88 g of a colorless oil (34.5 mmol, 60% yield).

^{1}**H NMR** (400 MHz, $CDCl_3$, 298 K): δ [ppm] = 6.39 (dd, J = 17.3, 1.5 Hz, 1H, C=C**H**$_2$), 6.11 (dd, J = 17.3, 10.4 Hz, 1H, CH$_2$=C**H**), 5.81 (dd, J = 10.4, 1.5 Hz, 1H, C=C**H**$_2$), 4.16 (t, J = 6.6 Hz, 2H, O=C-O-C**H**$_2$), 4.07 (m, 1H, O-C**H**), 4.03 (t, 1H, O-C**H**$_2$), 3.50 (t, J = 7.3 Hz, 1H, O-C**H**$_2$), 1.75-1.35 (m, 6H, C**H**$_2$), 1.40 (s, 3H, C**H**$_3$), 1.35 (s, 3H, C**H**$_3$).

^{13}**C NMR** (100 MHz, $CDCl_3$, 298 K): δ [ppm] = 166.42 (O-**C**=O), 130.74 (**C**H$_2$=CH), 128.65 (CH$_2$=**C**H), 108.89 (O-**C**-O), 75.99(O-**C**H), 69.53 (O-**C**H$_2$), 64.46 (O-**C**H$_2$), 33.33 (**C**H$_2$), 28.75 (**C**H$_2$), 27.07 (**C**H$_3$), 25.84 (**C**H$_3$), 22.44 (**C**H$_2$).
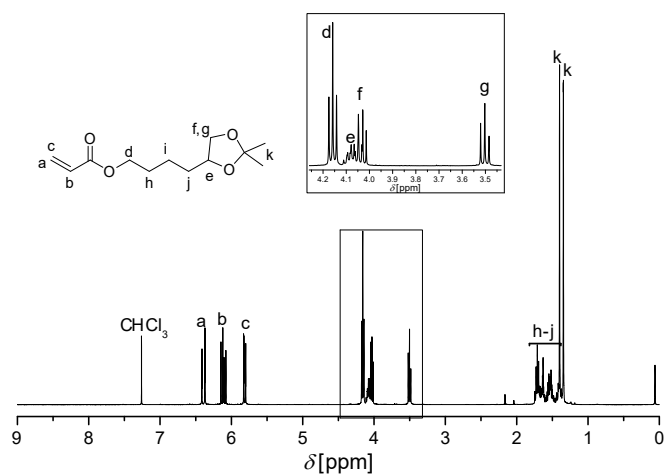
Figure 2.42: ^{1}H NMR spectrum of **4** in CDCl$_3$.
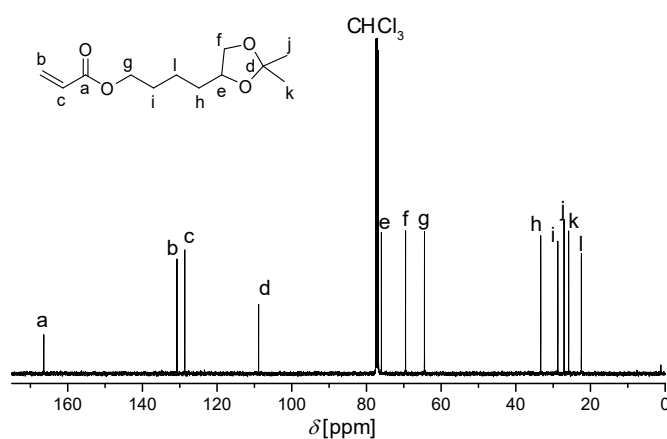
Figure 2.43: ^{13}C NMR spectrum of **4** in CDCl$_3$.

Synthesis of the Diol Monomer
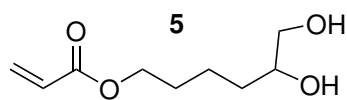
Scheme 2.24: Diol monomer **5**.

1.50 g of **4** (6.57 mmol, 1.00 eq) were dissolved in 10 mL of MeCN and 10 mL of H$_2$O. 0.9 mL of glacial acetic acid (0.91 g, 15.1 mmol, 2.30 eq) were added dropwise. The

solution was heated to 30°C and stirred openly for 48 h.

-Aqueous Work-Up

The mixture was extracted 5 times with 20 ml of EtOAc, the organic phase was washed 5 times with 20 ml of 0.5 M NaOH$_{aq}$. The organic phase was dried over MgSO$_4$ and filtered. The solvent was removed under reduced pressure. The product was obtained as 580 mg of a colorless oil (3.08 mmol, 47% yield).

-Work-Up by Evaporation under Vacuum

The solvent was removed and the residue was dried at 40 °C under vacuum. After 24 h of drying, significant amounts of acetic acid could still be found in the product. After another 24 h of drying, the product had polymerized to an insoluble material.

[1]**H NMR** (400 MHz, CDCl$_3$, 298 K): δ [ppm] = 6.39 (dd, J = 17.3, 1.5 Hz, 1H, C=C**H**$_2$), 6.11 (dd, J = 17.3, 10.4 Hz, 1H, C**H**$_2$=C**H**), 5.82 (dd, J = 10.5, 1.5 Hz, 1H, C=C**H**$_2$), 4.16 (t, J = 6.6 Hz, 2H, O=C-O-C**H**$_2$), 3.71 (m, 1H, O-C**H**), 3.64 (dd, J = 11.2, 3.0 Hz, 1H, C**H**$_2$), 3.44 (dd, J = 11.1, 7.6 Hz, 1H, C**H**$_2$), 1.75-1.35 (m, 6H, C**H**$_2$).
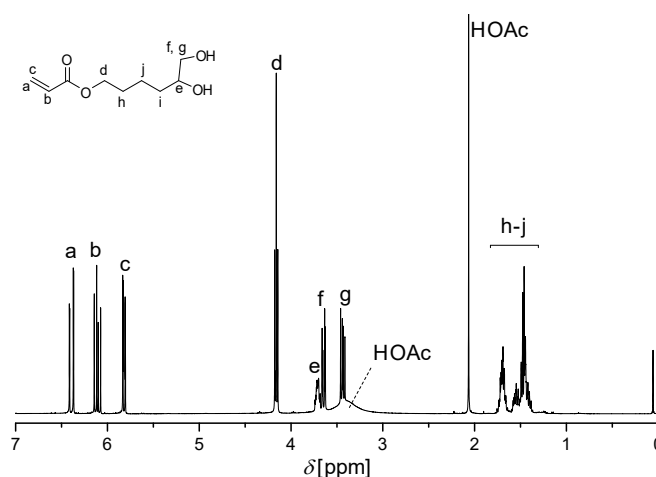
Figure 2.44: ^{1}H NMR spectrum of **5** in CDCl$_3$.

2.19.3.2 Copolymerization and Polymer Functionalization
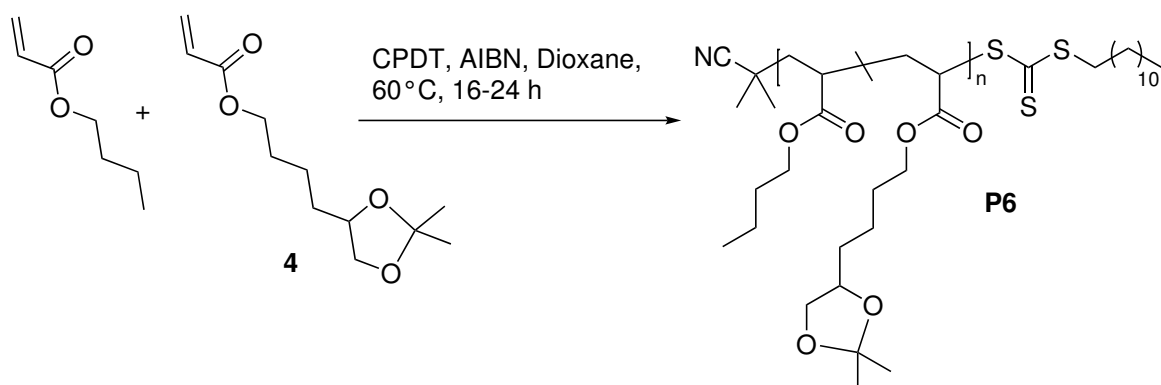
Scheme 2.25: RAFT copolymerization of **4** with *n*BA.
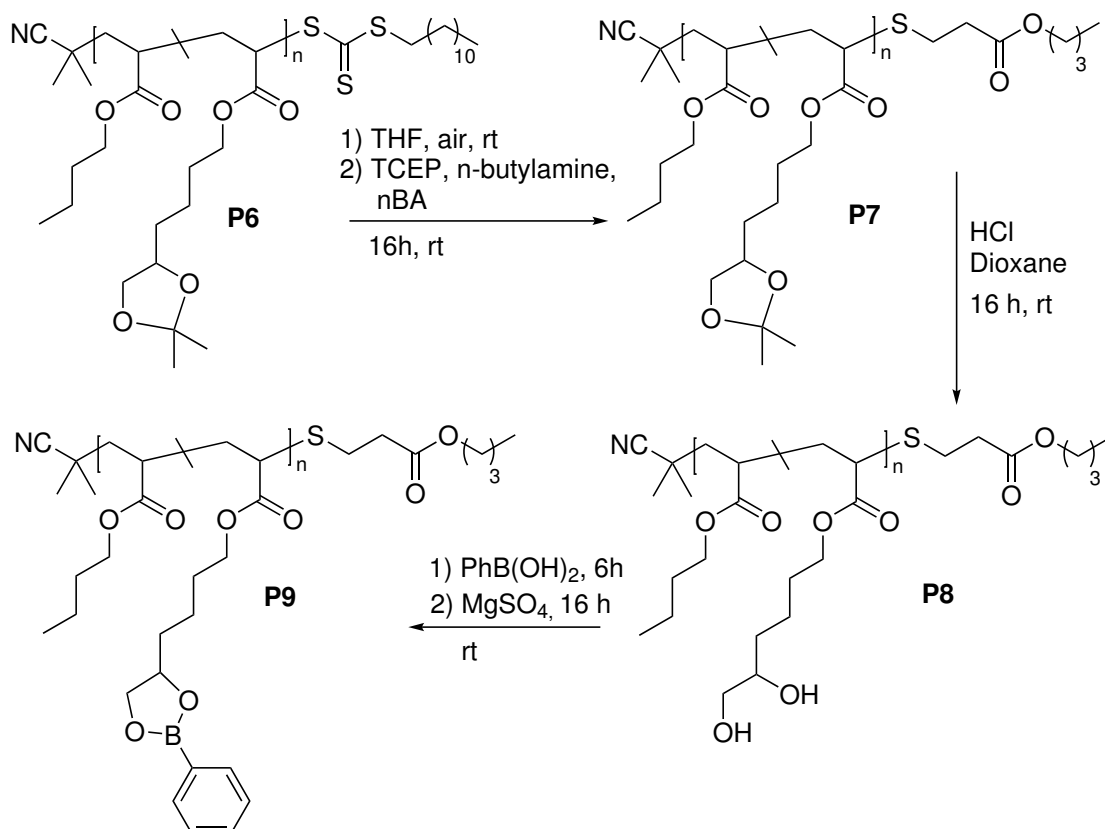
Scheme 2.26: Polymer functionalization of the precursor of **Network 1**.

Synthesis of Copolymer P6 and Subsequent RAFT End-Group Removal to yield P7
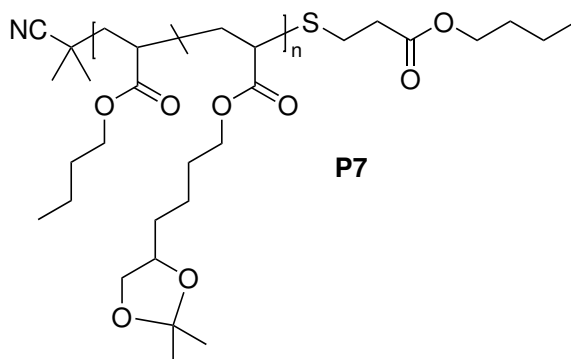
Scheme 2.27: Copolymer **P7** resulting of a RAFT polymerization of *n*BA with the pro-
tected diol functional monomer **4** and a subsequent removal of the RAFT
end-group.

General procedure:

In a typical experiment, 1000 eq of *n*BA, 115 eq of the protected diol functional monomer
4, 1.00 eq of CPDT in a stock solution in dioxane, 0.2 eq of AIBN in a stock solution in
dioxane, and the respective amount of dioxane (1:1 v/v to *n*BA + **4**) were added to a dry
100 mL Schlenk tube. The tube was sealed with a septum and oxygen was removed by
bubbling nitrogen for 1 h. Subsequently, the tube was placed into an oil bath thermostated
at 60 °C until a monomer conversion of 80-90 % was obtained. Subsequently, the
polymerization was stopped by cooling it, while exposing it to air and subsequently adding
several mL of THF. The solution was freed from oxygen by bubbling nitrogen for 30 min
again. A small amount of TCEP was added and the mixture was stirred for 10 min.
Subsequently, 50 eq of $BuNH_2$ were added and the mixture was stirred for 16 h, before
the mixture was precipitated twice in MeOH : H_2O (8 : 1 v/v). The residue was taken
up in THF and dried at 80 °C under reduced pressure to yield a colorless, transparent,
viscous polymer.

[1]**H NMR** (400 MHz, $CDCl_3$, 298 K): δ [ppm] = 4.02 (m, n×6H, O=COH_2, -O-CH_2, O-CH),
3.50 (t, n×1H, -O-CH_2), 2.26 (m, n×2H, $CH_{backbone}$), 1.90 (m, n×2H, $CH_{backbone}$), 1.58
(m, n×2H, CH_2), 1.58-1.28 (m, n×2H, $CH_{backbone}$), 1.39 (s, n×3H, CH_3), 1.36 (m, n×2H,
CH_2), 1.34 (s, n×3H, CH_3), 0.93 (t, n×3H, CH_3).
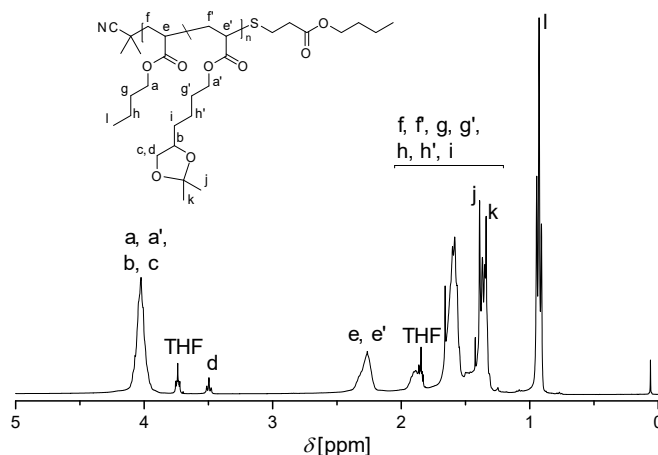
Figure 2.45: ^{1}H NMR spectrum of copolymer **P7** in CDCl$_3$.

Deprotection of Copolymer P7 to Yield P8
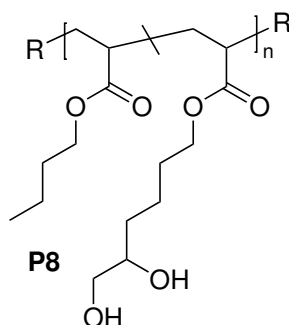
Scheme 2.28: Copolymer **P8**.

P7 was dissolved in 1,4-dioxane (20 mL/g polymer). 1 M HCl$_{aq}$ was added dropwise until the pH reached a value of 4 or less. The mixture stirred openly for 16 h. The solution was concentrated and precipitated twice into MeOH : H$_2$O (1 : 2 v/v). The precipitate was taken up in dioxane and the solvent was removed. The polymer was dried for 4 h at 45°C under vacuum. The polymer was obtained as a colorless, transparent, viscous liquid.

^{1}**H NMR** (400 MHz, CDCl$_3$, 298 K): δ [ppm] = 4.02 (m, n×2H, O=CO**H**$_2$), 3.70 (m, n×1H, HO-C**H**), 3.61 (m, n×1H, H-O-C**H**$_2$), 3.44 (m, n×1H, H-O-C**H**$_2$), 2.26 (m, n×2H, C**H$_{backbone}$**), 1.90 (m, n×2H, C**H$_{backbone}$**), 1.58 (m, n×2H, C**H**$_2$), 1.58-1.28 (m, n×2H, C**H$_{backbone}$**), 1.36 (m, n×2H, C**H**$_2$), 0.93 (t, n×3H, C**H**$_3$).
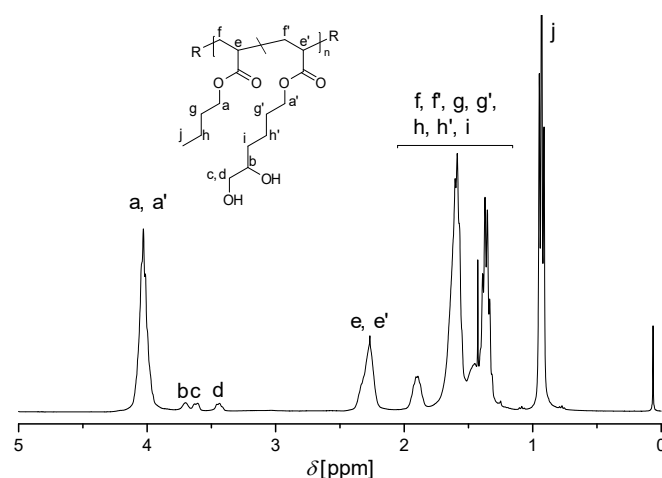
Figure 2.46: ^{1}H NMR spectrum of copolymer **P8** in CDCl$_3$.

Reprotection of Copolymer P8 with PBA to Yield P9
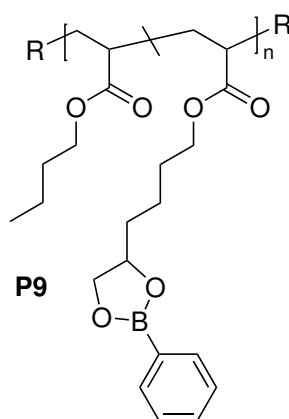
Scheme 2.29: Copolymer **P9**.

P8 was dissolved in anhydrous THF (10 mL/g polymer). 1.50 eq of PBA were immersed into a separate beaker containing THF. After 10 min, one drop of water was added and the mixture was stirred until the PBA was completely dissolved. It was then added to the polymer solution. After 6 h of stirring, 10 eq of MgSO$_4$ were dispersed stepwise into the solution. After 16 h, the mixture was centrifuged and the centrate filtered through a Por. 4 frit. The polymer solution was concentrated and precipitated once into cold MeCN and a second time into cold hexane. The polymer was dried for 16 h at 80°C under vacuum. The polymer was obtained as a colorless, transparent, viscous liquid. For

the calculation of the ratio of the monomers in the copolymer the NMR proton signals (compare Figure 2.47) of the functional monomer (H_a, 2H) and the *n*BA monomer (H_m, 3H) were employed.

Typical properties: M_n = 90 kDa, $Đ$ = 1.3, DP_n = 650, N_F = 65, f = 10 %;

^{1}H NMR (400 MHz, CDCl$_3$, 298 K): δ [ppm] = 7.79 (d, *J* = 7.5 Hz, n×2H, C$_{Ar}$**H**), 7.46 (t, *J* = 7.4 Hz, n×1H, C$_{Ar}$**H**), 7.37 (t, *J* = 7.5 Hz, n×2H, C$_{Ar}$**H**), 4.58 (m, n×1H, B-O-C**H**), 4.44 (m, n×1H, B-O-C**H$_2$**), 4.02 (m, n×2H, O=CO**H$_2$**), 3.97 (m, n×1H, B-O-C**H$_2$**), 2.26 (m, n×2H, C**H$_{backbone}$**), 1.90 (m, n×2H, C**H$_{backbone}$**), 1.58 (m, n×2H, C**H$_2$**), 1.58-1.28 (m, n×2H, C**H$_{backbone}$**), 1.36 (m, n×2H, C**H$_2$**), 0.95 (t, n×3H, C**H$_3$**).
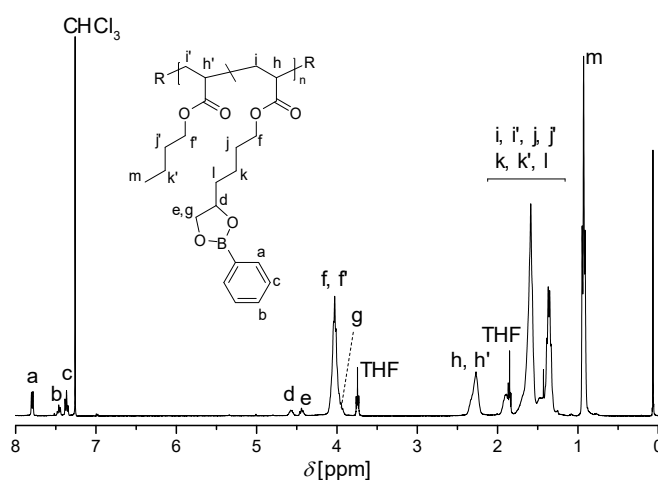
Figure 2.47: ^{1}H NMR spectrum of copolymer **P9** in CDCl$_3$.

2.19.3.3 Crosslinker Synthesis

1,4-bis(4-methyl-1,3,2-dioxaborolan-2-yl)benzene (10)
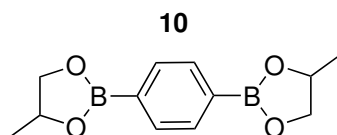
Scheme 2.30: 1,4-bis(4-methyl-1,3,2-dioxaborolan-2-yl)benzene **10**.

2.00 g of benzene-1,4-diboronic acid (12.1 mmol, 1.00 eq) and 1.82 mL of 1,2-propanediol (1.88 g, 24.1 mmol, 2.05 eq) were dissolved in 30 mL of THF and 30 mL of toluene. The

mixture stirred for 15 min at room temperature, before the solvent was removed at 45 °C under reduced pressure. Two times more, 30 mL of THF and 30 mL of toluene were added and the solvent was removed under the same conditions. The product crystallized as 2.90 g of a white solid (11.8 mmol, 98 % yield).

^{1}H NMR (400 MHz, CDCl$_3$, 298 K): δ [ppm] = 7.82 (s, 4H, **H$_{Ar}$**), 4.83-4.64 (m, 2H, C**H**), 4.46 (dd, *J* = 8.9, 7.7 Hz, 1H, C**H$_2$**), 3.90 (dd, *J* = 8.9, 7.3 Hz, 1H, C**H$_2$**), 1.42 (d, *J* = 6.2 Hz, 3H, C**H$_3$**).

^{13}C NMR (100 MHz, CDCl$_3$, 298 K): δ [ppm] = 134.15 (**C$_{Ar}$**), 73.98 (**C**H$_2$), 72.72(**C**H), 21.91 (**C**H$_3$). Carbon adjacent to boron not detected.
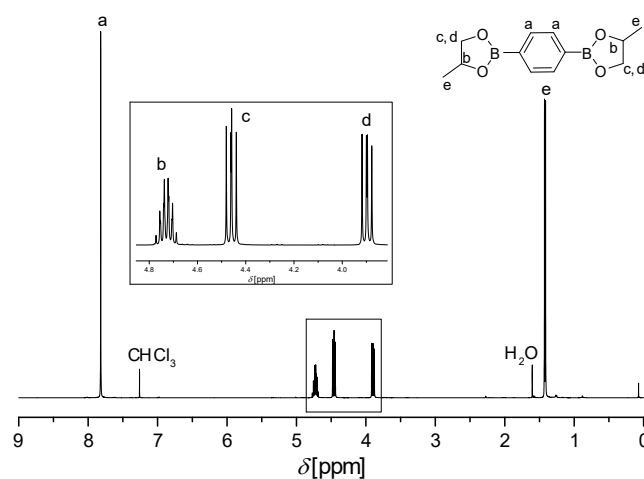
Figure 2.48: ^{1}H NMR spectrum of **10** in CDCl$_3$.
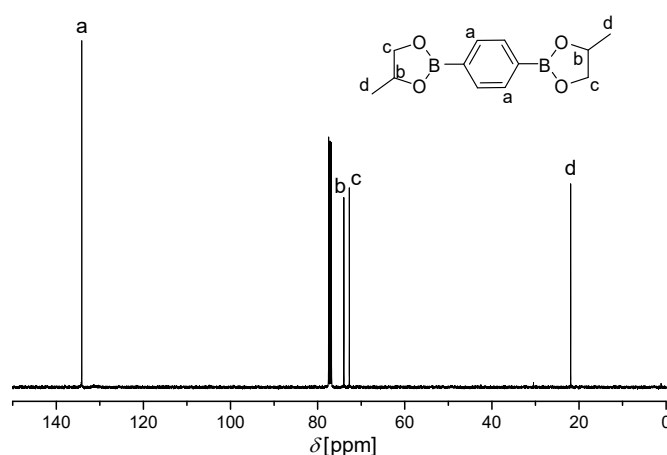
Figure 2.49: ^{13}C NMR spectrum of **10** in CDCl$_3$.

2.19.3.4 Crosslinking of the Thermoplastic Precursor

The amount of crosslinker was calculated with Equations 2.32, with f_{CL} as the ratio of functional groups crosslinked, m(P) mass of the polymer, f(P) functionality of the polymer, $N_f(CL)$ functionality of the crosslinker, and M(M_{Av}) average molecular mass of the monomers (calculated with Equation 2.33). The TP **P9** was dissolved in THF (1 : 3 w/w) and placed into a beaker. A respective amount of a solution of the crosslinker **10** (100 mg / mL THF) was added quickly. The mixture was vigorously stirred manually for 2 minutes, before it became too viscous to stir. The mixture rested openly at ambient temperature for 24 h, subsequently it was placed in a vacuum oven at 100°C for 16 h. The resulting material was torn into pieces and again dried under the same conditions for another 12 h. The network was obtained as a colorless, transparent foam.

$$n(CL) = \frac{f_{CL} \cdot m(P) \cdot f(P)}{N_f(CL) \cdot M(M_{Av})} \tag{2.32}$$

$$M(M_{Av}) = f(P) \cdot M(FM) + (1 - f(P)) \cdot M(nBA) \tag{2.33}$$

2.19.3.5 Addition of Dodecandiol

After the sample was crosslinked and dried, it was swollen in 200 wt% of THF. A solution of 1,2-dodecandiol in THF (amount determined via Equation 2.34, x = 0.05 or 0.1) was added. The solution was allowed to diffuse for 24 h, before the sample was dried at room temperature and under vacuum at 80°C for 16 h, respectively.

$$n(Dodecandiol) = \frac{x \cdot m(P) \cdot f(P)}{M(M_{Av})} \tag{2.34}$$

Bibliography

(1)   Hall, D. G., *Boronic Acids*, 2nd ed.; WILEY VCH Verlag GmbH: Weinheim, Germany, 2011.

(2)   Frankland, E. *Philos. Trans.* **1862**, 363–381.

(3)   Donald S. Matteson, *Stereodirected Synthesis with Organoboranes*, 1st ed.; Springer Verlag: Berlin/Heidelberg, Germany, 1995.

(4)   Duggan, P. J.; Tyndall, E. M. *Previous Rev. R. J. Ferrier* **2001**, *35*, 31–80.

(5)   Mancini, R. S.; Lee, J. B.; Taylor, M. S. *Org. Biomol. Chem.* **2016**, *15*, 132.

(6)   Fyfe, J. W. B.; Watson, A. J. B. *Chem* **2017**, *3*, 31–55.

(7)   Yang, W.; Gao, X.; Wang, B. *Med. Res. Rev.* **2003**, *23*, 346–368.

(8)   Zaidlewicz, M.; Cytarska, J.; Dzielendziak, A.; Ziegler-Borowska, M. *ARKIVOC* **2004**, *3*, 11–21.

(9)   Miyaura, N.; Yamada, K.; Suzuki, A. *Tetrahedron Lett.* **1979**, *20*, 3437–3440.

(10) Suzuki, A. *Proc. Jpn. Acad., Ser. B* **2004**, *80*, 359–371.

(11) Lennox, A. J. J.; Lloyd-Jones, G. C. *Chem. Soc. Rev* **2014**, *43*, 412.

(12) The Royal Swedish Academy of Science Press Release: The Nobel Prize in Chemistry, Stockholm, Sweden, 2010.

(13) Kuivila, H. G.; Keough, A. H.; Soboczenski, E. J. *J. Org. Chem.* **1954**, *19*, 780–783.

(14) Niu, W.; O'sullivan, C.; Rambo, B. M.; Smith, M. D.; Lavigne, J. J. *Chem. Commun.* **2005**, 4342–4344.

(15) Niu, W.; Smith, M. D.; Lavigne, J. J. *J. Am. Chem. Soc* **2006**, *128*, 16466–16467.

(16) Roberts, M. C.; Hanson, M. C.; Massey, A. P.; Karren, E. A.; Kiser, P. F. *Adv. Mater.* **2007**, *19*, 2503–2507.

(17) Piest, M.; Zhang, X.; Trinidad, J.; Engbersen, J. F. J. *Soft Matter* **2011**, *7*, 11111–11118.

(18) He, L.; Fullenkamp, D. E.; Rivera, J. J.; Messersmith, P. B. *Chem. Commun* **2011**, *47*, 7497–7499.

(19)   Tarus, D.; Hachet, E.; Messager, L.; Catargi, B.; Ravaine, V.; Auzély-Velty, R. *Macromol. Rapid Commun.* **2014**, *35*, 2089–2095.

(20)   Cash, J. J.; Kubo, T.; Bapat, A. P.; Sumerlin, B. S. *Macromolecules* **2015**, *48*, 2098–2106.

(21)   Qin, Y.; Cui, C.; Ja, F. *Macromolecules* **2007**, *40*, 1413–1420.

(22)   De, P.; Gondi, S. R.; Roy, D.; Sumerlin, B. S. *Macromolecules* **2009**, *42*, 5614–5621.

(23)   Bapat, A. P.; Roy, D.; Ray, J. G.; Savin, D. A.; Sumerlin, B. S. *J. Am. Chem. Soc* **2011**, *133*, 19832–19838.

(24)   Roy, C. D.; Brown, H. C. *J. Organomet. Chem.* **2007**, *692*, 784–790.

(25)   Roy, C. D.; Brown, H. C. *Monatshefte für Chemie* **2007**, *138*, 879–887.

(26)   Cromwell, O. R.; Chung, J.; Guan, Z. *J. Am. Chem. Soc* **2015**, *137*, 29.

(27)   Röttger, M.; Domenech, T.; Van Der Weegen, R.; Breuillac, A.; Nicolaÿ, R.; Leibler, L. *Science.* **2017**, *356*, 62–65.

(28)   Cash, J. J.; Kubo, T.; Dobbins, D. J.; Sumerlin, B. S. *Polym. Chem.* **2018**, *9*, 2011–2020.

(29)   Breuillac, A.; Kassalias, A.; Nicolaÿ, R. *Macromolecules* **2019**, *52*, 7102–7113.

(30)   Liu, Y.; Tang, Z.; Wang, D.; Wu, S.; Guo, B. *J. Mater. Chem. A* **2019**, *7*, 26867–26876.

(31)   Caffy, F.; Nicolaÿ, R. *Polym. Chem.* **2019**, *10*, 3107–3115.

(32)   Chen, Y.; Tang, Z.; Liu, Y.; Wu, S.; Guo, B. *Macromolecules* **2019**, *52*, 3805–3812.

(33)   Lyu, Z.; Wu, T. *Macromol. Rapid Commun.* **2020**, *41*, 2000265.

(34)   Saed, M. O.; Gablier, A.; Terentejv, E. M. *Adv. Funct. Mater.* **2020**, *30*, 1906458.

(35)   Yang, F.; Pan, L.; Ma, Z.; Lou, Y.; Li, Y.; Li, Y. *Polym. Chem* **2020**, *11*, 3285.

(36)   FUJIFILM Wako Pure Chemical Coperation AIBN Values `https://www.wako-chemicals.de/en/products/specialty-chemicals/oil-soluble-initiators/v-60-aibn` (accessed 08/02/2021).

(37)   Lima, V.; Jiang, X.; Brokken-Zijp, J.; Schoenmakers, P. J.; Klumperman, B.; Van Der Linde, R. *J. Polym. Sci. Part A Polym. Chem.* **2005**, *43*, 959–973.

(38)   Qiu, X. P.; Winnik, F. M. *Macromol. Rapid Commun.* **2006**, *27*, 1648–1653.

(39)   Merck KGaA, D. Sigma-Aldrich Supplier Information `https://www.sigmaaldrich.com/DE/de/product/aldrich/181404?context=product` (accessed 08/09/2021).

(40)   Ricarte, R. G.; Tournilhac, F.; Leibler, L. *Macromolecules* **2019**, *52*, 432–443.

(41)   Hajj, R.; Duval, A.; Dhers, S.; Avérous, L. *Macromolecules* **2020**, *53*, 3796–3805.

(42)   Ward, I. M.; Sweeney, J., *An Introduction to the Mechanical Properties of Solid Polymers*, 2nd ed.; John Wiley and Sons Inc.: Chichester, New York, USA, 1993.

(43)   Scheutz, G. M.; Lessard, J. J.; Sims, M. B.; Sumerlin, B. S. *J. Am. Chem. Soc.* **2019**, 16181–16196.

(44)   Capelot, M.; Unterlass, M. M.; Tournilhac, F.; Leibler, L. *ACS Macro Lett.* **2012**, *1*, 789–792.

(45)   Fang, Z.; Zheng, N.; Zhao, Q.; Xie, T. *ACS Appl. Mater. Interfaces* **2017**, *9*, 22077–22082.

(46)   Wen, Z.; McBride, M. K.; Zhang, X.; Han, X.; Martinez, A. M.; Shao, R.; Zhu, C.; Visvanathan, R.; Clark, N. A.; Wang, Y.; Yang, K.; Bowman, C. N. *Macromolecules* **2018**, *51*, 5812–5819.

(47)   He, C.; Shi, S.; Wang, D.; Helms, B. A.; Russell, T. P. *J. Am. Chem. Soc.* **2019**, *141*, 13753–13757.

(48)   Liu, H.; Zhang, H.; Wang, H.; Huang, X.; Huang, G.; Wu, J. *Chem. Eng. J.* **2019**, *368*, 61–70.

(49)   Gamardella, F.; Guerrero, F.; De la Flor, S.; Ramis, X.; Serra, A. *Eur. Polym. J.* **2020**, *122*, 109361.

(50)   Fancey, K. S. *J. Mater. Sci.* **2005**, *40*, 4827–4831.

(51)   Li, L.; Chen, X.; Jin, K.; Torkelson, J. M. *Macromolecules* **2018**, *51*, 5537–5546.

(52)   Ricarte, R. G.; Ois Tournilhac, F.; Cloître, M.; Leibler, L. *Macromolecules* **2020**, *53*, 1852–1866.

(53)   Denissen, W.; Rivero, G.; Nicolaÿ, R.; Leibler, L.; Winne, J. M.; Du Prez, F. E. *Adv. Funct. Mater.* **2015**, *25*, 2451–2457.

(54)   Montarnal, D.; Capelot, M.; Tournilhac, F.; Leibler, L. *Science.* **2011**, *334*, 965–968.

(55)   Dyre, J. C. *Rev. Mod. Phys.* **2006**, *78*, 953–972.

(56)   Van Zee, N. J.; Nicolaÿ, R. *Prog. Polym. Sci.* **2020**, *104*, 101233.

3 | P*n*BA Vitrimers Based on Dioxaborinane Exchange

Chapter Contents

3.1 Introduction

The dynamic exchange reactions between boronic esters have been proven as very promising to form vitrimer materials (refer to Chapter 2.1). To control the material properties of a vitrimer, such as mechanical, rheological and thermal behavior, it would be of great interest to be able to fine tune the exchange rate between the DCBs. Sumerlin *et al.* presented a study, where it was shown that the content of free diols or moisture significantly influence exchange rate dependent properties of a dioxaborolane CAN, such as self healing, creep and stress relaxation.[1] Nicolaÿ and colleagues showed that that the properties of dioxaborolane vitrimers can be altered by changing the crosslinking density.[2] Another tool to tune the properties of vitrimers based on a boronic ester exchange would be to vary the structure of the employed boronic ester group. Studies[3,4] showed that 6-membered boronic esters, so called dioxaborinanes, are thermodynamically more stable than their corresponding five-membered analogs, dioxaborolanes. This is due to the absence of ring strain in the 6-membered rings. The structures of both species are depicted in Scheme 3.1.
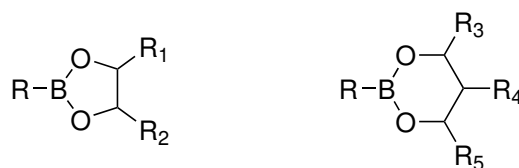
Scheme 3.1: Left: A 5-membered cyclic boronic ester, a dioxaborolane. Right: A 6-membered cyclic boronic ester, a dioxaborinane.

The metathesis kinetics of small molecules can give a good indication on the exchange rate of the dynamic crosslinking motif. For the 5-membered boronic ester exchange, the E_a was found to be 15.9 kJ/mol (compare Figure 3.1).[5,6] For the 6-membered boronic ester equivalents, values around 23.6 kJ/mol have been reported in literature.[7] However, independent studies conducted in our laboratory, whose outcomes are displayed in Figure 3.2, have revealed an E_a of 61.6 kJ/mol in bulk.[8] The group of Zi-Chen Li managed to incorporate dynamic dioxaborinane linkages into methacrylate based polymers.[7] The polymers were able to relax stress, were reprocessable and showed self-healing abilities. Our group was able to synthesize vitrimers by grafting dioxaborinane groups to polybutadiene.[8] It is of importance to see how the structural difference of 5-membered and 6-membered boronic esters are able to influence the property of a material. I order to do so, two model-systems were envisioned, one comprising dioxaborolane dynamic bonds, and one based on dioxaborinane dynamic bonds.
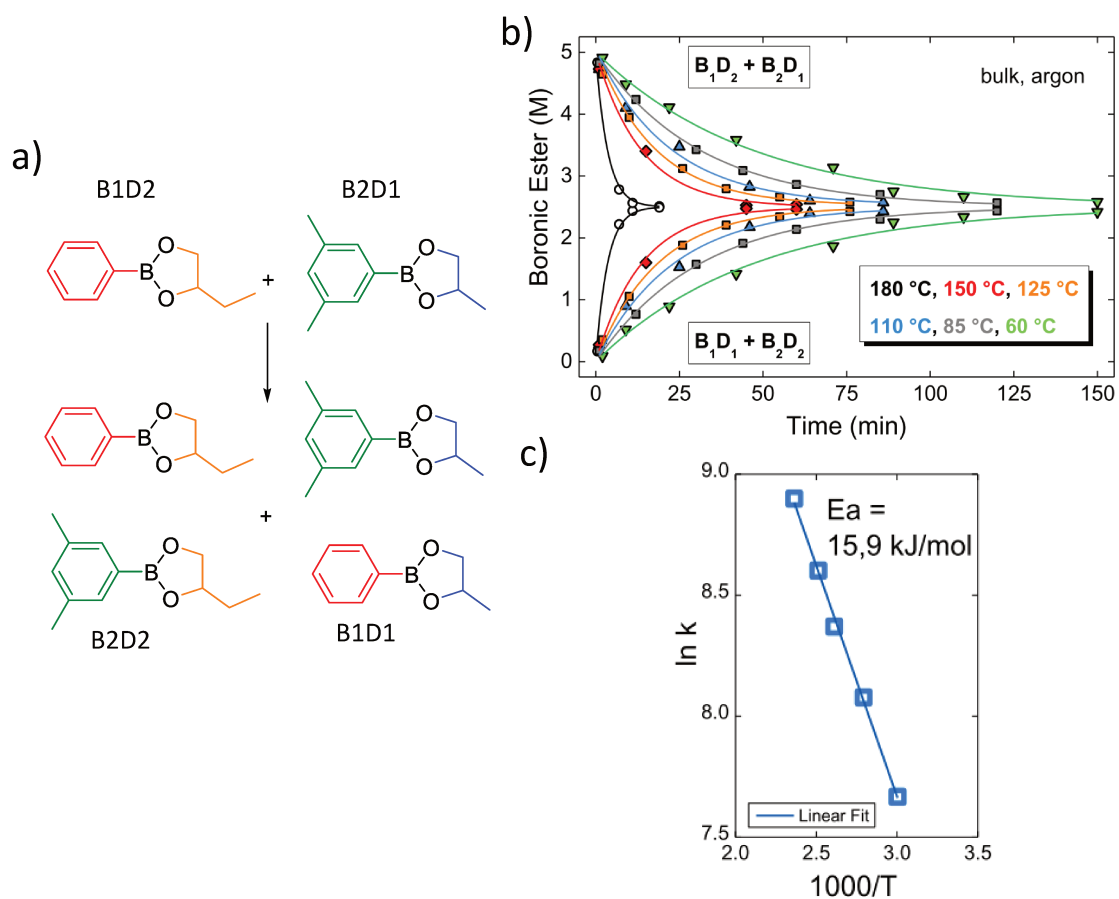
Figure 3.1: a) Exchange reaction between two dioxaborolanes. b) Kinetic plot of the exchange of highly pure 5-membered boronic esters in bulk at different temperature and under argon. c) Activation energy of the exchange. Adapted from Reference [6].
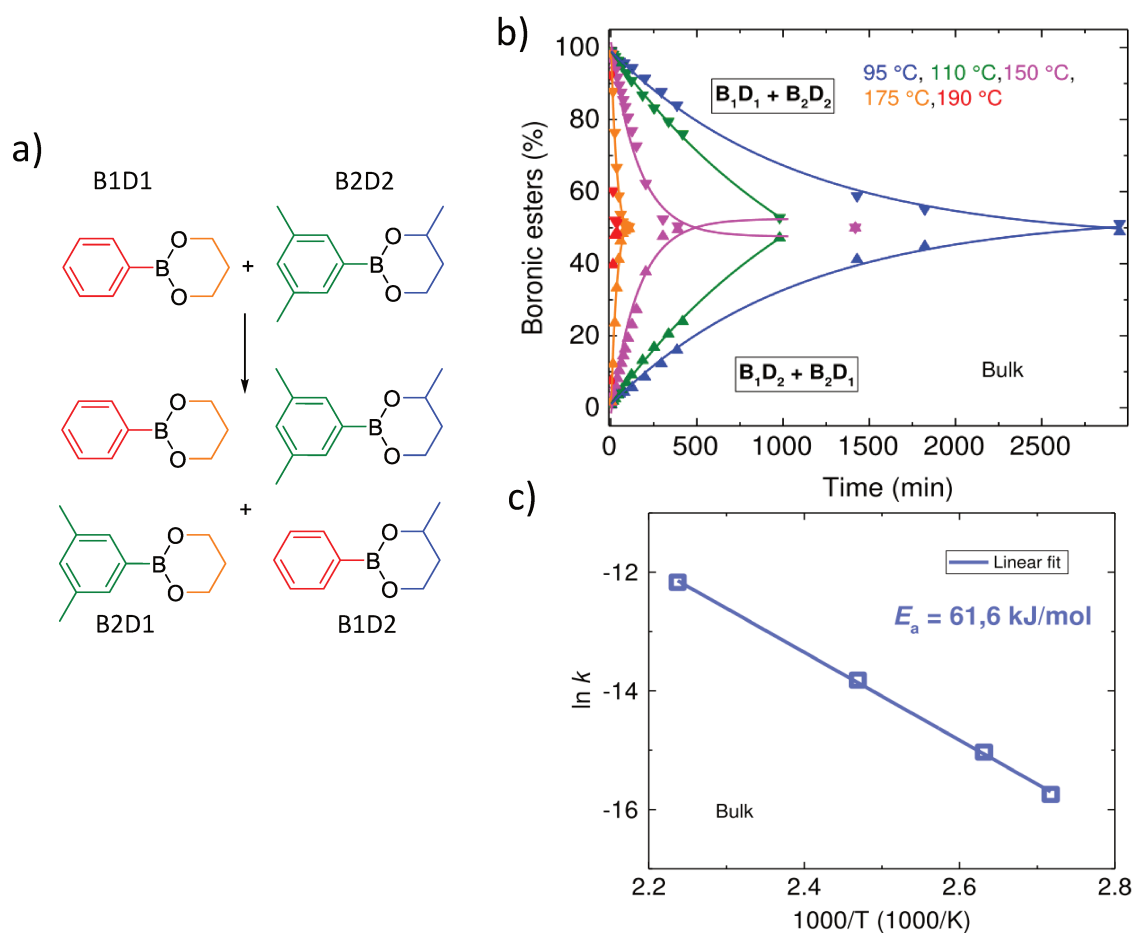
Figure 3.2: a) Exchange reaction between two dioxaborinanes. b) Kinetic plot of the exchange of highly pure 6-membered boronic esters in bulk at different temperature and under argon. c) Activation energy of the exchange. Adapted from Reference [8].

The systems are designed to be elastomers with a low T_g to access the system's dynamics at room temperature as well as at elevated temperatures. A dioxaborolane system based on a P*n*BA backbone (**Network 1**) was already prepared to serve as a subnetwork in the DDN. Its synthesis and characterization are thoroughly discussed in Chapter 2. The goal of this chapter is to synthesize and analyze a dioxaborinane counterpart and compare its properties to **Network 1**. To create a comparable dioxaborinane network, an acrylate monomer that comprises a six-membered bononic ester species (or a respective precursor) has to be prepared. A first monomer was synthesized according to a procedure developed by Marta Abellan Flos (Scheme 3.2). However, this procedure includes five steps of which most comprise an elaborate purification process. The aim of this project is to adapt the monomer synthesis to a more straightforward procedure.
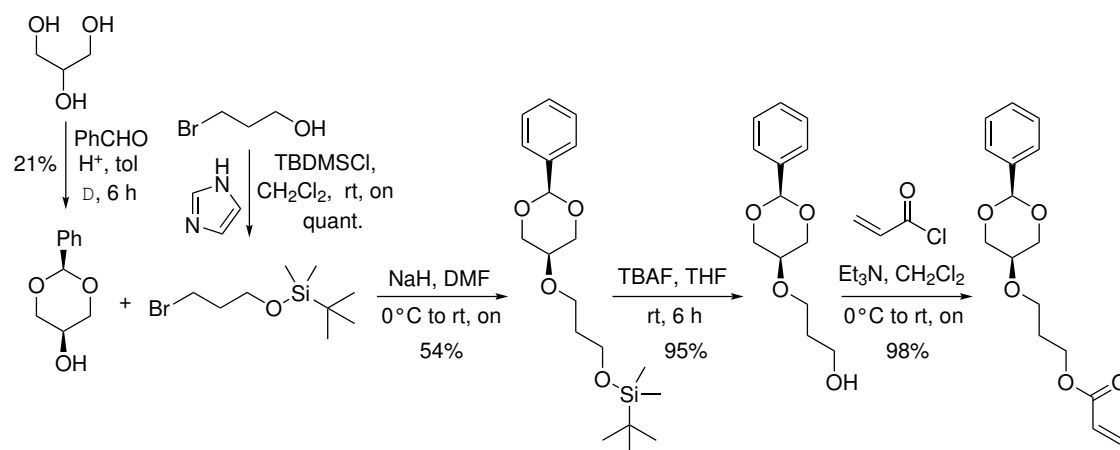
Scheme 3.2: Procedure to synthesize a dioxaborinane acrylate monomer developed and conducted by Marta Abellan Flos.

The so obtained monomer is copolymerized with *n*BA to obtain TPs that resemble as closely as possible to the TPs of **Network 1**. The obtained TPs are crosslinked in the same manner as **Network 1** to yield **Network 2**, based on a dioxaborinane exchange. The envisioned structure of the final **Network 2** is depicted in Scheme 3.3 (right), next to the one of **Network 1** (left). **Network 2** will be then subjected to a comparative study with **Network 1** to elaborate, how the difference in the molecular structure of the boronic esters influences the macroscopic properties of the material. A special focus will be placed on the evaluation of the dynamics of the exchange reaction inside the network.

Network 1
Dioxaborolane Exchange

Network 2
Dioxaborinane Exchange
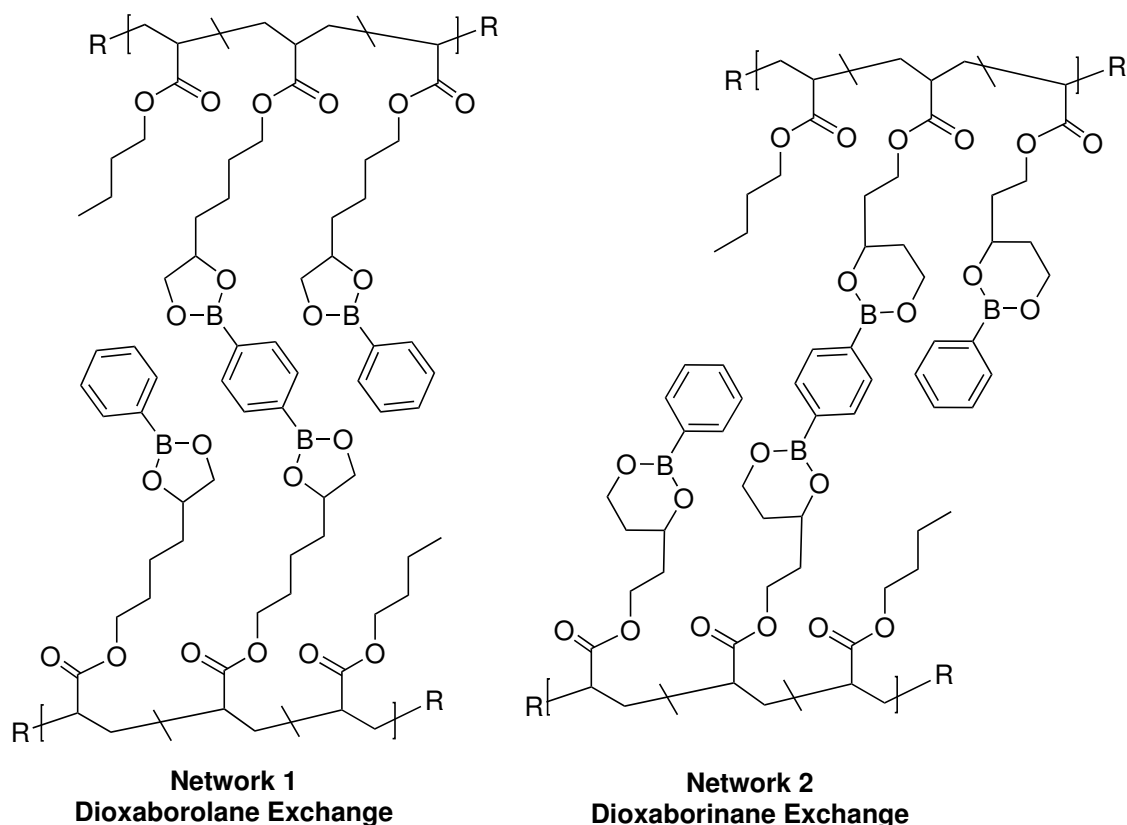
Scheme 3.3: The goal of this chapter is to compare two similar systems: one based on a dioxaborolane exchange (**Network 1**, left), and one based on a dioxaborinane exchange (**Network 2**, right).

3.2 Monomer Synthesis

To obtain a network, a TP based on P*n*BA with pendent dioxaborinane functions has to be synthesized. In order to do so, the corresponding functional monomer comprising an acrylate function has to be prepared. A synthetic protocol (Scheme 3.2) was already elaborated to obtain a protected six-membered diol. However, it was revised to find a more facile and straightforward way to obtain the targeted monomer. The new synthetic pathway is based on the already elaborated synthesis strategy for monomer **4** (refer to Chapter 2.2). The direct synthesis of a boronic ester monomer for the dioxaborolane network caused severe issues. In the end, a route via the respective acetal protected analogue was chosen. The same strategy will be applied for the thermoplastic precursor of the dioxaborinane **Network 2**. A six-membered cyclic acetal protected diol monomer will be synthesized and copolymerized with *n*BA. Subsequently, it will be further treated

to obtain a boronic ester on the final polymer. The envisioned route of the monomer synthesis is presented in Scheme 3.4.
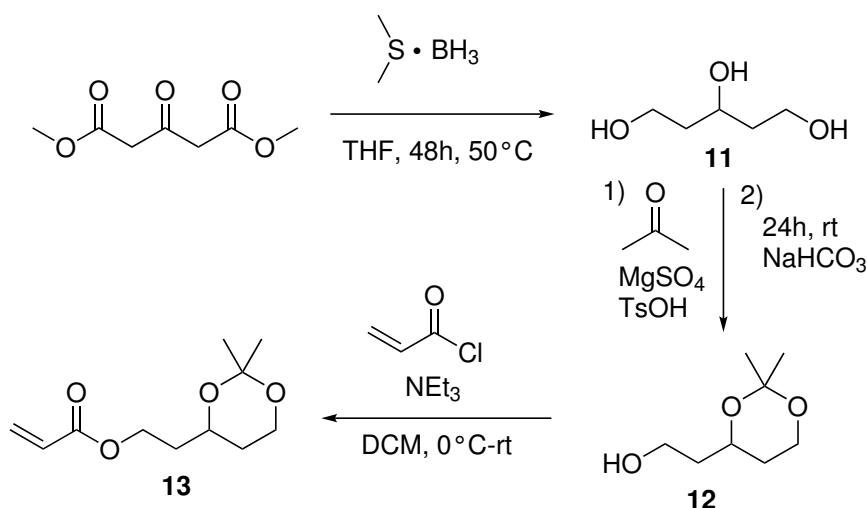
Scheme 3.4: Synthetic schema for the 6-membered acetal monomer **13**.

In contrast to the 5-membered equivalent, a suitable triol is not readily commercially available. It was therefore synthesized from dimethyl 3-oxopentanedioate according to literature.[9] For the reduction, a borane dimethylsulfide (BMS) complex was used, since it is known to be a highly efficient and selective reducing agent for carbonyl species.[10,11] The reduction worked well on a 30 g scale and the pentane-triol **11** was obtained after CC in medium to good yields (57-78 %). The acetalization of **11** was conducted using MgSO$_4$ as desiccating agent. Na$_2$SO$_4$ was envisaged as well, however it caused degradation of the material. The acetalization yielded the acetal protected compound **12** in medium yields (37-44 %). No CC was necessary, however a few percent of the starting material **11** could still be found in the NMR spectrum. The last step of the monomer synthesis is the introduction of the acrylate group using acryloyl chloride. After aqueous work up, the resulting NMR spectrum did not show any impurities. However, when the monomer was used for the copolymerization (compare next Section), a successive broadening of the Đ with increasing conversion was observed.

3.3 Copolymerization and Post-Polymerization Functionalization

The acetal protected monomer **13** was copolymerized with *n*BA as shown in Scheme 3.5. Like in the case of the 5-membered equivalent, a RAFT polymerization with CPDT as transfer agent was chosen as polymerization method. The reactant ratios were set to 1000 : 115 : 1 : 0.2 for $[nBA]_0 : [\mathbf{13}]_0 : [CPDT]_0 : [AIBN]_0$, for a target M_n of 100 kDa and a functional group ratio of 10 %, to match the values of the dioxaborolane TP **P9**.
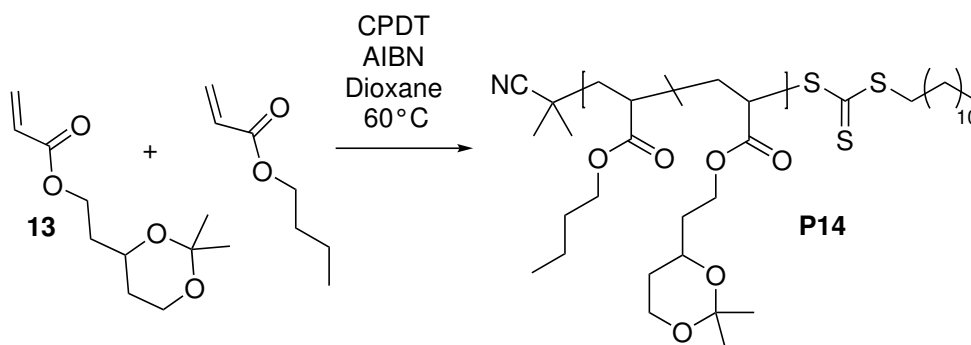
Scheme 3.5: RAFT copolymerization of *n*BA and the protected diol functional monomer **13** to yield the TP **P14** of **Network 2**.

3.3.1 Polymerization Kinetics

In a first try it was observed that the *Đ* of the obtained chains significantly increased with conversion (see Figure 3.3). The obtained polymer had a *Đ* superior to 2, a value much higher than anticipated for a typical RAFT polymerization. With the process of the polymerization, a broad shoulder towards higher molecular weights manifests in SEC (Figure 3.3, right). This is an indicator for branching or crosslinking. One reason might be unwanted di- or triacrylates in the monomer batch steming from the traces of **11** still present in the reactant during the acrylation. As a consequence, the monomer was carefully purified via CC and the copolymerization reattempted.

The SEC curves after 3, 4, 5, 6, and 6,75 h of the copolymerization performed with the purified monomer are displayed in Figure 3.4, right side. After 4 h, a shoulder towards higher molecular weights appears that becomes more pronounced with time. However, it is much less substantial than in the previous attempt. In the beginning, the M_n follows the theoretical M_n (see Figure 3.4, left). At higher conversion, the measured M_n deviates

from the theoretical one and the *Đ* increases. After 6.75 h a copolymer with a *Đ* of around 1.5 was obtained. This implies that by the additional purification of the monomer the amount of di- or triacrylate side products could be significantly decreased, and a better defined thermoplastic was obtained.
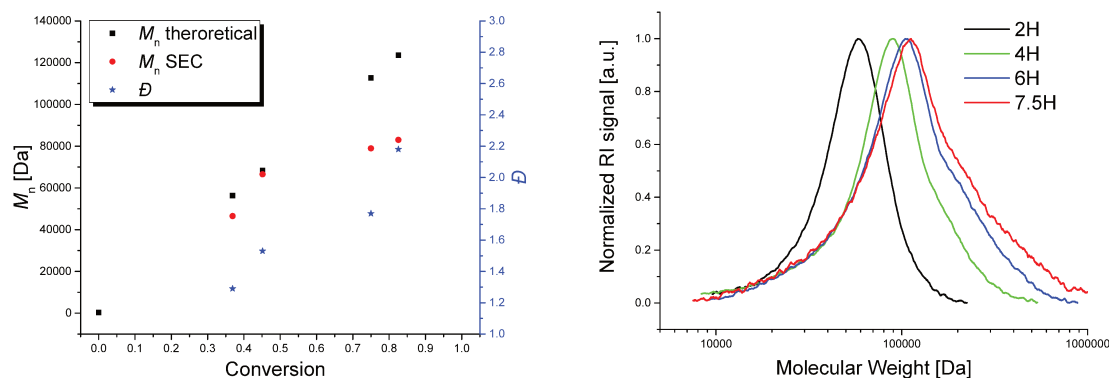
Figure 3.3: Kinetic study of the the RAFT polymerization of **13** and *n*BA ($[nBA]_0/[\mathbf{13}]_0/[CPDT]_0/[AIBN]_0 = 1000/115/1/0.2$, 1 : 1 (v/v) dioxane : monomers, 60 °C). Left: Comparison of the theoretical M_n and the values obtained by SEC. Development of M_n and *Đ* with increasing conversion. Right: SEC traces in THF (PS calibration) after 2, 4, 6, and 7.5 h.
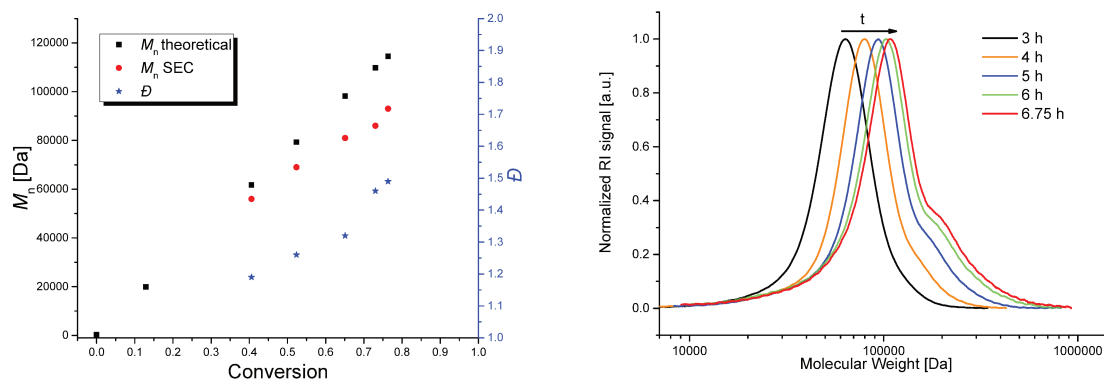
Figure 3.4: Kinetic study of the the RAFT polymerization of **13** and *n*BA ($[nBA]_0/[\mathbf{13}]_0/[CPDT]_0/[AIBN]_0 = 1000/115/1/0.2$, 1 : 1 (v/v) dioxane : monomers, 60 °C) after the additional purification of the monomer. Left: Comparison of the theoretical M_n and the values obtained by SEC. Development of M_n and *Đ* with increasing conversion. Right: SEC traces in THF (PS calibration) after 3, 4, 5, 6, and 6,75 h.

NMR analysis (compare Figure 3.5) shows that the functional monomer was copolymerized successfully without being deprotected, as could be confirmed by the presence of the

characteristic peaks of the protons adjacent to the acetal group (a-c) and the protons of the CH_3 group of the acetal protecting group (d + e) in the NMR spectrum of the obtained polymer **P15** (after aminolysis).
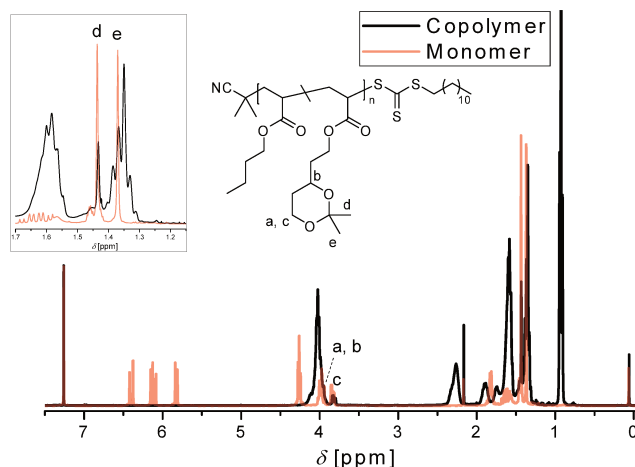
Figure 3.5: ^{1}H NMR spectra in CDCl$_3$ at 400 MHz of the TP **P15** (black) and of the functional monomer **13** (red). The monomer was copolymerized successfully without being deprotected, as can be seen by the presence of the characteristic peaks a-e in the copolymer spectrum.

3.3.2 Post-Polymerization Functionalization

To obtain a TP bearing dioxaborinane side-groups, the obtained polymer was further functionalized as depicted in Scheme 3.6. The procedure developed for the dioxaborolane TP was also applied here. For further details, refer to Chapter 2.3.2. First, the RAFT end group was removed by aminolysis to obtain **P15**. This was done directly at the end of the copolymerization, without isolation or purification of **P14**.

Subsequently, the acetal protecting group was removed in acidic environment using HCl. The deprotection worked well, the acetal protecting group was removed completely, as confirmed by ^{1}H NMR (Figure 3.6). The proton peaks adjacent to the functional group shifted (a, b, c, d → a', b', c', d'), a broad proton peak (g) for the hydroxy protons appeared, and the CH_3 peaks of the protecting group (e, f) disappeared. The obtained diol-functional polymer **P16** was then condensed with PBA to yield the final thermoplastic **P17**. The successful condensation was evidenced by ^{1}H NMR (Figure 3.7) with the presence of the aromatic phenyl peaks in the copolymer (d, e, f), as well as by the shift of the adjacent protons of the diol/boronic ester (a, b, c, d → a', b', c', d').
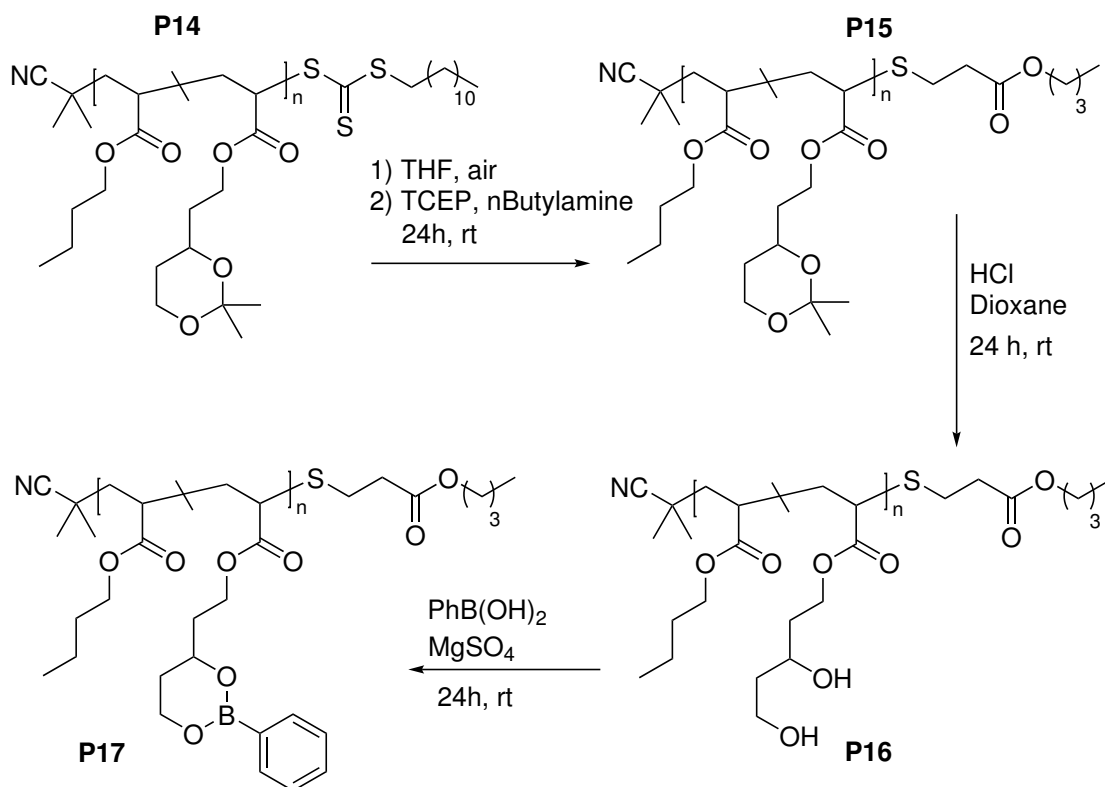
Scheme 3.6: Further functionalization of precursor **P14**. First the RAFT end-group is removed to yield polymer **P15**. Subsequently, the acetal protecting group is removed under acidic conditions to obtain **P16**. In the final step, the polymer is reprotected with PBA, to yield the TP **P17**.

The post-polymerization treatment did not influence the M_n or the $Đ$ of the TP as can be seen in Figure 3.8.

3.4 Crosslinking

The thermoplastic precursor **P17** was crosslinked to form **Network 2**. The crosslinking was realized in solution (Scheme 3.7) by adding the previously synthesized bis(boronic ester) **10** (see Chapter 2.4). The amount of crosslinker was calculated with the Equation 3.1, employing the average molecular mass of the monomers M(M_{Av}) calculated with Equation 3.2 using the molecular masses of nBA and the boronic ester functional monomer (FM). m(P) is the mass of of the employed thermoplastic. To match the properties of **Network 1**, it was envisioned to crosslink 20 % of the functional groups.
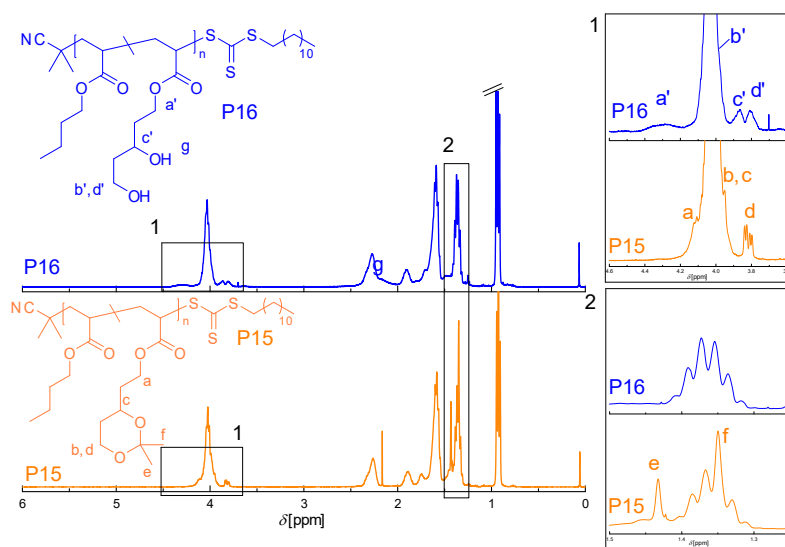
Figure 3.6: ^{1}H NMR spectra in CDCl$_3$ at 400 MHz of the TP before (**P15**, bottom, orange) and after (**P16**, top, blue) the acetal group removal. The successful removal is indicated by the shift of the adjacent proton peaks (a, b, c, d → a', b', c', d'), the appearance of a broad proton peak (g) for the hydroxy protons and the disappearance of the CH$_3$ peaks of the protecting group (e, f).
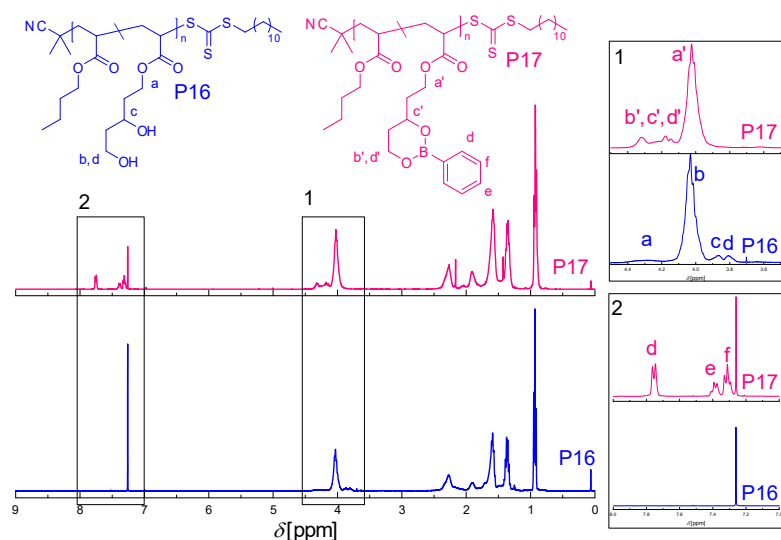
Figure 3.7: ^{1}H NMR spectra in CDCl$_3$ at 400 MHz of the thermoplastic precursor before (**P16**, bottom, blue) and after (**P17**, top, pink) the transesterification with PBA. The successful condensation is indicated by the shift of the adjacent proton peaks (a, b, c, d → a', b', c', d'), and the appearance of the phenylic peaks of the boronic ester group (d, e, f) in the copolymer spectrum.
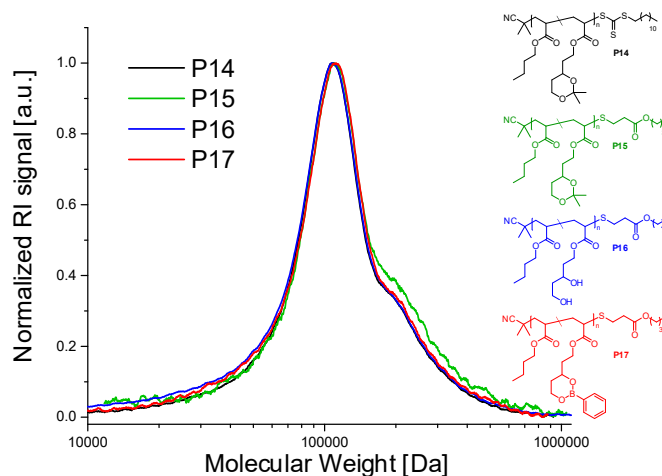
Figure 3.8: Development of the SEC trace in THF (PS calibration) of the thermoplastic precursor during the functionalization steps.

With a functionality of the polymer (f(P)) of 10 %, this results in a crosslinking density of 2 % with 20 % of the functional groups crosslinked (f_{CL}). The number of functional groups per crosslinker N_f(CL) is 2. The properties of **Networks 1 and 2** and their respective TPs (**P9** and **P17**) are compared in Table 3.1.

$$n(CL) = \frac{f_{CL} \cdot m(P) \cdot f(P)}{N_f(CL) \cdot M(M_{Av})} \tag{3.1}$$

$$M(M_{Av}) = f(P) \cdot M(FM) + (1 - f(P)) \cdot M(nBA) \tag{3.2}$$

The crosslinking took place within 20-30 min. After drying under vacuum, **Network 2** was obtained as a brittle elastomer as can be seen in Figure 3.9 (left).

Table 3.1: Overview over the properties of **Network 1** and **Network 2**, and their constituting TPs. N_f(chain): number of functional groups per chain, f_{CL}: functional groups crosslinked, N_{CL}(chain): number of crosslinks per chain.

Network	M_n[1] [kDa]	DP_n[1]	Đ	f(P) [%]	N_f(chain)	f_{CL} [%]	N_{CL} (chain)	ρ(CL) [%]
1	90	650	1.3	10	65	20	13.0	2
2	93	678	1.45	10	68	20	13.6	2

1: determined via SEC with a standard PS calibration.
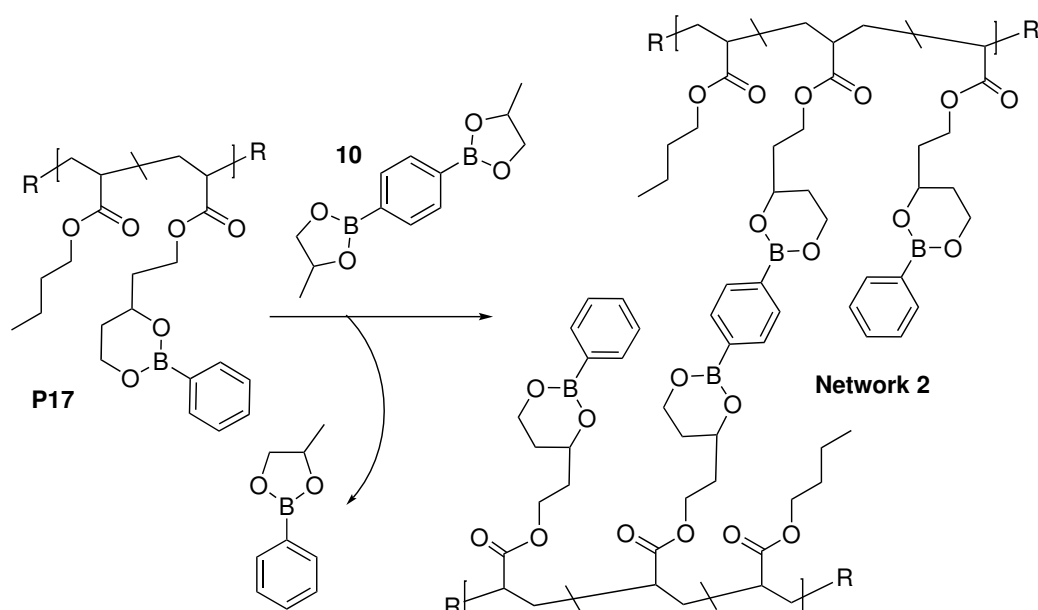
Scheme 3.7: The thermoplastic precursor **P17** is crosslinked with the bis(boronic ester) crosslinker **10** to form **Network 2**.

3.5 Compression Molding

The pieces of **Network 2** were introduced in a metal mold with the desired shape and pressed at 110 °C for 30-40 min with a load equivalent to 3 tons. The material was obtained as a homogenous, transparent, colorless elastomer as shown on the right side of Figure 3.9.

Figure 3.9: Pictures of **Network 2**. Left: after the crosslinking, before compression molding, right: after compression molding.

The network is thus well processable by compression molding, exhibiting short processing times at moderate temperatures. However, the processing times were somewhat longer than those of **Network 1**.

3.6 Thermal Characterization

3.6.1 TGA

The TGA of **Network 2** was conducted by applying a 10 K/min temperature ramp between 25 and 600 °C under nitrogen. The results are displayed in Figure 3.10a. The sample maintained 98 % of its mass up to 294 °C. It showed thereby a higher thermal stability than the dioxaborolane **Network 1**, which reached that value already at 264 °C (Figure 3.11). The isothermal treatment of **Network 2** is presented in Figure 3.10b. At 150 °C it showed good stability over the course of 10 h.
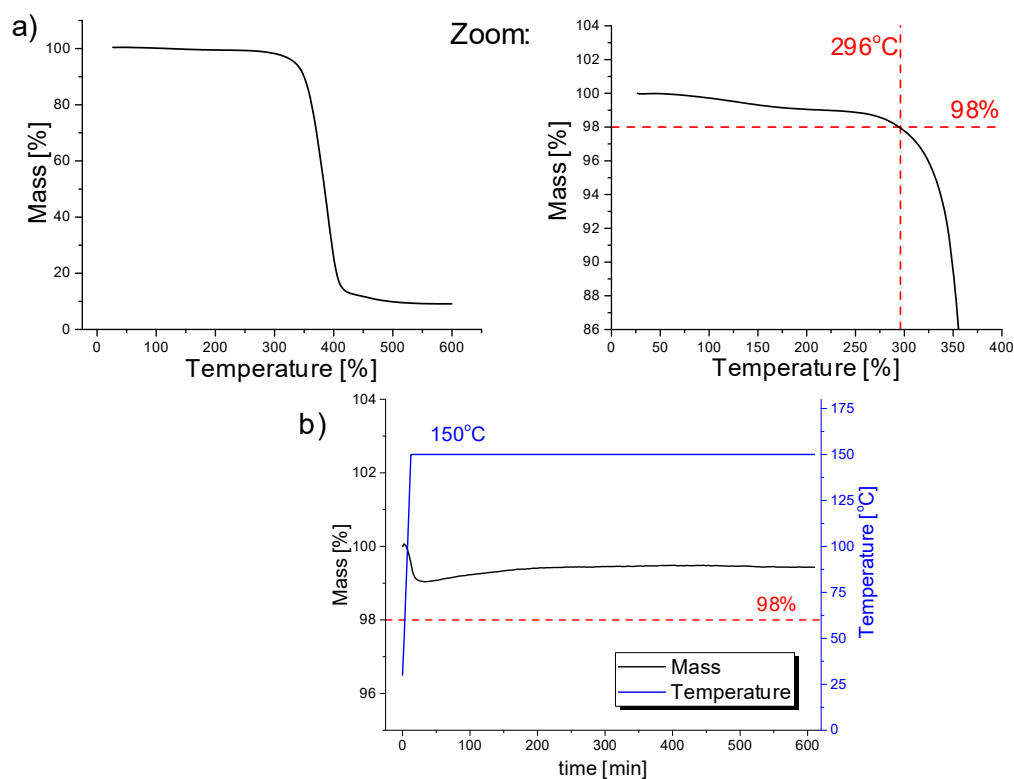
Figure 3.10: a) TGA temperature ramp of **Network 2** between 25 and 600 °C. b) Zoom of TGA isothermal treatment of **Network 2** at 150 °C during 10 h.
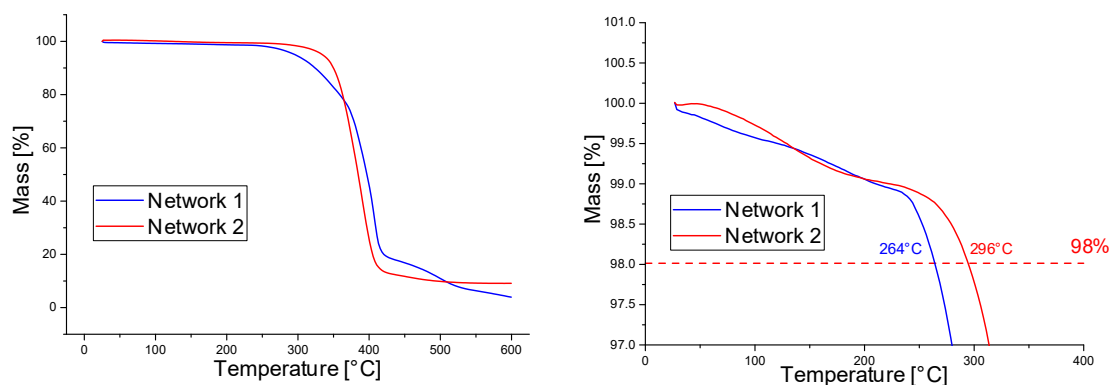
Figure 3.11: Left: TGA temperature ramps of **Networks 1 and 2** between 25 and 600 °C. Right: Zoom in 97-101 % remaining mass.

3.6.2 DSC

To determine the T_g of the sample, DSC measurements were conducted (Figure 3.12). It can be seen that the T_g of the crosslinked network is -34.2 °C, slightly higher than that of **Network 1** for which the T_g was was found to be -39.4 °C. DSC also shows that there is an exothermic transition (T_X) at around 136 °C. This transition is reversible, since it appears in all three heating/cooling cycles (Figure 3.12, left). The integration gave a normalized enthalpy of around 0.16 J/g. Most likely, at this temperature the functional groups in the polymer chain form some aggregates. This transition was not observed in **Network 1**. It can therefore be assumed that it is directly linked to the molecular structure of the functional groups.
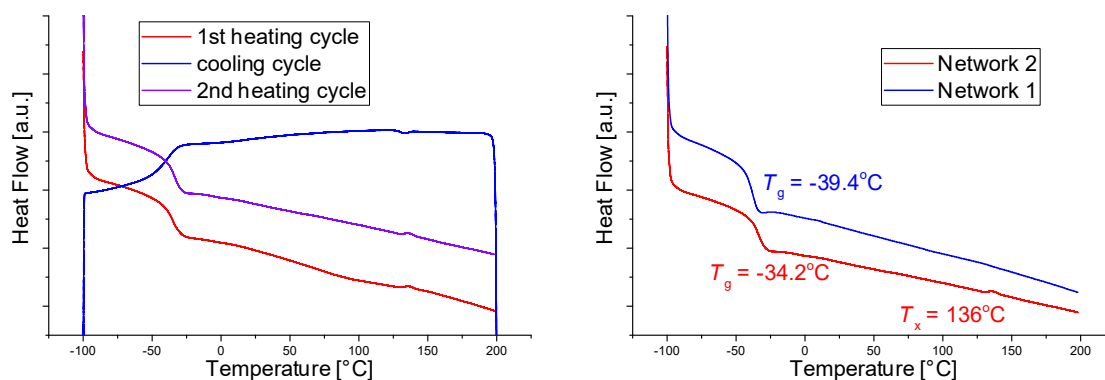
Figure 3.12: Left: DSC of **Network 2**, including all three heating/cooling cycles. Right: DSC result of the **Network 2** compared to **Network 1**.

147

3.6.3 DMA

The DMA of **Network 2** is displayed in Figure 3.13 (left). Below T_g, the storage modulus E' is decreasing continuously from around 1750 MPa at -75 °C. The T_g is determined at the maximum of the loss modulus function and located at -25.3 °C. After the T_g, the storage modulus drops to 0.69 MPa, before it starts to increase again. The network structure is maintained during the entire measured temperature range and the material behaves according to the rubber elasticity theory.
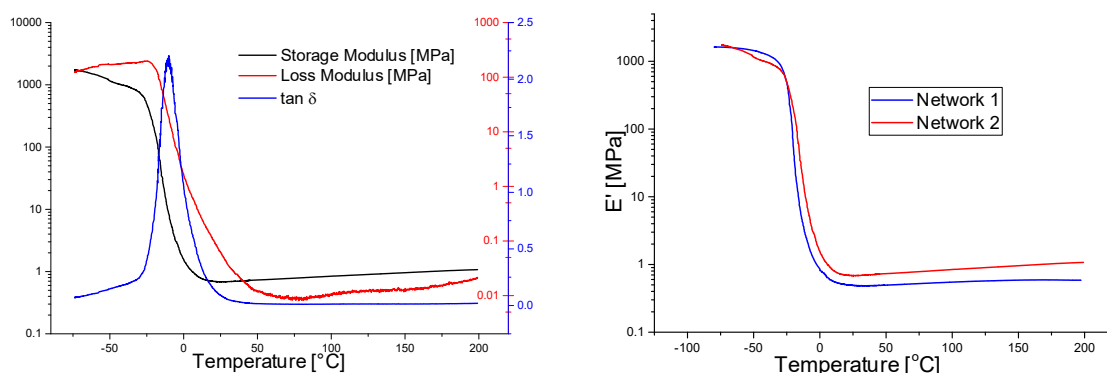
Figure 3.13: Left: DMA result of **Network 2**. Right: Storage moduli E' of **Networks 1 and 2**.

When the storage modulus is compared to the dioxaborolane **Network 1** (Figure 3.13, right), one can see that the two networks behave quite similarly. The modulus before T_g is in the same range. The T_g is with -25.0 vs. -25.3 °C practically identical. After the transition the storage modulus of **Network 2** is slightly higher. At 25 °C the storage modulus of **Network 1** is around 490 kPa, the one of **Network 2** 686 kPa. This can be explained by possible additional physical crosslinks stemming from the aggregates (see previous Subsection).

3.7 Frequency Sweeps

To test the viscoelastic behavior of the sample, frequency sweep experiments were conducted. Figure 3.14 (left) presents the frequency sweep experiments performed on the **Network 2** at the lowest, 25 °C, and the highest, 150 °C, measured temperature. The storage modulus shows a plateau around 250-300 kPa, the loss modulus around 50 kPa,

both increasing at higher frequencies. This indicates that the movement of the chains starts to be more restricted and the sample transits into the glassy state. In the measured frequency and temperature spectrum, the sample shows no crossover of the moduli towards lower frequencies, indicating no transition to the terminal flow regime. When compared to the frequency sweeps of **Network 1** (see Figure 3.14, right), one can see that G' of **Network 1** is inferior by a factor of 3. This might indicate a higher crosslinking density of **Network 3**, originating from the possible additional physical crosslinks. In general, the frequency sweeps follow the same behavior and show a rubber elasticity plateau over the measured spectrum. At high frequencies, G' of **Network 1** decreases, while the one of **Network 2** increases.
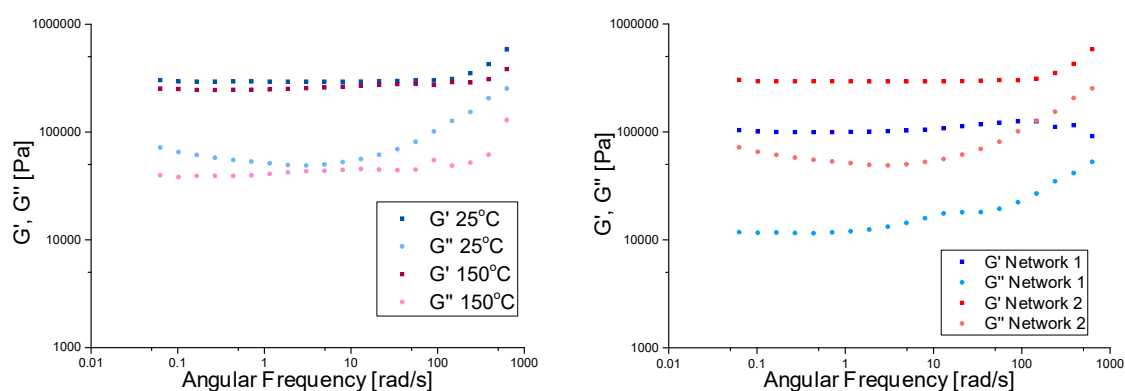
Figure 3.14: Left: Frequency sweeps of **Network 2** at the lowest measured temperature, 25 °C, (blue, light blue) and the highest measured temperature, 150 °C, (red, pink). Right: Frequency sweeps of **Network 1** (blue) and **Network 2** (red) at 25 °C.

3.8 Stress Relaxation

It is of great interest to compare the exchange reactions of the dioxaborinanes to those of the dioxaborolanes. In small molecules, a different dynamic behavior was observed (see Introduction, Section 3.1). The aim is to evaluate, how the molecular structure of the boronic esters can influence the material properties. The dynamics of the exchange reactions inside the material can be assessed via stress relaxation experiments. **Network 2** was submitted to comparable conditions to those of **Network 1**. The sample was equilibrated at 150 °C for several hours before stress relaxation was conducted at 1 % strain. Experiments were conducted from 150-110 °C in 10 °C steps. In Figure 3.15, the stress relaxation curves are displayed. For all temperatures, there is a stress relaxation at

short times. It becomes more pronounced at lower temperatures: at 150 °C about 10 % of the initial stress are relaxed by this mode, whereas at 110 °C it is almost 30 %. After this first relaxation, the samples exhibits a plateau in the relaxation modulus. This plateau persists longer at lower temperatures. After the plateau, there is another relaxation at longer time scales, most likely to be associated with the boronic ester exchange.
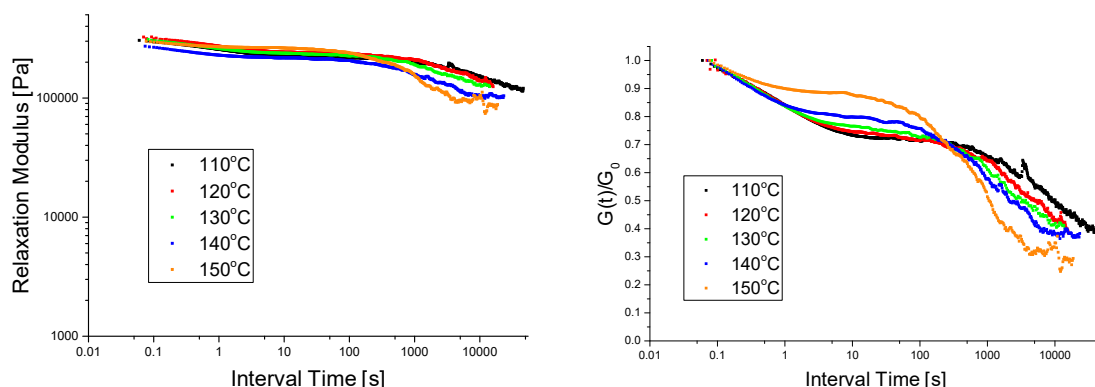
Figure 3.15: Stress relaxation curves of **Network 2**. Left: Development of the relaxation modulus with experiment time. Right: Relaxation modulus normalized to the initial modulus.

The characteristic relaxation times were determined via modeling to a KWW stretched exponential decay (refer to Section 2.14.1). The characteristic relaxation times were plotted against 1000/T to obtain an Arrhenius plot in order to determine the E_a and the Arrhenius prefactor τ_0. The resulting plot with the linear fit is compared to the one of **Network 1** in Figure 3.16. The results of the stress relaxation experiments are summarized in Table 3.2. One can see that the slope of **Network 2** is steeper, resulting in a higher E_a. This is in agreement with the experiments performed on small molecules that were presented in the introduction of this chapter. However, it must be stated that the relaxation process of **Network 2** comprised a significant amount of short time relaxation that might have altered the modeling and the calculation of the characteristic relaxation times.

Table 3.2: Overview over the results of the stress relaxation experiments of **Network 1** and **Network 2**.

Network	Functionl Group	E_a [KJ/mol]	$\ln(\tau_0)$	E_a [KJ/mol] (small molecule)
Network 1	dioxaborolane	72.8 ± 1.6	-15.2 ± 0.5	15.9[6]
Network 2	dioxaborinane	97.4 ± 1.7	-18.6 ± 0.5	61.6[8]
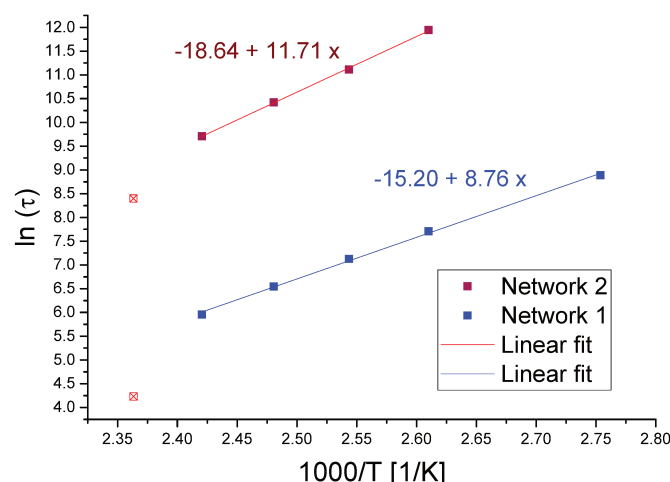
Figure 3.16: Arrhenius plot of the characteristic relaxation times of the stress relaxation experiments of **Network 2** (red) and **Network 1** (blue).

The β values of the KWW fit were in **Network 2** around 0.15-0.35, whereas for **Network 1** they were ranging from 0.53-0.60. This indicates that the second network has a broad spectrum of divers relaxation modes. The increase of short time relaxation suggests that there are more species in the network that are able to relax stress fast, such as dangling chain ends or even loose chains. This fraction increased from experiment to experiment. Another possible explanation is that this short time relaxation is associated with the disassembly of the aggregates already mentioned in the previous sections. At lower temperatures and with longer experiment time, more aggregates form and act as physical crosslinks.

3.9 Amplitude Sweep

An indication for the hypothesis of the increasing amount of short time relaxation can be found in the amplitude sweep of the **Network 2** (Figure 3.17). The storage modulus shows to be in the linear regime just up to 0.6 % strain and 2500 Pa shear stress. The network shows a significantly higher brittleness than **Network 1** that featured a linear regime up to 10 % strain. The stress relaxation was conducted at 1 % strain. It is very likely that this was enough to cause significant damage to the network that resulted in the increasing short time stress relaxation. This enhanced brittleness is consistent with the presence of additional crosslinks formed by the aggregates.
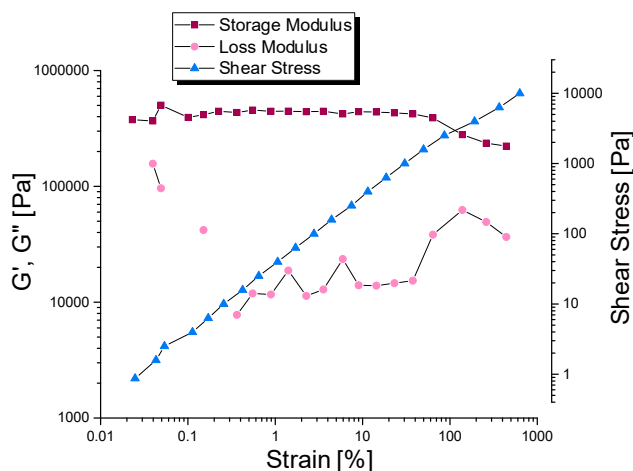
Figure 3.17: Amplitude sweep of **Network 2** at 25 °C.

3.10 Conclusion

The aim of this project was to prepare model networks to compare the exchange reactions of dioxaborinanes and dioxaborolanes within vitrimers. A dioxaborolane network (**Network 1**) has already been synthesized and characterized in Chapter 2. It was therefore envisioned to synthesize an equivalent **Network 2** comprising dioxaborinane moieties. In order to do so, the corresponding monomer was prepared. Since no adequate triol is commercially available, a pentane-triol was synthesized from the commercially available compound dimethyl 3-oxopentanedioate. The triol was protected with an acetal group and transformed to an acrylate monomer by condensation with acryloyl choride. The monomer had to be purified carefully, since the presence of di- and triacrylate side products led to branching and crosslinking during the copolymerization. The 6-membered acetal protected monomer was obtained in 16 % yield over three steps.

The monomer was copolymerized in its acetal form via RAFT polymerization with *n*BA. After the polymerization, the RAFT end-group was removed by aminolysis. Subsequently, the acetal protecting group was removed in acidic medium and the diol was esterified with PBA to yield dioxaborinane functionalized TPs. This TP had similar properties as the dioxaborolane TP with regard to M_n and Đ. The dioxaborinane functionalized TP was crosslinked with the bis(boronic ester) **10** to form **Network 2**. **Network 2** resembled the dioxaborolane **Network 1** in respect to functionality and ρ(CL), and had therefore excellent preconditions to be employed in a comparative study to **Network 1**.

During the crosslinking and the processing, **Network 2** showed a slightly slower exchange dynamic. **Network 2** showed higher thermal stability in TGA than **Network 1**. In DSC, **Network 2** featured a slightly higher T_g and an exothermic transition at around 136 °C that was not observed with **Network 1**. The transition was reversible and had an enthalpy of 0.16 J/g. Most likely, at this temperature the functional groups in the polymer chain form some aggregates. In DMA, both networks exhibited similar T_gs. The storage modulus E' of **Network 2** was higher. This also showed in frequency sweep experiments. The rubbery plateau of G' of **Network 2** was three times higher than the one of **Network 1**.

Stress relaxation was conducted to assess the exchange dynamics of **Network 2**. The determined E_a was 97.4 kJ/mol vs. 72.8 kJ/mol for the dioxaborolane network. This is in accordance to small molecule exchange experiments, where dioxaborinanes also exhibited a higher E_a than their dioxaborolane counterparts. However, during the stress relaxation experiments, **Network 2** showed next to the boronic ester exchange a second short time stress relaxation that became more pronounced with each relaxation experiment. Amplitude sweeps revealed that **Network 2** showed a significant higher brittleness than **Network 1**. The stress relaxation experiments might have been not conducted in the linear regime anymore. Increasing network damage by the applied strain might have been the origin of the short time stress relaxation and thereby have impacted the stress relaxation experiments and the determined characteristic relaxation times. The observed behavior can be linked to the second transition observed during DSC. Aggregation of the functional groups might lead to the formation of physical crosslinks and explain the observed increase in modulus as well as the brittleness of the material. To confirm this hypothesis and to get a better insight into the nature of these possible aggregations, additional experiments are envisioned. Transmission electron microscopy or X-ray diffraction are suitable methods to give information, if there are areas of ordered arrangement in the material.

3.11 Experimental Part

3.11.1 Materials

All chemicals were purchased from Sigma Aldrich, Alfa Aesar, TCI, Acros Organics and Fischer. All starting materials and reagents were of analytic grade and used without further purification, if not stated otherwise. AIBN was recrystallized from methanol prior

to use. *n*BA and 1,4-dioxane were passed through a short column of basic alumina to remove inhibitors or antioxidants.

3.11.2 Instrumental Data

NMR Spectroscopy

^{1}H NMR and ^{13}C NMR spectroscopy measurements were performed in oven dried NMR tubes on a Bruker Ultra Shield machine (400 MHz for ^{1}H NMR, 100 MHz for ^{13}C NMR) at ambient temperature. If not stated otherwise, samples of 10 mg for ^{1}H NMR and 30 mg for ^{13}C NMR were analyzed. CDCl$_3$ and methanol-d4 were employed as deuterated solvents. Chemical shifts are expressed in parts per million (ppm) and calibrated on characteristic solvent signals as internal standards (^{1}H NMR: CDCl$_3$: 7.26 ppm, methanol-d4: 3.31 ppm; ^{13}C NMR: CDCl$_3$: 77.16 ppm, methanol-d4: 49.00 ppm).

Size Exclusion Chromatography

The samples for SEC chromatography were prepared by dissolving the respective polymer in anhydrous THF to obtain a concentration of 1.0-1.2 mg/mL. A drop of toluene was added and the sample was passed through a 0.20 μm PTFE filter and placed in a Malvern GPC vial. SEC was performed on a Viscotek GPCmax/VE2001 connected to a Triple detection array (TDA 305) from Malvern. Obtained raw data were treated with a PS calibration.

DSC

DSC analyses were performed on TA DSC 250 apparatus. Two heating cycles, from -100 to 200 °C, were performed employing a heating rate of 10 °C min^{-1}. The values of T_g were determined with the data obtained on the second heating cycle.

TGA

TGA measurements were performed on a TG 209 F1 Libra from Netzsch. The samples were heated constantly with a rate of 10 °C min^{-1} from 30 to 600 °C. Isothermal analyses were conducted by heating samples constantly with a rate of 10 °C min^{-1} from 30 to 150 °C, and keeping the sample at this temperature for 10 h.

DMA

DMA measurements were conducted on a TA Instruments Q800 in tension mode. Heating ramps were performed from -80 to 200 °C at a constant rate of 3 °C min^{-1} with a fixed frequency of 1 Hz and a maximum strain amplitude of 1 %. The T_g of the sample was determined at the maximum of the loss modulus function E".

Rheological Characterizations

All rheological characterizations were conducted on a Anton Paar MCR 501 rotational rheometer with a parallel plate geometry with a diameter of 25 mm. If not otherwise stated, the experiments were run in a convection oven under nitrogen. For solid samples a normal force of 0.4 N was employed.

Frequency sweeps were conducted at 1 % strain between 0.01 and 100 Hz on a logarithmic ramp with 5 measuring points per decade (if not stated otherwise).

Stress relaxations were conducted with an applied strain of 1 %. Before the experiment, samples were allowed to equilibrate for 5-6 h at 150 °C. Before every stress relaxation, a frequency sweep was conducted. The relaxation time τ was calculated from the obtained data using the KWW model after Equation 3.3.

$$\frac{G(t)}{G_0} = exp\left\{-\left(\frac{t}{\tau}\right)^{\beta}\right\} \tag{3.3}$$

E_a and the Arrhenius prefactor τ_0 were determined by a linear fit on the characteristic relaxation times τ according to Equation 3.4.

$$\tau(T) = \tau_0 exp\left(\frac{E_a}{R \cdot T}\right) \tag{3.4}$$

Table 3.3: Relaxation times τ and β determined via the modeling employing Equation 3.3 during the stress relaxation experiments of **Network 1** and **Network 2** going down from 150 to 90 °C.

T [°C]	τ [s] **Network 1**	β **Network 1**	τ [s] **Network 2**	β **Network 2**
150	69	0.55	4437	0.33
140	387	0.60	16485	0.22
130	696	0.59	33518	0.18
120	1245	0.58	67077	0.16
110	2226	0.57	153870	0.15
90	7254	0.53	-	-

Amplitude sweeps were conducted between 0.1-10 % strain on a logarithmic ramp with 6 measuring points per decade at a frequency of 20 rad/s at 25 °C.

Crosslinking of the Thermoplastic Precursor

The amount of crosslinker was calculated with Equations 3.5, with f_{CL} as the ratio of functional groups crosslinked, m(P) mass of the polymer, f(P) functionality of the polymer, N_f(CL) functionality of the crosslinker, and M(M_{Av}) average molecular mass of the monomers (calculated with Equation 3.6). The TP was dissolved in THF (1 : 3 w/w) and placed into a beaker. A respective amount of a solution of the crosslinker **10** (100 mg / mL THF) was added. The mixture was vigorously stirred manually. The mixture rested openly at ambient temperature for 72 h, subsequently it was placed in a vacuum oven at 80 °C for 16 h. The resulting material was torn into pieces and again dried under the same conditions for another 16 h. The network was obtained as a colorless foam.

$$n(CL) = \frac{f_{CL} \cdot m(P) \cdot f(P)}{N_f(CL) \cdot M(M_{Av})} \tag{3.5}$$

$$M(M_{Av}) = f(P) \cdot M(FM) + (1 - f(P)) \cdot M(nBA) \tag{3.6}$$

Compression Molding

Compression molding was conducted using a hydraulic press applying a pressure equivalent to 3 tons. Dry samples were placed into a metal mold and pressed at 110°C for 30-40 min.

3.11.3 Synthesis

3.11.4 Synthesis of the Monomer
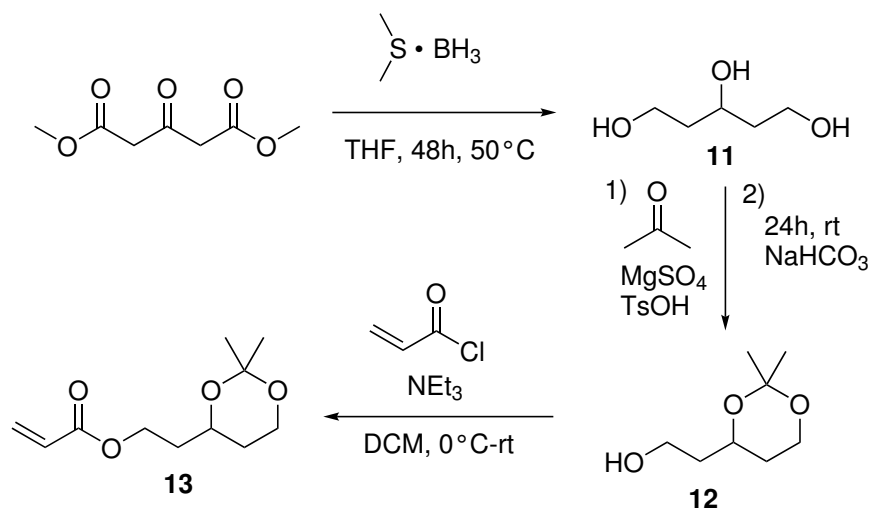
Scheme 3.8: Synthetic scheme for the 6-membered acetal monomer.

Synthesis of Pentane-1,3,5-triol
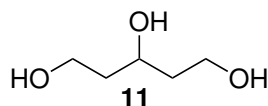
Scheme 3.9: Pentane-1,3,5-triol **11**.

25 mL of dimethyl 3-oxopentanedioate (30.0 g, 172 mmol, 1.00 eq) were dissolved in 200 mL of THF. The mixture was bubbled with N_2 to remove oxygen from the solution. 49.0 mL of the BMS complex ($BH_3 \cdot Me_2S$) (39.3 g, 517 mmol, 3.00 eq) were added

dropwise and the mixture was allowed to stir at 50°C for 48 h. Subsequently, the solution was carefully immersed into 200 mL of MeOH under the formation of gas. After 2 h, the solvent was removed and the crude product obtained as a yellow oil. The product **11** was isolated after CC (SiO$_2$, EtOAc 100 % → EtOAc : MeOH 9:1, 20 cm × 5 cm) as a colorless viscous oil (15.7 g, 130 mmol, 76 % yield).

R$_f$ (EtOAc) = 0.1
R$_f$ (EtOAc : MeOH 9:1) = 0.4

^{1}H NMR (400 MHz, Methanol-d4, 298 K): δ [ppm] = 3.88 (tt, *J* = 8.4, 4.4 Hz, 1H, HO-C**H**), 3.70 (t, *J* = 6.5 Hz, 4H, HO-C**H**$_2$), 1.77-1.54 (m, 4H, C**H**$_2$).

^{13}C NMR (100 MHz, Methanol-d4, 298 K): δ [ppm] = 67.53 (**C**H), 60.16 (**C**H$_2$), 41.06 (**C**H$_2$).
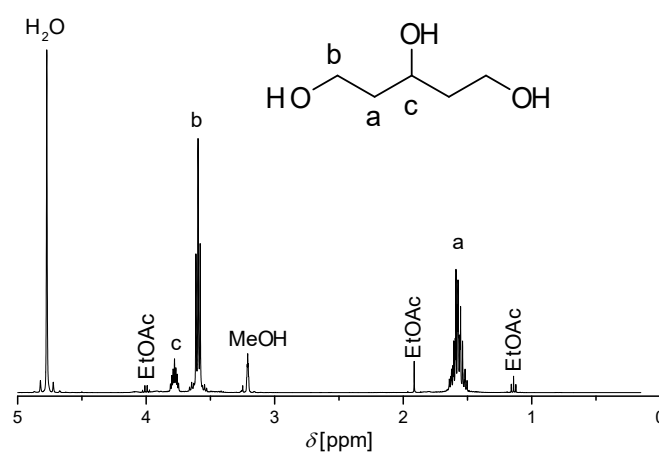
Figure 3.18: ^{1}H NMR spectrum of pentane-1,3,5-triol **11** in methanol-d4.
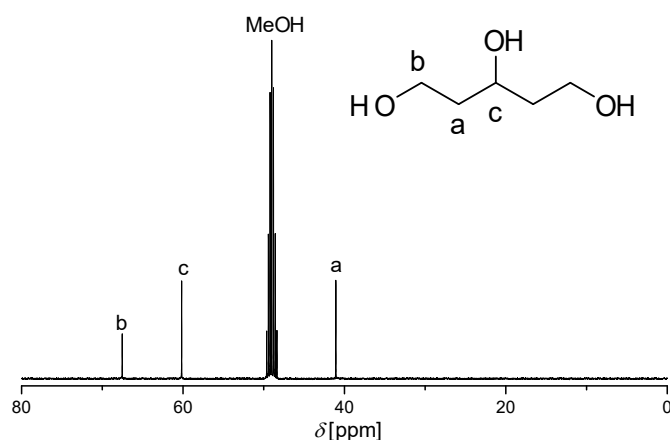
Figure 3.19: ^{13}C NMR spectrum of pentane-1,3,5-triol **11** in methanol-d4.

Synthesis of 2,2-Dimethyl-1,3-dioxane-4-ethanol
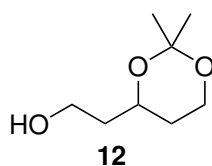
Scheme 3.10: 2,2-Dimethyl-1,3-dioxane-4-ethanol **12**.

12.3 g of pentane-1,3,5-triol **11** (102.2 mmol, 1.0 eq) were dissolved in 200 mL of acetone under slight heating. 36.9 g of $MgSO_4$ (306.6 mmol, 3.00 eq) were introduced into the solution and 3.50 g of TsOH (18.4 mmol, 0.18 eq) were added bit by bit. The mixture was stirred at room temperature for 72 h, before 1.54 g of $NaHCO_3$ were added. The mixture stirred for another 16 h, before it was filtered. The filtrate was concentrated and 200 mL of H_2O were added. The aqueous phase was extracted 5 times with 150 mL of EtOAc. The organic phase was dried over Na_2SO_4 and the solvent removed under reduced pressure. The product **12** was obtained as a yellow oil (7.12 g, 43.9 mmol, 44 % yield).

^{1}**H NMR** (400 MHz, Methanol-d4, 298 K): δ [ppm] = 4.14-4.07 (m, 1H, O-C**H**), 4.03 (td, *J* = 11.9, 3.3 Hz, 1H, O-C**H**$_2$), 3.78 (ddd, J = 11.8, 5.2, 1.8 Hz, 1H, O-C**H**$_2$), 3.63 (t, J = 6.4 Hz, 2H, HO-C**H**$_2$), 1.72-1.45 (m, 4H, C**H**$_2$), 1.46 (s, 3H, C**H**$_3$, 1.32 (s, 3H, C**H**$_3$).

^{13}**C NMR** (100 MHz, Methanol-d4, 298 K): δ [ppm] = 99.65 (**C**), 67.49 (**C**H), 60.99 (**C**H$_2$), 59.03 (**C**H$_2$), 40.33 (**C**H$_2$), 32.52 (**C**H$_2$), 30.28 (**C**H$_3$), 19.57 (**C**H$_3$).
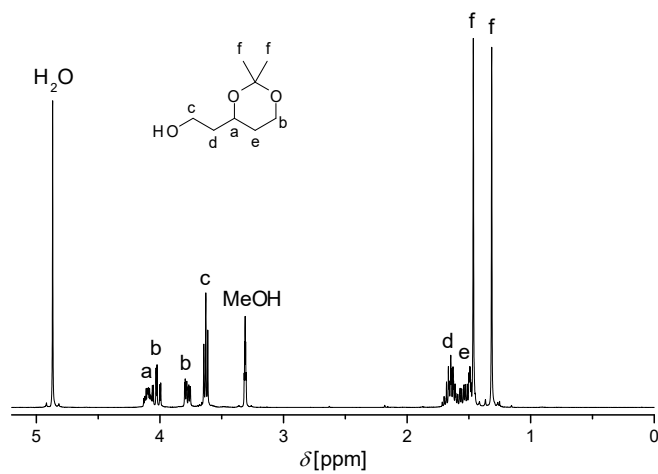
Figure 3.20: ^{1}H NMR spectrum of **12** in methanol-d4.
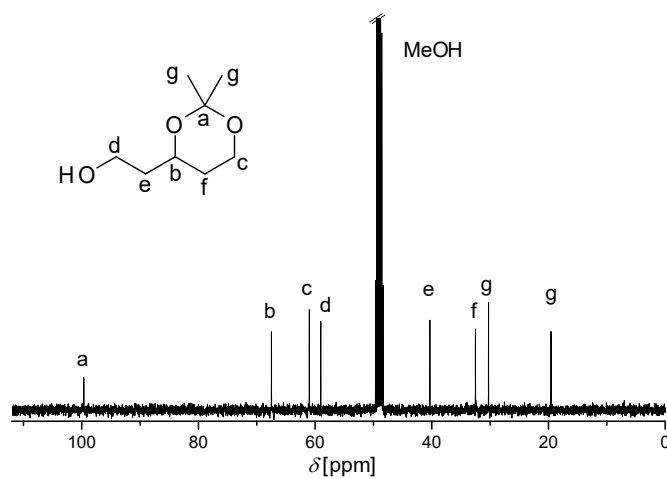
Figure 3.21: ^{13}C NMR spectrum of **12** in methanol-d4.

Synthesis of 2-(2,2-Dimethyl-1,3-dioxan-4-yl)ethyl acrylate
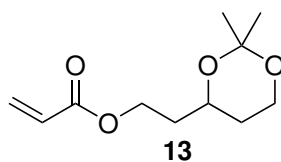
Scheme 3.11: 2-(2,2-Dimethyl-1,3-dioxan-4-yl)ethyl acrylate **13**.

5.95 g of compound **12** (37.1 mmol, 1.00 eq) were dissolved in 50 mL of DCM and 8.28 mL of NEt$_3$ (6.02 g, 59.4 mmol, 1.6 eq) were added. The mixture was freed from oxygen by bubbling nitrogen for 30 min, before it was put into an ice bath to cool it to 0 °C. Subsequently, 4.53 mL of acryloyl chloride (5.04 g, 55.7 mmol, 1.50 eq) were added slowly. The mixture was stirred for 4 h at 0 °C and then 15 h at ambient temperature, before some MeOH was added. The solution was stirred at room temperature for another 5 h before it was washed 3 times with 30 mL of 1M HCl$_{aq}$, 3 times with 30 mL of saturated NaHCO$_3$ solution, and 2 times with 30 mL of brine. The organic phase was dried over MgSO$_4$, filtered and the solvent was removed under reduced pressure to yield a yellowish oil. The crude product was purified by CC (hex : EtOAc 1 : 1). The product **13** was obtained as a colorless oil (3.86 g, 17.5 mmol, 47 % yield).

R$_f$ = 0.8

^{1}H NMR (400 MHz, CDCl$_3$, 298 K): δ [ppm] = 6.33 (dd, *J* = 17.4, 1.5 Hz, 1H, C**H**$_2$=CH), 6.05 (dd, *J* = 17.3, 10.4 Hz, 1H, CH$_2$=C**H**), 5.76 (dd, *J* = 10.4, 1.5 Hz, 1H, C**H**$_2$=CH), 4.20 (ddd, *J* = 7.2, 6.2, 1.2 Hz, 2H, O-C**H**$_2$), 3.93 (m, 1H, O-C**H**), 3.91 (td, *J* = 12.0, 2.9 Hz, 1H, O-C**H**$_2$), 3.77 (ddd, *J* = 11.8, 5.4, 1.7 Hz, 1H, O-C**H**$_2$), 1.76 (m, 2H, C**H**$_2$), 1.56 (m, 2H, C**H**$_2$), 1.37 (s, 3H, C**H**$_3$), 1.30 (s, 3H, C**H**$_3$).

^{13}C NMR (100 MHz, Methanol-d4, 298 K): δ [ppm] = 167.69 (O-**C**=O), 131.41 (**C**H$_2$=CH), 129.62 (CH$_2$=**C**H), 99.68 (O-**C**-O), 67.23 (O-**C**H), 61.97 (O-**C**H$_2$), 60.90 (O-**C**H$_2$), 36.50 (**C**H$_2$), 32.41 (**C**H$_2$), 30.24 (**C**H$_3$), 19.47 (**C**H$_3$).
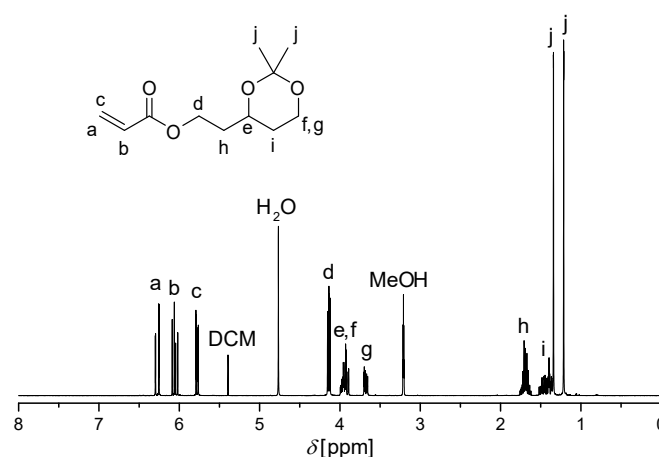
Figure 3.22: ^{1}H NMR spectrum of monomer **13** in methanol-d4.
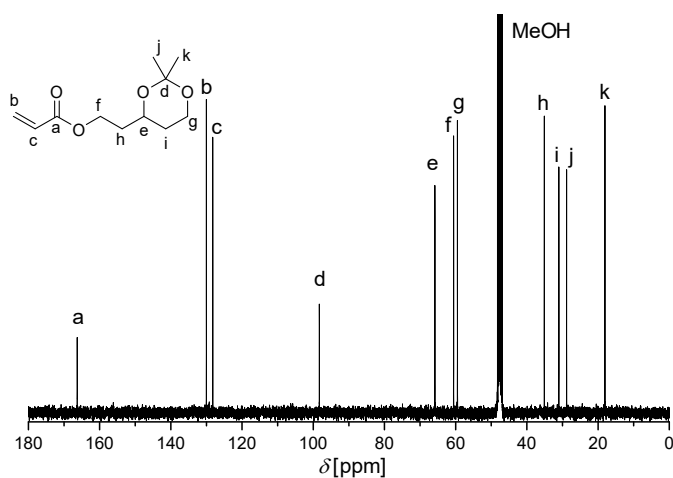
Figure 3.23: ^{13}C NMR spectrum of monomer **13** in methanol-d4.

3.11.5 Copolymerization and Polymer Functionalization
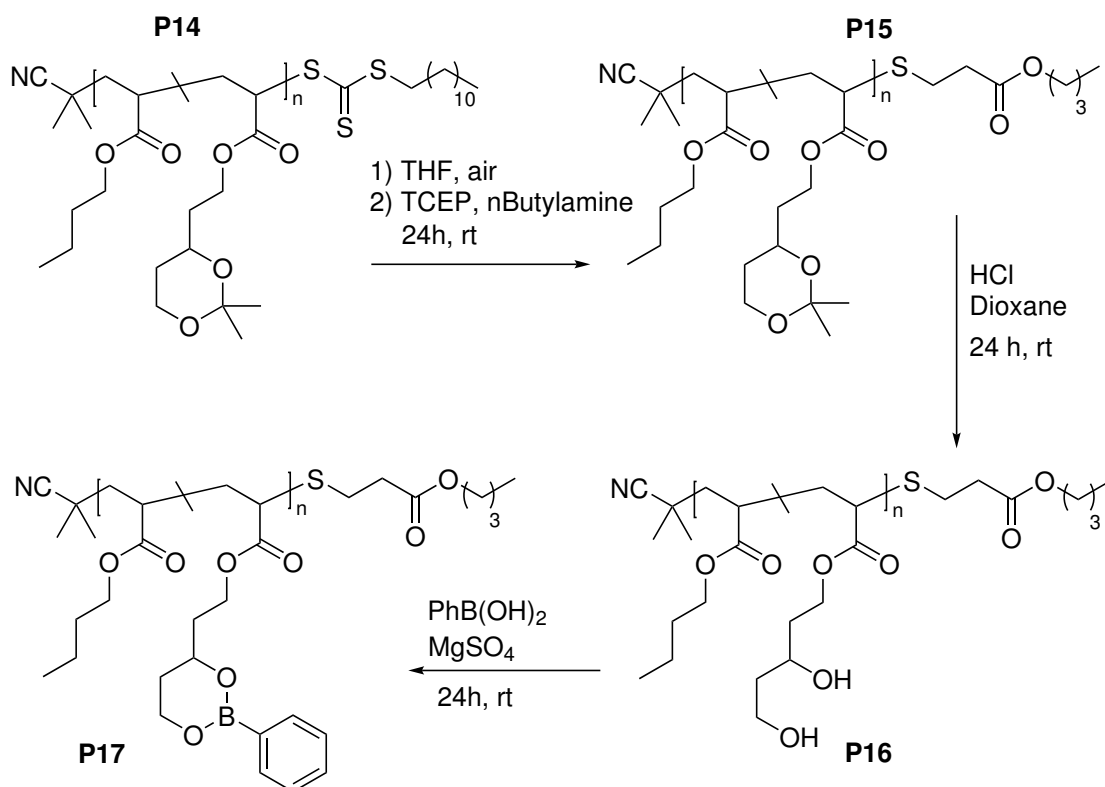
Scheme 3.12: Polymer functionalization of the TP of **Network 2**.

Synthesis of Copolymer P14 and Subsequent RAFT End Group Removal to yield P15
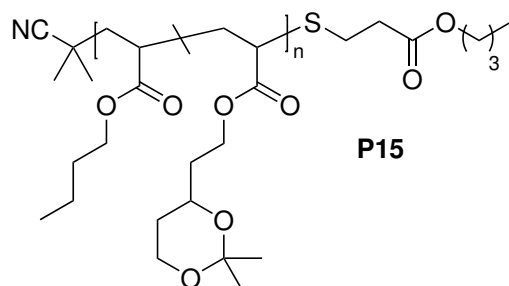
Scheme 3.13: Copolymer **P15** resulting from the RAFT polymerization of *n*BA with the protected diol functional monomer **13**, and the subsequent removal of the RAFT group.

General procedure:

In a typical experiment, 1000 eq of *n*BA, 115 eq of the functional monomer **13**, 1.00 eq of CPDT in a stock solution in dioxane, 0.2 eq of AIBN in a stock solution in dioxane, and the respective amount of dioxane (1:1 v/v to *n*BA + **13**) were added to a dry 100 mL Schlenk tube. The tube was sealed with a septum and oxygen was removed by bubbling nitrogen for 1 h. Subsequently, the tube was placed into an oil bath thermostated at 60°C until a monomer conversion of 80 % was obtained. The polymerization was stopped by cooling it, while exposing it to air and subsequently adding several mL of THF. The solution was freed from oxygen by bubbling nitrogen for 30 min again. A catalytic amount of TCEP was added and the mixture was stirred for 10 min. Subsequently, 50 eq BuNH$_2$ were added and the mixture was stirred for 16 h, before the mixture was precipitated twice into MeOH : H$_2$O (8 : 1 v/v). The residue was taken up in THF and dried at 80°C under reduced pressure to yield a colorless, transparent, viscous polymer.

[1]**H NMR** (400 MHz, CDCl$_3$, 298 K): δ [ppm] = 4.11 (m, n×2H, O=CO**H**$_2$), 4.02 (m, n×2H, O=CO**H**$_2$), 4.02-3.90 (m, n×2H, -O-C**H**$_2$, -O-C**H**), 3.82 (dd, *J* = 11.5, 4.9 Hz, n×2H, -O-C**H**$_2$), 2.26 (m, n×2H, C**H**$_{backbone}$), 1.92 (m, n×2H, C**H**$_{backbone}$), 1.76 (m, n×2H, C**H**$_2$), 1.62 (m, n×2H, C**H**$_2$), 1.58 (m, n×2H, C**H**$_2$), 1.58-1.28 (m, n×2H, C**H**$_{backbone}$), 1.43 (s, n×3H, C**H**$_3$), 1.36 (m, n×2H, C**H**$_2$), 1.35 (s, n×3H, C**H**$_3$), 0.93 (t, n×3H, C**H**$_3$).

163
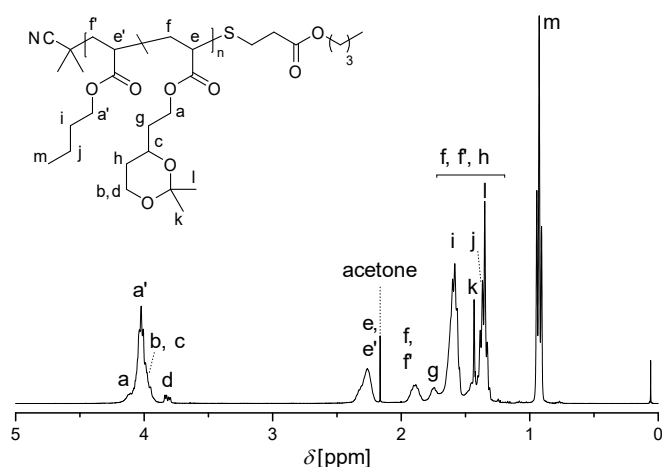
Figure 3.24: ^{1}H NMR spectrum of copolymer **P15** in CDCl$_3$.

Deprotection of Copolymer P15 to Yield P16
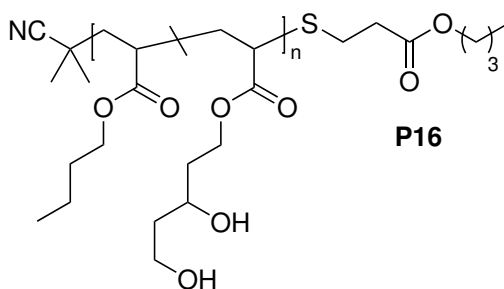
Scheme 3.14: Copolymer **P16**.

P15 was dissolved in 1,4-dioxane (20 ml/g polymer). 1 M HCl$_{aq}$ was added dropwise until the pH reached a value of 4 or less. The mixture was then stirred openly for 16 h. The solution was concentrated and precipitated twice into MeOH : H$_2$O (1 : 2 v/v). The precipitate was taken up in dioxane and the solvent was removed. The polymer was dried for 4 h at 40 °C under vacuum and obtained as a colorless, transparent, viscous liquid.

^{1}**H NMR** (400 MHz, CDCl$_3$, 298 K): δ [ppm] = 4.31 (m, n×1H, HO-C**H**$_2$), 4.03 (m, n×2H, O=CO**H**$_2$), 3.86 (m, n×1H, HO-C**H**), 3.80 (m, n×1H, H-O-C**H**$_2$), 2.28 (m, n×2H, C**H$_{backbone}$**), 2.15 (s, n×2H, **H**O), 1.90 (m, n×2H, C**H$_{backbone}$**), 1.71 (m, n×2H, C**H**$_2$), 1.65-1.28 (m, n×2H, C**H$_{backbone}$**), 1.59 (m, n×2H, C**H**$_2$), 1.48 (m, n×2H, C**H**$_2$), 1.36 (m, n×2H, C**H**$_2$), 0.93 (t, n×3H, C**H**$_3$).
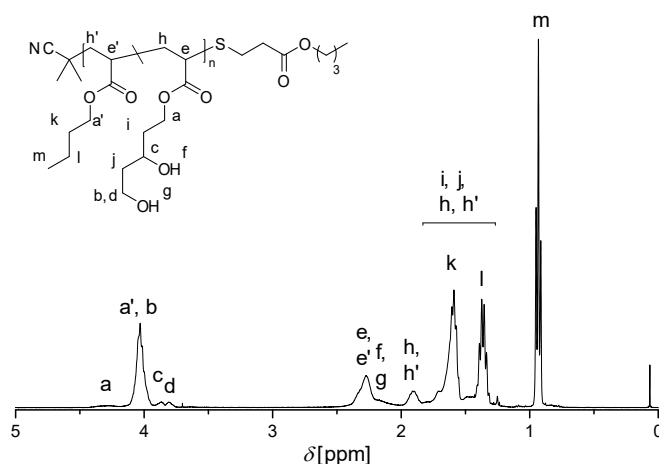
Figure 3.25: ^{1}H NMR spectrum of copolymer **P16** in CDCl$_3$.

Esterification of Copolymer P16 with PBA to Yield P17
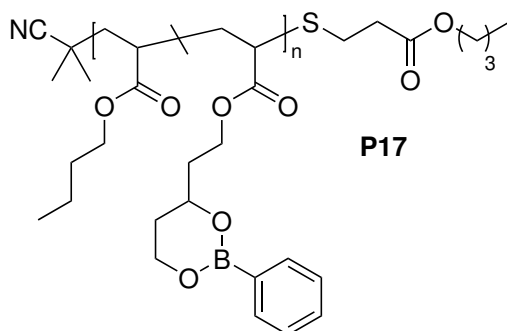
Scheme 3.15: Copolymer **P17**.

P16 was dissolved in anhydrous THF (10 mL/g polymer). 1.50 eq of PBA were immersed into a separate beaker containing THF. After 10 min one drop of water was added, and the mixture was stirred until the PBA was completely dissolved. It was then added to the polymer solution. After 6 h of stirring, 10 eq of MgSO$_4$ were dispersed stepwise into the solution. After 16 h, the mixture was centrifuged and the centrate filtered through a Por. 4 frit. The polymer solution was concentrated and precipitated once into cold MeCN and a second time into cold hexane. The polymer was dried for 16 h at 80 °C under vacuum. The polymer was obtained as a colorless, transparent, viscous liquid. For the calculation of the ratio of the monomers in the copolymer the NMR proton signals

(compare Figure 3.26) of the functional monomer (H$_a$, 2H) and the *n*BA monomer (H$_m$, 3H) were employed.

Properties: M_n = 93 kDa, Đ = 1.45, DP$_n$ = 678, N$_F$ = 68, f = 10 %;

¹H NMR (400 MHz, CDCl$_3$, 298 K): δ [ppm] = 7.75 (d, *J* = 7.3 Hz, n×2H, C$_{Ar}$**H**), 7.39 (m, n×1H, C$_{Ar}$**H**), 7.31 (t, *J* = 7.3 Hz, n×2H, C$_{Ar}$**H**), 4.32 (m, n×1H, B-O-C**H**), 4.18 (m, n×1H, B-O-C**H$_2$**), 4.02 (m, n×2H, O=CO**H$_2$**), 2.27 (m, n×2H, C**H**$_{backbone}$), 1.90 (m, n×2H, C**H**$_{backbone}$), 1.58 (m, n×2H, C**H$_2$**), 1.70-1.30 (m, n×2H, C**H$_2$**), 1.58-1.28 (m, n×2H, C**H**$_{backbone}$), 1.35 (m, n×2H, C**H$_2$**), 0.92 (t, *J* = 7.3 Hz, n×3H, C**H$_3$**).
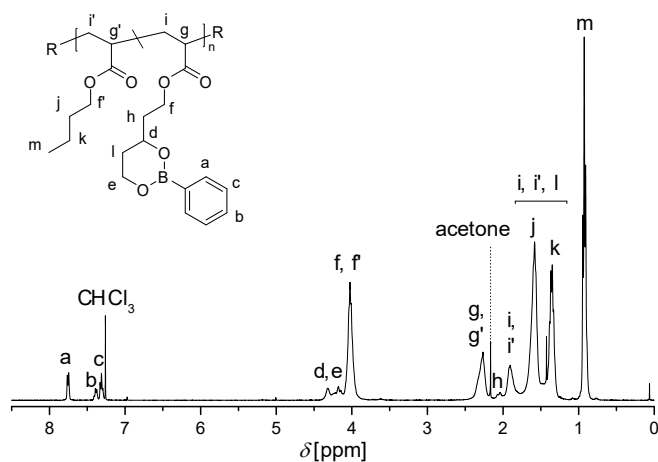
Figure 3.26: ¹H NMR spectrum of copolymer **P17** in CDCl$_3$.

Bibliography

(1)   Cash, J. J.; Kubo, T.; Dobbins, D. J.; Sumerlin, B. S. *Polym. Chem.* **2018**, *9*, 2011–2020.

(2)   Breuillac, A.; Kassalias, A.; Nicolaÿ, R. *Macromolecules* **2019**, *52*, 7102–7113.

(3)   Roy, C. D.; Brown, H. C. *Monatshefte für Chemie* **2007**, *138*, 879–887.

(4)   Roy, C. D.; Brown, H. C. *J. Organomet. Chem.* **2007**, *692*, 784–790.

(5)   Röttger, M.; Domenech, T.; Van Der Weegen, R.; Breuillac, A.; Nicolaÿ, R.; Leibler, L. *Science.* **2017**, *356*, 62–65.

(6)   Röttger, M. Associative Exchange Reactions of Boron or Nitrogen Containing Bonds and Design of Vitrimers, Ph.D. Thesis, Université Pierre et Marie Curie - Paris VI, 2016.

(7)   Yang, Y.; Du, F.-S.; Li, Z.-C. *Polym. Chem.* **2020**, 1860–1870.

(8)   Breuillac, A. Recyclable and reprocessable elastomers relying on the vitrimer concept, Ph.D. Thesis, Université Paris Sciences et Lettres, 2019.

(9)   Riatto, V. B.; Carneiro, M. N. M.; Carvalhoc, V. B.; Victor, M. M. *J. Braz. Chem. Soc.,* **2011**, *22*, 172–175.

(10)   Saito, S.; Ishikawa, T.; Akiyoshi, K.; Koga, K.; Moriwake, T. *Tetrahedron* **1992**, *48*, 4067–4086.

(11)   Du, D.-M.; Fang, T.; Xu, J.; Zhang, S.-W. *Angew. Chem., Int. Ed. Engl* **1998**, *37*, 13819–13824.

4 | P*n*BA Vitrimers Based on Imine-Aldehyde Exchange

Chapter Contents

4.1 Introduction

Imines are organic compounds comprising a carbon-nitrogen double bound connected to a hydrogen or organic group.[1] If this organic group is not a hydrogen atom, the resulting compound can be referred to as Schiff's base, named after Hugo Schiff, the chemist who firstly reported the reaction between an amine and a carbonyl group.[2] The term "imine" was coined later by Albert Ladenburg.[3] Imines are related to ketones and aldehydes by the replacement of the oxygen with an amino group. In fact, imines are most commonly synthesized by the condensation of primary amines and aldehydes or ketones like shown in Scheme 4.1.[4] The reaction is reversible, hence the water has to be removed during the reaction to drive the equilibrium to the product side. Imines are prone to undergo hydrolysis. In the presence of water they cleave into amines and aldehydes/ketones. Mechanism-wise, imine formation occurs in a stepwise manner: the amino group undertakes a nucleophilic attack on the unsaturated carbon of the carbonyl compound, forming a intermediate tetrahedral carbinolamine. The final C=N linkage is then formed by the subsequent elimination of water.[4] These steps can be either acid or base catalyzed.[5] The equilibrium of the reaction can be determined by many factors, such as pH, solvent, concentration, and temperature, as well as steric and electronic factors.[6] Imines are in general less reactive than their parent carbonyl compounds. Yet, their reactivity towards water or hydroxide ions as nucleophiles can be significantly increased by the protonation of the imine.[5] N-Protonation in the tetrahedral intermediate transforms the amine into a superior leaving group.

$$R_1\text{—}NH_2 \ + \ \underset{R_2}{\overset{O}{\overset{\|}{\diagup}}}R_3/H \ \underset{+H_2O}{\overset{-H_2O}{\rightleftharpoons}} \ \underset{R_2}{\overset{N\diagup^{R_1}}{\overset{\|}{\diagup}}}R_3/H$$
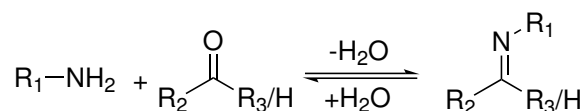
Scheme 4.1: Imines are synthesized by the condensation of primary amines and aldehydes or ketones. The reaction is reversible by hydrolysis.

Imines are able to undergo other typical dynamic reactions like shown in Scheme 4.2. They can undergo transiminations with either an aldehyde or an amine.[1,7] They are also able to participate in metathesis reactions with other imines. All reactions were reported to proceed catalyst-free, although reaction kinetics can be influenced by pH.[5] The metathesis was shown to be accelerated by the presence of aldehydes[7] or amines[8]. All reactions proceed via an associative pathway.[1,7,8]

The reversibility of imines makes them suitable for the application in many fields, such as the identification of lead compounds for drug discovery,[9] template-directed synthesis
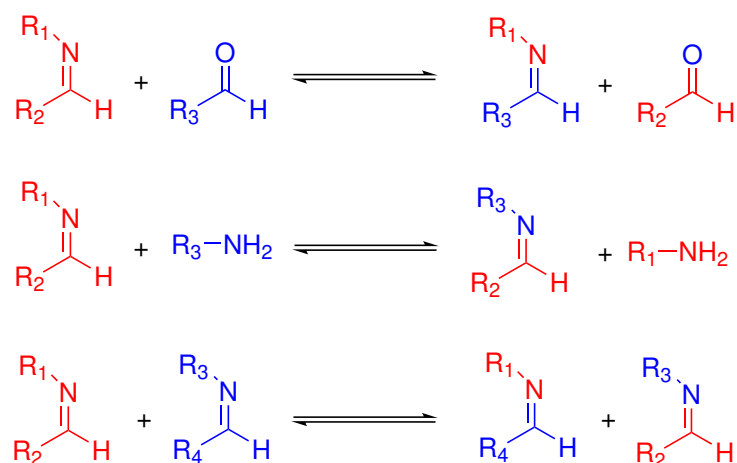
Scheme 4.2: Imines can undergo dynamic exchange reactions: transiminations with other aldehydes (top) or amines (middle), or metathesis reactions with other imines (bottom).

in organic chemistry,[10] self-assembling structures,[11] molecular walkers,[12], artificial enzymes,[13] or covalent organic frameworks[14]. Their dynamic reaction portfolio has made imines ideal candidates for the application as dynamic linkages in CANs. Materials comprising dynamic imine linkages showed properties like controlled degradability,[15–18] self-healing,[16,19–21] and recyclability.[16,19,20,22–25] Imine based CANs feature responsiveness to pH,[15,18] heat,[23–26] or moisture,[23,25,26] as well as to competitive molecules. The degenerate nature of the imine exchange allows to create materials that show vitrimer properties.[25–28]

The exchange reactions of imines proceed via a degenerative pathway without any significant side reactions. This chemistry seems therefore well suited to form the second subnetwork in the DDN. Imines or aldehydes are not reported to react with boronic esters or alcohols, and should thus feature orthogonality to the boronic ester network. In this chapter, the synthesis, characterization and optimization of the imine-aldehyde subnetwork are described. First, an aldehyde functional monomer is synthesized. It is polymerized to yield a TP that is subsequently crosslinked to form the subnetwork that is processed by compression molding. The obtained network should act as the structural network within the DDN. It is envisioned to be loosely crosslinked and not dynamic at ambient conditions. Yet, it should feature good processability and recyclability at elevated temperatures. To achieve this dynamic behavior, the density of free functional groups as possible exchange partners is kept low. To evaluate if it fulfills these requirements, characterizations, such as swelling and solubility tests, DMA, DSC, TGA, tensile tests

and rheometry (stress relaxation, creep resistance) were employed. The properties of the subnetwork are compared to those of the double network in Chapter 5.

4.2 Monomer Synthesis

The second subnetwork is based on the same polymer matrix as **Network 1**, P*n*BA. In order to obtain a network structure based on an imine-aldehyde exchange (hereinafter referred to as **Network 3**), a TP with pendent aldehydes is targeted. An aldehyde functional acrylate monomer **19** was prepared to this aim. It was synthesized according to the procedure depicted in Scheme 4.3, which was adapted from the literature.[29] However, the first step of this reaction, leading to p-(2-hydroxyethoxy)benzaldehyde **18**, is time-consuming when it comes to the removal of the solvent (dimethylformamide (DMF)) and the purification by CC. In addition to that, the reaction had low yields (8-16%) and the product was sometimes not obtained pure despite the CC. Changes in reaction mixture, temperature, reaction time or work up did not improve the result.
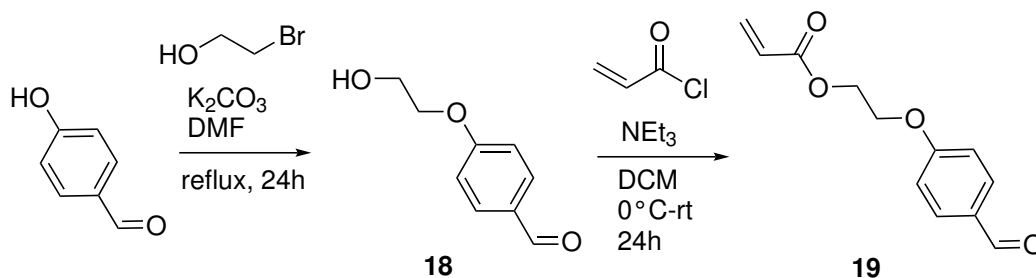
Scheme 4.3: Synthesis of aldehyde functional monomer **19** via the intermediate product **18**.

Therefore, another procedure found in the literature[30] (see Scheme 4.4) has been attempted. Instead of DMF the more volatile acetone is used. In addition to that, tetra-*n*-butylammonium bromide (TBAB) was added as a transfer catalyst. This reaction was also conducted several times under changing conditions, but the yield never surpassed 16 %. Since the literature procedures did not lead to an acceptable result, a new approach like shown in Scheme 4.5 was tested. Instead of K_2CO_3, NaOH was added as base. To dissolve it, the solvent system was changed to a mixture of EtOH and H_2O. With this approach the yield could be raised to up to almost 90% and a purification via CC was not necessary. Aqueous washing proved to be sufficient as purification method.
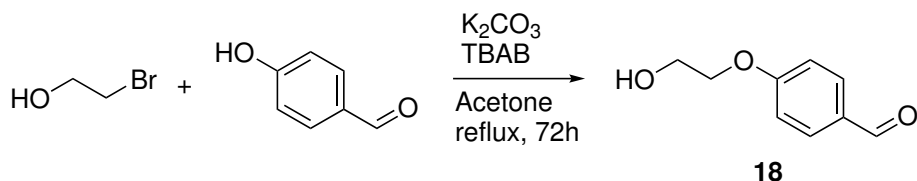
Scheme 4.4: Alternative reaction conditions to obtain **18**.
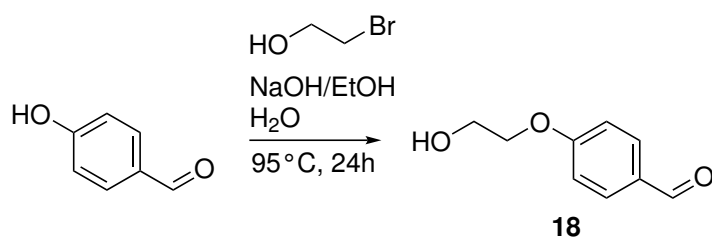
Scheme 4.5: Approach to obtain **18** using NaOH as base.

The intermediate product **18** was then transformed with acryloyl chloride to the final monomer **19** like depicted in Scheme 4.3. The product was sufficiently pure after the washing steps according to the NMR spectrum. However, the product tended to undergo self-polymerization. This was prevented by additional purification via CC and subsequent cooling of the sample. The sample was obtained as a white to yellow powder with around 60 % total yield over two steps.

4.3 Crosslinker Synthesis

The crosslinking of the imine-aldehyde subnetwork requires a crosslinker containing two imine groups. A crosslinking employing amines would in principle work as well, but a complexation reaction with the boronic ester groups of the other network cannot be excluded and represents a major drawback that can be avoided by using imines instead. In a first attempt, hexanediamine was reacted with butyraldehyde to yield the bis(imine) **20** like depicted in Scheme 4.6. This approach was chosen, because butyraldehyde has a relatively low boiling point (T_B = 74.8 °C) and is not as hazardous as propionaldehyde or formaldehyde. However, the product could not be isolated, the aliphatic imine has a too low stability.
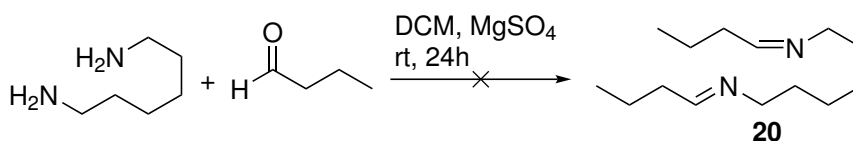
Scheme 4.6: The bis(imine) **20** between butyraldehyde and hexanediamine could not be obtained.

Therefore, the reaction was repeated using the aromatic benzaldehyde like shown in Scheme 4.7. The reaction worked, however, in the NMR spectrum was still a significant amount of free aldehyde (18 mol%) visible. The aldehyde could be removed in greater parts by drying under vacuum at 150 °C for 16 h, yielding the targeted bis(imine) with a purity of 98.2 mol% (by NMR) and a yield of 79 %.
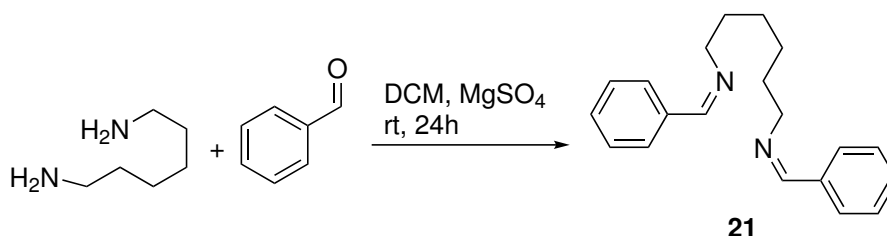
Scheme 4.7: Bis(imine) crosslinker formation between benzaldehyde and hexanediamine yielding crosslinker **21**.

4.4 TP 500 kDa, 0.5 % Functionality

4.4.1 Copolymerization

Network 3 represents the structural network. It is envisioned to have a low ρ(CL) and a low number of free functional groups. The network was designed to have 0.5 % functionality, of which 50 % are crosslinked to have a crosslinking density of 0.25 %. Ideally, all chains should be incorporated into the network, as unattached chains would impact the physical properties of the final material. Thus, a sufficient amount of functional groups has to be present in one chain to ensure a reasonable probability for the chain to be incorporated into the network. The functionality of the polymer is low, therefore, the number-average degree of polymerization (DP_n) of the chains must be sufficiently high to have a certain number of groups. The M_n of the thermoplastics of **Network 3** was hence targeted to be around 500 kDa.

Due to its facile reaction conditions, its tolerance towards functional groups, the absence of reactive end-groups, and the possibility to obtain large molecular masses, free radical polymerization (FRP) was chosen as method to synthesize the TP. The main disadvantage of FRP is uncontrolled molecular weight distribution as a consequence of unavoidable fast radical-radical termination reactions. A typical $Đ$ of a FRP is around 2. In contrast to RDRP methods, such as RAFT or atom-transfer radical polymerization (ATRP), in FRP the M_n does not follow the conversion linearly. The resulting M_n is determined by the nature and concentration of the monomer(s), initiator and solvent, as well as the temperature. Therefore, it is of importance to evaluate the reaction conditions carefully. In order to do so, test polymerizations with nBA were conducted like depicted in Scheme 4.8. An overview over the conditions and results is given in Table 4.1. A relatively low reaction temperature was chosen to achieve long polymers. For all experiments, the $Đ$ is around 2, i.e., in the expected range. As can be seen especially in the experiments 3 and 4, from a certain point an increase of the ratio of $[M]_0/[I]_0$ does no longer lead to an increase of M_n of the resulting polymer. There seems to be a threshold regarding the M_n for the homopolymerization. However, 300-400 kDa seemed to be enough to have a sufficient amount of functional groups per chain for the crosslinking. It was thus decided to copolymerize **19** using the conditions from experiment 3.
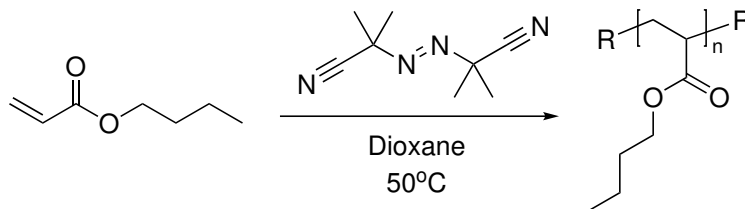
Scheme 4.8: Test polymerization of nBA via FRP.

Table 4.1: Overview over the test polymerizations to achieve a homopolymer of nBA with a target M_n of 500 kDa using FRP. $[M]_0$: initial monomer concentration, $[I]_0$: initial initiator concentration, $[S]$: solvent (S) concentration, t : reaction time.

Exp. No	$[M]_0/[I]_0$	nBA : S (v/v)	T [°C]	t [h]	M_n [kDa]	M_w [kDa]	$Đ$
1	5000/1	1 : 2	50	30	295	590	2.0
2	8000/1	1 : 2	50	80	259	516	2.0
3	10k/1	1 : 1	50	44	380	754	2.0
4	20k/1	1 : 1	50	48	370	760	2.1

The functional monomer **19** was copolymerized with *n*BA via FRP according to Scheme 4.9. The polymerization worked as well as the previous test polymerization. During the polymerizations thermoplastics (**P22**) with a M_n between 300-400 kDa and a Đ of 2.0-2.5 could be obtained at a monomer conversion of around 65 % (Table 4.2). The functional group could be well identified by ^{1}H NMR (compare Figure 4.1). The ratio of functional groups was around 0.5 %. However, their concentration was too low to quantify with accuracy their ratio in the polymer by integration.
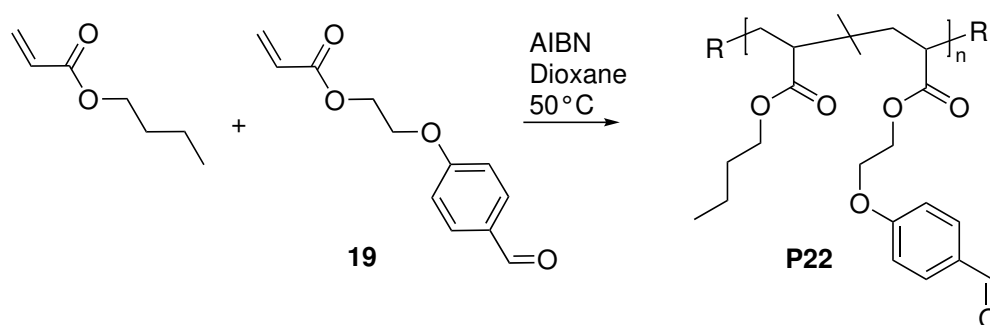
Scheme 4.9: Free radical copolymerization of *n*BA with the functional aldehyde monomer **19**.
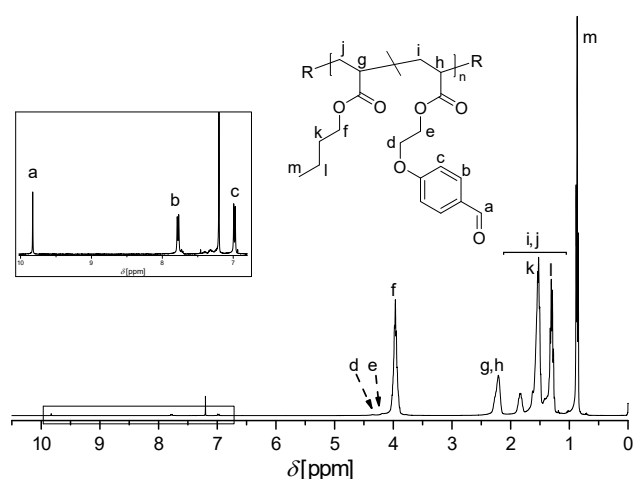
Figure 4.1: ^{1}H NMR spectrum in CDCl$_3$ at 400 MHz of copolymer **P22**.

4.5 Network 3a: M_n = 500 kDa, f = 0.5 %, ρ(CL) = 0.25 %

4.5.1 Crosslinking

The crosslinking of TP **P22** was conducted like shown in Scheme 4.10. The amount of crosslinker was calculated with the Equation 4.1, employing the average molecular mass of the monomers $M(M_{Av})$ calculated with Equation 4.2 using the molecular masses of *n*BA and the aldehyde functional monomer (**19**). The functionality of the polymer (f(P)) is 0.005 and the functionality of the crosslinker (N_f(CL)) is 2. m(P) is the mass of the employed thermoplastic. To reach a ρ(CL) of 0.25 %, 50 % of the 0.5 % functional groups have to be crosslinked (f_{CL}). The properties of the TP and the formed network are listed in Table 4.2. The precursor **P22** was diluted in THF (1 : 10 w/w) and the crosslinker **21** was added using a THF stock solution. The most part of the THF was evaporated at ambient conditions over 24-48 h, subsequently the solvent was removed under vacuum at 110 °C for 16 h. The sample rested then at ambient conditions. The crosslinking took place within 3-5 days and **Network 3a** was obtained as a stretchable film.
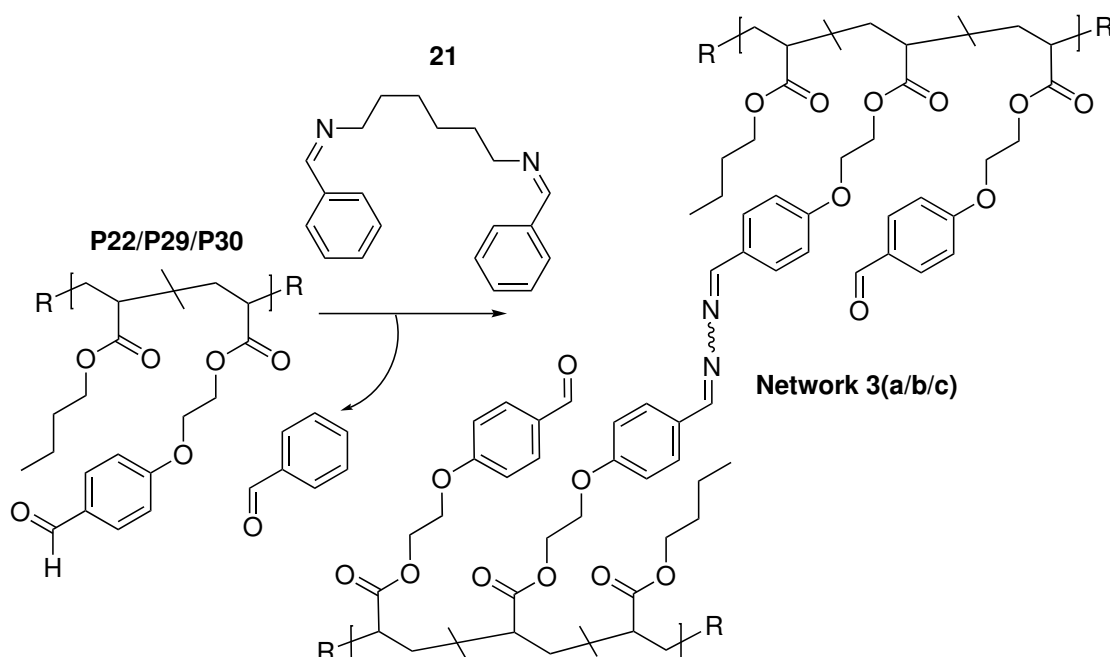
Scheme 4.10: Crosslinking of the aldehyde thermoplastic precursor **22** (or **P29**/**P30**) with the crosslinker **21** to **Network 3a** (or **3b/c**, refer to Sections 4.8 and 4.9).

$$n(CL) = \frac{f_{CL} \cdot m(P) \cdot f(P)}{N_f(CL) \cdot M(M_{Av})} \qquad (4.1)$$

$$M(M_{Av}) = f(P) \cdot M(19) + (1 - f(P)) \cdot M(nBA) \tag{4.2}$$

Table 4.2: Overview over the properties of TP **P22** and **Network 3a**. N_f(chain): number of functional groups per chain, f_{CL}: functional groups crosslinked, N_{CL}(chain): number of crosslinks per chain.

M_n[1] [kDa]	DP_n[1]	Đ	f [%]	N_f(chain)	f_{CL} [%]	N_{CL}(chain)	ρ(CL) [%]
400	3100	2.1	0.5	15.5	50	6.5	0.25

1: determined via SEC with a standard PS calibration.

4.5.2 Compression Molding

The material was processed via compression molding. Since the sample showed limited dynamic behavior during the crosslinking, long processing times were anticipated. After relatively short processing times (1-2 h), it was observed that the samples were inhomogeneous and started to shrink after removal from the mold. After pressing with 3 tons at 110 °C for 16 h, a transparent, homogenous, flexible elastomer was obtained as can be seen in Figure 4.2, left. After several days (approx. one to two weeks), the material visibly started to shrink and became inhomogeneous as can be seen in Figure 4.2, on the right side. This indicates that the material is not fully relaxed after the molding. It was attempted to press the samples at higher temperatures. After 16 h at 150 °C, the sample appeared slightly yellow compared to samples that were pressed during lower temperatures. 150 °C is already a too high temperature for compression molding, since the color change is a sign for degradation.

Figure 4.2: Pictures of **Network 3a**. Left: a sample directly after the processing. Right: a sample after two weeks at ambient conditions.

4.5.3 Swelling and Solubility Tests

A swelling test was performed on **Network 3a** to determine the swelling ratio as well as the insoluble fraction. After the compression molding, pieces with the mass m(dry) were cut out and immersed into THF for 24 h. Subsequently, the excess of solvent was removed and the mass of the swollen network (m(swollen)) was determined. Then, the samples were dried at 80 °C for 24 h and the polymer pieces were weighted again (m(dried)). The results are listed in Table 4.3. The swelling ratio and the insoluble fraction were calculated with Equations 4.3 and 4.4, respectively. The low soluble fraction of 5.5 ± 1.4 % indicates that almost all chains are included in the network.

$$\text{Swelling ratio} = \frac{m(\text{swollen}) - m(\text{dried})}{m(\text{dried})} \tag{4.3}$$

$$\text{Insoluble fraction} = \frac{m(\text{dried})}{m(\text{dry})} \tag{4.4}$$

Table 4.3: Results of swelling test of **Network 3a** in THF.

Sample	m(dry) [mg]	m(swollen) [mg]	m(dried) [mg]	Swelling ratio	Insoluble fraction [%]
1	254.3	3572	237.9	13.8	93.6
2	409.0	4467	392.9	10.4	96.1
3	250.9	3480	235.3	13.8	93.8
Average				12.7± 2.0	94.5± 1.4

4.5.4 Thermal Characterization

4.5.4.1 TGA

Ramp

The TGA of the TP **P22** and the crosslinked **Network 3a** are depicted in Figure 4.3, top. Both curves have been recorded under ambient atmosphere. The samples show stability (below 2% loss of mass) up to 263 °C and 240 °C, respectively.

Isothermal Treatment

To evaluate the long term thermal stability of **Network 3a**, an isothermal treatment was conducted at 200 °C under nitrogen atmosphere. The results can be seen in Figure 4.3, bottom. It shows that after the initial drop, no significant mass loss took place. The sample shows good stability at elevated temperatures. The thermoplastic precursor was tested as well. In Figure 4.3, bottom left, the TGA isothermal at 200 °C is displayed. After the initial drop, no further mass loss can be detected. After the TGA, the polymer was still well soluble in THF, however when the SEC curve of the TP after the heating was compared to the pristine thermoplastic (Figure 4.4), it was observed that the Đ increased as well as M_n. This is likely a sign of intermolecular reactions between the polymer chains. At 200 °C, these reactions might be either due to the functional side-groups or to the backbone of the polymer. However, no significant shoulders were observed by SEC and the sample was still well soluble. This indicates that these reactions took place in a limited amount.
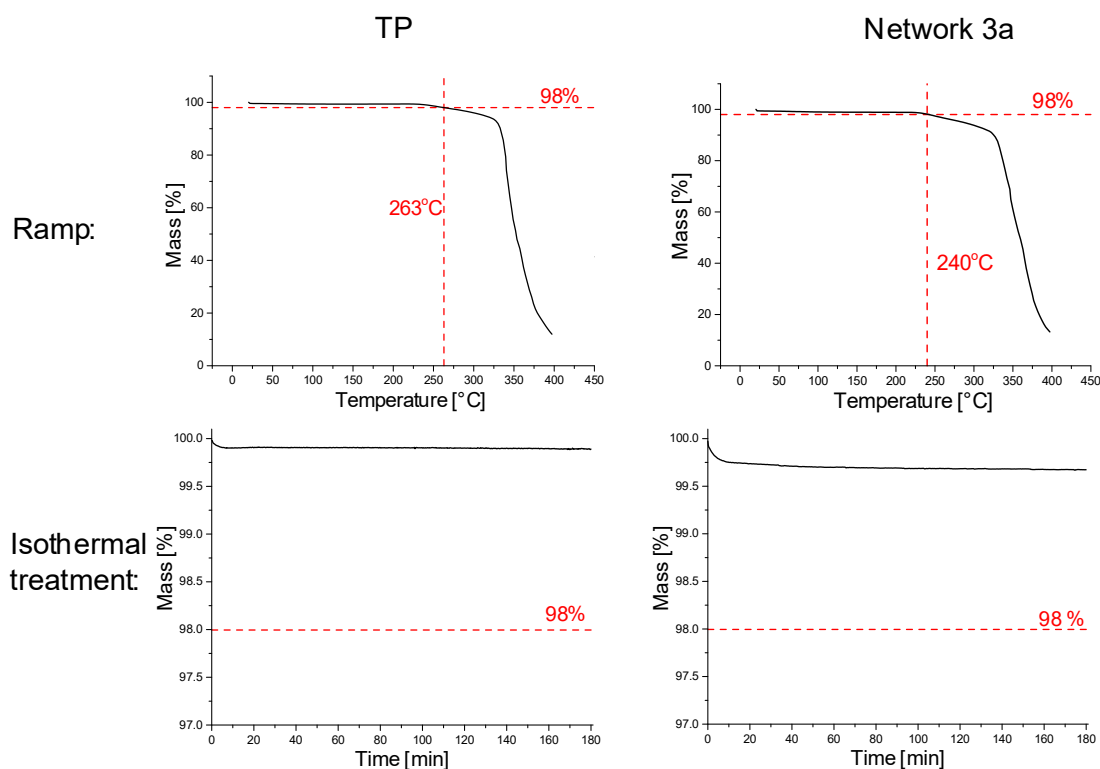
Figure 4.3: TGA results of TP **P22** (left) and **Network 3a** (right). Top: temperature ramp from 30-400 °C under ambient conditions. Bottom: isothermal treatment at 200 °C during 3 h under nitrogen atmosphere.
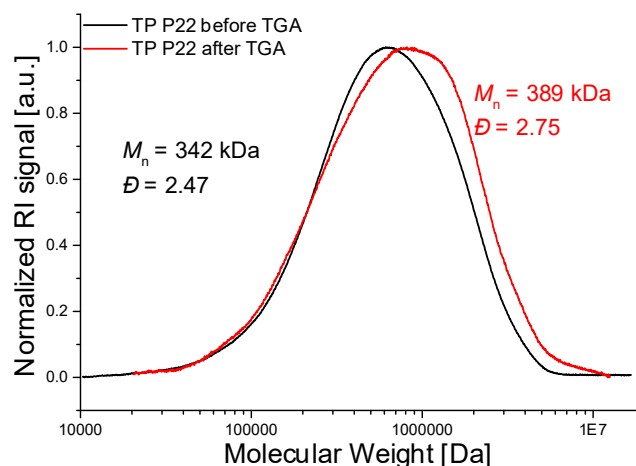
Figure 4.4: SEC traces in THF (PS calibration) of TP **P22** before and after the TGA.

4.5.4.2 DSC

Figure 4.5 presents the DSC analysis of **Network 3a**. The T_g of **Network 3a** was found to be -46.7 °C. No other transition than the glass transition could be observed.
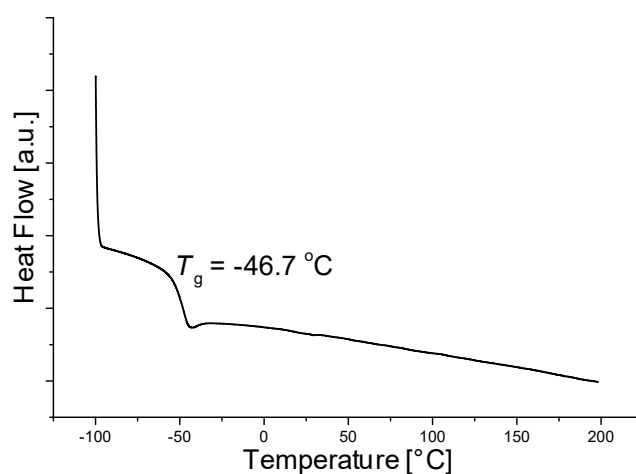
Figure 4.5: DSC analysis of **Network 3a**, second heating cycle.

4.5.4.3 DMA

In Figure 4.6 the DMA results of **Network 3a** are displayed. Before the T_g, the sample shows a plateau at 1620 MPa. The T_g was determined at the maximum of E" and was

located at -35 °C. After the glass transition, E' decreases and reaches a plateau around 150 kPa at 150 °C. There is no steep drop in the modulus with increasing temperature, likely indicating that the network structure is maintained during the measured temperature range. The absence of rubber elasticity (an increase of the modulus with temperature due to entropic effects) is probably due to the low crosslinking density.
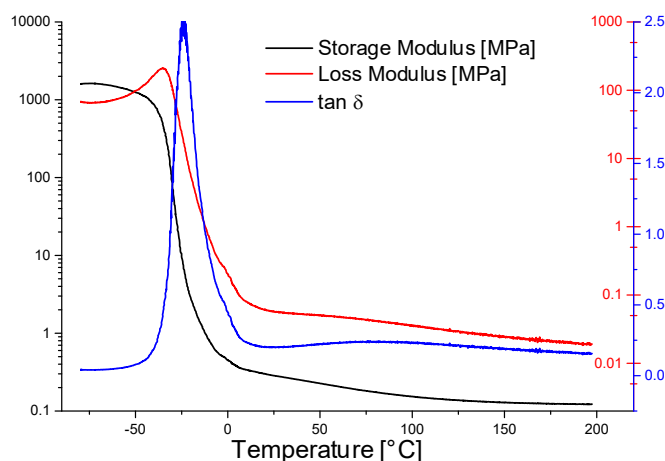
Figure 4.6: DMA of **Network 3a**.

4.5.5 Stress Relaxation

Stress relaxation was performed on **Network 3a**. The sample was subjected to 1 % strain at 110 °C for 24 h. The result is shown in Figure 4.7. As can be seen, the sample relaxed stress in only very limited amounts before it reached a plateau. The network was not able to relax stress under these conditions.
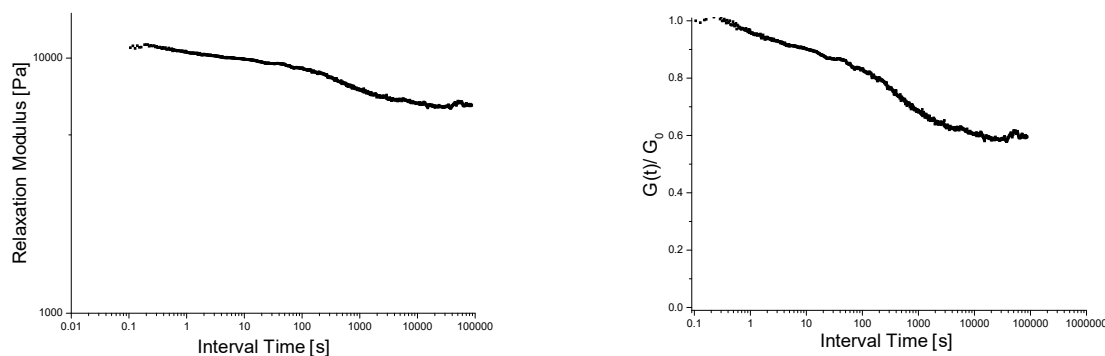
Figure 4.7: Left: stress relaxation of **Network 3a** at 110 °C for 24 h. Right: normalized to G_0.

4.5.6 Creep

Creep experiments confirmed these results. First an amplitude sweep was conducted for **Network 3a** (Figure 4.8, left) at 50 °C. The sample showed linear behavior in the measured spectrum (0.01-10 %). For the creep experiments a shear stress of 500 Pa was chosen, which corresponds to a strain of 5 %. The sample was subjected to the stress for 10 h at 110 °C, subsequently it recovered at 0 stress for another 10 h at the same temperature. As can be seen in Figure 4.8, right, the sample creeps only in very limited amounts. After 10 h of recovery, the remaining stain is at 0.6 %, indicating an overall elastic behavior of the sample.
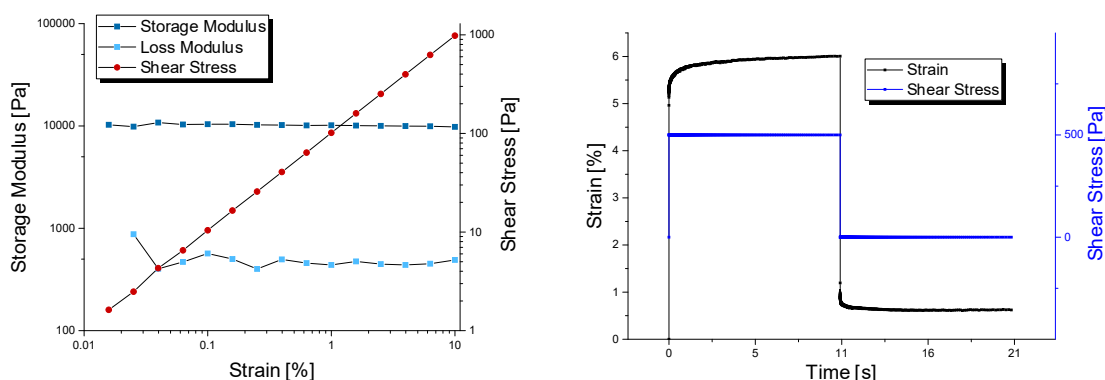
Figure 4.8: Left: strain sweep of **Network 3a** at 50 °C. Right: creep/recovery experiment of **Network 3a** at 110 °C.

4.5.7 Conclusion

A TP for the imine-aldehyde network featuring a M_n of 300-400 kDa and a functionality of 0.5 % was prepared via FRP. This TP was crosslinked to obtain a network with a crosslinking density of 0.25 %. The polymer was compression molded to obtain a flexible material with a T_g around -48 °C. The network showed good integrity when immersed into THF during 24 h, indicating the ρ(CL) is high enough to integrate almost all the chains into the network. DMA showed that the network structure is maintained up to high temperature. The sample showed thermal stability up to 240°C and long term stability at 200°C. The aim was that the network shows no or very slow dynamics at ambient conditions, but is still well processable at elevated temperatures. The slow dynamics showed during the crosslinking reaction, which took place during several days. To process the sample, long processing times at 110°C were necessary to obtain a homogenous

material, since an increase of the processing temperature led to a color change of the sample (likely reflecting degradation). The sample showed shriveling with time after the processing, a sign that the sample did not reach a relaxed state during the compression molding. Stress relaxation confirmed this hypothesis. At 110 °C, the sample hardly relaxes stress. Creep experiments confirmed that the sample exhibits almost full elasticity at 110 °C. These results lead to the conclusion that the sample has to be adapted to fulfill the requirement of processability at high temperatures. This can be achieved by two different ways: One possibility would be to lower the M_n of the chains to present fewer entanglements. However, the drawback here would be to risk that a significant number of chains are not connected to the network anymore due to the low ρ(CL). Another possibility would be to increase the number of free functional groups. In this way, more exchange partners are available and the exchange reactions are kinetically more likely to occur.

4.6 TP 500 kDa, 2.0 % Functionality

It was concluded that **Network 3** in its current form is not dynamic enough. The exchange of the functional groups is too slow to guarantee an efficient processing. It was therefore decided to raise the number of functional groups from 0.5 % to 2.0 % in the system, while maintaining a high M_n. In addition, it would be beneficial to synthesize the TP in a controlled manner via RDRP to obtain a polymer with a tunable M_n. Furthermore, it would be desirable to drive the polymerizations to high conversions to avoid a waste of functional monomer, which becomes more significant, now that the ratio of functional monomer is to be increased.

4.6.1 RAFT Polymerization

It was first tried to synthesize the TP via RAFT polymerization according to Scheme 4.11. CPDT was employed as a CTA with AIBN as initiator and 1,4-dioxane as solvent. The ratio of $[n\text{BA}]_0 : [\textbf{19}]_0 : [\text{CPDT}]_0 : [\text{AIBN}]_0$ was set to 5,000 : 100 : 1 : 0.3, with 1 : 1 (v/v) 1,4-dioxane : nBA. Figure 4.9 shows the development of the molecular weight of **P23** with the polymerization time. It was aimed to obtain a M_n of around 500 kDa. As can be seen, the M_n grows only slowly with time. This is due to the low concentration of AIBN in the mixture. RAFT polymerization in this form is not suitable to synthesize polymers with a M_n as high as targeted. The limitations of RAFT in regards of maximal achievable

molecular weight are well known.[31] Excellent results can be only achieved in a range of an M_n of 1000-100,000 Da. Above this value, more elaborate reaction conditions are often necessary.
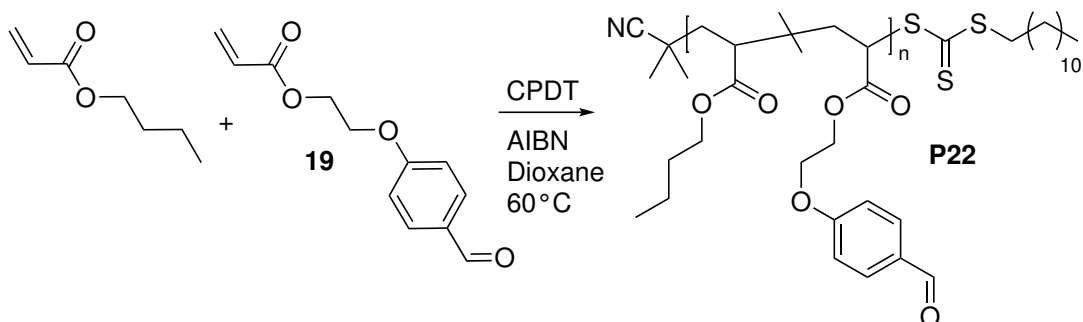
Scheme 4.11: RAFT copolymerization of *n*BA with **19**.
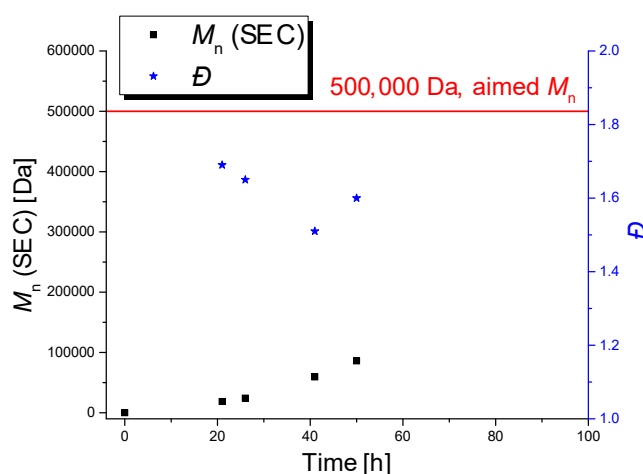
Figure 4.9: Development of the M_n during the RAFT copolymerization with an attempted M_n of 500 kDa of **19** with *n*BA ([*n*BA]$_0$: [**19**]$_0$: [CTA]$_0$: [AIBN]$_0$ = 5,000 : 100 : 1 : 0.3 with 1 : 1 (v/v) 1,4-dioxane : *n*BA at 60 °C) with the polymerization time.

4.6.2 ATRP

An alternative RDRP method is ATRP. The polymerization takes place by the activation of alkyl halides to a radical via atom transfer and oxidation of a Cu^I complex to a Cu^{II} species. The activated growing chain adds monomer units until it is deactivated by the Cu^{II} complex, which is reduced to Cu^I again. In this process, it can come to a loss of chain-end

functionality that leads to a irreversible transformation of Cu^{I} to Cu^{II}. In polymerizations operating with a low concentration of catalyst this might lead to an insufficient amount of Cu^{I} complexes to continue the polymerization. Systems have been developed to reverse this unwanted permanent deactivation by continuous reactivation of the Cu complex. One of them is the addition of zero-valent metals, most commonly Cu^{0}.[32] It acts as a reducing agent for the Cu^{II} as well as an supplemental activator for the alkyl halides (although only in limited amounts).[33–35] This process is hence named activators regenerated by electron transfer (ARGET) ATRP. Adding elemental copper has the advantage of having a relatively simple experimental setup due to the heterogeneous nature of the system. The experimental setup was tested for the homopolymerization of *n*BA. The polymerization was conducted in dimethyl sulfoxide (DMSO) with methyl 2-bromopropionate (MBP) as the initiator and tris[2-(dimethylamino)ethyl]amine (Me$_6$TREN) as the ligand like shown in Scheme 4.12. The ratio was set to $[nBA]_0 : [CuBr_2]_0 : [Me_6TREN]_0 : [MBP]_0 = 6{,}000 : 0.1 : 0.2 : 1$, with 1 : 1 (v/v) DMSO : *n*BA. Elemental copper was added in form of a copper wire wrapped around the stirring bar.
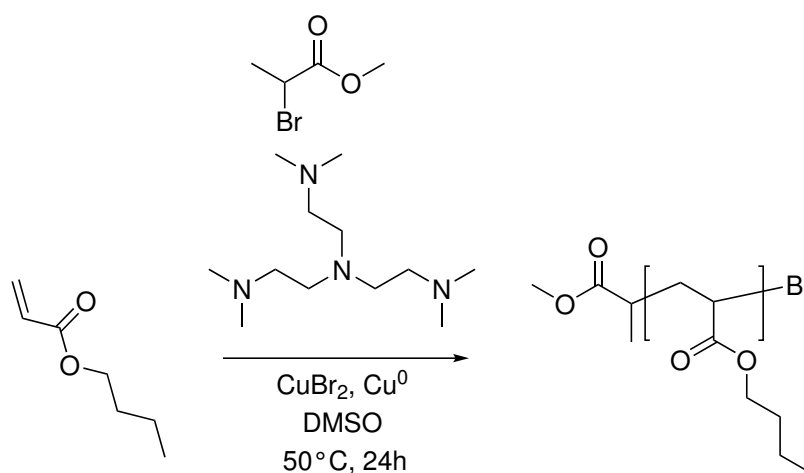
Scheme 4.12: ARGET ATRP homopolymerization of *n*BA.

The polymerization was followed kinetically via SEC and NMR. The development of the M_n and $Đ$ with time is displayed in Figure 4.10. As can be seen a high M_n is obtained very quickly. After 6 h the polymerization has reached a conversion of 71 % and the aimed M_n of 500 kDa is almost reached. After 24 h the conversion is 79 % and the aimed M_n already surpassed. At 24 h an increase of $Đ$ can be observed, indicating that the polymerization should be stopped earlier. After purification, the polymer was obtained with $M_n = 568$ kDa, $Đ = 1.34$ and a overall yield by weight of 60 %. The applied conditions seemed to be very well suited for the aimed TP for **Network 3**.
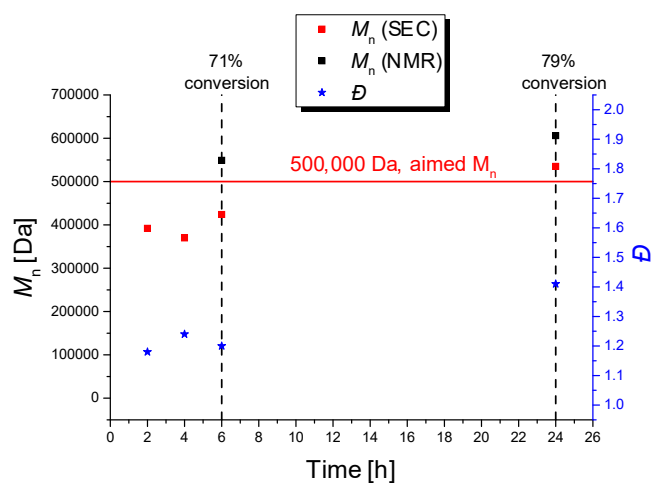
Figure 4.10: Development of the molecular weight with the polymerization time during the ARGET ATRP homopolymerization of *n*BA.

However, when the aldehyde monomer **19** was added ([*n*BA]$_0$: [**19**]$_0$: [CuBr$_2$]$_0$: [Me$_6$TREN]$_0$: [MBP] = 6,000 : 123 : 0.1 : 0.2 : 1, with 1 : 1 (v/v) DMSO : *n*BA) and the polymerization was conducted like depicted in Scheme 4.13, either no polymerization took place or the product **P24** was obtained as an insoluble crosslinked material. Several attempts with different batches of monomer were performed and all yielded similar results.
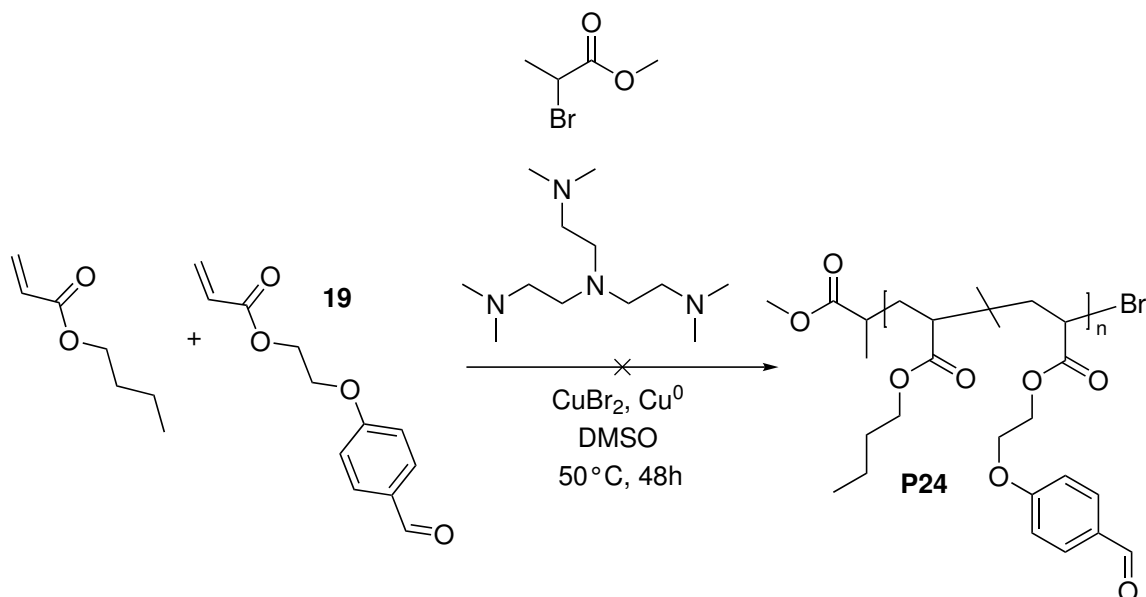
Scheme 4.13: Attempted ARGET ATRP copolymerization of **19** with *n*BA to obtain **P24**.

The copolymer could not be obtained with ATRP under these conditions. Since homopolymerizations with *n*BA worked without a problem, the cause of this issue stems most likely from the functional monomer.

4.6.3 Free Radical Polymerization

The polymerization was repeated changing back to FRP like shown in Scheme 4.9. This technique gave reliable results when synthesizing the TP **P22** with 0.5 % functionality. However, when the functional monomer ratio was increased to 2.0 %, and the polymerization was conducted with the ratios $[nBA]_0 : [19]_0 : [AIBN]_0 = 10,000 : 204 : 1$, with 1 : 1 (v/v) dioxane : *n*BA at 50 °C, it came repeatedly to crosslinking.

4.6.4 Acetal Protection of the Aldehyde Monomer

To avoid crosslinking caused by the functional monomer, it was tried to protect the aldehyde monomer **19** with an acetal group. In order to do so, the aldehyde group was reacted with a diol in presence of an acid. In a first try, the monomer, 1,3-propandiol and TsOH were mixed in DCM. $MgSO_4$ was added to remove water from the reaction equilibrium. However, the 1,3-propanediol reacted with the salt and formed a hard white solid. In a second attempt, the monomer was heated with 1,3-propandiol in the presence of TsOH under constant removal of water with a Dean-Stark apparatus like displayed in Scheme 4.14.
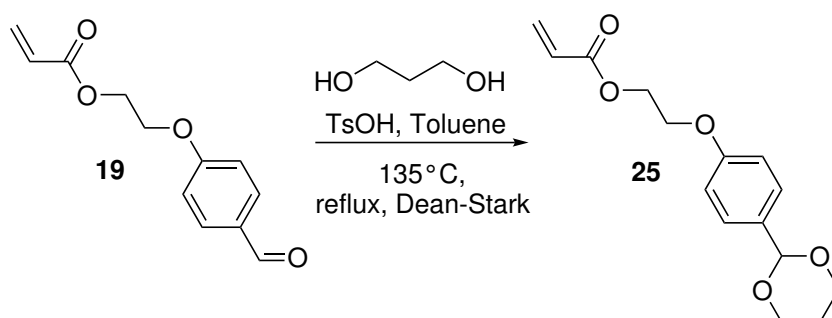
Scheme 4.14: Acetal protection of the aldehyde monomer using 1,3-propandiol under Dean-Stark conditions to obtain monomer **25**.

However, after (basic) aqueous work-up to remove the residual propandiol and the acid, next to the product **25** there were still some unidentified impurities in the NMR spectrum.

This can be explained by the heating to high temperatures during the reaction. In addition, there is still unreacted aldehyde in the mixture, although in not very significant amounts (Figure 4.11).
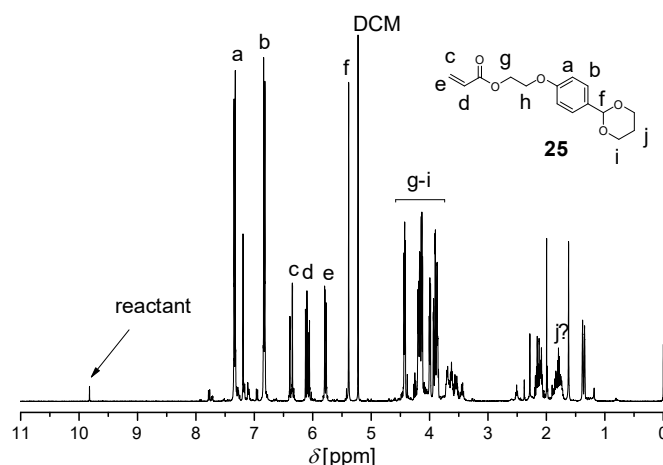
Figure 4.11: ^{1}H NMR spectrum in CDCl$_3$ at 400 mHz of the acetal protected aldehyde monomer **25** after the reaction with 1,3-propanol under Dean-Stark conditions.

It was attempted to use ethylene glycol instead of 1,3-propanediol to obtain compound **26**. The Dean-Stark method was used like shown in Scheme 4.15. However, after 7 h only 33 % of the aldehyde monomer reacted. After the work up, there were still large amounts of ethylene glycol in the mixture, as well as some unidentified impurities (Figure 4.12).
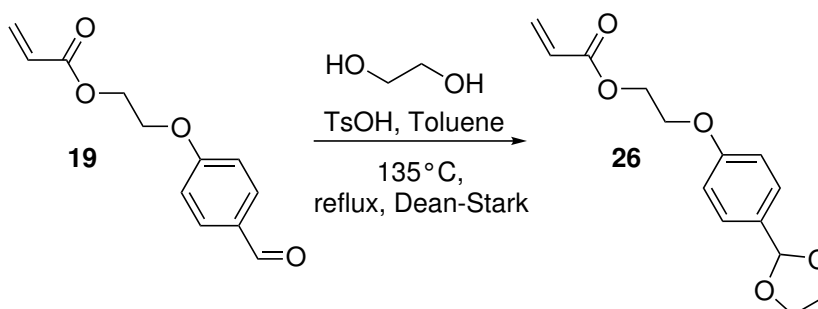
Scheme 4.15: Acetal protection of the aldehyde monomer **19** using ethylene glycol under Dean-Stark conditions to obtain monomer **26**.
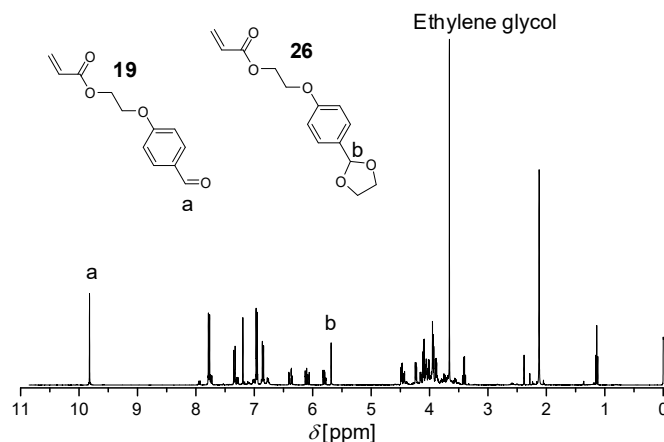
Figure 4.12: ^{1}H NMR spectrum in CDCl$_3$ at 400 mHz of the mix after the reaction of **19** with ethylene glycol under Dean-Stark conditions.

The reaction was repeated at room temperature using molecular sieves as drying agents, like displayed in Scheme 4.16. After the work up, the NMR revealed that also only 30 % of the aldehyde monomer **19** reacted and there was still a large amount of ethylene glycol in the mixture. Besides the product **26** and the starting materials, no impurities could be detected (see Figure 4.13). Under milder conditions, no side-reactions seemed to take place. Since the second attempt (Scheme 4.14) led to the desired product **25** (even if not pure), it was used to retry the ATRP, like displayed in Scheme 4.17. After the polymerization, the polymer **P27** was still soluble and could be precipitated in MeOH/H$_2$O. However, after the polymer was dried under vacuum over night, the material showed to be crosslinked.
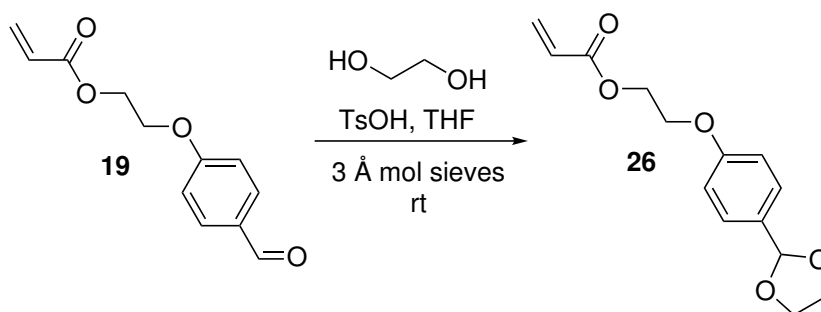
Scheme 4.16: Acetal protection of the aldehyde monomer **26** using ethylene glycol with molecular sieves.
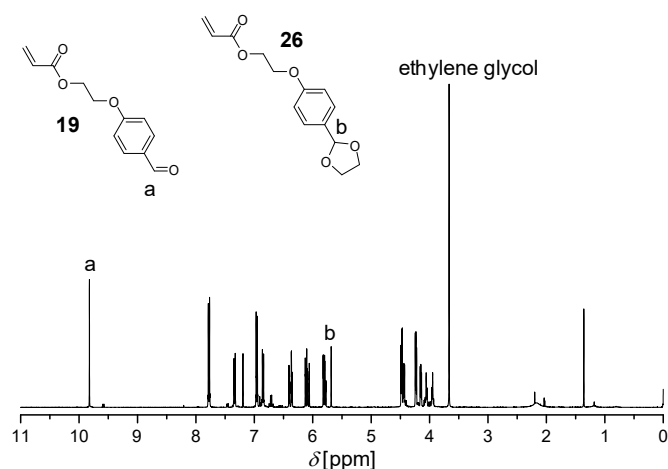
Figure 4.13: ^{1}H NMR spectrum in CDCl$_3$ at 400 mHz of the aldehyde monomer **26** after the reaction with ethylene glycol with molecular sieves.
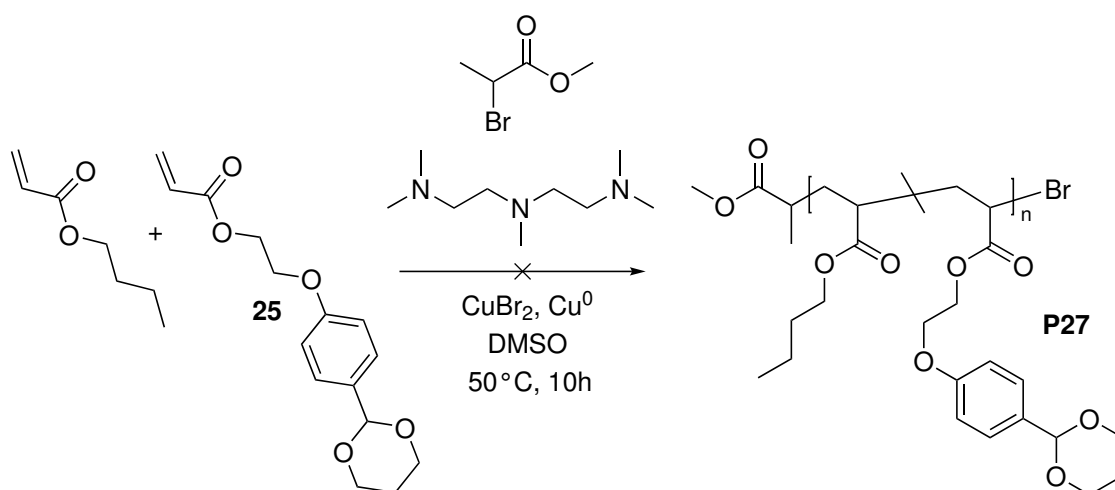
Scheme 4.17: ATRP of the acetal protected aldehyde monomer **25** with *n*BA.

4.6.5 Conclusion

It was tried to synthesize a TP with a M_n of 500 kDa and a functionality of 2.0 %. Several polymerization techniques, such as RAFT polymerization, ATRP and FRP, with various conditions were utilized to reach that goal. However, it came to unwanted crosslinking of the material. Presumably, this is due to the tendency of the functional monomer to undergo side reactions with other polymer chains. The probability of such a side reaction

is in general low, but with an increasing amount of functional monomer per chain and increasing chain length statistically more likely to take place. A protection of the functional monomer was also not successful, since the final polymer also showed crosslinking. One solution to avoid this problem would be to shorten the attempted chain length. This possibility was not envisioned before, since there was the concern that the functional group density would be too low to incorporate all of the chains into the network. The number of functionalities is now increased by four, a shortening of the chains can thus be attempted.

4.7 TP 100 kDa, 2.0 % Functionality

Since it came to unwanted crosslinking during the ATRP and the FRP of the aldehyde monomer with *n*BA, the copolymerization was revised. An idea to avoid crosslinking is to reduce the aimed molecular mass.

4.7.1 Free Radical Polymerization

Another FRP was conducted: The initiator concentration was increased as well as the polymerization temperature. Instead of a ratio of $[nBA]_0 : [\mathbf{19}]_0 : [AIBN]_0 = 10{,}000 : 204 : 1$, with 1 : 1 (v/v) dioxane : *n*BA at 50 °C, the polymerization was conducted with a ratio of 2,500 : 51 : 1 at 65 °C like depicted in Scheme 4.18. The reaction was followed via NMR and SEC over the course of 4 h. The conversion, M_n (SEC) and $Đ$ are visualized in Figure 4.14 (left). The SEC traces can be found in Figure 4.14, right. With increasing conversion, $Đ$ becomes larger. After 2 h, a trimodality manifests that becomes more pronounced with increasing conversion.
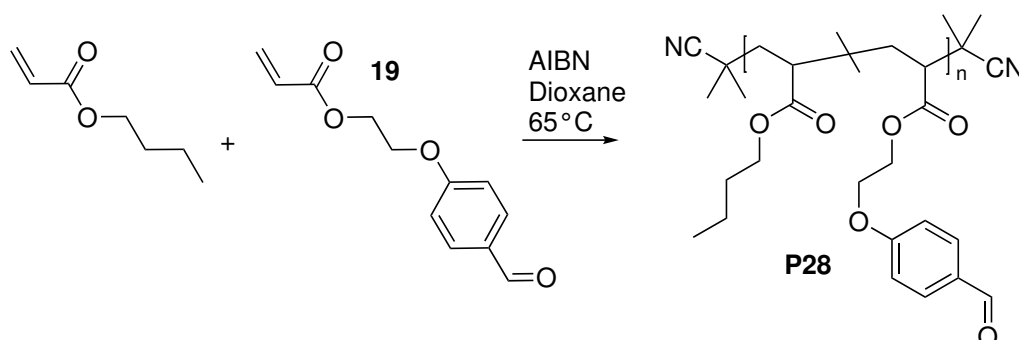
Scheme 4.18: FRP of the aldehyde monomer with *n*BA to yield copolymer **P28**.
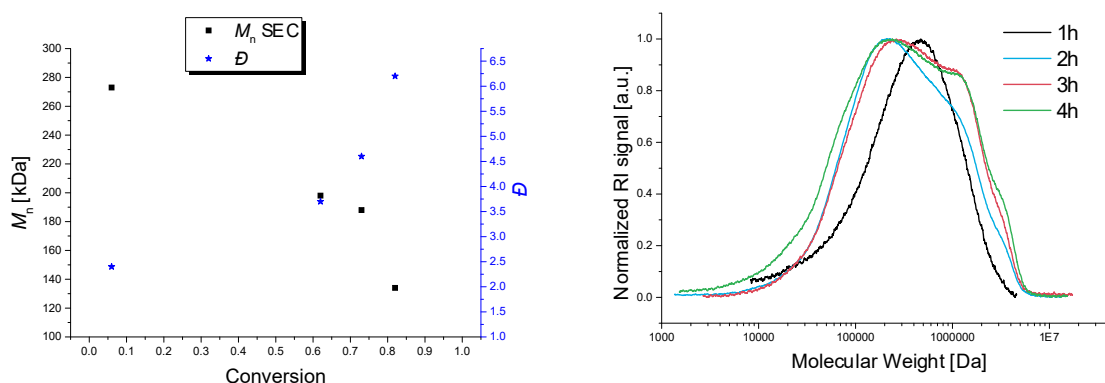
Figure 4.14: Kinetic study of a FRP with $[n\text{BA}]_0 : [\mathbf{19}]_0 : [\text{AIBN}]_0 = 2{,}500 : 51 : 1$, with 1 : 1 (v/v) dioxane : nBA at 65 °C. Left: Development of M_n and $Đ$ with increasing conversion. Right: SEC traces in THF (PS calibration) after 1, 2, 3 and 4 h.

It was tried to reduce the radical concentration by lowering the polymerization temperature to 60 °C and doubling the amount of solvent. As can be seen in Figure 4.15, there is an inhibition period of 2 h before the polymerization starts. After that, the polymerization shows the typical $Đ$ of FRPs (see Figure 4.15). After 6 h, the conversion did not increase significantly anymore and the reaction was terminated. The $Đ$ goes up towards the end of the reaction, but the final SEC curve (Figure 4.15, right, red curve) is monomodal and shows no significant shoulders. Proceeding this way could be a strategy to obtain the desired thermoplastic. However, it showed that already after 50 % conversion the polymerization slows down and the $Đ$ is increasing. Stopping the polymerization at this point would lead to a significant loss of starting material.
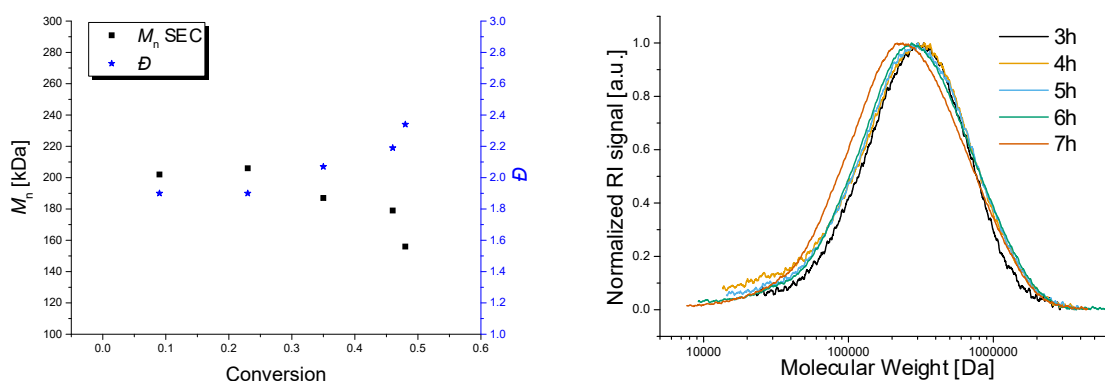
Figure 4.15: Kinetic study of a FRP with $[n\text{BA}]_0 : [\mathbf{19}]_0 : [\text{AIBN}]_0 = 2{,}500 : 51 : 1$, with 2 : 1 (v/v) dioxane : nBA at 60 °C. Left: Development of the M_n and $Đ$ with increasing conversion. Right: SEC traces in THF (PS calibration) after 3, 4, 5, 6 and 7 h.

194

4.7.2 RAFT Polymerization

An alternative to FRP would be to synthesize the thermoplastics via RAFT polymerization. This method represents a feasible option now, since chains with a lower molecular weight are targeted. In this way, the polymerization could also be driven to higher yields, which would avoid the waste of functional monomer. In addition, the polymer could be obtained with low $Đ$ and tunable M_n. The disadvantage of RAFT polymerization is that the obtained polymers have reactive and colorful end-groups. An efficient procedure was already established polymerizing nBA with the acetal functional monomer **4** (see Chapter 2.3.1).

Similar conditions were applied to the aldehyde system, like shown in Scheme 4.19. The ratio of the compounds was set to $[n\text{BA}]_0 : [\textbf{19}]_0 : [\text{CTA}]_0 : [\text{I}]_0 = 1000 : 21 : 1 : 0.2$, with 1 : 1 (v/v) dioxane : nBA. The kinetics of the reaction did not differ significantly from the one described in Chapter 2.3.1, since the aimed conversion of about 80 % was achieved after 16-24 h. The NMR spectrum and the SEC trace of a representative polymer (**P29**) can be found in Figure 4.16 and Figure 4.17, respectively. The SEC curve shows a slight shoulder towards higher molecular weights. The $Đ$s for this polymerization were typically around 1.3-1.6, somewhat higher than the $Đ$s obtained for the copolymerization of the acetal protected acrylate monomer. This can be explained by the proneness of the aldehyde monomer to cause branching/crosslinking. However, the SEC curve showed no apparent crosslinking or bimodality. It can be assumed that there was only limited branching.
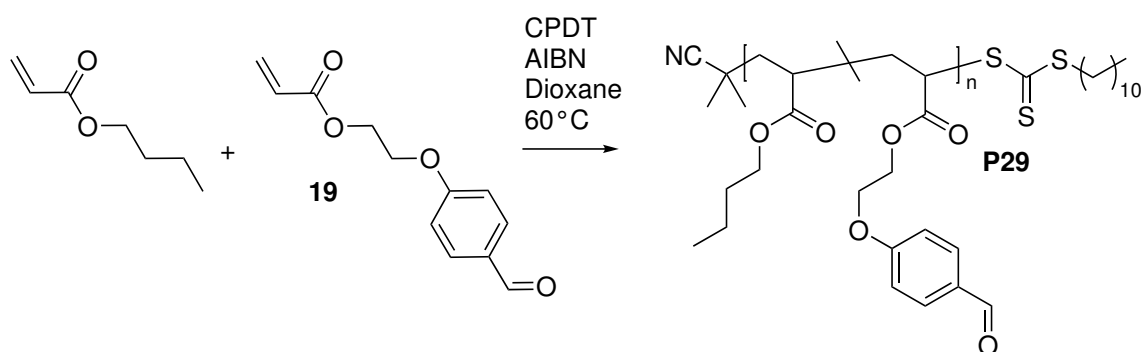
Scheme 4.19: RAFT copolymerization of the aldehyde monomer **19** with nBA to yield thermoplastic **P29**.
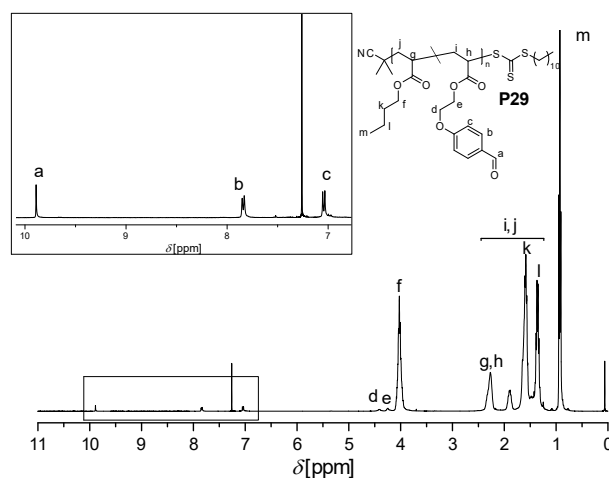
Figure 4.16: ^{1}H NMR spectrum in CDCl$_3$ at 400 mHz of the polymer **P29** after the RAFT copolymerization of the aldehyde monomer **19** with *n*BA.
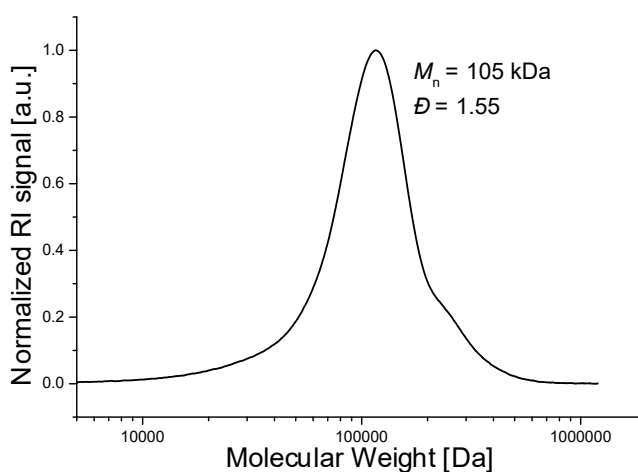
Figure 4.17: SEC trace in THF (PS calibration) of **P29**.

4.8 Network 3b: M_n = 100 kDa, f = 2.0 %, ρ(CL) = 0.25 %

4.8.1 Crosslinking

The crosslinking density of this imine-aldehyde network should resemble the one of the previous **Network 3a** (0.5 % functionality, 50 % crosslinked, ρ(CL): 0.25 %). To get the same crosslinking density in a system with 2 % functionality, 12.5 % of the

functional groups have to be crosslinked (f_{CL}). The crosslinking takes place by adding the bis(imine) crosslinker, like displayed in Scheme 4.10. The amount of crosslinker n(CL) was calculated employing Equation 4.5, with the functionality of the polymer f(P) = 0.02. m(P) is the mass of the polymer, N_f(CL) is the functionality of the crosslinker (2) and M(M_{Av}) is the average molecular mass of the monomers (see Equation 4.2).

$$n(CL) = \frac{f_{CL} \cdot m(P) \cdot f(P)}{N_f(CL) \cdot M(M_{Av})} \tag{4.5}$$

The TP **P29** was dissolved in THF (1 : 3 w/w) and the respective amount of bis(imine) crosslinker in THF stock solution was added. The mixture was stirred and the solvent slowly evaporated. After 72 h, the sample was cured under vacuum for 16 h at 80 °C. The **Network 3b** was obtained as a sticky film after another 72 h at ambient conditions (see Figure 4.18). The properties of the TP **P29** and the resulting **Network 3b** are listed in Table 4.4.

Table 4.4: Overview over the properties of TP **P30** and **Network 3b**. N_f(chain): number of functional groups per chain, f_{CL}: functional groups crosslinked, N_{CL}(chain): number of crosslinks per chain.

$M_n{}^1$ [kDa]	$DP_n{}^1$	Đ	f(P) [%]	N_f(chain)	f_{CL} [%]	N_{CL}(chain)	ρ(CL) [%]
90	690	1.3	2.0	13.8	12.5	1.7	0.25

1: determined via SEC with a standard PS calibration.

4.8.2 Compression Molding

The material was pressed at 110 °C for 6 h with a pressure equivalent to 3 tons. The material was obtained as a sticky, soft, transparent disk (see Figure 4.19). To see, if the sample was stable it was observed for 4 weeks. After this time, the sample showed no apparent optical changes (compare Figure 4.19, left and right). A shriveling like observed with **Network 3a** did not take place. The **Network 3b** exhibits thus a better processability than **Network 3a**.

Figure 4.18: Picture of **Network 3b** after curing, before the compression molding.
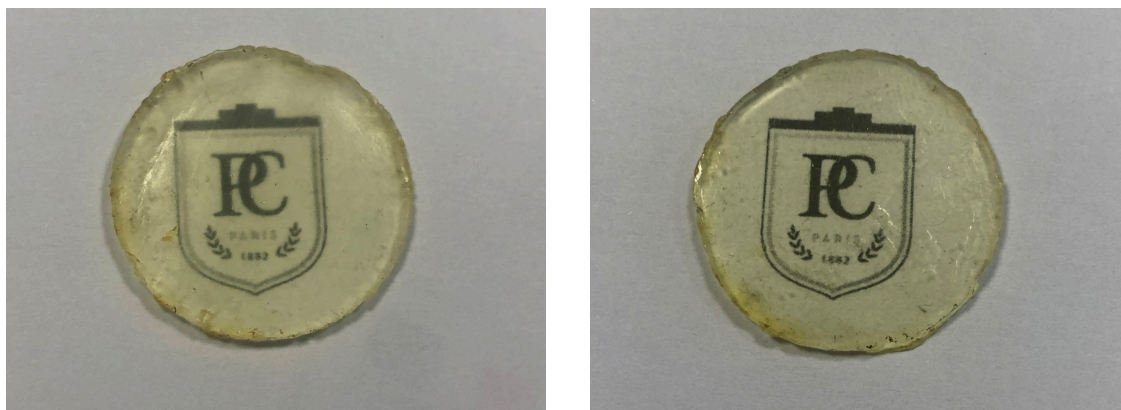
Figure 4.19: Pictures of **Network 3b**. Left: Just after compression molding. Right: The same sample, 4 weeks later. The sample showed good stability with time.

4.8.3 RAFT End-Group Removal

Since the network showed promising properties, a procedure was elaborated to remove the RAFT end-groups of the TP. This has the advantage to get rid of the yellow color and to avoid possible side reactions including the reactive trithiocarbonates. The established procedure using aminolysis has the disadvantage that the amines that are used to cleave the RAFT end-groups might also react with the aldehyde functional groups to form imines. Therefore, an additional step was added to the procedure like shown in Scheme 4.20: After the RAFT end-group was removed and the *n*BA reacted in a thiol-Michael reaction, HCl is added to the mixture to cleave possible imines. In the end, the polymer is purified by precipitation in MeOH and H_2O.
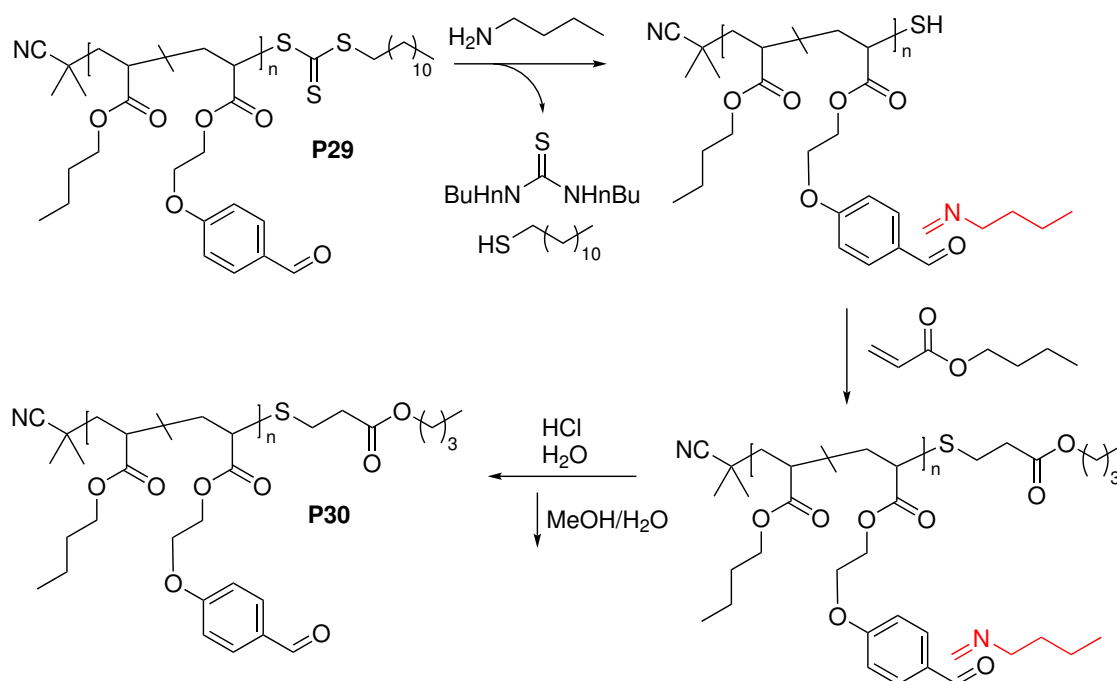
Scheme 4.20: RAFT end-group removal of the aldehyde thermoplastic **P29**. In a first step, n-butylamine is added to cleave the trithiol. In a second step, *n*BA reacts in a thiol-Michael addition with the resulting thiol. In the final step, an acid is added to cleave potentially formed imines. The polymer **P30** is purified by precipitation in MeOH and H_2O.

The polymer **P30** was obtained colorless and in the NMR spectrum no traces of imine formation could be found. The colorless thermoplastic was crosslinked like before (refer to Scheme 4.10). The thermoplastic was dissolved in THF and the crosslinker was added in a diluted THF stock solution. Both solutions were homogenous. After the crosslinker was added to the polymer solution, the mixture became heterogeneous and a phase separation occurred. During the curing under vacuum at elevated temperatures, the sample turned yellow. After several curing attempts, the sample showed still the properties of a thermoplastic (sticky liquid, dissolved easily in acetone). A crosslinking did not take place. The applied crosslinking procedure showed previously to be effective, using the thermoplastic before the removal of the RAFT end-group. A possible explanation could be the presence of residual traces of acid in the mixture (coming from the end-group removal, see Scheme 4.20). Acid would prevent the imine formation and in consequence crosslinking. The RAFT end-group removal was therefore revised and a neutralization step added. After the first purification, NEt_3 was added to the dissolved polymer to neutralize the remaining hydrochloric acid. After the mixture showed neutral to slightly

basic pH, the polymer was again precipitated twice into MeOH/H$_2$O. While drying, a white solid formed in the polymer. It could be filtered off. Presumably, it was triethylammonium chloride that was formed during the neutralization. The crosslinking was reattempted. This time, the reaction mixture crosslinked. To facilitate the route of synthesis for the TP, an alternative RAFT end-group removal procedure was developed to avoid the employment of acid and hence the salt removal. First, water is added to avoid imine formation. In addition to that, possibly formed imines on the polymer backbone are retransformed to aldehydes by adding a large excess of benzaldehyde like shown in Scheme 4.21. The benzaldehyde functions as a competitive molecule and engages in transiminations. After the work up, no traces of imine groups could be detected in the NMR spectrum of the purified TP. The integration of the respective peaks in the NMR confirmed a constant amount of aldehyde groups in the polymer.

Scheme 4.21: RAFT end-group removal of the aldehyde thermoplastic **P29** avoiding the use of acid. Water is added to shift the equilibrium to the amine side. In addition, after the reaction, an excess of benzaldehyde is added. The benzaldehyde can exchange with possibly formed imines.

The sample was crosslinked like shown in Scheme 4.10. Crosslinking took place slowly, the sample was dried under vacuum several times. After three weeks the sample was

processed. The resulting disks of this sample had obviously different properties than the one obtained without the RAFT end-group removal, such as increased stickiness. To investigate if the RAFT end-group or its removal have any influence on the crosslinking efficiency, a polymer was prepared of which half was crosslinked with the RAFT end-group, and the other half was subjected to RAFT end-group removal, before crosslinking. All samples and their properties are compared in Table 4.5 below.

Table 4.5: Overview over the imine-aldehyde **Networks 3b** synthesized with ρ(CL) = 0.25% with and without RAFT end-groups. f: functionality, N_f(chain): number of functional groups per chain, f_{CL}: functional groups crosslinked, N_{CL}(chain): number of crosslinks per chain.

TP	RAFT removed	M_n[1] [kDa] DP_n[1]	Đ	m [g]	f [%] N_f(chain)	f_{CL} [%] N_{CL}(chain)	Swelling ratio[2]	Soluble fraction[2] [%]
b1	No	102 781	1.49	3.59	2.10 16.3	12.5 2.0	15.7 ± 0.2	7.6 ±0.6
b2	Yes	93 713	1.44	5.57	1.85 13.2	12.5 1.65	25.5 ± 2.1	13.8 ±1.5
b3	No	87 767	1.30	5.40	1.96 15.0	12.5 1.9	27.7 ± 0.7	18.0 ±0.8
b3	Yes	87 767	1.30	9.57	1.96 15.0	12.5 1.9	37.0 ± 1.3	26.5 ±4.9

1: determined via SEC with a standard PS calibration. 2: For the experimental conditions and equations to calculate swelling ratio and insoluble fraction refer to the Experimental Part (Section 4.11).

As can be seen in Table 4.5, the values for swelling ratio and soluble fraction differ significantly. This is a sign that the crosslinking takes place with varying efficiency. Also the samples, where the RAFT end-group has not been removed differ in their properties. The removal of the end-group can therefore not be identified as the sole cause for the inconsistency in the crosslinking efficiency. The samples with the identical chain length and functionality (b3) also showed significantly different properties. This was confirmed via rheometry. In Figure 4.20 the frequency sweeps of the network with the RAFT end-group (**Network 3b3+RAFT**) and without the RAFT end-group (**Network 3b3-RAFT**) after equilibration at 150 °C are shown. The sample with the RAFT end-group (**Network 3b3+RAFT**) (and the lower swelling ratio and soluble fraction) shows a higher storage modulus, indicating a higher crosslinking density. A possible explanation for these inconsistent material properties is that the crosslinking is a statistical process. With not even two crosslinks per chain at 100 % crosslinking yield, limited variations in crosslinking

efficiency are expected to significantly impact the properties of the resulting materials.
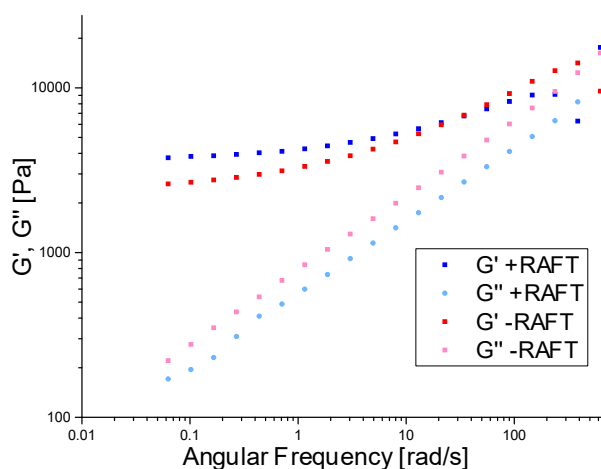
Figure 4.20: Frequency sweeps of **Network 3b** with the RAFT end-group (**Network 3b3+RAFT**, blue) and without the RAFT end-group (**Network 3b3-RAFT**, red) at 150 °C.

4.8.4 Stress Relaxation

Stress relaxation experiments confirmed this hypothesis. The experiment was conducted at 110 °C with **Network 3b3-RAFT**, after equilibration at 150 °C for several hours. The stress relaxation was conducted for somewhat 24 h and is depicted in Figure 4.21. Approximately 60 % of the stress relaxed in the first few seconds, before a plateau in the relaxation modulus is reached. A second slow relaxation takes place at longer time scales. The first relaxation is likely due to dangling ends and free polymer chains not attached to the network. The second relaxation process can be attributed to the imine exchange process. These results indicate that this network might not provide the necessary stability for the double network (DN).

4.8.5 Creep

The free chains also influence the creep behavior as can be seen in Figure 4.22. After an elastic response in which the sample showed significant deformation (83 % after 5 min of stress) the sample begins to creep and reaches a deformation of 148 % after 24 h (Figure 4.22, left). After the stress is removed, the sample responds elastically and recovers part of its strain (5 min after stress removal, the strain is at 77 %). After
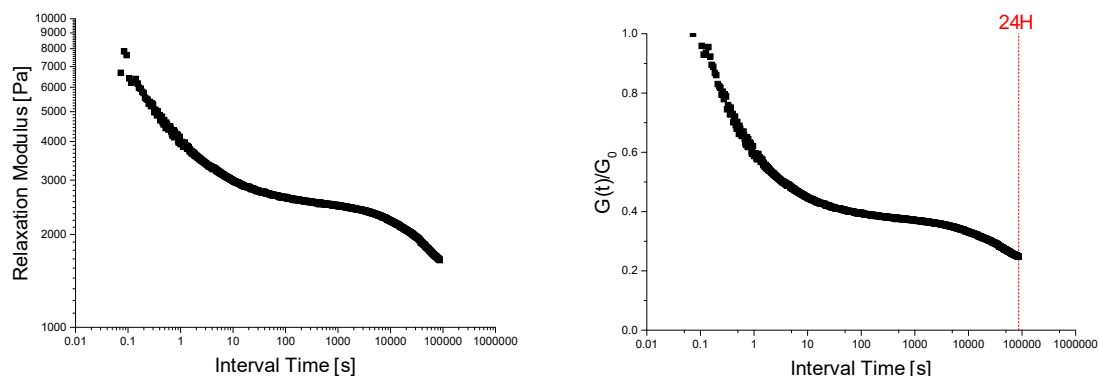
Figure 4.21: Left: Stress relaxation of **Network 3b3-RAFT**. Right: normalized to G_0.

24 h, some of the creep is recovered. However, 27 % residual strain remain. The strain rate during the creep experiment was used to determine the viscosity of the sample by using Equation 4.7 (see Experimental Part). The strain rate is displayed in Figure 4.22, right, as a function of time. The last value was taken to calculate the viscosity, which was determined to be $1.10 \cdot 10^9$ Pa·s at 25 °C. However, it shows that the strain rate decreases with time, leading to an increase in viscosity.
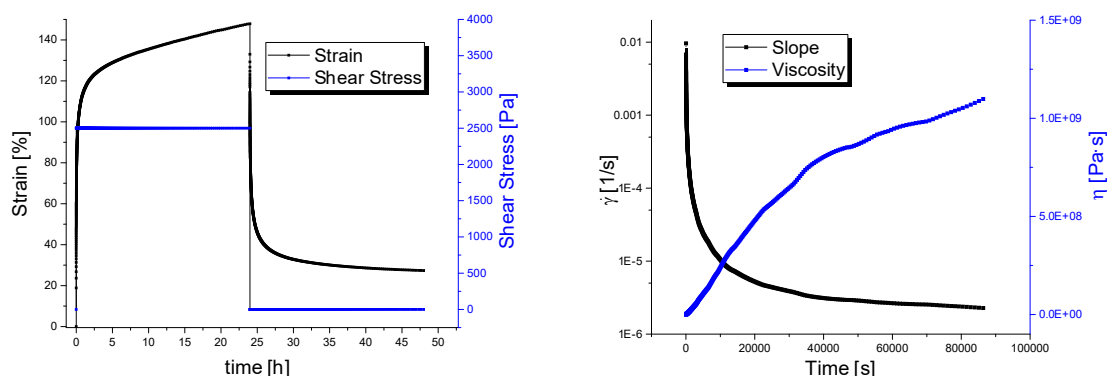
Figure 4.22: Creep behavior of **Network 3b3-RAFT**. A shear stress of 2500 Pa was applied for 24 h, before the sample was allowed to recover for another 24 h. Left: Strain as a function of the applied shear stress with time. Right: $\dot{\gamma}$ and viscosity in function of the creep experiment time.

4.8.6 DMA

The DMA of **Network 3b3-RAFT** is presented in Figure 4.23. Below the T_g, there is a plateau of the storage modulus around 510 MPa. The T_g is determined at the maximum

of the loss modulus function and located at -37.0 °C. Above the T_g, there is no steep drop in the storage modulus. However, the storage modulus is continuously decreasing and no real plateau establishes, which likely reflects the low ρ(CL) and the presence of free chains in the network.
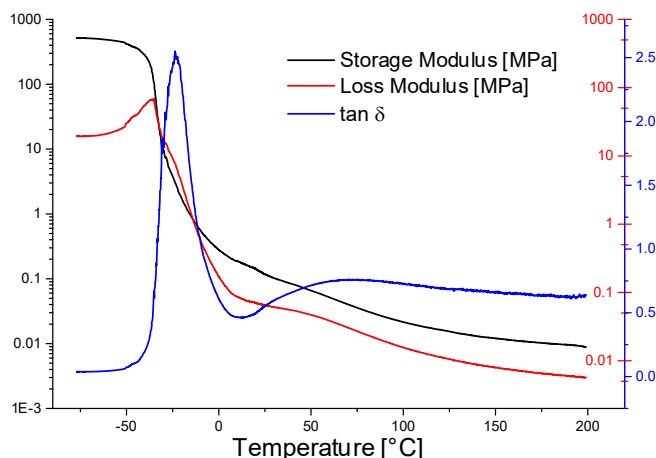
Figure 4.23: DMA of **Network 3b3-RAFT**.

4.8.7 Conclusion

The crosslinking of TP **P29**/**P30** targeting ρ(CL) = 0.25 % led to inconsistent network formation. The crosslinking was not reproducible, resulting in materials with varying properties. This showed clearly in the swelling ratio, soluble fraction and shear modulus. Similar precursors gave samples with significantly different crosslinking densities. Due to the low envisioned ρ(CL), a significant amount of chains were not attached to the network and were able to diffuse freely. This affected the network properties: the sample showed a significant amount of short time stress relaxation and residual creep. Since this network is supposed to display a high dimensional stability, the network properties need to be adapted. It was hence decided to double the crosslinking density.

4.9 Network 3c: M_n = 100 kDa, f = 2.0 %, ρ(CL) = 0.5 %

4.9.1 Crosslinking and Processing

A new network was prepared targeting a two times higher ρ(CL). The thermoplastic pre-cursor **P30** features 2 % functionality (f(P)). Instead of 12.5 %, now 25 % of these groups were crosslinked (f_{CL}) to obtain a ρ(CL) of 0.5 %, instead of 0.25 %. The crosslinking takes place by adding the bis(imine) crosslinker, like displayed in Scheme 4.10. The amount of crosslinker n(CL) was calculated employing Equation 4.6. m(P) is the mass of the polymer, N_f(CL) is the functionality of the crosslinker (2) and M(M_{Av}) is the average molecular mass of the monomers (see Equation 4.2).

$$n(CL) = \frac{f_{CL} \cdot m(P) \cdot f(P)}{N_f(CL) \cdot M(M_{Av})} \tag{4.6}$$

Two batches were prepared (properties are displayed in Table 4.6) to compare the crosslinking efficiency. One with the RAFT end-group still present (**Network 3c+RAFT**) and one with the RAFT end-group removed (**Network 3c-RAFT**). The samples gelified reliably after evaporation of the solvent within a few hours. To complete the crosslinking, the sample rested for 72 h at ambient condition, before the remaining solvent and the formed benzaldehyde were removed under vacuum. A homogeneous material was obtained after compression molding for 20-30 min at 110 °C, with a pressure equivalent to 3 tons (Figure 4.24).

Table 4.6: Overview over the imine-aldehyde networks synthesized with 0.5% crosslinking density. N_f(chain): number of functional groups per chain, f_{CL}: functional groups crosslinked, N_{CL}(chain): number of crosslinks per chain.

Network	M_n[1] [kDa] DP_n[1]	Đ	m [g]	f(P) [%] N_f(chain)	f_{CL} [%] N_{CL}(chain)	Swelling ratio[2]	Soluble fraction[2] [%]
3c+RAFT	86 659	1.39	4.90	1.98 13.0	25 3.25	17.1 ± 0.7	10.8 ± 0.4
3c-RAFT	93 713	1.44	5.31	1.85 13.2	25 3.30	15.2 ± 0.4	9.7 ± 0.2

1: determined via SEC with a standard PS calibration. 2: For the experimental conditions and equations to calculate swelling ratio and insoluble fraction refer to the Experimental Part (Section 4.11).

Figure 4.24: Pictures of **Network 3c** with ρ(CL) = 0.5 % after compression molding. Left: Sample **Network 3c+RAFT**. Right: Sample **Network 3c-RAFT**.

Both samples showed similar swelling ratios and soluble fractions, indicating a similar crosslinking efficiency. The removal of the RAFT end-group did not seem to influence the crosslinking process nor the material properties. All further experiments have been conducted with samples free of RAFT end-groups.

4.9.2 Solubility Behavior

4.9.2.1 Long Term THF Stability

To study the behavior of the network when immersed in solvent for a longer period, the sample was immersed into THF for 7 days. The sample was subsequently dried and its mass (m(dried)) compared to the sample mass before the solubility test (m(dry)). As can be seen in Table 4.7, the average soluble fraction was around 10 %. This result is in the exact same range as the results obtained after 24 h (compare Table 4.6). The sample is thus able to maintain a stable structure over a longer period when immersed into THF. The exchange reaction is not dynamic enough for the chains to form loops and other soluble branched species that would be able to diffuse into the solvent during this time.

4.9.2.2 Selective "De-crosslinking"

The sample was subjected to solubility tests. The imine crosslinks can be selectively cleaved by adding an excess of a monofunctional small molecule that replaces the crosslinker by a reaction with the imine groups.[1,7] In this experiment, this was attempted

Table 4.7: Results of solubility test of **Network 3c** in THF over 7 days.

Sample	m(dry) [mg]	m(dried) [mg]	Insoluble fraction [%]
1	231.5	209.1	90.3
2	224.8	200.8	89.3
3	209.0	188.9	90.4
Average			90.0± 0.6

in three different ways like shown in Scheme 4.22: either by adding an amine, an aldehyde, or water.
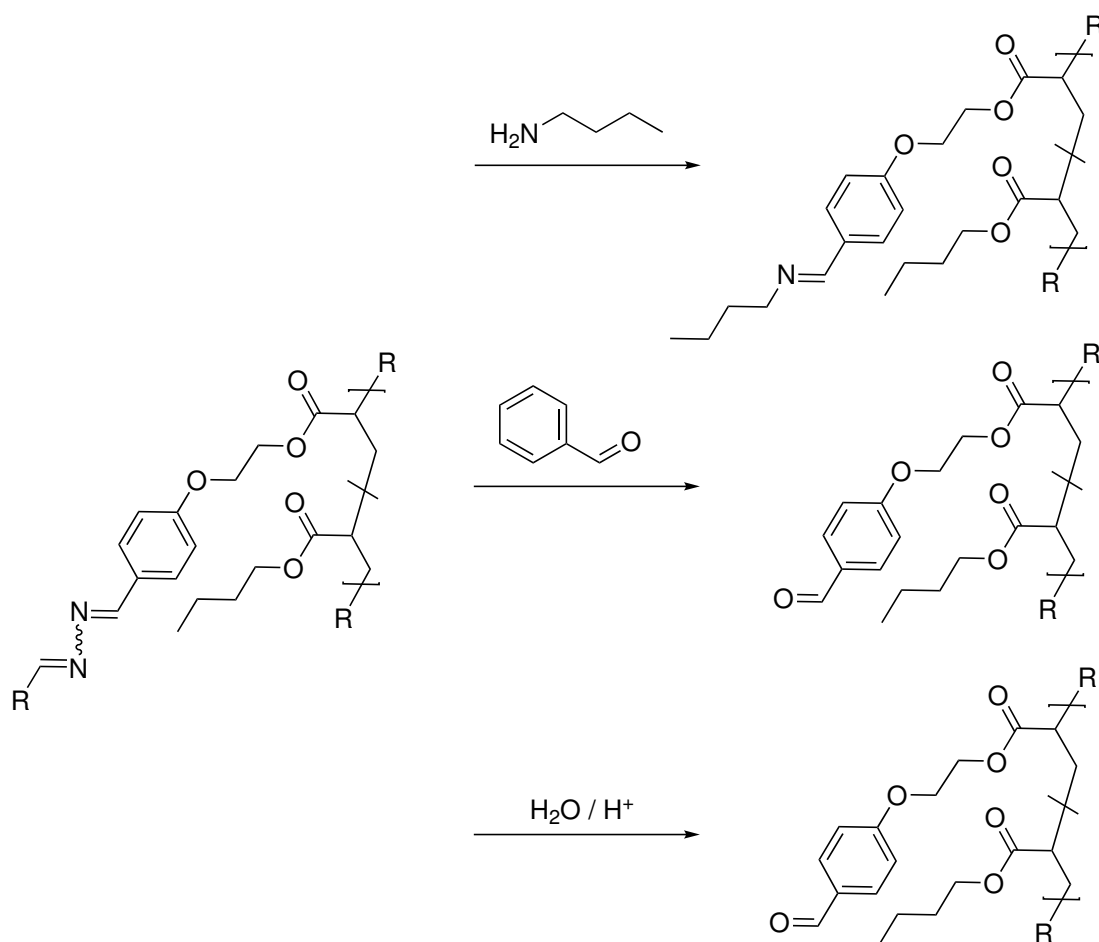
Scheme 4.22: Decrosslinking of the imine network utilizing small molecules like amines, aldehydes, or water.

For the tests, the insoluble parts of the network were immersed in THF before 1000

eq (in respect to present imine bonds) of a competitive small molecule were added. The small molecules were benzaldehyde, n-butylamine , water, and 1 M HCl_{aq}. All samples except for the one with benzaldehyde dissolved completely after a few hours. The sample to which benzaldehyde was added dissolved only after several days. This indicates that the exchange reaction between imines and aldehydes proceeds much slower than the other ones. The test with benzaldehyde was repeated with a higher concentration of the small molecule (5,000 eq). This time the network dissolved within a few hours. Solubility tests are highly dependent on temperature and concentration of the competitive molecule. In literature, it is reported that the hydrolysis is pH dependent.[5,36,37] However, the dependence of the hydrolysis kinetics on the pH is non-linear and highly dependent on the system.[5] The present network is able to undergo hydrolysis under both neutral and acidic conditions rapidly. After each solvolysis the obtained thermoplastic was compared to the pristine one. As can be seen in Figure 4.25 and Table 4.8, the curves after the solvolysis match very well the one of the original thermoplastic. The one after the solvolysis with n-butylamine is slightly shifted towards higher molecular weights. This could be due to the change of functional group of the thermoplastic. The pristine thermoplastic was functionalized with pendent aldehydes, whereas after the aminolysis it is transformed to an imine (compare Scheme 4.22).
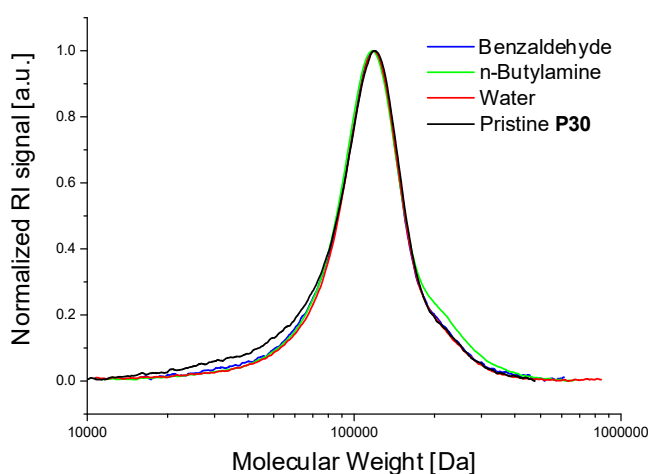
Figure 4.25: SEC traces in THF (PS calibration) before (black) and after the selective "de-crosslinking" of **Network 3c** with benzaldehyde (blue), n-butylamine (green), or water (red).

In another test, the orthogonality of the imine-aldehyde network with propanediol was tested. Theoretically, the imine bonds should be stable in the presence of a diol (see Scheme 4.23). 1000 eq of 1,2-propanediol (in respect to the imine bonds) were added

Table 4.8: SEC results of the selective "de-crosslinking" experiments of **Network 3c**.

-	Pristine **P30**	Benzaldehyde	*n*-Butylamine	H_2O
M_n [kDa]	107	109	104	105
Đ	1.28	1.20	1.24	1.18

to the network in THF. After 72 h, the solvent was removed and the network dried. The soluble fraction was around 5 %. However, some excess of the diol could have still remained in the insoluble fraction after drying. The amount of the insoluble fraction might therefore be overestimated. Yet, the network seemed to show good stability in the presence of diols.
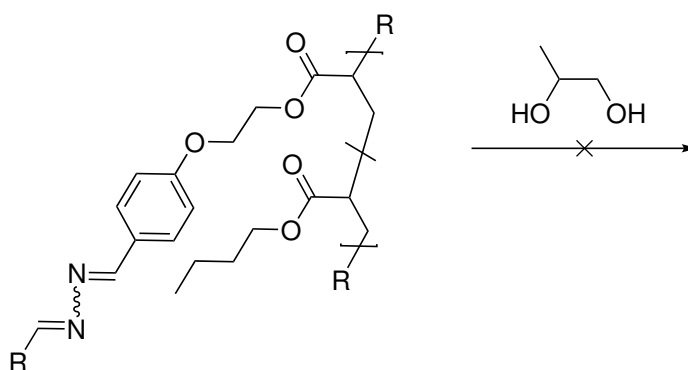
Scheme 4.23: **Network 3c** shows good stability towards diols.

4.9.3 Thermal Characterization

4.9.3.1 TGA

Temperature Ramp

Network 3c was subjected to TGA by applying a 10 K/min temperature ramp between 25 and 600 °C under nitrogen. The results are shown in Figure 4.26a. The sample maintained 98 % of its mass up to 261 °C.

Isothermal

The long term stability of the network was tested with an isothermal measurement at 150 °C for 10 h. The results presented in Figure 4.26b indicate that the network features excellent stability at 150 °C.
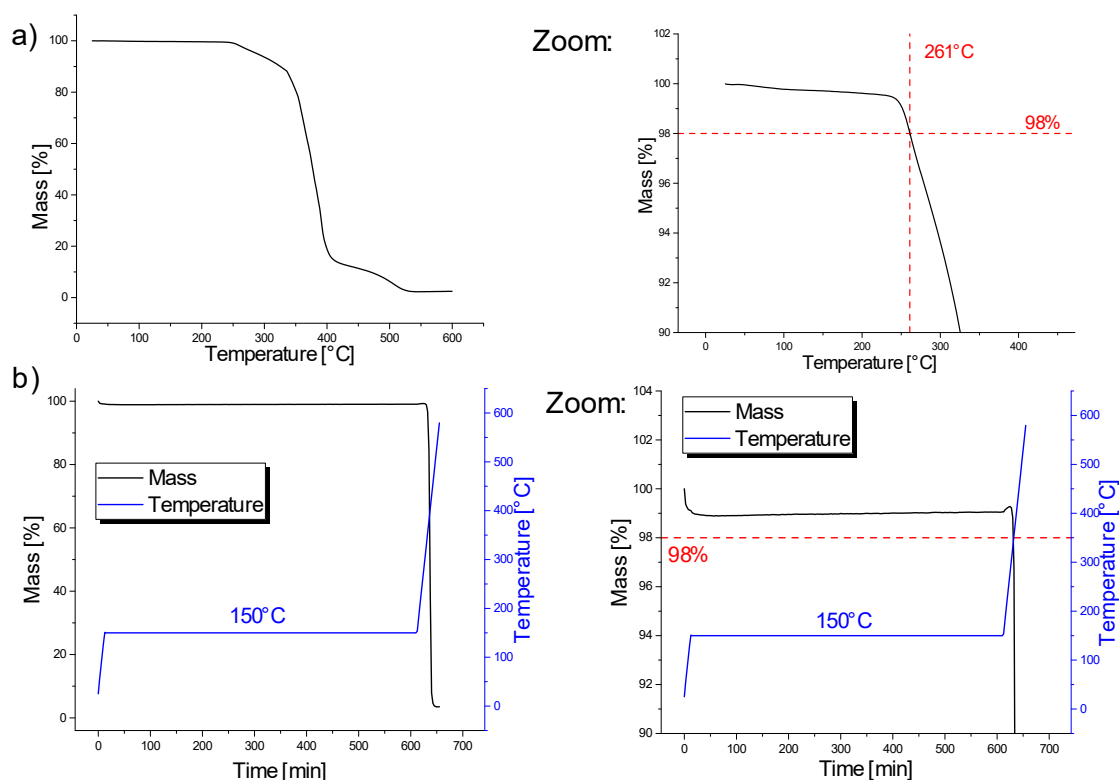
Figure 4.26: TGA of the **Network 3c**. a) Temperature ramp. b) Isothermal at 150 °C. Left: Full thermogram. Right: Zoom to the 98 % limit.

4.9.3.2 DMA

In Figure 4.27 the DMA results of **Network 3c** are displayed. Before the T_g, the sample shows a plateau at 986 MPa. The T_g was determined at the maximum of E" and was located at -37 °C. After the glass transition, E' decreases and reaches a plateau around 80,000 Pa at 100 °C. From this point, the modulus increases slightly in accordance to the rubber elasticity theory. The sample maintains its network structure over the entire measured temperature spectrum.
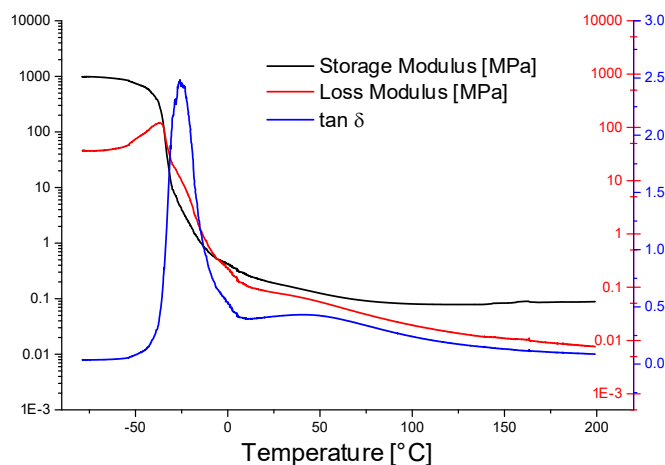
Figure 4.27: DMA of **Network 3c**.

4.9.3.3 DSC

Analysis via DSC (Figure 4.28) showed no transition but the glass transition. The T_g was found at -47.1 °C and is thus very similar to the one of **Network 3a** (see Figure 4.5).
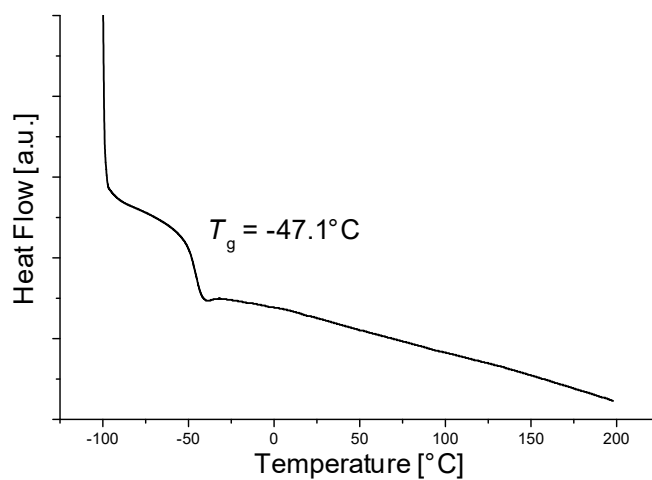
Figure 4.28: DSC analysis of the **Network 3c**, second heating cycle.

4.9.4 Tensile Tests

The results of the uniaxial tensile tests of **Network 3c** are displayed in Figure 4.29. The strain rate was set to 10 mm/s, and a 100 N transducer was employed.
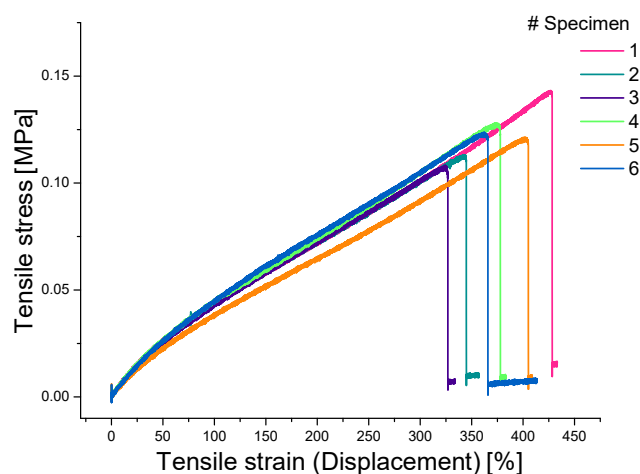
Figure 4.29: Stress/strain curves of the uniaxial tensile tests of **Network 3c**.

The Young's modulus was calculated by determining the slope in the linear regime between 2-5 % strain. The values determined for all specimen can be found in Table 4.9. The average tensile strain at break was at 377 % with an average tensile stress at break of 124 kPa. The Young's modulus of **Network 3c** is around 66.1 kPa.

Table 4.9: Results of the uniaxial tensile test of **Network 3c**.

Specimen #	1	2	3	4	5	6	Average
Tensile strain at break [%]	428	363	325	378	403	365	377 ± 36
Tensile stress at break [kPa]	142	122	108	127	121	123	124 ± 11
Young's modulus [kPa]	68.7	70.0	66.8	68.7	60.0	62.4	66.1 ± 4.0

4.9.5 Frequency Sweeps

Frequency sweep experiments performed on the **Network 3c** at the lowest, 25 °C, and the highest, 150 °C, measured temperature are displayed in Figure 4.30. It can be seen that at high temperature the storage modulus is constant, it exhibits a rubbery plateau. There is no crossover of G' and G" towards lower frequencies that wound indicate a transition to the terminal flow regime. When going to lower temperatures, the moduli

increase towards higher frequencies. The movement of the chain segments becomes slower and the sample starts transitioning from the rubbery zone to the glassy regime.
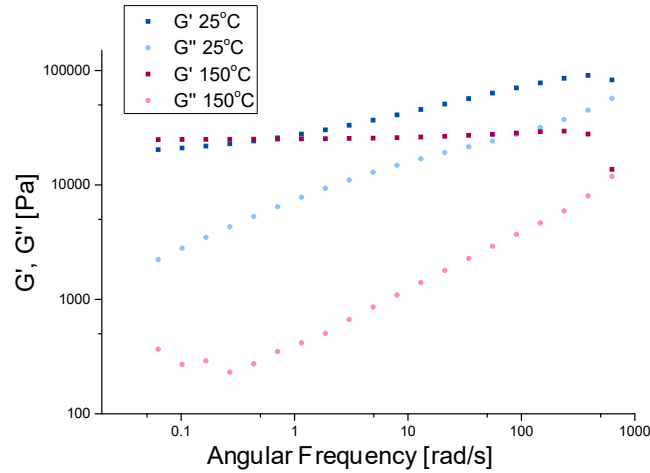
Figure 4.30: Frequency sweeps of **Network 3c** at 25 °C and 150 °C.

4.9.6 Stress Relaxation

The stress relaxation curves of **Network 3c** at 110 °C after equilibration can be found in Figure 4.31.
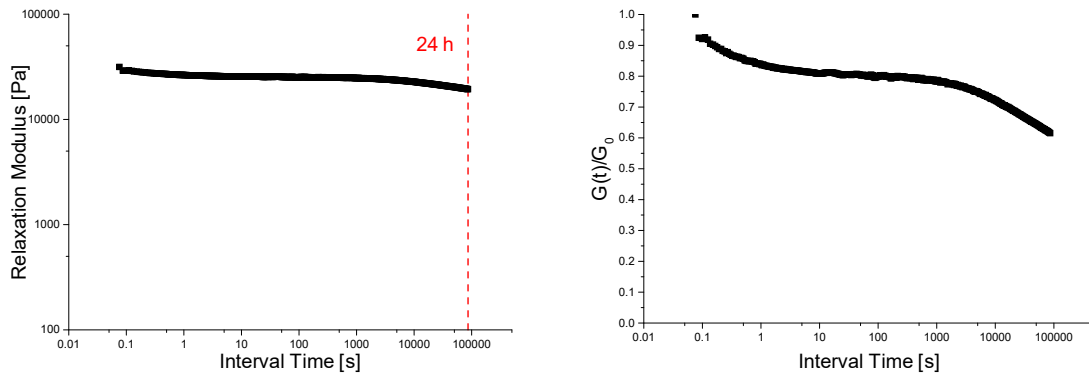
Figure 4.31: Left: Stress relaxation of **Network 3c**. Right: normalized to G$_0$.

Here again, a relaxation takes place on short time scales. This can be attributed to dangling chain ends and free chains within the network. This causes a relaxation of about 20 % of the initial stress, which is much less pronounced than the one of **Network 3b3-RAFT** (Figure 4.21). After this first relaxation, there is a plateau of the relaxation modulus,

where hardly any stress is relaxed for about one hour, before a second relaxation process takes place. This process is rather slow and can be attributed to the imine-aldehyde exchange reactions. After 24 h, about 40 % of the initial stress have been relaxed.

4.9.7 Creep

The creep behavior of **Network 3c** is depicted in Figure 4.32. The material showed an elastic response of 13 % strain 5 min after the stress was applied. From there it crept 2.7 % over the next 24 h. After the stress was removed, the strain recovered to 2.0 %. The sample showed only very weak viscous behavior, which is likely mainly due to network defects.
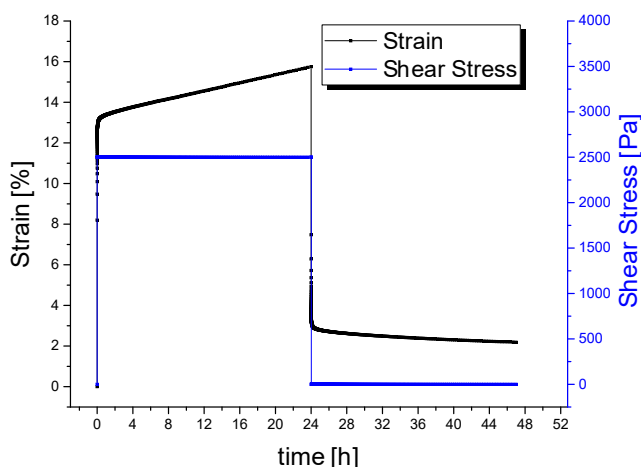
Figure 4.32: Creep behavior of **Network 3c**. A shear stress of 2500 Pa was applied for 24 h, before the sample was allowed to recover for another 24 h.

The strain rate was determined by calculating the slope of the strain over 30 time points. The slope is shown as a function of time in Figure 4.33 (left). Despite some fluctuations, the slope maintains a rather steady value. The last value was taken and the viscosity was calculated using Equation 4.7. The sample shows a viscosity of $\eta = 9.12 \cdot 10^9$ Pa·s at 25 °C. The creep compliance J(t) and the creep recovery compliance $J_r(t)$ with time are displayed in Figure Figure 4.33 (right). J(t) does not achieve the steady-state flow scaling of 1 during the measured time.[38] Therefore, the system does not reach terminal relaxation.
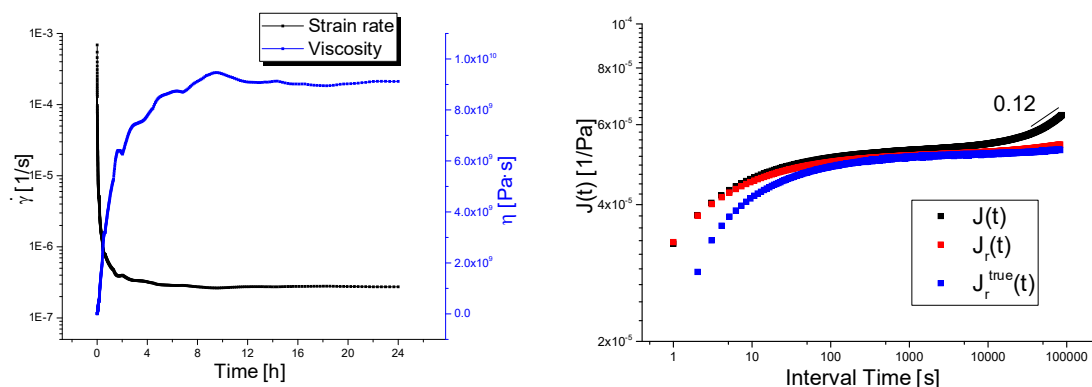
Figure 4.33: Left: $\dot{\gamma}$ and the viscosity of **Network 3c** as a function of the creep experiment time. Right: J(t), J_r(t), and J_r^{true}(t) of **Network 3c** as a function of the creep/recovery experiment time.

4.9.8 Conclusion

The thermoplastic **P30** with a M_n of 100 kDa and a functionality of 2.0 % was crosslinked with the double amount of crosslinker to yield networks with a ρ(CL) of 0.5 %. The obtained networks crosslinked reproducibly within a few days to materials with similar properties. Compression molding for 30 min at 110 °C yielded homogeneous, stable elastomers with a Young's modulus of 66.1 kPa and a T_g of -47 °C. The material shows good thermal stability up to 260 °C, as well as excellent long term stability at 150 °C. The shear modulus was around 25 kPa on the rubbery plateau, and the tensile modulus was around 80 kPa at ambient conditions. During stress relaxation experiments, the samples showed only minimal short time relaxation (due to dangling ends). The stress relaxation by the exchange reactions takes place slowly and only to a limited extend at longer time scales. This sample shows mainly elastic behavior during creep experiments. The viscosity at 25 °C was determined to be 9.12 · 10^9 Pa·s, which does not correspond to steady-state flow. The sample showed good long term stability in THF with insoluble fractions around 90 % after one week of immersion. The network could be selectively "de-crosslinked" using an amine, aldehyde, or water. It features thus the ability to be chemically recyclable.

4.10 Conclusion

The goal of the work described in this chapter was to synthesize and characterize the structural subnetwork of the double network. This subnetwork has to fulfill the requirements of being dimensionally stable and soft at ambient conditions, while being able to be processable and recyclable at elevated temperatures. To obtain a (highly) stretchable network, a low crosslinking density was envisioned. At a given M_n and $\rho(CL)$, the dynamic behavior of the system is controlled by the number of pendent functional groups. Imine-aldehyde exchange was chosen as a degenerate exchange. An aldehyde acrylate monomer was synthesized in two steps. In addition, a bis(imine) crosslinker was synthesized in one step. To guarantee a slow exchange at room temperature, only a small amount of aldehyde groups was incorporated into the thermoplastic precursor. In a first attempt, 500 kDa and a functionality of 0.5 % was targeted. The functional monomer was copolymerized with nBA via FRP and crosslinked with the bis(imine) to yield a soft elastomer with a crosslinking density of 0.25 %. The material was processed via compression molding over 16 h at 110 °C. A homogeneous material was obtained. However, the material started to shrivel with time. This is a sign that the material was not fully relaxed and in equilibrium after processing. Stress relaxation confirmed that the material was not able to relax stress at elevated temperatures. Creep experiments revealed a fully elastic behavior of the sample. The material showed the targeted structural stability at ambient conditions, yet it did not fulfill the requirement of processability at elevated temperatures.

Consequently, it was decided to make the material more dynamic by increasing the numbers of functional groups per chain by a factor of four. However, when attempting chains with M_n = 500 kDa, unwanted crosslinking occured. Apparently, the aldehyde functional monomer tends to induce intermolecular side reactions. To avoid crosslinking, polymers with a shorter chain length were envisioned. The chains were synthesized via RAFT copolymerization to yield thermoplastics with M_n = 100 kDa and 2.0 % functionality. This polymerization method was reliable and led to well-defined polymers. A procedure to transform the RAFT end-groups without impacting the functional groups was also elaborated.

The thermoplastic precursors were crosslinked to yield elastomers with a $\rho(CL)$ of 0.25 %. The samples were well processable via compression molding. Homogeneous materials were obtained within 30 min at 110 °C, which remained stable and showed no sign of shriveling. However, the crosslinking took several days and turned out to be not

reproducible. Different batches gave materials with varying properties, such as swelling ratio, soluble fraction, or shear modulus. It showed that small fluctuations in crosslinking efficiency are able to impact the properties of the resulting materials significantly at this ρ(CL). This showed also in stress relaxation experiments, where a significant amount of stress was dissipated immediately by these free chains. These network defects also led to a significant amount of creep.

It was hence decided to double the crosslinking density to 0.5 %. This resulted in materials with reproducible crosslinking densities and consistent properties. The network showed good processability and was obtained as a homogeneous, stable material. The elastomer showed limited short term stress relaxation and relaxed stress slowly at longer time scales. The material's creep response at room temperature was mainly elastic. The network was able to be chemically recyclable using small competitive molecules, such as benzaldehyde. The requirements for the structural networks were: stability at ambient conditions, but sufficient processablility at higher temperatures. The final subnetwork proved to fulfill these premisses and was therefore chosen to be employed in the DDN.

4.11 Experimental Part

4.11.1 Materials

All chemicals were purchased from Sigma Aldrich, Alfa Aesar, TCI, Acros Organics and Fischer. All starting materials and reagents were of analytic grade and used without further purification, if not stated otherwise. AIBN was recrystallized from methanol prior to use. *n*BA and 1,4-dioxane were passed through a short column of basic alumina to remove inhibitors or antioxidants. Molecular sieves were stored in an drying oven at 100 °C overnight and were activated prior to use by heating under vacuum.

4.11.2 Instrumental Data

NMR Spectroscopy

^{1}H NMR and ^{13}C NMR spectroscopy measurements were performed in oven dried NMR tubes on a Bruker Ultra Shield machine (400 MHz for ^{1}H NMR, 100 MHz for ^{13}C NMR) at ambient temperature. If not stated otherwise, samples of 10 mg for ^{1}H NMR and 30 mg

for ^{13}C NMR were analyzed. CDCl$_3$was employed as deuterated solvent. Chemical shifts are expressed in parts per million (ppm) and calibrated on characteristic solvent signals as internal standards (^{1}H NMR: CDCl$_3$: 7.26 ppm; ^{13}C NMR: CDCl$_3$: 77.16 ppm).

Size Exclusion Chromatography

The samples for SEC chromatography were prepared by dissolving the respective polymer in anhydrous THF to obtain a concentration of 1.0-1.2 mg/mL. A drop of toluene was added and the sample was passed through a 0.20 μm PTFE filter and placed in a Malvern GPC vial. SEC was performed on a Viscotek GPCmax/VE2001 connected to a Triple detection array (TDA 305) from Malvern. Obtained raw data were treated with a PS calibration.

DSC

DSC analyses were performed on TA DSC 250 apparatus. Two heating cycles, from -100 to 200 °C, were performed employing a heating rate of 10 °C min^{-1}. The values of T_g were determined with the data obtained on the second heating cycle.

TGA

TGA measurements were performed on a TG 209 F1 Libra from Netzsch. The samples were heated constantly with a rate of 10 °C min^{-1} from 30 to 400/600 °C. For isothermal treatments, the samples were heated to 200 °C and kept at that temperature for 3 h under a N$_2$ flow or it was conducted by heating samples constantly with a rate of 10 °C min^{-1} from 30 to 150 °C, and keeping the sample at 150 °C for 10 h.

DMA

DMA measurements were conducted on a TA Instruments Q800 in tension mode. Heating ramps were performed from -80 to 200 °C at a constant rate of 3 °C min^{-1} with a fixed frequency of 1 Hz and a maximum strain amplitude of 1 %. The T_g of the sample was determined at the maximum of the loss modulus function E".

Rheological Characterizations

All rheological characterizations were conducted on a Anton Paar MCR 501 rotational rheometer with a parallel plate geometry with a diameter of 25 mm. If not otherwise stated, the experiments were run in a convection oven under nitrogen. For solid samples, a normal force of 0.4 N was employed.

Frequency sweeps were conducted at 1 % strain between 0.01 and 100 Hz on a logarithmic ramp with 5 measuring points per decade (if not stated otherwise).

Stress relaxations were conducted with an applied strain of 1 % at 110 °C for 24 h. Before the experiments for **Networks 3b** and **3c**, samples were equilibrated for 5-6 h at 150 °C. A frequency sweep was conducted, before every stress relaxation experiment.

Amplitude sweeps were conducted between 0.1-10 % strain on a logarithmic ramp with 6 measuring points per decade at a frequency of 20 rad/s at 50 °C.

Creep experiments were conducted at 110 °C/25 °C with a constant shear stress of σ = 500/2,500 Pa for 10/24 h. Subsequently, the sample rested at 0 shear stress at the same temperature for another 10/24 h. Before the experiment at 2.5 kPa, samples were allowed to equilibrate for 5-6 h at 150 °C and a frequency sweep was conducted.

The viscosity was calculated according to Equation 4.7. The strain rate was obtained via the slope of the strain as a function of time. The value over last 30 points was taken to calculate $\dot{\gamma}$.

$$\eta = \frac{\sigma}{\dot{\gamma}} \tag{4.7}$$

Creep compliance, J(t), creep recovery compliance J_r(t), and the true creep recovery compliance J_r^{true}(t) were calculated via Equations 4.8-4.10.[38]

$$J(t) = \gamma(t)/\sigma \tag{4.8}$$

$$J_r(t) = (\gamma_f - \gamma(t))/\sigma \tag{4.9}$$

$$J_r^{\text{true}}(t) = J_r(t) - \frac{dJ_r}{dt_r}t_r \tag{4.10}$$

Tensile Tests

Uniaxial tensile tests were performed on dumbbell-shaped specimens (l x w x h = 13 x 1.6 x 2.1 mm) using an Instron 5564 tensile machine mounted with a 100 N transducer cell. The specimens were tested at a fixed cross-head speed of 10 mm/min. Testing was carried out at room temperature for all materials. Engineering stress-strain curves were obtained through measurements of the tensile force F and cross-head displacement Δl by defining the engineering stress as $\sigma = F/S_0$ and the strain as $\gamma = \Delta l/l_0$, where S_0 and l_0 are the initial cross section and gauge length of the specimens, respectively. The Young's modulus E was determined as the slope of the engineering stress-strain curves between 2-5 % strain.

Crosslinking of the Thermoplastic Precursor

The amount of crosslinker was calculated with Equation 4.11, with f_{CL} as the ratio of functional groups crosslinked, m(P) mass of the polymer, f(P) functionality of the polymer, $N_f(CL)$ functionality of the crosslinker, and $M(M_{Av})$ average molecular mass of the monomers (calculated with Equation 4.12). The TP was dissolved in THF (1 : 3 - 1 : 10 w/w) and placed into a beaker. A respective amount of a solution of the crosslinker **21** (10 mg / mL THF) was added. The mixture was vigorously stirred manually. The mixture rested openly at ambient temperature for 48 h-3 weeks, subsequently it was placed in a vacuum oven at 110 °C for 16 h. The resulting material was torn into pieces and again dried under the same conditions for another 16 h. The network was obtained as a slightly yellow (or yellow when the RAFT end-group was still present), sticky film.

$$n(CL) = \frac{f_{CL} \cdot m(P) \cdot f(P)}{N_f(CL) \cdot M(M_{Av})} \qquad (4.11)$$

$$M(M_{Av}) = f(P) \cdot M(19) + (1 - f(P)) \cdot M(nBA) \qquad (4.12)$$

Compression Molding

Compression molding was conducted using a hydraulic press applying a pressure equivalent to 3 tons. The dried samples were placed into a metal mold and pressed at the indicated temperature (110 or 150 °C) for the indicated time.

Swelling and Solubility Experiments

The network was compression molded into disk like shapes and cut into parts of 200-300 mg (m(dry)). 20 mL of THF were added and the sample was allowed to swell for 24 h. Subsequently, the excess of THF was removed with a syringe. The swelled samples were weighted (m(swollen)). The samples were dried under vacuum at elevated temperatures to remove the THF that was taken up. In the end, the mass of the dried sample was evaluated (m(dried)). The swelling ratio was determined via Equation 4.13, the insoluble fraction via Equation 4.14.

$$\text{Swelling ratio} = \frac{m(\text{swollen}) - m(\text{dried})}{m(\text{dried})} \tag{4.13}$$

$$\text{Insoluble fraction} = \frac{m(\text{dried})}{m(\text{dry})} \tag{4.14}$$

Selective "De-crosslinking"

The insoluble fraction of the network was immersed into 20 mL of THF. 2000 eq/10,000 eq of a competitive small molecule in respect to crosslinks were added. If there was still a macroscopic insoluble fraction, the excess of solvent was removed and the sample dried. The insoluble fraction was determined after Equation 4.14.

Table 4.10: Solubility tests of **Network 3c**.

Entry	1	2	3	4	5	6
Molecule	benz-aldehyde	n-butyl-amine	H_2O (pH=4-5)	HCl 1M (pH=1-2)	propan-diol	benz-aldehyde
m(P) [mg]	274	213	192	258	213	182
f(P) [%]	1.85	1.85	1.85	1.96	1.96	1.96
% f crosslinked	25	25	25	25	25	25
n(CL) [μmol]	4.87	3.79	3.41	4.86	4.02	3.23
eq(Mol)	2000	2000	2000	2000	2000	10,000
n(Mol) [mmol]	9.74	7.59	6.82	9.72	8.03	32.3
m(Mol) [g]	1.03	0.555	0.123	0.355	0.611	3.42
ρ(Mol) [g/mL]	1.04	0.74	1.00	1.02	1.04	1.04
V(Mol) [mL]	0.99	0.75	0.12	0.35	0.59	3.28
Insoluble fraction [%]	0[1)]	0[2)]	0[2)]	0[2)]	95[3)]	0[2)]

1) After 7 days, 2) after 12 h, 3) after 72 h.

After the selective "'de-crosslinking'", a part of the mixture was precipitated in MeOH, the precipitate was dissolved in THF and subjected to SEC analysis.

4.11.3 Synthesis

4.11.3.1 Synthesis of the Aldehyde Monomer
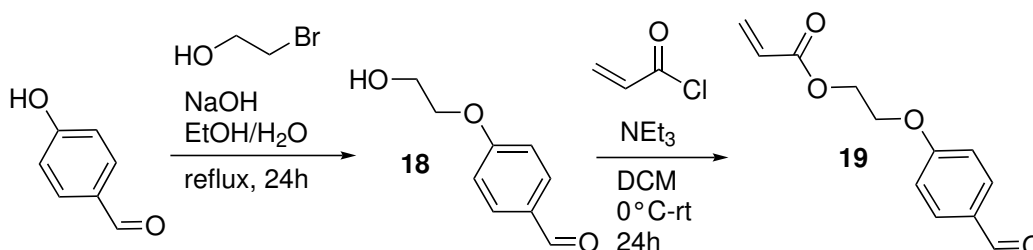
Scheme 4.24: Synthesis of the aldehyde monomer **19**.

4-(2-Hydroxyethoxy)benzaldehyde (18)

18
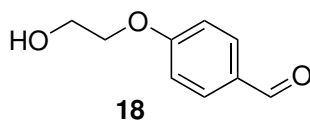
Scheme 4.25: 4-(2-Hydroxyethoxy)benzaldehyde **18**.

12.3 g of 2-bromoethanol (6.96 mL, 98.3 mmol, 1.20 eq) and 10.0 g of 4-hydroxybenzaldehyde (82.0 mmol, 1.00 eq) were dissolved in 100 mL of DMF in a 250 mL flask, before the addition of 34.0 g of K_2CO_3 (245 mmol, 3.00 eq). The mixture was stirred for 24 h at 80 °C under reflux, before it was filtered and the DMF was removed. The remains were taken up in 120 mL of DCM and the organic phase was washed 2 times with 100 mL of brine. The organic phase was dried over $MgSO_4$, filtered and the solvent was removed. The crude product was purified by CC (SiO_2, 3 x 25 cm, hex : EtOAc 1 : 1) and obtained as 2.10 g of a yellow oil (12.6 mmol, 16 % yield).

12.3 g of 2-Bromoethanol (6.96 mL, 98.3 mmol, 1.20 eq), 10.0 g of 4-hydroxybenzaldehyde (82.0 mmol, 1.00 eq) and 480 mg of TBAB (8.20 mmol, 0.1 eq) were dissolved in 100 mL of acetone in a 250 mL flask, before the addition of 34.0 g of K_2CO_3 (245 mmol, 3.00 eq). The mixture was stirred for 72 h at 80 °C under reflux, before it was filtered and the acetone was removed. The remains were taken up in 100 mL of DCM and 150 mL of H_2O. The aqueous phase was extracted with 2 times 75 mL of DCM. The organic layers were collected, dried over $MgSO_4$, and filtered. Subsequently, the solvent was removed. The crude product was purified by CC (SiO_2, 3 x 25 cm, hex : EtOAc 1 : 1) and obtained as 2.00 g of a yellow oil (12.0 mmol, 15 % yield).

R_f = 0.4

10.0 g of 4-hydroxybenzaldehyde (81.9 mmol, 1.00 eq) and 3.93 g of NaOH (98.0 mmol, 1.20 eq) were added to 150 mL of EtOH and 5 mL of H_2O in a 250 mL flask and dissolved under heating. After 30 minutes, 12.3 g of 2-bromoethanol (7.00 mL, 98.3 mmol, 1.20 eq) were added dropwise and the mixture was stirred for another 24 h at 95 °C. The solvent was removed and 200 mL of H_2O were added. The aqueous phase was extracted with 3 times 100 mL of EtOAc. The organic phases were collected and washed 3 times with 100 mL of 1 M $NaOH_{aq}$ and once with 100 mL of brine. The organic phase was dried

over MgSO$_4$, filtered and the solvent was removed. The product was obtained as 12.0 g
of a slightly yellow oil (72.2 mmol, 88% yield).

^{1}H NMR (400 MHz, CDCl$_3$, 298 K): δ [ppm] = 9.86 (s, 1H, O=C-**H**), 7.82 (d, *J* = 8.9 Hz,
2H, **H$_{Ar}$**), 7.00 (d, *J* = 8.7 Hz, 2H, **H$_{Ar}$**), 4.16 (dd, *J* = 5.1, 4.0 Hz, 2H, O-C**H$_2$**), 4.03-3.92
(m, 2H, HO-C**H$_2$**), 2.41 (s, 1H, O**H**).

^{13}C NMR (100 MHz, CDCl$_3$, 298 K): δ [ppm] = 191.07 (H-**C**=O), 163.82 (O-**C$_{Ar}$**), 132.12
(H-**C$_{Ar}$**), 130.15 (C-**C$_{Ar}$**), 114.88 (H-**C$_{Ar}$**), 69.65 (O-**C**H$_2$), 61.13 (HO-**C**H$_2$).
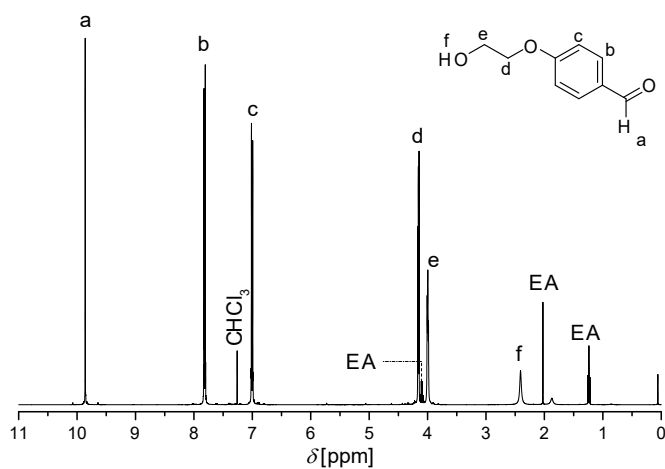
Figure 4.34: ^{1}H NMR spectrum of **18** in CDCl$_3$.
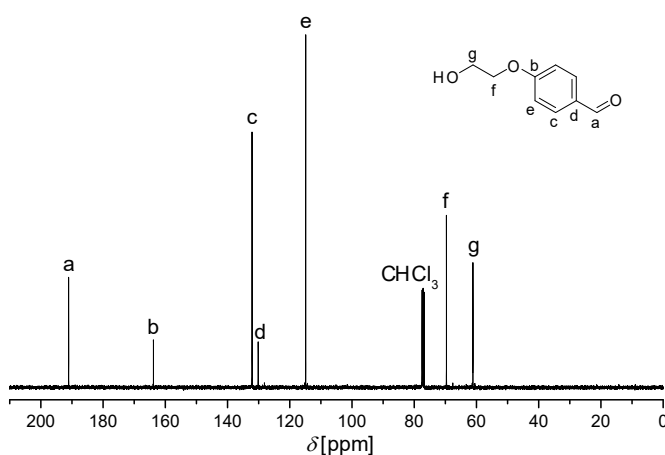
Figure 4.35: ^{13}C NMR spectrum of **18** in CDCl$_3$.

2-(4-Formylphenoxy)ethyl acrylate (19)
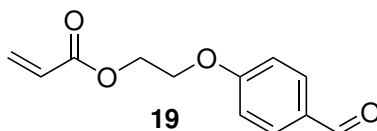
Scheme 4.26: 2-(4-Formylphenoxy)ethyl acrylate **19**.

8.40 g of **18** (50.5 mmol, 1.00 eq) were dissolved in 50 mL of DCM and 9.86 mL of NEt$_3$ (7.17 g, 70.8 mmol, 1.4 eq) were added. The mixture was freed from oxygen by bubbling nitrogen for 30 min, before it was put into an ice bath to cool it to 0 °C. Subsequently, 5.34 mL of acryloyl chloride (5.95 g, 65.7 mmol, 1.3 eq) were added slowly. The mixture was stirred for 4 h at 0 °C and then 15 h at ambient temperature, before some MeOH was added. The solution was stirred at room temperature for another 5 h, before it was washed 3 times with 50 mL of 1 M HCl$_{aq}$, 3 times with 50 mL of saturated NaHCO$_3$ solution, and twice with 30 mL of brine. The organic phase was dried over MgSO$_4$, filtered and the solvent was removed under reduced pressure to yield an orange oil. The crude product was purified by CC (hex : EtOAc 2 : 1). The product was obtained as 7.61 g of a white/yellow powder (34.6 mmol, 68% yield).

R$_f$ = 0.3

^{1}**H NMR** (400 MHz, CDCl$_3$, 298 K): δ [ppm] = 9.88 (s, 1H, O=C-**H**), 7.92-7.79 (m, 2H, **H**$_{Ar}$), 7.07-6.92 (m, 2H, **H**$_{Ar}$), 6.45 (dd, J = 17.3, 1.4 Hz, 1H, C**H**$_2$=CH), 6.15 (dd, J = 17.3, 10.4 Hz, 1H, CH$_2$=C**H**), 5.87 (dd, J = 10.4, 1.4 Hz, 1H, C**H**$_2$=CH), 4.58-4.51 (m, 2H, O-C**H**$_2$), 4.35-4.26 (m, 2H, O-C**H**$_2$).

^{13}**C NMR** (100 MHz, CDCl$_3$, 298 K): δ [ppm] = 190.90 (H-**C**=O), 166.11 (O-**C**$_{Ar}$), 163.55 (O-**C**=O), 132.12(H-**C**$_{Ar}$), 131.75 (**C**H$_2$=CH), 130.42(C-**C**$_{Ar}$), 128.00 (CH$_2$=**C**H), 114.95 (H-**C**$_{Ar}$), 66.24 (O-**C**H$_2$), 62.61 (O-**C**H$_2$).
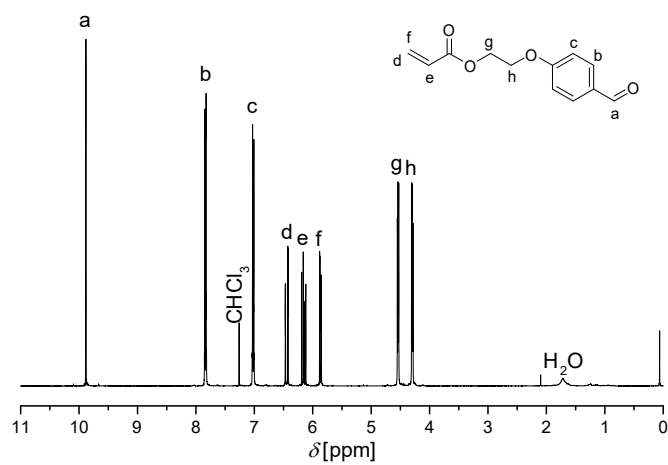
Figure 4.36: ^{1}H NMR spectrum of **19** in CDCl$_3$.
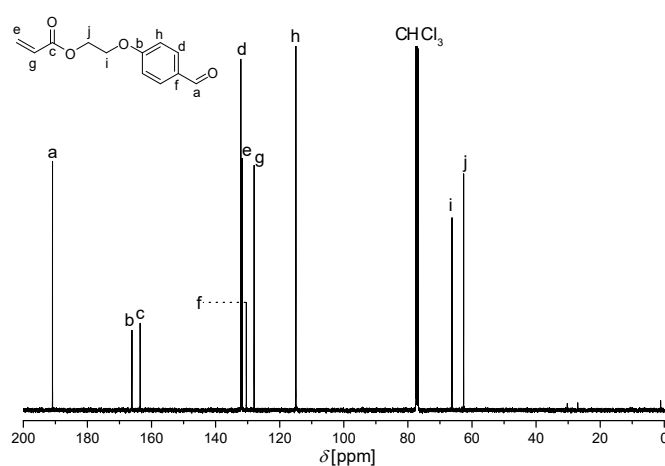
Figure 4.37: ^{13}C NMR spectrum of **19** in CDCl$_3$.

Acetal protection of the Aldehyde Monomer 19

Scheme 4.27: Acetal protected aldehyde monomer **25** (1,3-propandiol).
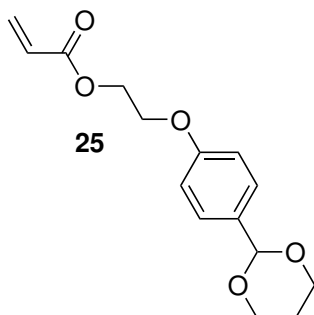
1.00 g of the aldehyde monomer **19** (4.54 mmol, 1.00 eq) were dissolved in 20 mL of DCM. A huge excess of 1,3-propanediol and a catalytic amount of TsOH were added. 5.00 g of $MgSO_4$ (45.4 mmol, 9.00 eq) were added. The $MgSO_4$ turned to a concrete-like solid.

1.00 g of the aldehyde monomer **19** (4.54 mmol, 1.00 eq) were dissolved in 20 mL of toluene. A huge excess of 1,3-propanediol and a catalytic amount of TsOH were added and the mixture was put to reflux at 135 °C using a Dean-Stark apparatus to remove water constantly. After 5 h, the mixture was cooled down and 30 mL of saturated $NaHCO_3$ solution were added. The aqueous phase was extracted 3 times with 30 mL of DCM. The organic layer was washed 2 times with 30 mL of brine. The organic layer was dried over $MgSO_4$, filtered and the solvent was evaporated. The product was not obtained pure, the side products could not be identified. The same procedure was repeated by replacing DCM with Et_2O. In this case the product was also not obtained pure and the side products could not be identified.

^{1}H NMR (400 MHz, $CDCl_3$, 298 K): δ [ppm] = 7.35-7.33 (m, 2H, **H$_{Ar}$**), 6.84-6.82 (m, 2H, **H$_{Ar}$**), 6.37 (dd, J = 17.3, 1.4 Hz, 1H, **CH$_2$=CH**), 6.08 (dd, J = 17.3, 10.4 Hz, 1H, **CH$_2$=CH**), 5.78 (dd, J = 10.4, 1.4 Hz, 1H, **CH$_2$=CH**), 5.39 (s, 1H, O-**CH**-O), 4.42 (m, 2H, O-**CH$_2$**), 4.20-3.80 (m, 4H, O-**CH$_2$**), 4.13 (m, 2H, O-**CH$_2$**), 1.90-1.70 (m, 2H, **CH$_2$**).
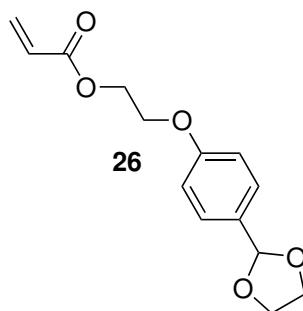
Scheme 4.28: Acetal protected aldehyde monomer **26** (ethylene glycol).

1.00 g of the aldehyde monomer **19** (4.54 mmol, 1.00 eq) was dissolved in 20 mL of toluene. A huge excess of ethylene glycol and a catalytic amount of TsOH were added and the mixture was put to reflux at 135 °C using a Dean-Stark apparatus to remove water constantly. After 7 h, the mixture was cooled down and 30 mL of saturated NaHCO$_3$ solution were added. The aqueous phase was extracted 3 times with 30 mL of Et$_2$O. The organic layer was dried over MgSO$_4$, filtered and the solvent was evaporated. Only 33 % of the reactant was converted, the product was not isolated from the reactants and some unidentified impurities showed.

1.00 g of the aldehyde monomer **19** (4.54 mmol, 1.00 eq) were dissolved in 20 mL of THF. A huge excess of ethylene glycol and a catalytic amount of TsOH were added. 3 g of activated 3-Å molecular sieves were added. The mixture stirred for 24 h. The molecular sieves turned to dust, which was filtered off. The THF was removed and 30 mL of saturated NaHCO$_3$ solution were added. The aqueous phase was extracted 3 times with 30 mL of Et$_2$O. The organic layer was dried over MgSO$_4$, filtered and the solvent was evaporated. Only 33 % of the reactant was converted, the product was not isolated from the reactants. However, no unidentified impurities were detected.

^{1}H NMR (400 MHz, CDCl$_3$, 298 K): δ [ppm] = 7.35-7.33 (m, 2H, **H$_{Ar}$**), 6.86-6.84 (m, 2H, **H$_{Ar}$**), 6.37 (dd, J = 17.3, 1.4 Hz, 1H, C**H**$_2$=CH), 6.08 (dd, J = 17.3, 10.4 Hz, 1H, CH$_2$=C**H**), 5.78 (dd, J = 10.4, 1.4 Hz, 1H, C**H**$_2$=CH), 5.69 (s, 1H, O-C**H**-O), 4.42 (m, 2H, O-C**H**$_2$), 4.13 (m, 2H, O-C**H**$_2$), 4.10-3.80 (m, 4H, O-C**H**$_2$).

4.11.3.2 Crosslinker Synthesis

N,N'-(hexane-1,6-diyl)bis(butan-1-imine)
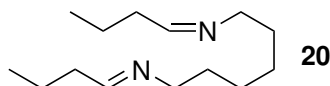
Scheme 4.29: N,N'-(hexane-1,6-diyl)bis(1-phenylmethanimine) **20**.

3.00 g of hexamethylenediamine (3.37 mL, 25.8 mmol, 1.00 eq) and 4.89 mL of butyralde-hyde (3.91 g, 54.2 mmol, 2.10 eq) were dissolved in 50 mL of DCM. Subsequently, 9.32 g of $MgSO_4$ (77.4 mmol, 3.00 eq) were added and the mixture stirred for 24 h at room temperature, before the solution was filtered and concentrated under reduced pressure to yield a milky yellow oil. The crude product was attempted to be purified by

a) washing: A few drops of the crude product were dissolved in 2 mL of DCM and washed 3 times with 2 mL of 1M NaOH and 2 times with 2 mL of brine. The product could not be isolated.

b) filtration through basic Alox: A few drops of the crude product were filtered through a column of basic alumina using DCM as eluent. The filtrate was analyzed via NMR and the alumina was extracted with DCM and analyzed via NMR. The product could not be isolated.

N,N'-(hexane-1,6-diyl)bis(1-phenylmethanimine) (21)
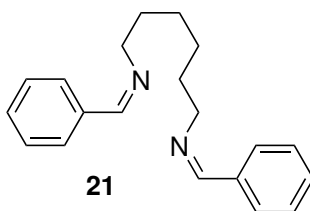
Scheme 4.30: N,N'-(hexane-1,6-diyl)bis(1-phenylmethanimine) **21**.

5.62 g of benzaldehyde (5.38 mL, 52.9 mmol, 2.05 eq) and 3.00 g of 1,6-hexanediamine (25.8 mmol, 1.00 eq) were dissolved in 50 mL of DCM, before 10 g of $MgSO_4$ (3.00 eq) were added. The mixture was stirred at room temperature for 24 h, filtered and the solvent was removed. The product was dried for 16 h at 150 °C under vacuum. The product

was obtained as 6.00 g of an orange oil consisting of 98.2 mol% product and 1.8 mol% benzaldehyde (calculated from the integration areas of the NMR spectrum (Figure 4.38)). Calculated yield **21** : 5.89 g, 20.4 mmol, 79%.

^{1}H NMR (400 MHz, CDCl$_3$, 298 K): δ [ppm] = 8.27 (s, 2H, N=C-**H**), 7.73-7.70 (m, 4H, **H$_{Ar}$**), 7.42-7.39 (m, 4H, **H$_{Ar}$**), 3.61 (td, J = 7.0, 1.2 Hz, 4H, N-C**H$_2$**), 1.74-1.71 (m, 4H, C**H$_2$**), 1.44-1.41 (m, 4H, C**H$_2$**).

^{13}C NMR (100 MHz, CDCl$_3$, 298 K): δ [ppm] = 160.94 (**C**=N), 136.48 (C-**C$_{Ar}$**), 130.58 (H-**C$_{Ar}$**), 128.70 (H-**C$_{Ar}$**), 128.16 (H-**C$_{Ar}$**), 61.83 (N-**C**H$_2$), 30.98 (**C**H$_2$), 27.29 (**C**H$_2$).
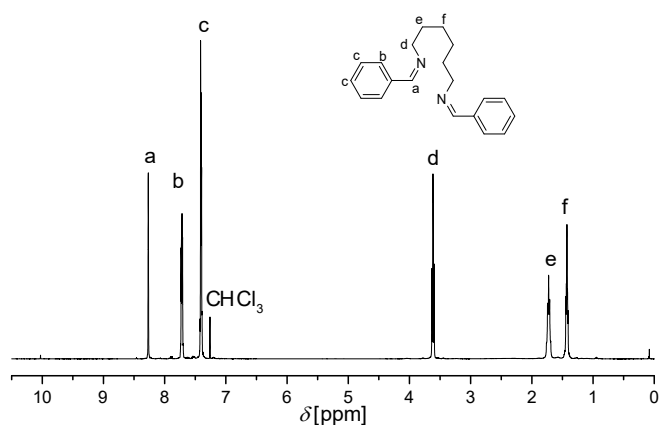
Figure 4.38: ^{1}H NMR spectrum of **21** in CDCl$_3$.
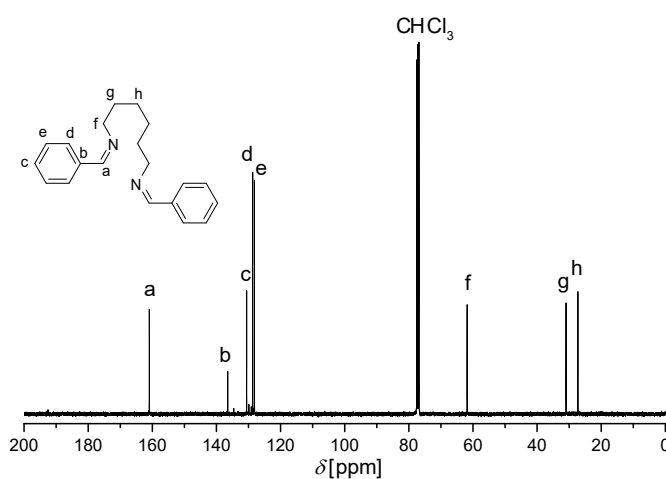
Figure 4.39: ^{13}C NMR spectrum of **21** in CDCl$_3$.

4.11.3.3 Copolymerizations

FRP, M$_n$ = 500 kDa, f = 0.5 %
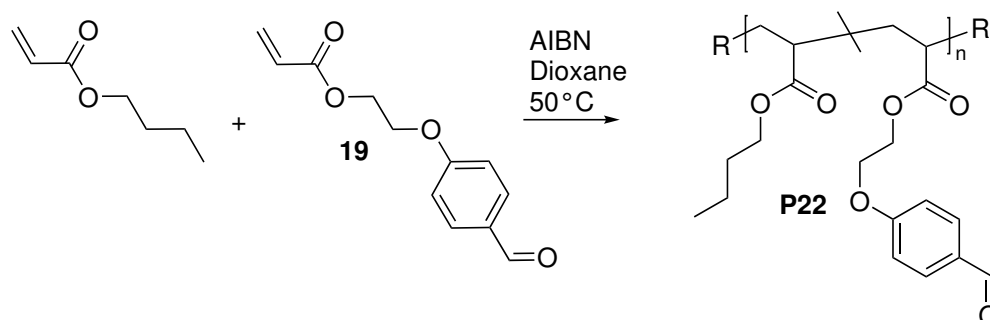
Scheme 4.31: Copolymer **P22** with 0.5 % pendent aldehyde functions prepared by FRP.

General Procedure:

In a typical experiment, 10k eq of *n*BA, 50 eq of monomer **19**, 1.00 eq of AIBN in a dioxane stock solution, and dioxane (1 : 1 v/v to *n*BA) were added to a 25 mL Schlenk tube. The tube was sealed with a septum and oxygen was removed by bubbling nitrogen for 1 h. Subsequently, the tube was placed in an oil bath thermostated at 50 °C. When a monomer conversion of 65 % was reached (approx. 40 h), the polymerization was stopped by cooling down the mixture and exposing it to air. The mixture was diluted with THF and precipitated twice in a mixture of MeOH : H$_2$O 10 : 1. The polymer was dried at 50 °C under vacuum to yield a slightly yellowish, transparent, viscous polymer.

For the calculation of the composition of the copolymer, the NMR proton signals (compare Figure 4.40) of the functional monomer (H$_b$, 2H) and of the *n*BA (H$_m$, 3H) were employed.

Typical values: M_n = 400 kDa, Đ = 2.1; DP$_n$ = 3100, N$_f$ = 15.5, f = 0.5 %;

^{1}H NMR (400 MHz, CDCl$_3$, 298 K): δ [ppm] = 9.89 (s, n×1H, O=C-**H**), 7.84 (d, n×2H, **H$_{Ar}$**), 7.04 (d, n×2H, **H$_{Ar}$**), 4.03 (m, n×6H, O-C**H$_2$**), 2.27 (m, n×2H, C**H$_{backbone}$**), 1.89 (m, n×2H, C**H$_{backbone}$**), 1.58 (m, n×2H, C**H$_2$**), 1.58-1.28 (m, n×2H, C**H$_{backbone}$**), 1.29 (m, n×2H, C**H$_2$**), 0.93 (t, n×3H, C**H$_3$**).
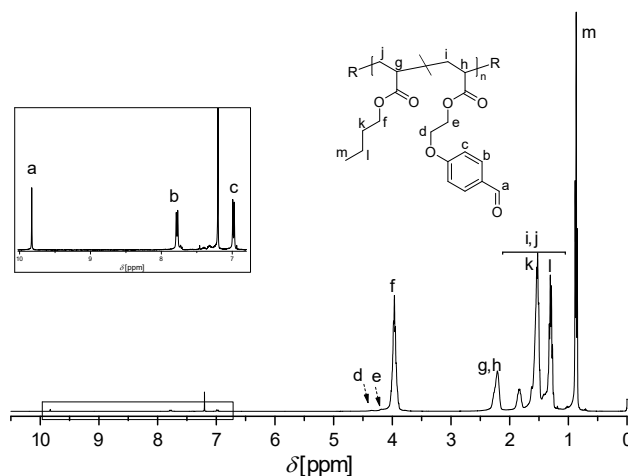
Figure 4.40: ^{1}H NMR spectrum of copolymer **P22** in CDCl$_3$.

RAFT Polymerization, M$_n$ = 500 kDa, f = 2.0 %
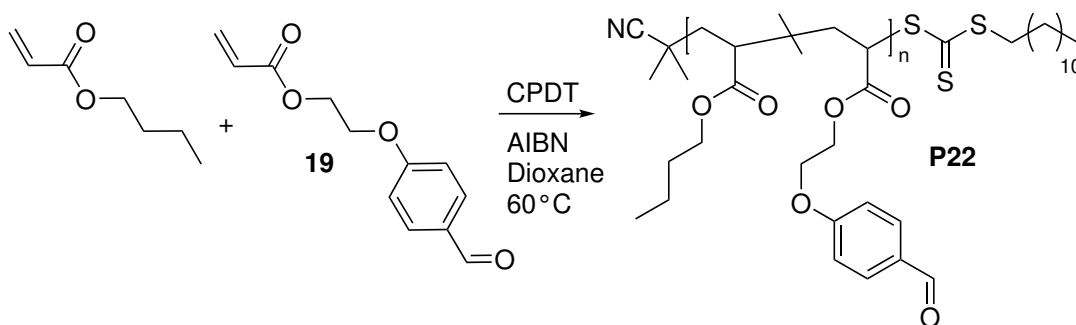
Scheme 4.32: Copolymer **P23** with 2 % pendent aldehyde functions prepared by RAFT polymerization.

11.2 mL of *n*BA (10.0 g, 78 mmol, 5,000 eq), 343 mg of monomer **19** (1.56 mmol, 100 eq), 0.54 mL of a CPDT solution (100 mg CPDT in 10.0 mL dioxane) resulting in 5.4 mg (15.6 µmol, 1.00 eq), 0.3 mL of an AIBN solution (26.0 mg AIBN in 10.00 mL dioxane) resulting in 769 µg (4.68 µmol, 0.30 eq), and 10 mL of dioxane were mixed and distributed equally to two 20 mL headspace vials A and B that were subsequently sealed with a septum. Oxygen was removed by bubbling nitrogen for 30 min. The vials were placed in a heating block thermostated at 60 °C. Samples for SEC were taken with a nitrogen flooded syringe after 21, 26, 41 and 50 h (see Table 4.11). The polymerization was then stopped by cooling, while exposing the sample to air and adding THF.

Table 4.11: Kinetic of the RAFT copolymerization of monomer **19** and *n*BA.

Time (h)	21	26	41	50
A M_n (SEC) (Da)	18700	24300	59500	86000
B M_n (SEC) (Da)	25000	26000	81000	116000

SEC Sample A: M_n = 86 kDa, M_w = 139 kDa, Đ = 1.60;
SEC Sample B: M_n = 116 kDa, M_w = 192 kDa, Đ = 1.66;

Test ARGET-ATRP (homopolymerization), M$_n$ = 500 kDa, f = 0 %
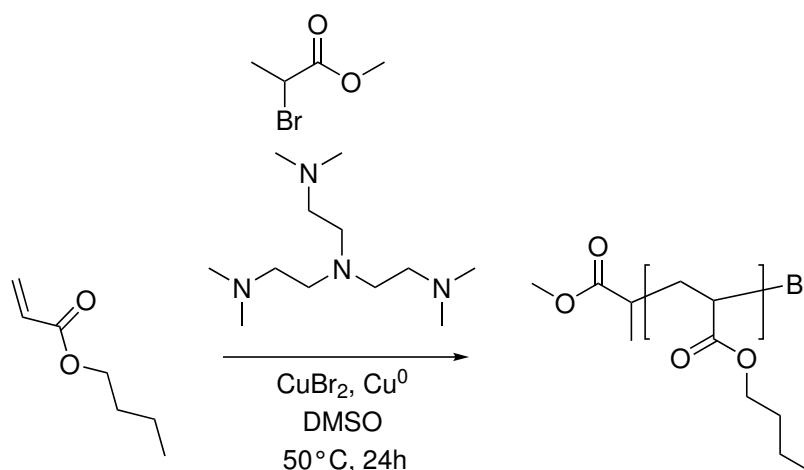
Scheme 4.33: P*n*BA test polymerization prepared by ARGET-ATRP.

A stirring bar was wrapped with a copper wire and placed into a 50 mL Schlenk tube. The tube was sealed, set under N_2 and 2 mL of HCl$_{conc.}$ added. The mix was heated until the HCl$_{conc.}$ boiled and then let cool down. The HCl$_{conc.}$ was removed and the stirring bar rinsed with several mLs of deionized water. The flask was flame dried under vacuum and 10.0 mL of *n*BA (8.90 g, 69.4 mmol, 6,000 eq), 0.25 mL of a CuBr$_2$ solution (10.0 mg CuBr$_2$ in 10.0 mL DMSO) resulting in 250 µg (1.16 µmol, 0.10 eq), 0.21 mL of an Me$_6$TREN solution (25.0 mg Me$_6$TREN in 10.0 mL DMSO) resulting in 533 µg (2.31 µmol, 0.20 eq), and 10 mL of DMSO were added to the flask. The mixture was freed from oxygen by three consecutive freeze-pump-thaw (FPT) cycles, before 0.193 mL of a MBP solution (100 mg MBP in 10.0 mL DMSO) resulting in 1.93 mg (11.6 µmol, 1.00 eq) was added and another two FPT cycles were performed. The flask was heated

to 50 °C. Phase separation occurred between the polymer and the rest of the mixture after 1-2 h. After 2, 4, 6, and 24 h, samples were withdrawn from the reaction mixture using a nitrogen flooded syringe for SEC and/or NMR analysis. After 24 h, the polymerization was stopped at 79 % monomer conversion by exposing the mixture to air and decanting the liquid phase. The polymer was dissolved in THF and filtered through a short column of basic alumina. The polymer was then precipitated in MeOH : H_2O (10 : 1) to yield 5.35 g (60 %) of a colorless, transparent, viscous liquid.

SEC: M_n = 568 kDa, M_w = 763 kDa, $Đ$ = 1.34;

Table 4.12: Kinetic of the ARGET-ATRP of *n*BA.

Time [h]	2	4	6	24
M_n (SEC) [kDa]	392	370	424	535
M_n(theo) (NMR) [kDa]*	-	-	549	606
X [%]	-	-	71	79
$Đ$	1.18	1.24	1.20	1.41

*calculated via Equation 4.15, with X, the monomer conversion, determined by the ratio of integrals of the acrylate and the DMSO signals of the NMR spectra.

$$M_{n,theo} = M(I) + \left(\frac{[nBA]_0}{[I]_0} \times M(nBA) \right) \times X \qquad (4.15)$$

ARGET-ATRP, M$_n$ = 500 kDa, f = 2.0 %
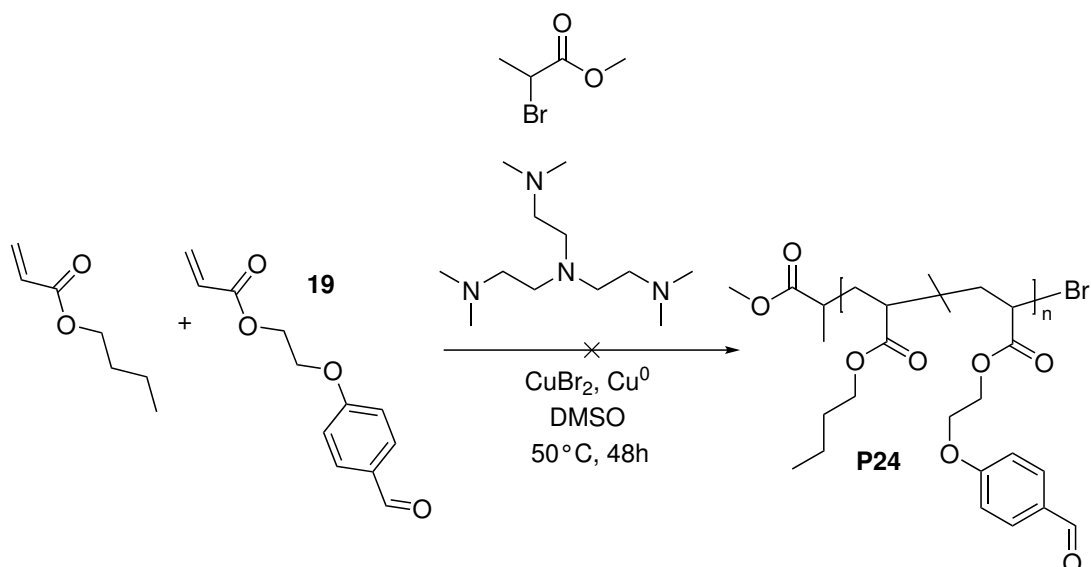
Scheme 4.34: Copolymer **P24** with pendent aldehyde functions prepared by ARGET-ATRP.

In a typical experiment, a stirring bar was wrapped with a copper wire and placed inside a 50 mL Schlenk tube. The tube was sealed, set under N$_2$ and 2 mL of HCl$_{conc.}$ were added. The mix was heated until the HCl$_{conc.}$ boiled. The flask was cooled down and the HCl$_{conc.}$ was removed. The stirring bar was rinsed two times with several mLs of deionized water, before the flask was flame dried. 10.0 mL of *n*BA (8.90 g, 69.4 mmol, 6,000 eq), 325 mg of the aldehyde monomer **19** (1.42 mmol, 123 eq), 0.25 mL of a CuBr$_2$ solution (10.0 mg CuBr$_2$ in 10.0 mL DMSO) resulting in 250 μg (1.16 μmol, 0.10 eq), 0.210 mL of an Me$_6$TREN solution (25.0 mg Me$_6$TREN in 10.0 mL DMSO) resulting in 533 μg (2.31 μmol, 0.20 eq), and 10 mL of DMSO were added to the flask. The mixture was freed from oxygen by three consecutive FPT cycles, before 0.193 mL of an MBP solution (100 mg MBP in 10.0 mL DMSO) resulting in 1.93 mg (11.6 μmol, 1.00 eq) was added and another two FPT cycles were performed. The flask was heated to 50 °C. Either no polymerization could be observed or the polymer was obtained crosslinked.

FRP, M$_n$ = 500 kDa, f = 2.0 %
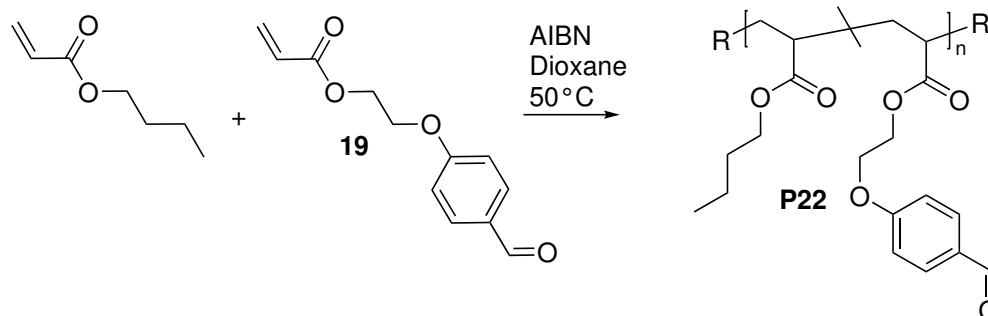
Scheme 4.35: Copolymer **P22**a with 2.0 % pendent aldehyde functions prepared by FRP.

In a typical experiment, 12.0 mL of *n*BA (10.7 g, 83.5 mmol, 10k eq), 375 mg of the aldehyde monomer **19** (1.70 μmol, 204 eq), 10 mL of dioxane and 0.52 mL of an AIBN solution (2.6 mg AIBN/ 1 mL dioxane) resulting in 1.37 mg (8.35 μmol, 1.00 eq) were added to a 50 mL Schlenk tube. The tube was sealed with a septum and oxygen was removed by bubbling with nitrogen for 2 h. Subsequently, the tube was placed into an oil bath thermostated to 50°C for 24-48 h. To stop the polymerization the mixture was cooled down, while exposing it to air and adding some mLs of THF.

-The polymer was crosslinked. A insoluble gel was obtained.
-After 48 h (33 % conversion) the mixture was diluted with THF and precipitated twice in a mixture of MeOH : H$_2$O 10 : 1. The polymer was dried at 80°C under vacuum to yield a insoluble, crosslinked polymer.

ARGET-ATRP, M$_n$ = 500 kDa, f = 2.0 %, acetal protected monomer
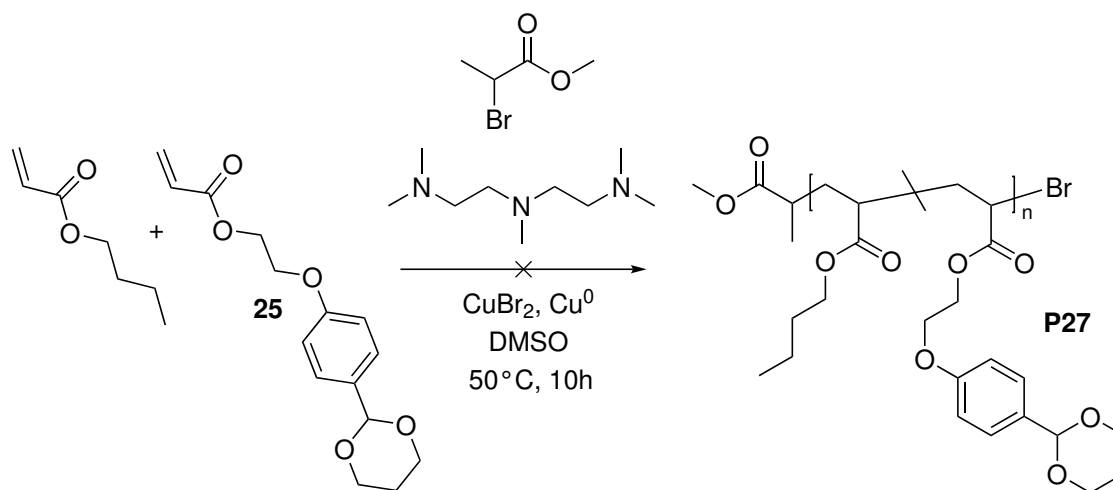
Scheme 4.36: Copolymer **P27** with pendent acetal protected aldehyde functions prepared by ARGET-ATRP.

The procedure was conducted like described in Subsubsection 4.11.3.3 instead of monomer **19**, the acetal protected aldehyde monomer **31** (396 mg, 1.42 mmol, 123 eq) was used. After 67 h, the polymerization was stopped and the product precipitated into MeOH/H$_2$O. The polymer was dried under vacuum, during which it crosslinked to an insoluble material.

FRP, M$_n$ = 100 kDa, f = 2.0 %
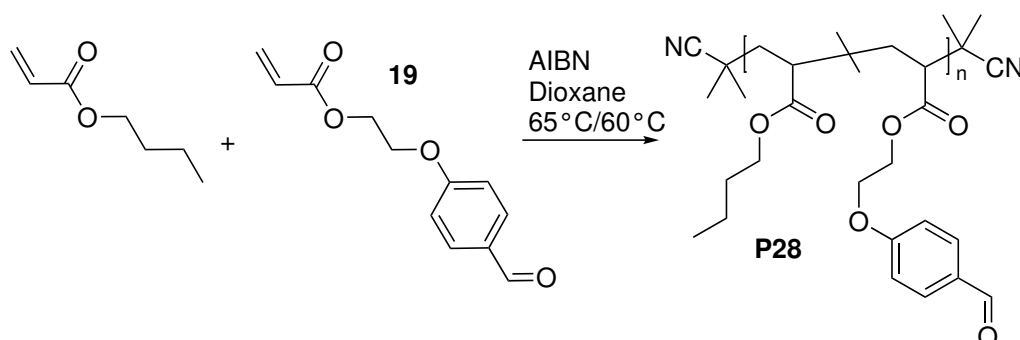
Scheme 4.37: Copolymer **P28** with 2.0 % pendent aldehyde functions prepared by FRP.

10.0 mL of *n*BA (8.90 g, 69.4 mmol, 2500 eq), 312 mg of the aldehyde monomer **19** (1.41 μmol, 51 eq), 12 mL (or 22 mL) of dioxane and 1.75 mL of an AIBN solution (2.6 mg AIBN/ 1 mL dioxane) resulting in 4.56 mg (27.8 μmol, 1.00 eq) were added to a 50 mL Schlenk tube. The tube was sealed with a septum and oxygen was removed by bubbling nitrogen for 2 h. Subsequently, the tube was placed into an oil bath thermostated at 65°C (60°C) for 4 h (7.5 h). A kinetic study was conducted: samples were taken after 1, 2, 3, and 4 h (1, 2, 3, 4, 5, 6 and 7.5 h). To terminate the polymerization the mixture was exposed to air and THF was added. The polymer was precipitated 2 times into MeOH : H_2O (10 : 1 v/v). The resulting polymer was dried under vacuum at 80°C.

Table 4.13: Data of kinetic study of the FRP of nBA and the aldehyde monomer **19** with $[nBA]_0 : [\mathbf{19}]_0 : [AIBN]_0 = 2{,}500 : 51 : 1$, with 1 : 1 (v/v) dioxane : *n*BA at 65 °C.

t (h)	X [%]	M_n [kDa]	Đ
1	6	275	2.20
2	62	198	3.73
3	73	188	4.60
4	82	134	6.20

Table 4.14: Data of kinetic study of the FRP of nBA and the aldehyde monomer **19** with $[nBA]_0 : [\mathbf{19}]_0 : [AIBN]_0 = 2{,}500 : 51 : 1$, with 2 : 1 (v/v) dioxane : *n*BA at 60 °C.

t (h)	X [%]	M_n [kDa]	Đ
1	0	-	-
2	0	-	-
3	9	202	1.90
4	23	206	1.90
5	35	187	2.07
6	46	179	2.19
7.5	48	156	2.34

RAFT, M$_n$ = 100 kDa, f = 2.0 %
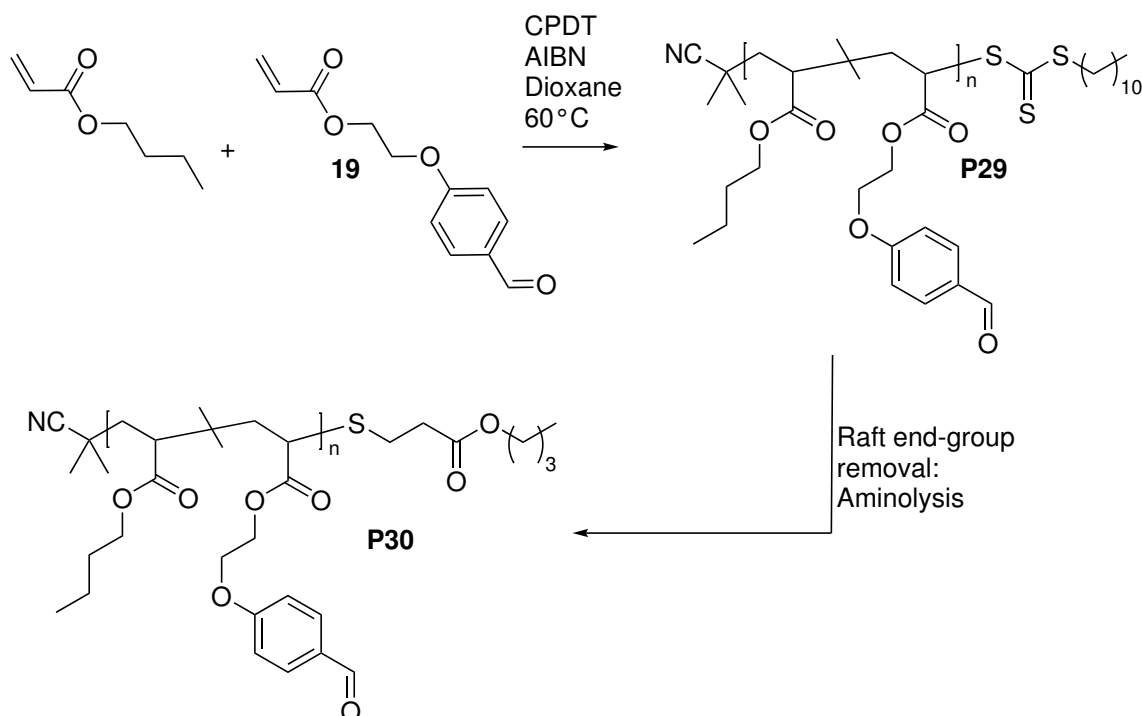
Scheme 4.38: Copolymer **P30** with 2 % pendent aldehyde functions prepared by RAFT polymerization with subsequent aminolysis.

General procedure:

In a typical experiment, 20.0 mL of *n*BA (17.8 g, 139 mmol, 1000 eq), 642 mg of **19** (2.92 mmol, 21 eq), 2.40 mL of a CPDT solution (200 mg CPDT in 10.0 mL dioxane) resulting in 48.0 mg (138 μmol, 1.00 eq), 1.75 mL of an AIBN solution (26.0 mg AIBN in 10.0 mL dioxane) resulting in 4.6 mg (27.8 μmol, 0.20 eq), and 20 mL of dioxane were added to a 100 mL Schlenk flask. The tube was sealed with a septum and oxygen was removed by bubbling nitrogen for 2 h. Subsequently, the tube was placed into an oil bath thermostated at 60 °C for 16 h (80-90 % conversion). The polymerization was stopped by cooling it, while exposing it to air and a subsequent addition of around 100 mL of THF.

1) No RAFT end-group removal: In case the RAFT end-group was not removed, the polymer was precipitated twice in a mixture of MeOH : H$_2$O 10 : 1. The polymer was obtained as a yellow, transparent, viscous liquid.

2) RAFT end-group removal with HCl: A catalytic amount of TCEP was added, before

the mixture was again bubbled with nitrogen. 1.5 mL of *n*-butylamine were added (1.11 g, 15.3 mmol, 110 eq), after 30 min 1 mL of additional *n*BA was added. After 24 h, 8 mL of HCl (6 M) were added. The mixture became opaque and stirred for another 24 h. Subsequently, the mixture was concentrated and precipitated twice in MeOH : H_2O (1 : 1) to yield a slightly yellow, transparent, viscous liquid polymer.

3) RAFT end-group removal with HCl and NEt$_3$: A catalytic amount of TCEP was added, before the mixture was again bubbled with nitrogen. 1.5 mL of *n*-butylamine were added (1.11 g, 15.3 mmol, 110 eq), after 30 min, 1 mL of additional *n*BA was added. The mixture became less yellow. After 24 h, 8 mL of HCl (6 M) were added. The mixture became opaque and stirred for another 24 h. Subsequently, the mixture was concentrated and precipitated once in MeOH : H_2O (1 : 1). The polymer was taken up in THF and NEt$_3$ was added until the solution turned slightly basic. The polymer was precipitated twice in MeOH : H_2O (1 : 1) and the solvent was removed. An insoluble salt formed inside the polymer. The polymer was dissolved in THF and filtered. The solvent was removed and the polymer obtained as a slightly yellow, transparent, viscous liquid.

4) RAFT end-group removal with benzaldehyde: A catalytic amount of TCEP and 5 mL of water were added before the mixture was again bubbled with nitrogen. 1.2 mL of *n*-butylamine were added (914 mg, 12.5 mmol, 90.0 eq), after 30 min 1 mL of additional *n*BA was added. The mixture became less yellow. After 4 h, 12.7 mL of benzaldehyde (13.2 g, 125 mmol, 900 eq) were added. The mixture was allowed to stir for another 24 h. Subsequently, the mixture was concentrated and precipitated three times into MeOH : H_2O 10 : 1 to yield a slightly yellow, transparent, viscous liquid polymer **P30**.

Typical values: SEC: M_n = 90 kDa, $Đ$ = 1.3; DP$_n$ = 690, N_f = 13.8, f = 2.0 %;

¹H NMR (400 MHz, CDCl$_3$, 298 K): δ [ppm] = 9.89 (s, n×1H, O=C-**H**), 7.84 (d, n×2H, **H$_{Ar}$**), 7.04 (d, n×2H, **H$_{Ar}$**), 4.35 (m, n×2H, O-C**H$_2$**), 4.18 (m, n×2H, O-C**H$_2$**), 4.03 (m, n×2H, O-C**H$_2$**), 2.27 (m, n×2H, C**H$_{backbone}$**), 1.89 (m, n×2H, C**H$_{backbone}$**), 1.58 (m, n×2H, C**H$_2$**), 1.58-1.28 (m, n×2H, C**H$_{backbone}$**), 1.29 (m, n×2H, C**H$_2$**), 0.93 (t, n×3H, C**H$_3$**).
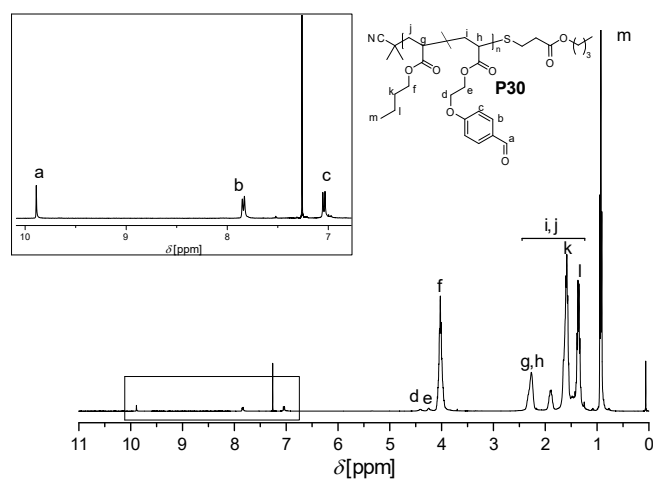
Figure 4.41: ^{1}H NMR spectrum of the aldehyde copolymer **P30** prepared via RAFT polymerization in CDCl$_3$.

Bibliography

(1) Ciaccia, M.; Di Stefano, S.; Stefano, S. D. *Org. Biomol. Chem.* **2015**, *13*, 646–654.

(2) Schiff, H. *Justus Liebigs Ann. Chem.* **1864**, *131*, 118–119.

(3) Ladenburg, A. *Berichte der Dtsch. Chem. Gesellschaft* **1883**, *16*, 1149–1152.

(4) Layer, R. W. *Chem. Rev.* **1963**, *63*, 489–510.

(5) Carey, F. A.; Sundberg, R. J., *Advanced Organic Chemistry*, 5th ed.; Springer: New York, NY, USA, 2007.

(6) Belowich, M. E.; Stoddart, J. F. *Chem. Soc. Rev* **2012**, *41*, 2003–2024.

(7) Röttger, M. Associative Exchange Reactions of Boron or Nitrogen Containing Bonds and Design of Vitrimers, Ph.D. Thesis, Université Pierre et Marie Curie - Paris VI, 2016.

(8) Ciaccia, M.; Cacciapaglia, R.; Mencarelli, P.; Mandolini, L.; Stefano, S. D. *Chem. Sci.* **2013**, *4*, 2253.

(9) O, R.; JM, L. *Nat. Rev. Drug Discov.* **2002**, *1*, 26–36.

(10) Meyer, C. D.; Joiner, S.; Stoddart, J. F.; Meier, M. A. R.; Metzger, J. O.; Schubert, U. S. *Chem Soc Rev Pages* **2007**, *36*, 1697–1844.

(11) Giuseppone, N. *Acc. Chem. Res.* **2011**, *45*, 2178–2188.

(12) Von Delius, M.; Geertsema, E. M.; Leigh, D. A. *Nat. Chem.* **2010**, *2*, 96–101.

(13) Garrabou, X.; M Wicky, B. I.; Hilvert, D. *J. Am. Chem. Soc* **2016**, *138*, 6972–6974.

(14) Uribe-Romo, F. J.; Hunt, J. R.; Furukawa, H.; Klö, C.; O'keeffe, M.; Yaghi, O. M. *J. Am. Chem. Soc.* **2009**, *131*, 4570–4571.

(15) Guo, B.; Finne-Wistrand, A.; Albertsson, A.-C. *Biomacromolecules* **2011**, *12*, 2601–2609.

(16) Li, H.; Bai, J.; Shi, Z.; Yin, J. *Polymer (Guildf).* **2016**, *85*, 106–113.

(17) Ma, S.; Webster, D. C. *Prog. Polym. Sci.* **2018**, *76*, 65–110.

(18) Xie, W.; Huang, S.; Liu, S.; Zhao, J. *Chem. Eng. J.* **2021**, *404*, 126598.

(19) Lei, Z. Q.; Xie, P.; Rong, M. Z.; Zhang, M. Q. *J. Mater. Chem. A* **2015**, *3*, 19662–19668.

(20) Zhang, H.; Wang, D.; Liu, W.; Li, P.; Liu, J.; Liu, C.; Zhang, J.; Zhao, N.; Xu, J. *J. Polym. Sci. Part A Polym. Chem.* **2017**, *55*, 2011–2018.

(21) Li, X.; Wu, T. *J. Appl. Polym. Sci.* **2021**, *138*, 50953.

(22) Zhu, C.; Xi, C.; Doro, W.; Wang, T.; Zhang, X.; Jin, Y.; Zhang, W. *RSC Adv.* **2017**, *7*, 48303–48307.

(23) Taynton, P.; Yu, K.; Shoemaker, R. K.; Jin, Y.; Qi, H. J.; Zhang, W. *Adv. Mater.* **2014**, *26*, 3938–3942.

(24) Taynton, P.; Ni, H.; Zhu, C.; Yu, K.; Loob, S.; Jin, Y.; Qi, H. J.; Zhang, W. *Adv. Mater.* **2016**, *28*, 2904–2909.

(25) Zheng, H.; Liu, Q.; Lei, X.; Chen, Y.; Zhang, B.; Zhang, Q. *J. Mater. Sci.* **2019**, *54*, 2690–2698.

(26) Zheng, H.; Liu, Q.; Lei, X.; Chen, Y.; Zhang, B.; Zhang, Q. *J. Polym. Sci. Part A Polym. Chem.* **2018**, *56*, 2531–2538.

(27) Wang, S.; Ma, S.; Li, Q.; Xu, X.; Wang, B.; Huang, K.; Liu, Y.; Zhu, J. *Macromolecules* **2020**, *53*, 2919–2931.

(28) Hajj, R.; Duval, A.; Dhers, S.; Avérous, L. *Macromolecules* **2020**, *53*, 3796–3805.

(29) Jackson, A. W.; Stakes, C.; Fulton, D. A. *Polym. Chem.* **2011**, *2*, 2500–2511.

(30) Ma, G.; Li, A. D.; Wang, A. J.; Zhang, A. X. *Aust. J. Chem.* **2013**, *66*, 1576–1583.

(31) Perrier, S. S. *Macromolecules* **2017**, *50*, 7433–7447.

(32) Magenau, A. J.; Kwak, Y.; Matyjaszewski, K. *Macromolecules* **2010**, *43*, 9682–9689.

(33) Matyjaszewski, K.; Tsarevsky, N. V.; Braunecker, W. A.; Dong, H.; Huang, J.; Jakubowski, W.; Kwak, Y.; Nicolay, R.; Tang, W.; Yoon, J. A. *Macromolecules* **2007**, *40*, 7795–7806.

(34) Konkolewicz, D.; Wang, Y.; Krys, P.; Zhong, M.; Isse, A. A.; Gennaro, A.; Matyjaszewski, K. *Polym. Chem.* **2014**, *5*, 4396–4417.

(35) Augustine, K. F.; Ribelli, T. G.; Fantin, M.; Krys, P.; Cong, Y.; Matyjaszewski, K. *J. Polym. Sci. Part A Polym. Chem.* **2017**, *55*, 3048–3057.

(36) Hine, J.; Craig, J. C.; Underwood, J. G.; Via, F. A. *J. Am. Chem. Soc.* **1970**, *92*, 5194–5199.

(37) Anadi Dash, B. C.; Dash, B.; Praharaj, S. *J. Chem. Soc., Dalt. Trans.* **1981**, 2063–2069.

(38)   Ricarte, R. G.; Ois Tournilhac, F.; Cloître, M.; Leibler, L. *Macromolecules* **2020**, *53*, 1852–1866.

5 | Dual Dynamic Networks of P*n*BA Vitrimers Based on Imine-Aldehyde and Dioxaborolane Exchanges

Chapter Contents

5.1 Introduction

DDNs offer numerous possibilities in terms of material design. Employing two or more dynamic modes in one system allows the precise tailoring of thermal, rheological, and mechanical properties of a material. DDNs are able to unite diverse responses and abilities in a single system and have the capacity to combine dimensional stability, bond dynamicity, and multi-responsiveness. A key challenge in the design of DDNs is to identify the adequate combination of crosslinkers to obtain the targeted set of properties. The employed crosslinking strategies have to fulfill the premises of orthogonality and facile implementation into the system. Furthermore, they have to show sufficiently contrasted properties (in terms of bond dynamicity or responsiveness) to create an added value to the system. The aim of this thesis is to create a vitrimer DDN based on boronic ester and imine-aldehyde exchanges. The goal is to evaluate, if a double dynamic system comprising these bonds can be prepared and to finely characterize it in order to assess the potential of such systems. The targeted network consists of two interpenetrated subnetworks, one crosslinked by dioxaborolanes and the other by imines. The network will be synthesized from functional TPs, which will be crosslinked simultaneously as presented in Figure 5.1.
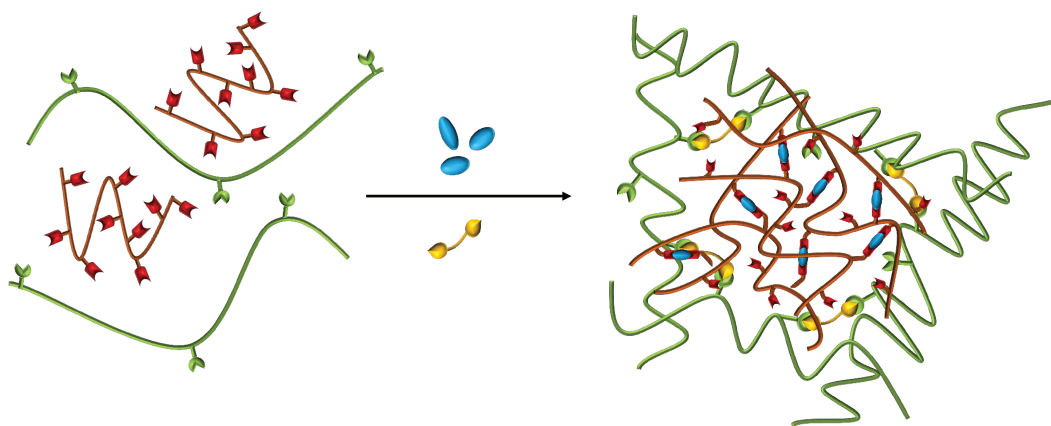
Figure 5.1: Synthetic strategy to create the DDN. Two functional thermoplastics are crosslinked simultaneously. The orthogonality of the reactions is essential to obtain an interpenetrated network with two independent subnetworks.

The orthogonality of the two dynamic bonds is sine qua non condition for the two networks to be interpenetrated but not connected to each other. The so obtained material will

be carefully characterized to see, how the individual subnetworks contribute to the system and if synergistic effects arise. The two subnetworks were envisioned so they feature distinct properties in order to fulfill specific tasks. The boronic ester network should present fast exchange reactions between the dynamic bonds in order to dissipate energy and relax stress under service conditions. Previous studies showed that by introducing sacrificial bonds into a network, stiffness and toughness can be enhanced and material failure can be postponed.[1–3] In this way, for example, Creton and co-workers developed elastomers based on ethylacrylate-methylacrylate double and triple networks that showed significant reinforcement due to bond breakage of sacrificial prestretched chains inside the material.[3] However, the bond breaking in these systems was irreversible, generating permanent damage in the material. Replacing static covalent crosslinks by dynamic covalent bonds could allow enhancing the fatigue resistance of such kinds of materials. The implementation of vitrimer materials in DDN has therefore great potential for innovation in this field. Vitrimers have already been generally employed in DDN (compare Section 1.6), however they functioned as structural component in combination with supramolecular exchange reactions acting as dissipating moieties.[4–7] The application of vitrimer exchanges as dissipating mechanism was not yet explored in DDN. Networks that are dynamic at application temperature typically show limited dimensional stability. The second subnetwork, the structural network, is supposed to compensate this shortcoming. It is designed to hold the dynamic network in place and to impart elasticity to the DDN. The DDN should feature excellent processability and reprocessability. Therefore, both networks were designed to show dynamic behavior at elevated temperature. The vitrimer character of both subnetworks should allow the DDN to be mechanically recycled in its crosslinked form. Next to this mechanical recycling, the responsiveness of the dynamic bonds of both subnetworks gives access to chemical recycling. The orthogonality of the bonds should even allow to separate the interwoven subnetworks from each other and recover the individual TPs.

In this chapter, the preparation and characterization of the DDN employing both boronic ester and imine-aldehyde exchanges is described. First, the orthogonality of the DDN's components was examined. Then the preparation of the DDN is presented, followed by a comparative study of the characteristics of the DDN with the ones of the individual SNs. The thermal, mechanical and rheological properties of the materials are compared and discussed. In the end, the DDN is tested for mechanical and chemical recyclability.

5.2 Orthogonality Tests

The two subnetworks are supposed to be interwoven, but not chemically connected to each other. This requires that the crosslinking process of both networks takes place in an orthogonal fashion. Experiments were conducted to see if this requirement is fulfilled: The TPs of each subnetwork were mixed with an excess of the crosslinking agent of the other network. In addition to that, both TPs were mixed. The mixtures were processed (curing, compression molding) following a procedure similar to that of the DN. After the processing, the mixtures were evaluated to see if the M_n or $Đ$ of the original TP changed or if there had been any chemical changes to the TPs or crosslinkers.

5.2.1 Boronic Ester Thermoplastic With Bis(Imine) Crosslinker

To test the orthogonality of the dioxaborolane TP of **Network 1** with the bis(imine) crosslinker **21** of **Network 3**, both components were combined as presented in Scheme 5.1.
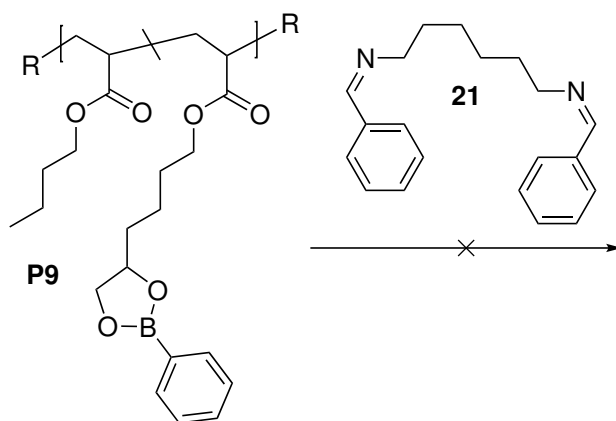
Scheme 5.1: Evaluation of the chemical orthogonality between the dioxaborolane TP **P9** of **Network 1** and the bis(imine) crosslinker **21** of **Network 3**.

0.5 Equivalents of the bis(imine) crosslinker **21** per boronic ester group were mixed with the dioxaborolane TP **P9** and the mixture was cured at 80 °C overnight. The mix was then transferred into a mold and pressed for 3 h at 110 °C with a pressure equivalent of 3 tons, mimicking the compression molding process of the DDN. Subsequently, the (still liquid) mixture was transferred into a vial. To see, if any network formation took place, 10 mL of THF were added. The polymer dissolved completely within minutes, still showing properties of a thermoplastic. An NMR spectrum was recorded to exclude any

chemical changes of the thermoplastic or the crosslinker. In Figure 5.2 the spectra of the bis(imine) crosslinker **21** (red), the pristine dioxaborolane thermoplastic **P9** (blue), and the mix after the compression molding (black) are compared. Apart from the peaks of the starting materials, no other peaks can be found in the spectrum of the mix after the treatment, indicating no chemical changes. SEC was run to detect any changes in M_n or $Đ$ (Figure 5.3). The SEC curves of the dioxaborolane functional polymer before and after the processing in the presence of the bis(imine) crosslinker were almost identical, and fluctuations of M_n and $Đ$ were not significant. No shoulders or other signs of crosslinking could be detected.
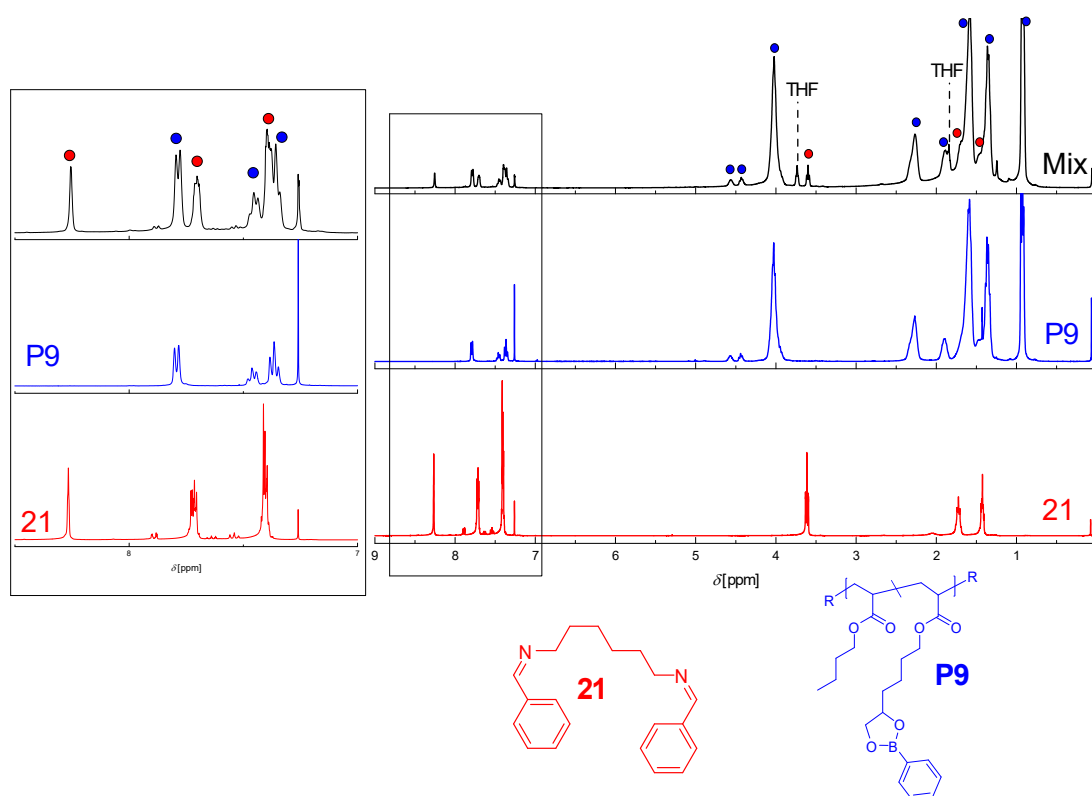
Figure 5.2: ^{1}H NMR in CDCl$_3$ at 400 MHz spectra of the bis(imine) crosslinker **21** (red), the pristine dioxaborolane TP **P9** (blue), and the mix after compression molding (black). Apart from the peaks of the starting materials, no other peaks can be found in the spectrum of the mix after the treatment, indicating no chemical changes.
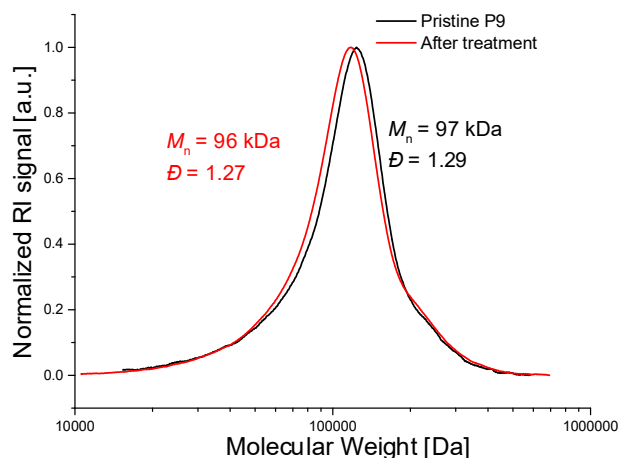
Figure 5.3: SEC curves in THF (PS calibration) of the dioxaborolane TP **P9** before (black) and after the processing with the bis(imine) crosslinker **21** (red).

5.2.2 Aldehyde Thermoplastic With Bis(Boronic Ester) Crosslinker

To test the chemical orthogonality of the aldehyde TP **P30** of **Network 3c** with the bis(boronic ester) crosslinker **10**, **P30** and **10** were combined as presented in Scheme 5.2.
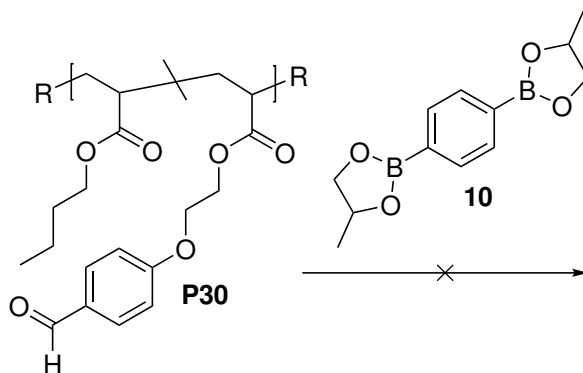
Scheme 5.2: Evaluation of the chemical orthogonality between the aldehyde TP **P30** of **Network 3** and the bis(boronic ester) crosslinker **10** of **Network 1**.

Like for the orthogonality test of **P9**, 0.5 equivalent bis(boronic ester) crosslinker per aldehyde group was used. The sample was cured overnight and compression molded, before the mixture was transferred to a vial and 10 mL of THF were added. The polymer dissolved completely. A NMR was conducted to investigate any chemical changes of the thermoplastic. In Figure 5.4, the spectra of the bis(boronic ester) crosslinker **10** (red),

the pristine aldehyde TP **P30** (blue), and the mix after compression molding (black) are compared.
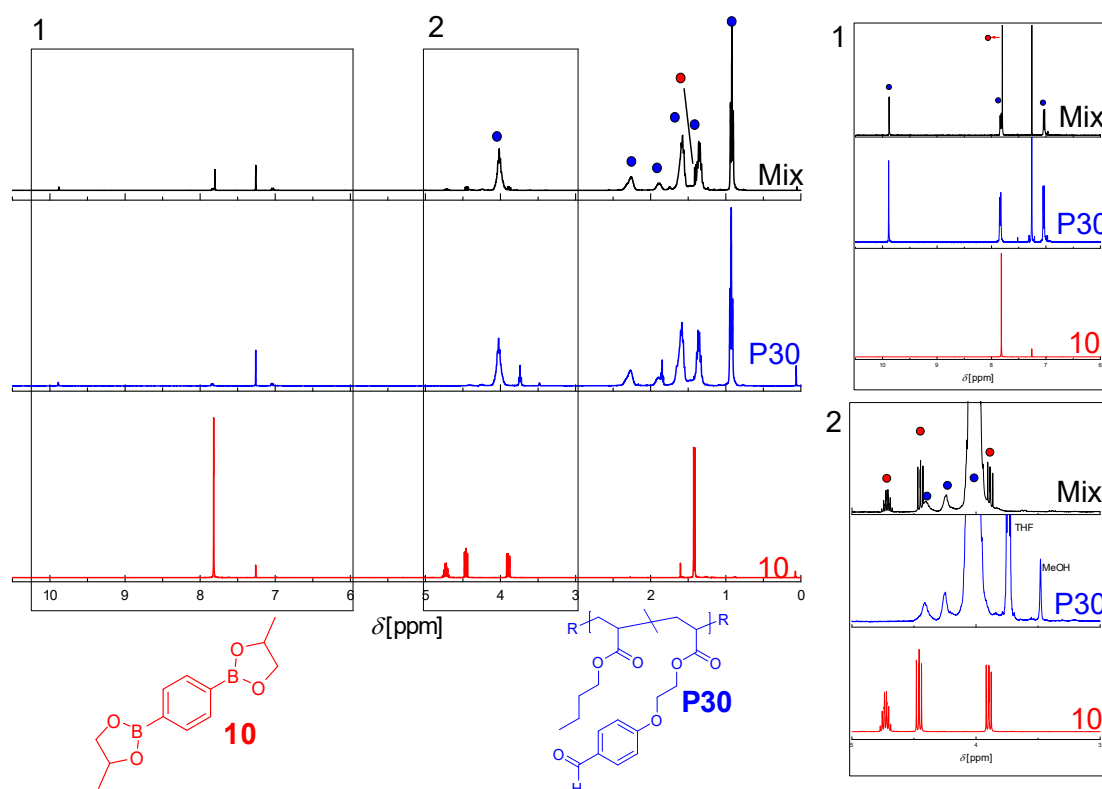
Figure 5.4: ^{1}H NMR spectra in CDCl$_3$ at 400 MHz of the bis(boronic ester) crosslinker **10** (red), the pristine aldehyde TP **P30** (blue), and the mix after the compression molding (black). In the mix all the peaks of the constituent compounds are present, and there are no additional peaks or shifting.

As can be seen, in the mix all the peaks of the constituent compounds are present, and there are no additional peaks or shifting. A SEC was run to compare the material before and after the compression molding (Figure 5.5). No crosslinking or branching could be detected, the curves superimpose. This indicates that there was no chemical reactions between the two compounds, indicating that they are orthogonal to each other under these conditions.
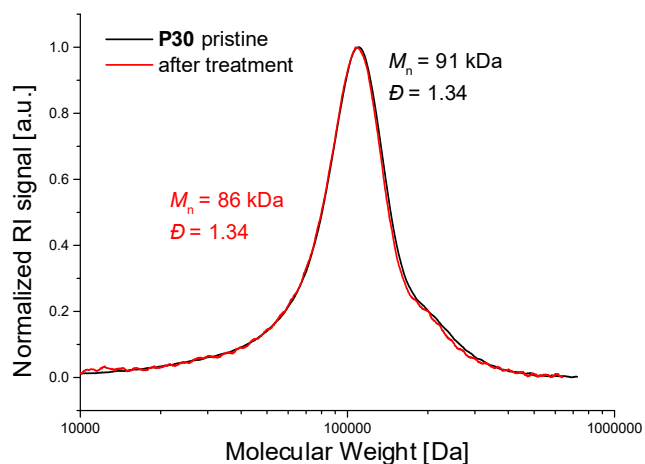
Figure 5.5: SEC curves in THF (PS calibration) of the aldehyde TP **P30** before (black) and after the compression molding with the bis(boronic ester) crosslinker **10** (red).

5.2.3 Boronic Ester Thermoplastic with Aldehyde Thermoplastic

The next experiment was set up to verify that the two TPs are chemically orthogonal to each other. For this experiment, the boronic ester TP **P9** and the aldehyde TP **P30** were mixed and processed following a procedure similar to that of the DDN (Scheme 5.3), including drying at 80 °C overnight and compression molding for 3 h at 110 °C with a pressure equivalent to 3 tons.
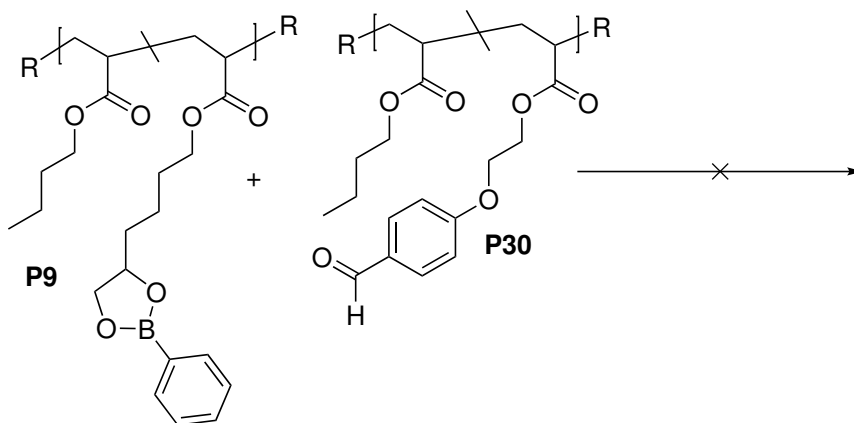
Scheme 5.3: Evaluation of the chemical orthogonality between the TPs **P9** and **P30**. The polymers were mixed and processed together. No chemcial reactions between the two polymers could be detected.

The resulting material was soluble in THF within minutes and analyzed via NMR. As can be seen in Figure 5.6, the NMR after the test only comprises the functional groups of the original TPs **P9** and **P30**, no additional peaks show and no chemical shifts occurred.
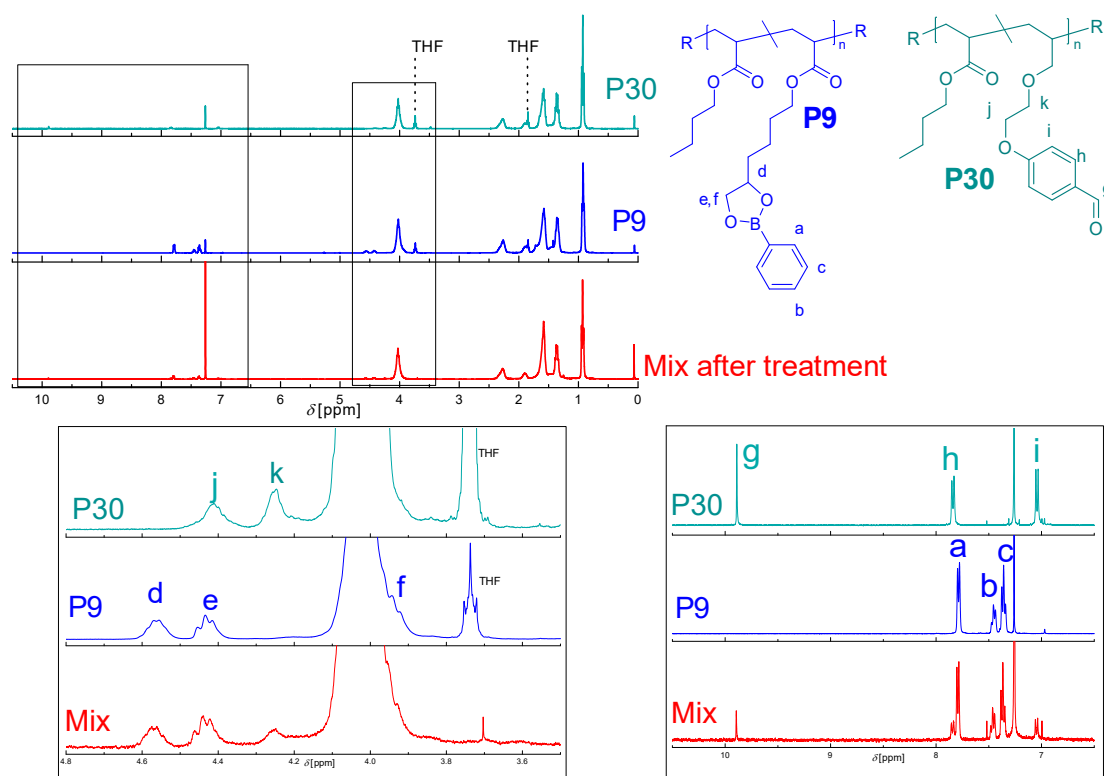
Figure 5.6: ^{1}H NMR spectra in CDCl$_3$ at 400 MHz of the pristine TPs **P9** (blue, middle) and **P30** (cyan, top), and the mix after compression molding (red, bottom). In the mix all the peaks of the constituent TPs are present, and there are no additional peaks or shifting.

5.2.4 Conclusion

The boronic ester and the imine-aldehyde moieties show excellent orthogonality to each other under the conditions used to process the DDN. The boronic ester TP does react neither with the bis(imine) crosslinker nor with the aldehyde TP. The aldehyde TP does react neither with the bis(boronic ester) crosslinker nor with the boronic ester TP. No interference of these compounds is hence expected during the preparation of the DDN.

5.3 Compositions and Syntheses

It is envisioned to create a DDN comprising 50 wt.% of **Network 1** (see Chapter 2.5) and 50 wt.% of **Network 3c** (see Chapter 4.9). This ratio was chosen as a starting point for the design of double dynamic systems comprising these two subnetworks. The ratio can be adapted in response to the outcome of the characterization of the 1 : 1 DN. The formed DN is labeled **DN1-3c**. In order to synthesize the network, the TPs (Scheme 5.4) of the respective subnetworks were combined. The overall properties of the employed TPs are summarized in Table 5.1.
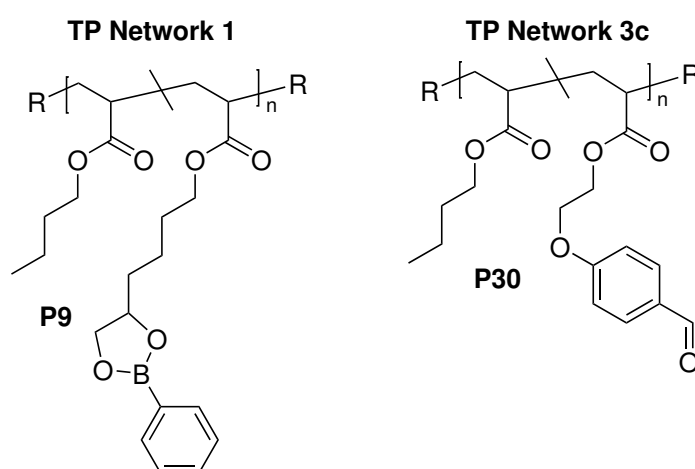
Scheme 5.4: TPs of the DDN. Left: TP **P9** functionalized with a boronic ester moiety. Right: TP **P30** functionalized with an aldehyde moiety.

Table 5.1: Overview over the properties of the employed TPs for the DDN **DN1-3c**. f: functionality, N_f: number of functional groups per chain, f_{CL}: functional groups crosslinked, N_{CL}: number of crosslinks per chain.

TP	Subnetwork	Functional Group	M_n^1 [kDa] DP_n^1	Đ	m [g]	f [%] N_f	f_{CL} [%] N_{CL}
9	**Network 1**	Boronic Ester	100 721	1.22	4.87	9.7 70.3	20 14.1
30	**Network 3c**	Aldehyde	92 713	1.33	4.87	1.95 13.9	25 3.47

1: determined via SEC with a standard PS calibration.

Both TPs are similar in M_n and Đ. The TPs were mixed in equal ratios and analyzed. SEC analysis showed that both TPs eluate around the same time and the curve of the

mixture is still well defined as can be seen in Figure 5.7.
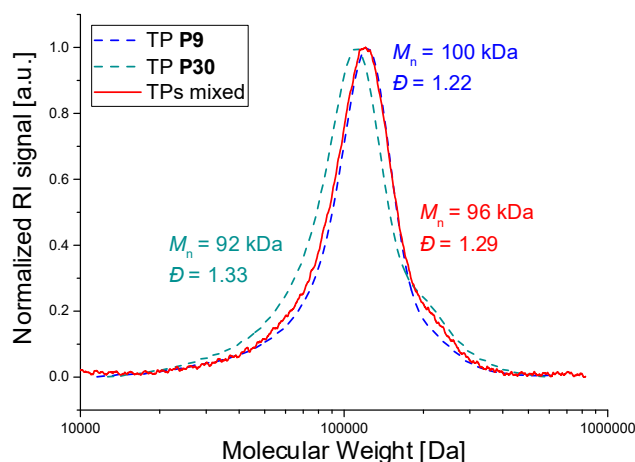
Figure 5.7: SEC traces in THF (PS calibration) of the individual TPs **P9** (boronic ester, blue) and **P30** (aldehyde, cyan), and the the mixture of them (red) used to prepare the DDN.

By combining an equal mass of both, it can be assumed to have an equivalent number of chains in the double network. The NMR spectrum of the combined TPs can be found in Figure 5.8. The integration of the respective functional group peaks (i for **P30** and c for **P9**) and normalization to the respective functionality of the chain reveals a ratio of the TPs of 0.97 : 1.03 (**P9** : **P30**). In the range of the experimental error, one can suppose an equal amount of both thermoplastics.

The united TPs were dissolved in anhydrous THF. The respective amount of crosslinker was calculated with the Equations 5.1 and 5.2. f_{CL} is the ratio of functional groups crosslinked, m(P) the mass of the polymer, f(P) the functionality of the polymer, N_f(CL) the functionality of the crosslinker, and M(M_{Av}(P)) the average molecular mass of the monomers of the respective polymer (calculated with Equation 5.3). The ρ(CL) was set to match the ones of **Network 1** (2 %) and **Network 3c** (0.5 %).

The boronic ester crosslinker showed to gel the network quickly (see Chapter 2.5) and thereby might impede a homogenous distribution of the other crosslinker. Therefore, the bis(imine) crosslinker **21** was added first and mixed with the thermoplastics, before the bis(boronic ester) **10** was added. The network was crosslinked and processed like the least dynamic subnetwork **3c**. The TPs crosslinked to a slightly yellow foam (see Figure 5.9, left). The sample was compression molded like the **Networks 1** and **3c**. After
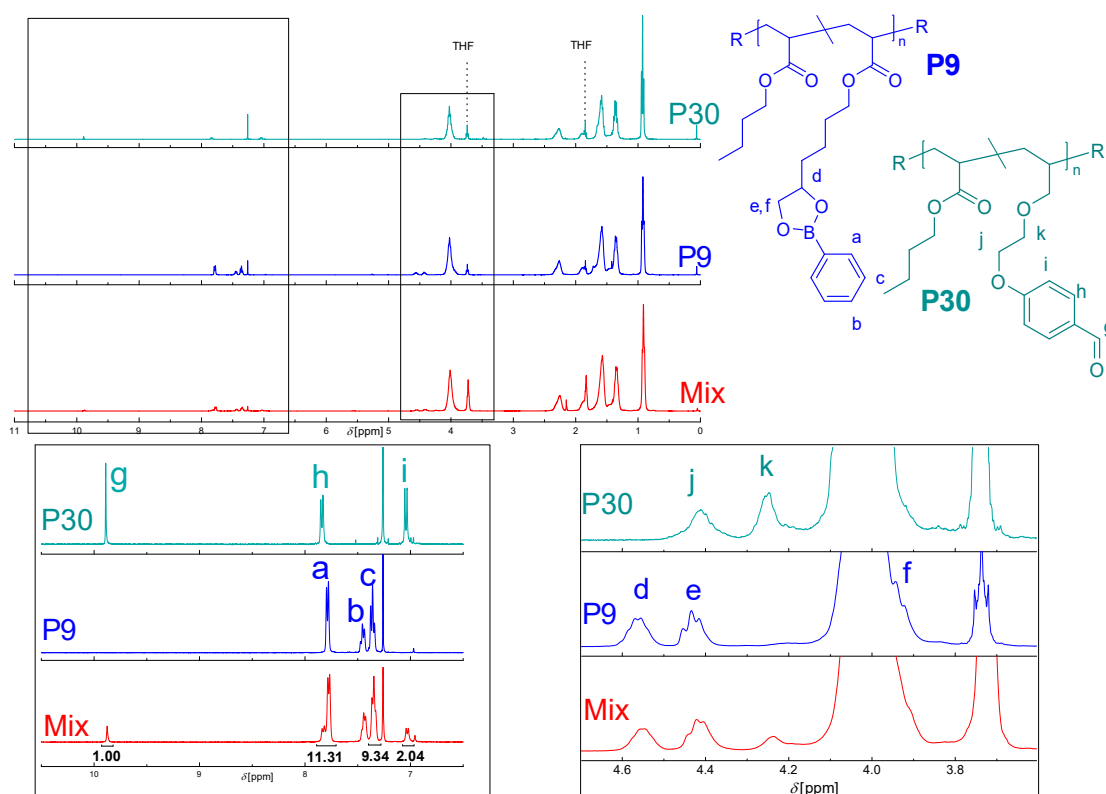
Figure 5.8: ^{1}H NMR spectra in CDCl$_3$ at 400 MHz of the individual TPs **P9** (boronic ester, blue) and **P30** (aldehyde, cyan), and the the mixture of them (red) used to prepare the DDN. The integration area of the respective functional groups reveals a ratio of the TPs of 0.97 : 1.03 (**P9** : **P30**).

20-30 min at 110 °C with a pressure equivalent to 3 tons, a homogenous, slightly yellow elastomer was obtained (Figure 5.9, right).

$$n(10) = \frac{f_{CL}(\mathbf{P9}) \cdot m(\mathbf{P9}) \cdot f(\mathbf{P9})}{N_f(10) \cdot M(M_{Av}(\mathbf{P9}))} \tag{5.1}$$

$$n(21) = \frac{f_{CL}(\mathbf{P30}) \cdot m(\mathbf{P30}) \cdot f(\mathbf{P30})}{N_f(21) \cdot M(M_{Av}(\mathbf{P30}))} \tag{5.2}$$

$$M(M_{Av}(P)) = f(P) \cdot M(FM) + (1 - f(P)) \cdot M(nBA) \tag{5.3}$$
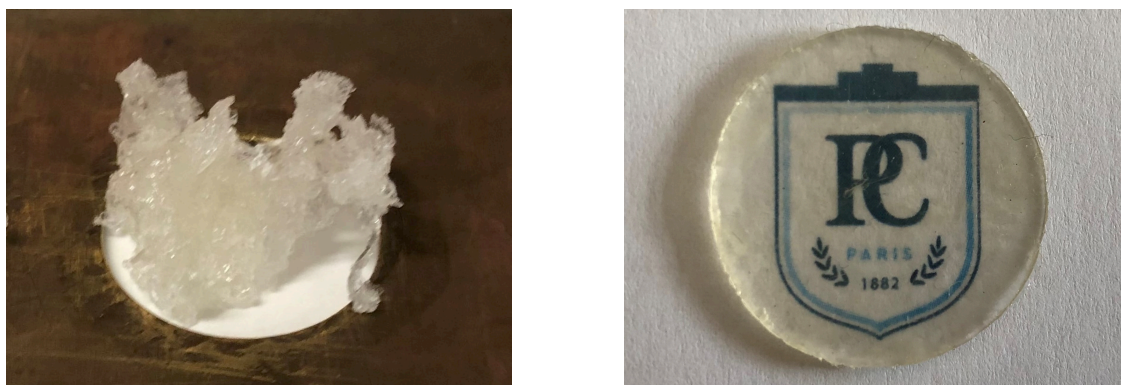
Figure 5.9: Pictures of **DN1-3c**. Left: After the crosslinking, before compression molding. Right: After compression molding.

5.4 Swelling and Solubility Tests

DN1-3c was subjected to swelling and solubility tests. For the experimental conditions and equations to calculate swelling ratio and insoluble fraction refer to the Experimental Part (Section 5.13). After 24 h in THF, the DN has a remaining insoluble fraction of around 95 % (Figure 5.10, left). This value lies in between the ones of **Network 1** and **Network**
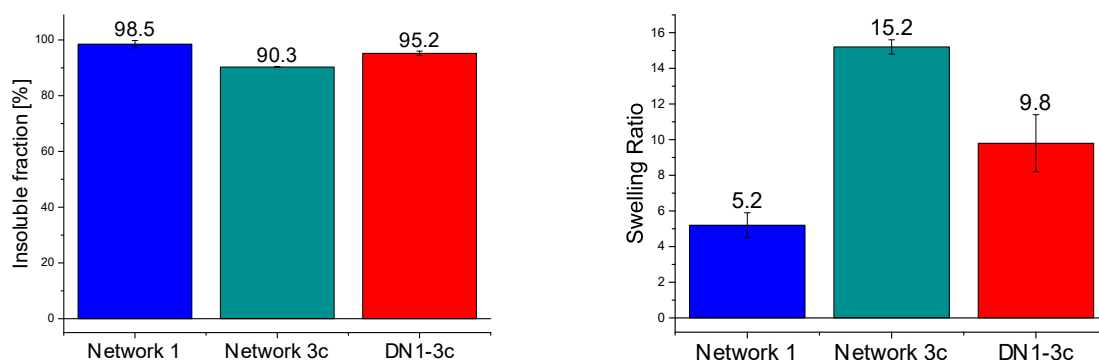
Figure 5.10: Results of the swelling and solubility test of **DN1-3c** (red) in THF over 24 h compared to the single networks **Networks 1** (blue) and **3c** (cyan). Left: Insoluble fraction. Right: Swelling ratio.

3c. This could indicate that both subnetworks in **DN1-3c** exhibit a similar connectivity than the parent SNs. The swelling test (Figure 5.10, right) revealed a swelling ratio of **DN1-3c** in between the SNs. It could have been expected that the more densely crosslinked network (**Network 1**) could have restricted the swelling of the less crosslinked network (**Network 3c**). However, **Network 1** shows a high exchange dynamic in solvent (compare Chapter 2.9.2). Fast rearrangements of the boronic ester bonds in combination with the

swelling pressure of **Network 3c** likely caused **Network 1** to expand more than it does as a single network.

5.5 Thermal Characterization

5.5.1 TGA

In Figure 5.11 the TGA of **DN1-3c** is displayed. The network showed good thermal stability up to 336 °C. During the isothermal measurement at 150 °C, the sample was stable during the entire measuring period of 10 h.
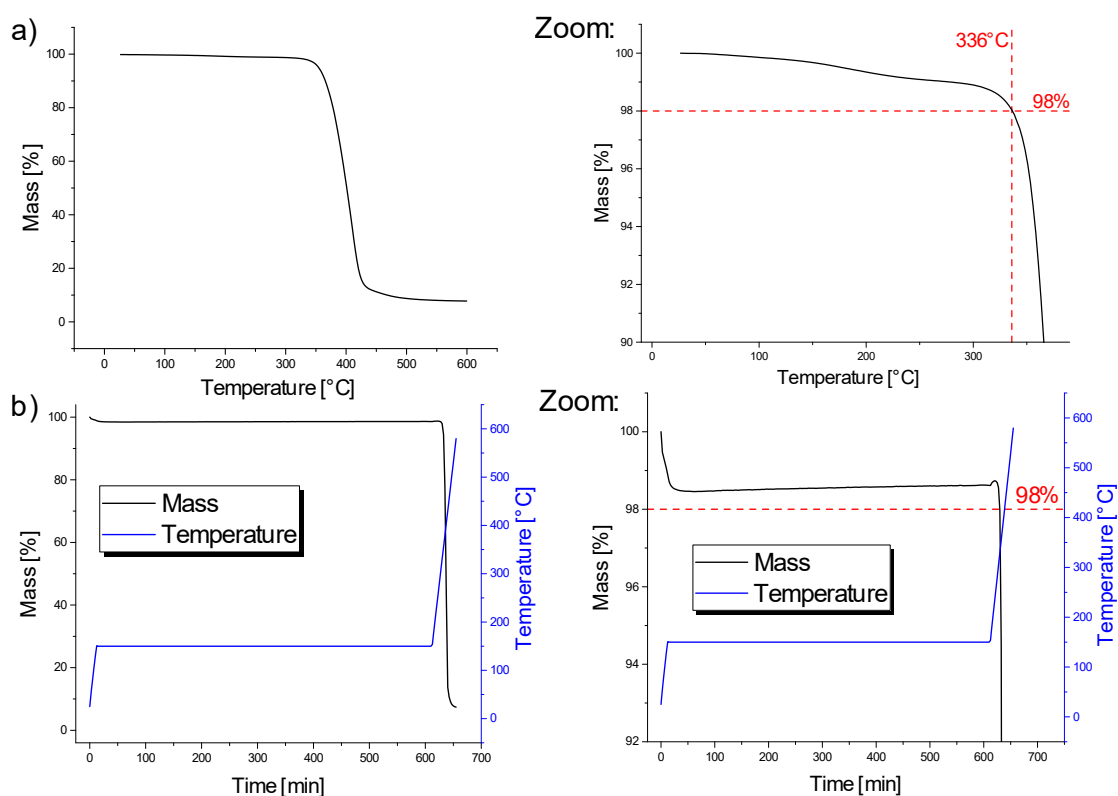
Figure 5.11: TGA of the **DN1-3c**. a) Temperature ramp. b) Isothermal at 150 °C. Left: Full thermogram. Right: Zoom to the 98 % limit.

In Figure 5.12 the TGA results are compared to those of the SNs. It shows that the DN is thermally more stable than the respective SNs. The degradation (loss of >2 % of the initial mass) sets on about 70 °C above the degradation of the single networks.
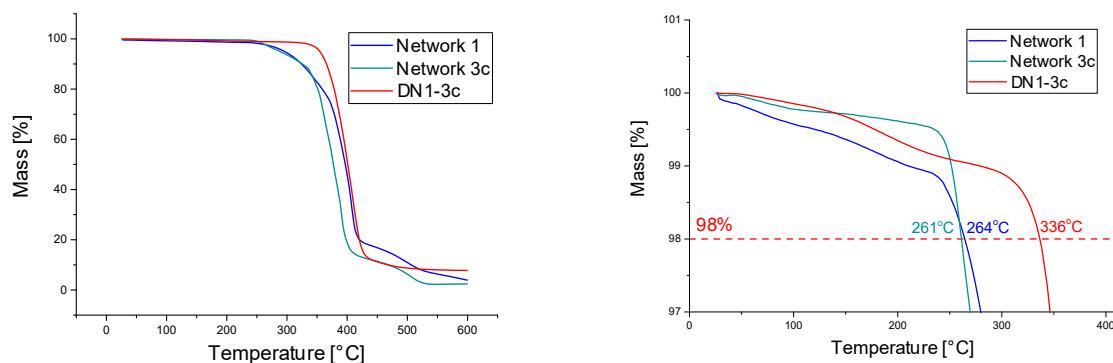
Figure 5.12: TGA ramp of the **DN1-3c** (red), **Network 1** (blue) and **Network 3c** (cyan). Left: Full thermogram. Right: Zoom to the 98 % limit.

5.5.2 DSC

Figure 5.13 features the DSC results of **DN1-3c** (red), as well as those of the SNs (blue and cyan). The midpoint of the glass transition is located at -44.6 °C. No other transition was detected in the measured temperature range. In Table 5.2, the obtained value is compared to those of the single networks. The transition of the DN is much broader than those of the SNs. The transition of **Network 3c** takes place at slightly lower temperatures than the transition of **Network 1**. The transition of **DN1-3c** covers the entire transition region of both SNs. It is difficult to tell at this stage if the transition of the DN is in fact a composition of the two glass transitions of the subnetworks or a broad single transition.
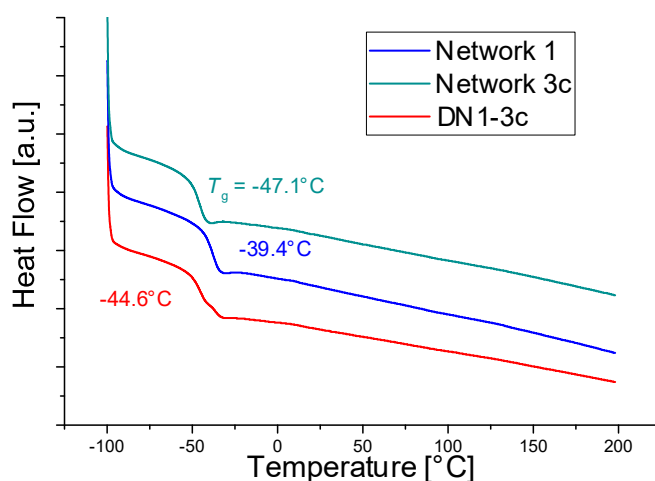
Figure 5.13: DSC of the **DN1-3c** (red), of **Network 1** (blue) and of **Network 3c** (cyan).

5.5.3 DMA

The DMA of **DN1-3c** is displayed in Figure 5.14a. Above the T_g, the sample shows a plateau at 2200 MPa. The T_g was determined at the maximum of E" and was located at -31.9 °C.
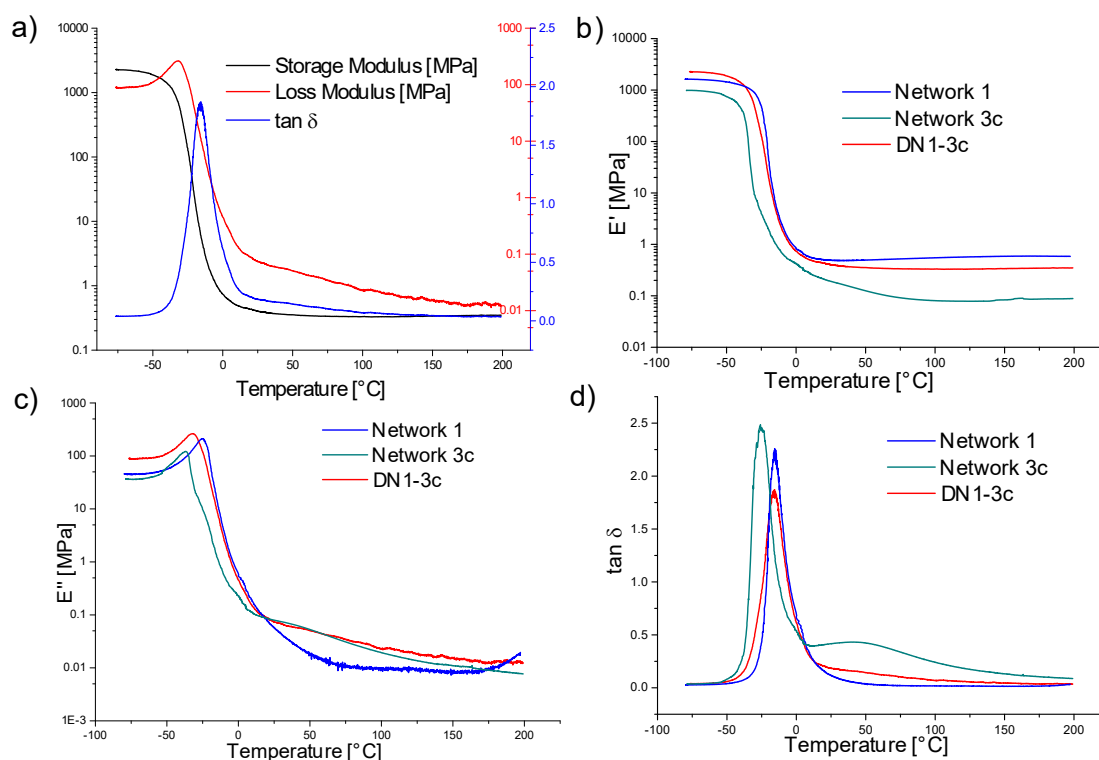
Figure 5.14: DMA of **DN1-3c** (red), of **Network 1** (blue) and of **Network 3c** (cyan). a) DMA of **DN1-3c**, b) Storage modulus E', c) Loss modulus E", d) tan δ.

After the glass transition, E' decreases and reaches a plateau around 330 kPa at 70 °C. From this point, the modulus increases slightly in accordance to the rubber elasticity theory. The sample maintains its network structure over the entire measured temperature spectrum. In Figure 5.14b-d, the storage modulus, loss modulus and tan δ of the DN are compared graphically to those of the SNs. In Table 5.2, the T_gs as well as the storage moduli at 25 and 150°C are compared. It shows that the modulus of the DN below 25 °C is mainly dominated by the properties of **Network 1**. The E' of the DN is generally a little lower though and the increase of the plateau with temperature due to rubber elasticity is not as pronounced as in **Network 1**. The T_g of the DN is in between the ones of the two subnetworks. Both phenomena can be explained by the overall lower crosslinking density

of the double network compared to the boronic ester network, which allow the chains more degrees of freedom to move. The loss modulus of the DN behaves more similar to the one of **Network 3c** above 25 °C. The narrow and monodisperse tan δ observed by DMA for **DN1-3c** indicates a homogeneous network free of phase separation.

Table 5.2: Comparison of the values obtained by DSC and DMA for the single networks with the double network.

Material	**Network 1**	**Network 3c**	**DN1-3c**
T_g (DSC) [°C]	-39.4	-47.1	-44.6
T_g (DMA) [°C]	-25.0	-37.0	-31.9
E'(25 °C) [MPa]	0.491	0.191	0.403
E'(150 °C) [MPa]	0.587	0.083	0.337

5.6 Tensile Tests

The results of the uniaxial tensile tests of **DN1-3c** are displayed in Figure 5.15. The strain rate was set to 10 mm/s and a 100 N transducer was employed. The Young's modulus was calculated by determining the slope in the linear regime between 2-5 % strain. The values determined for all specimen can be found in Table 5.3. The average tensile strain at break was at 180 %, with an average tensile stress at break of 150 kPa. The Young's modulus of **DN1-3c** is around 218 kPa.
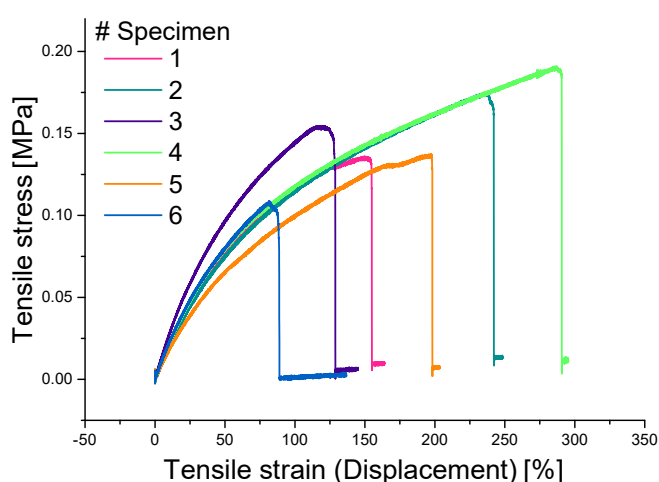
Figure 5.15: Stress/strain curves of the uniaxial tensile tests of **DN1-3c**.

Table 5.3: Results of the uniaxial tensile test of **DN1-3c**.

Specimen #	1	2	3	4	5	6	Average
Tensile strain at break [%]	153	238	125	288	198	82	180 ± 76
Tensile stress at break [kPa]	134	174	153	190	137	108	150 ± 29
Young's modulus [kPa]	195	201	276	223	183	228	218 ± 33

In Figure 5.16a, an average strain-stress curve of **DN1-3c** is shown in comparison to average strain-stress curves of the SNs **1** and **3c**. Figure 5.16 displays as well the average values for Young's modulus (b), tensile strain at break (c) and tensile stress at break (d) of the three materials.
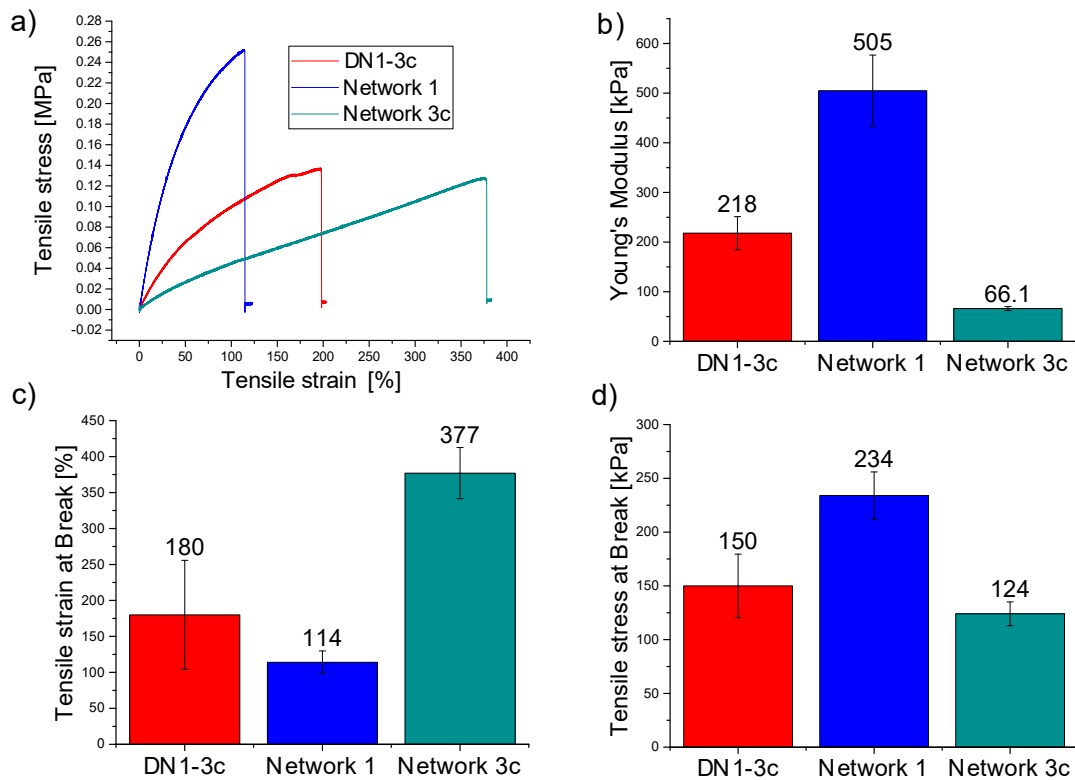
Figure 5.16: Comparative study of uniaxial tensile tests of **DN1-3c** (red) with the single **Networks 1** (blue) and **3c** (cyan). a) Average Stress/strain curves, b) average Young's modulus, c) average tensile strain at break, d) average tensile stress at break.

As expected, the most loosely crosslinked network (**Network 3c**) has the lowest Young's modulus, the highest strain at break and the lowest stress at break. The most densely crosslinked network (**Network 1**) has the highest modulus and stress at break, as well as the lowest strain at break. The **DN1-3c** ranges in the middle of the values of the SNs. An ideal outcome would have been to see strain hardening: to reach equally long elongations at higher stress levels. This would have been achieved, if the dynamic network dissipated energy and prevented thus damage from the structural subnetwork. To observe such a behavior, it is necessary that the rate of deformation of the material and the lifetime of the DCBs are adequately matching, so that the chemical network can rearrange its topology and dissipate stress before the material ruptures. However, as in Chapter 2 indicated, the dynamic network did not show to dissipate stress fast enough under ambient conditions. It therefore acts as an additional structural network. The DN properties in the tensile tests are primarily determined by the mix of different crosslinking densities.

5.7 Frequency Sweeps

To test the viscoelastic behavior of **DN1-3c**, frequency sweep experiments have been conducted. Figure 5.17 (left) presents the frequency sweep experiments performed on **DN1-3c** at the lowest, 25 °C, and the highest, 150 °C, measured temperatures.
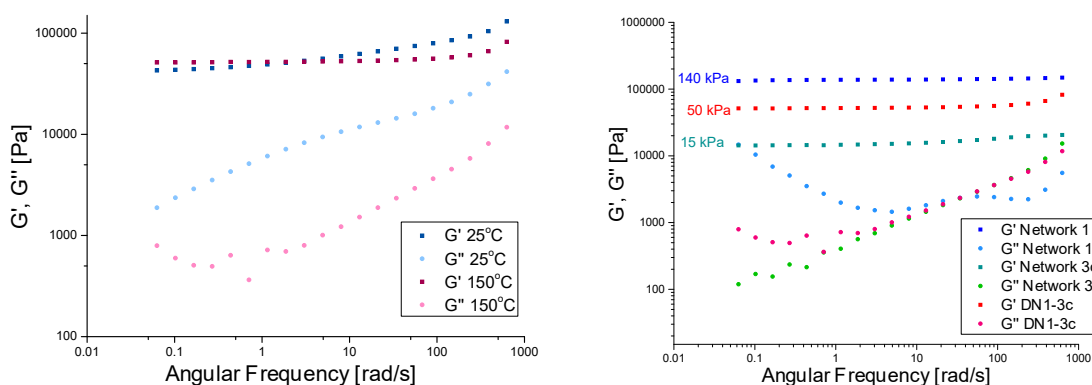
Figure 5.17: Left: Frequency sweeps of **DN1-3c** at the lowest measured temperature, 25 °C, (blue and light blue) and the highest measured temperature, 150 °C, (red and pink). Right: Frequency sweeps of **Network 1** (blue), **Network 3c** (cyan) and **DN1-3c** (red) at 150 °C.

The storage modulus shows a plateau around 50-60 kPa, slightly increasing towards high frequencies. The loss modulus increases from several hundred Pa at low frequencies to

ten thousand(s) Pa at high frequencies. This indicates that the movement of the chains starts to be more restricted and the sample transits into the glassy state. In the measured frequency and temperature spectrum, the sample shows no crossover of the moduli towards lower frequencies, indicating no transition into the terminal flow regime. The results at 150 °C are compared to the ones of the respective SNs in Figure 5.17, right. In general, the storage moduli follow the same behavior and show a rubber elasticity plateau over the measured spectrum. The G' of the DN ranges in between the ones of the SNs. This can be explained by the average crosslinking density of **DN1-3c**. The loss modulus of the DN follows the one of **Network 3c** at frequencies higher than 1 rad/s. Before that it is more dominated by the one of **Network 1**.

5.8 Stress Relaxation

The dynamic behavior of **DN1-3c** has been assessed via stress relaxation experiments and compared to the constituting SNs. The sample was equilibrated at 150 °C for several hours before stress relaxation was conducted at 1 % strain for 24 h at 110 °C. The stress relaxation curves of **Network 1**, **Network 3c** and **DN1-3c** are presented in Figure 5.18.
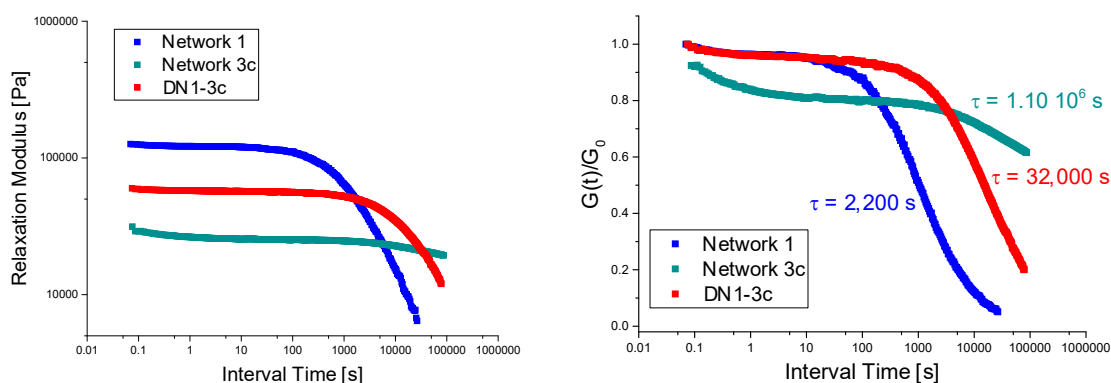
Figure 5.18: Left: Stress relaxation curves of **Network 1** (blue), **Network 3c** (cyan) and **DN1-3c** (red) at 110 °C. Right: normalized to G_0.

The initial relaxation modulus of the DN is in between those of the SNs, which is to be expected due to the average crosslinking density. Interestingly, the DN does not feature a short time stress relaxation like **Network 3c**. This relaxation is attributed to loose chain ends and free chains not attached to the network. Apparently, the incorporation into the interpenetrated network prevents this relaxation mode. All three networks show a plateau,

before (a second) relaxation takes place. This relaxation is attributed to the respective bond exchange. The relaxation time of **DN1-3c** is with 32,000 s much higher than the one of **Network 1** (2200 s) (see Table 5.4). The relaxation times were calculated applying a KWW stretched exponential decay model (refer to Chapter 2.14.1 and Equation 5.4).

Table 5.4: Values obtained by stress relaxation at 110 °C employing the KWW model.

Material	**Network 1**	**Network 3c**	**DN1-3c**
τ [s]	2226	$1.11 \cdot 10^6$	32042
β	0.57	0.48	0.54

The relaxation of **DN1-3c** has with β = 0.54 a similar value as the relaxation of **Network 1**. If the stress relaxation of **DN1-3c** would have been an overlay of the two relaxations of the subnetworks, this value should have significantly decreased, since β reflects the broadness of the relaxation distribution. It can therefore be assumed that the relaxation of **DN1-3c** can be attributed to the boronic ester exchange reactions. These are now significantly slower than in the respective SN. This can be explained by the IPN structure. The exchange reaction is now kinetically more hindered to proceed by the second, interwoven subnetwork. It would be interesting to see, how the E_a of the DN differs from **Network 1**. Stress relaxation experiments at several temperatures can be envisioned to create an Arrhenius plot of the characteristic relaxation times. However, long experiment times due to the prolonged relaxation times will complicate the experimental setup.

5.9 Creep

Before creep experiments were conducted, the sample was subjected to an amplitude sweep (Figure 5.19). The sample remained in the linear regime over the entire measured spectrum up to 10 % strain and 6.8 kPa shear stress. In order to assess the creep behavior and with it the structural stability of the system at ambient conditions, creep/recovery experiments have been conducted at 25 °C. A shear stress of 2500 Pa was applied for 24 h, before the sample was allowed to recover for another 24 h. The strain development during experiment time is displayed in Figure 5.20 (left).
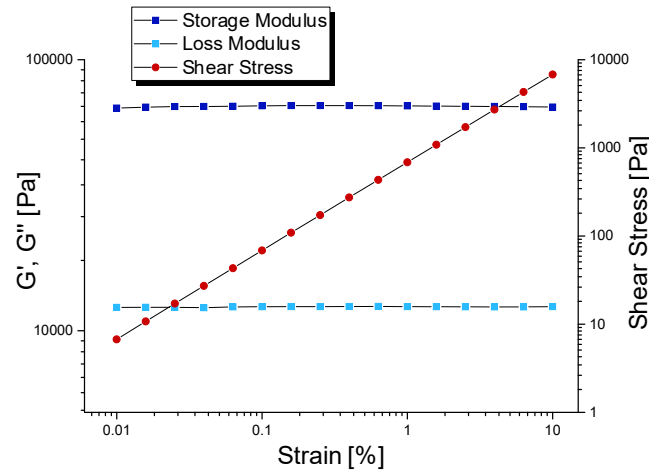
Figure 5.19: Amplitude sweep of the **DN1-3c** at 25 °C. The sample remains in the linear regime over the entire measured spectrum.
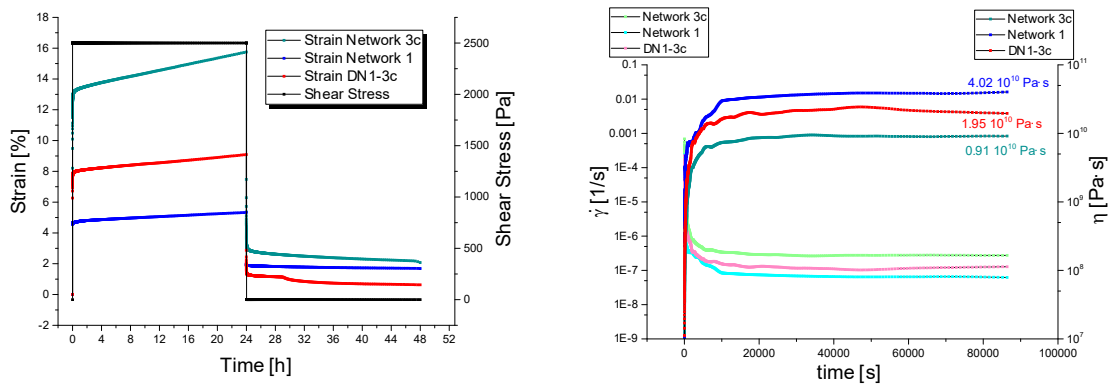
Figure 5.20: Creep behavior of **Network 1** (blue), **Network 3c** (cyan) and **DN1-3c** (red). A shear stress of 2500 Pa was applied for 24 h, before the sample was allowed to recover for another 24 h. Left: Strain and shear stress with experiment time. Right: $\dot{\gamma}$ and the viscosity in function of the experiment time.

One can see that the elastic response of the DN is in between the ones of the SNs. The slope of the strain, the strain rate $\dot{\gamma}$, is displayed in Figure 5.20 on the right side. The strain rate, and with it the viscosity η is in between the ones of the SNs. When the stress is released however, the DN shows an elastic response superior to those of the SNs. After the 24 h of recovery, the **DN1-3c** shows a residual strain of only 0.63 %, much lower than the SNs, with 1.7 % and 2.0 % residual strain for **Network 1** and **Network 3c**, respectively. This can be explained by the interpenetrating network structure. The interwoven subnetworks restrict each others degrees of freedom. Their ability to flow

under stress is more limited than in form of the SNs. The creep compliance J(t), creep recovery compliance J_r(t), and true creep compliance J_r^{true}(t) of **DN1-3c** in function of the creep/recovery experiment time is shown in Figure 5.21 (left). J(t) does not achieve the steady-state flow scaling of 1 during the measured time. The system does not reach terminal relaxation. In Figure 5.21 on the right side, the creep compliance is compared to those of the SNs. The compliance ranges in between those of the SNs. None of the three materials reaches terminal relaxation.
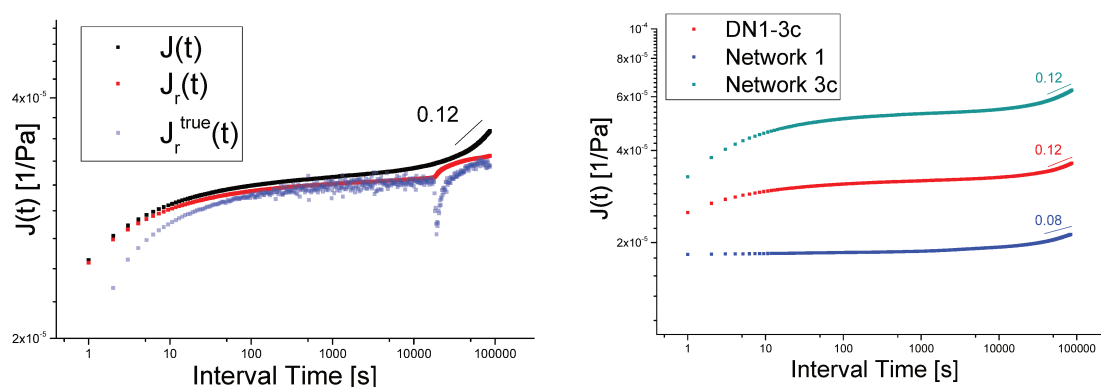
Figure 5.21: Left: J(t), J_r(t), and J_r^{true}(t) of **DN1-3c** in function of the creep/recovery experiment time. Right: J(t) of **Network 1** (blue), **Network 3c** (cyan) and **DN1-3c** (red).

These results indicate that DDN vitrimers present a better creep resistance than single vitrimers. Interestingly, this creep resistance was obtained even though the **DN1-3c** has a lower average ρ(CL) than the dioxaborolane crosslinked **Network 1** and endures thus more stress per crosslink. In other words, when compared to the boronic ester vitrimer **Network 1**, the DDN allows increasing at the same time creep resistance and elongation at break, which is really challenging to achieve, yet highly desirable for most elastomers. This unique behavior is likely a direct consequence of the structure of the IPN. The loosely crosslinked, slow dynamic imine-aldehyde vitrimer **Network 3c** restricts the reshuffling of the dynamic crosslinks and the topology rearrangement of the more dynamic dioxaborolane **Network 1**. More studies will have to be conducted to better understand the mechanisms at play and optimize the properties of the DDN through the adjustment of the functionality, crosslinking density, M_n of the TPs and weight fraction of both networks.

5.10 Mechanical Recyclability

Both subnetworks rely on degenerate exchange reactions. The DN should thus show vitrimer properties. One remarkable feature of vitrimers is their ability to be mechanically recyclable in their network form. This sets them apart from conventional thermosets and elastomers. To test the mechanical recyclability of the DN, **DN1-3c** was subjected to consecutive cycles of mechanical testing and reprocessing. As mechanical tests, uniaxial tensile tests and DMA measurements have been performed. Before each test, the samples were cut to small pieces and reprocessed by compression molding at 110 °C for 30 min at a pressure equivalent to 3 tons.

5.10.1 Tensile Tests

The pristine samples have been subjected to uniaxial tensile tests. After the tests, the samples have been reprocessed and tested again. All in all, three cycles have been conducted. The results are displayed in Figure 5.22.
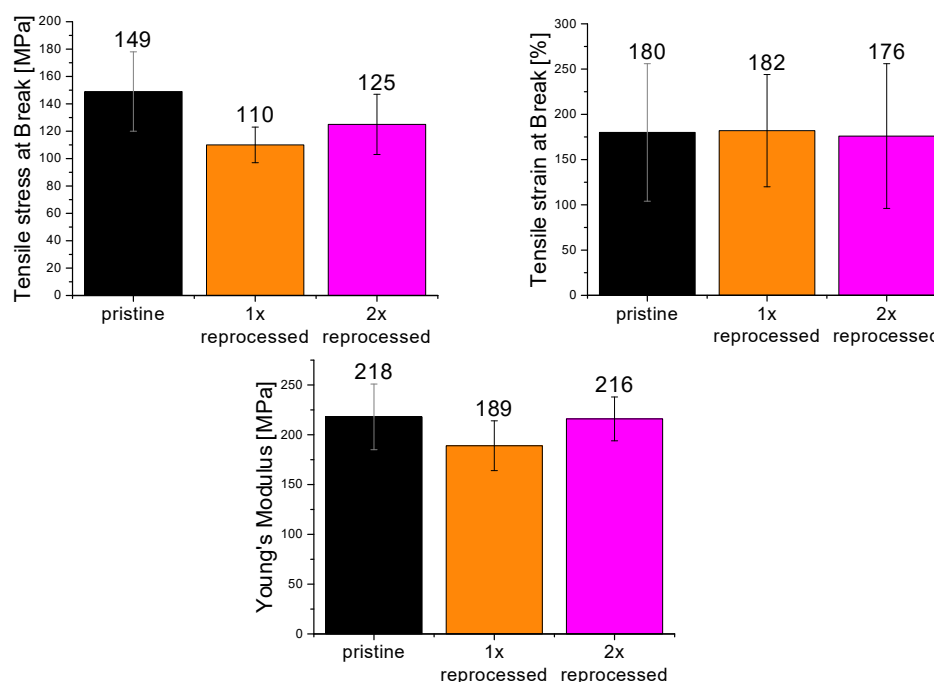
Figure 5.22: Results of uniaxial tensile tests of **DN1-3c** after the first processing (pristine, black), first reprocessing (1x reprocessed, yellow) and second reprocessing (2x reprocessed, pink). Top, left: average tensile stress at break. Top, right: average tensile strain at break. Bottom: average Young's modulus.

In the range of the experimental error, all samples showed similar properties regarding average tensile stress at break, average tensile strain at break and Young's modulus. The recycling does not affect the mechanical properties of the network.

5.10.2 DMA

For DMA, three samples have been prepared, one that was compression molded once (pristine), one that was torn into pieces after the first molding and was reprocessed (1x reprocessed), and one that was two times reprocessed like described (2x reprocessed). Figure 5.23 and Table 5.5 compare the results.
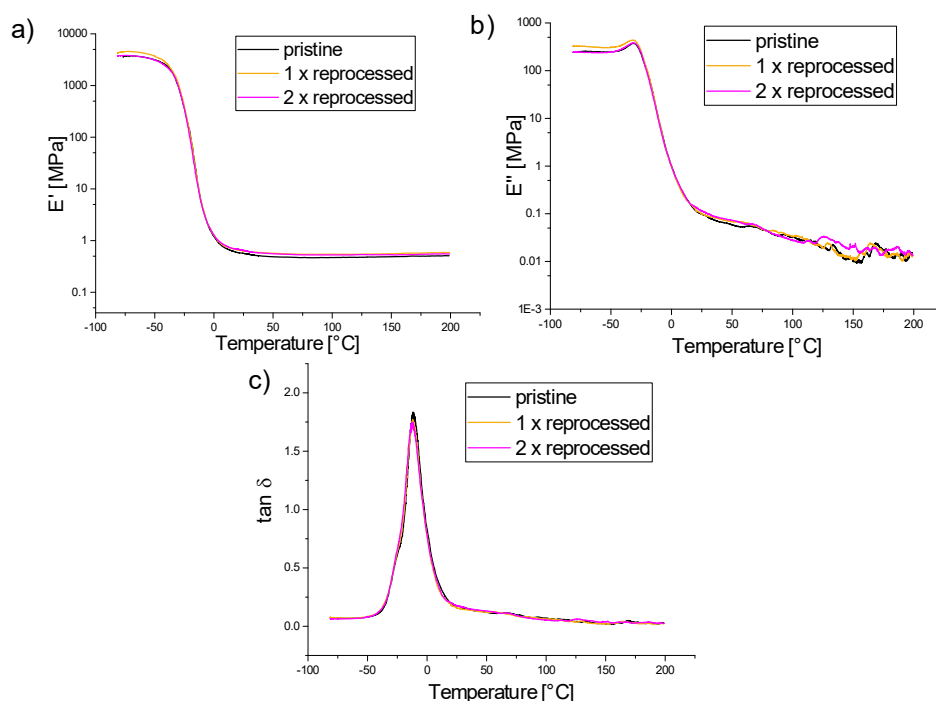
Figure 5.23: Results of the DMA of **DN1-3c** after the first processing (pristine, black), first reprocessing (1x reprocessed, yellow) and second reprocessing (2x reprocessed, pink). a) Storage modulus E', b) loss modulus E", c) tan δ.

The results after the first and second reprocessing match very well with the ones obtained for the pristine sample. The storage modulus is not affected by the recycling, which indicates a constant crosslinking density. Slight differences can be explained by the error margin of the measurement method. The mechanical recycling does hence not affect the thermomechanical properties of the sample.

Table 5.5: Results of the DMA of **DN1-3c** after the first processing (pristine), first reprocessing (1x reprocessed) and second reprocessing (2x reprocessed).

Sample	Pristine	1x reprocessed	2x reprocessed
T_g (DMA) [°C]	-32.9	-31.41	-35.4
E'(25 °C) [kPa]	403	188	609
E'(150 °C) [kPa]	337	197	556

5.11 Chemical Recycling

5.11.1 Recovery of the Thermoplastic Precursors

The dynamic exchange reactions in **DN1-3c** could allow chemical recycling of the material, that is to say the recovery of the TPs, by the addition of competitive small molecules. To reobtain the TPs of the DN, the most straightforward way is the hydrolysis of both subnetworks like shown in Scheme 5.5. The **DN1-3c** was swollen in THF and 1 M $HCl_{aq.}$ was added. After 24 h the network dissolved completely. The mixture was concentrated and precipitated in MeOH. The sample was dried at ambient conditions due to the susceptibility of the diol groups to engage in transesterification reactions at higher temperatures. The obtained polymer was analyzed by NMR (Figure 5.24). Two species could be identified: the aldehyde TP **P30** and the diol TP **P8** still comprising some uncleaved boronic ester moieties. The integration of the respective functional group peaks (k for **P30** and e and a + b for **P8/9**) and normalization to their respective functionality reveals a ratio of the of the TPs of 0.98 : 1.02 (**P8/9** : **P30**). This corresponds to the initial ratio of the constituent TPs of 0.97 : 1.03 (compare to Chapter 5.3).
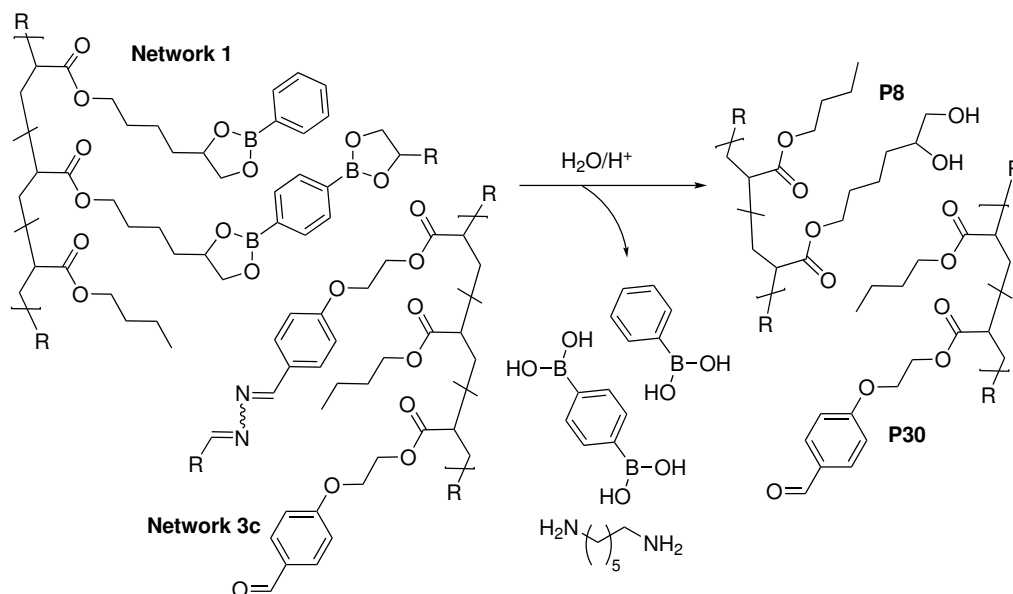
Scheme 5.5: Chemical recycling: Recovery of the TPs of the DN by hydrolysis. The crosslinks are cleaved and the soluble TPs **P8** and **P30** are recovered by precipitation.
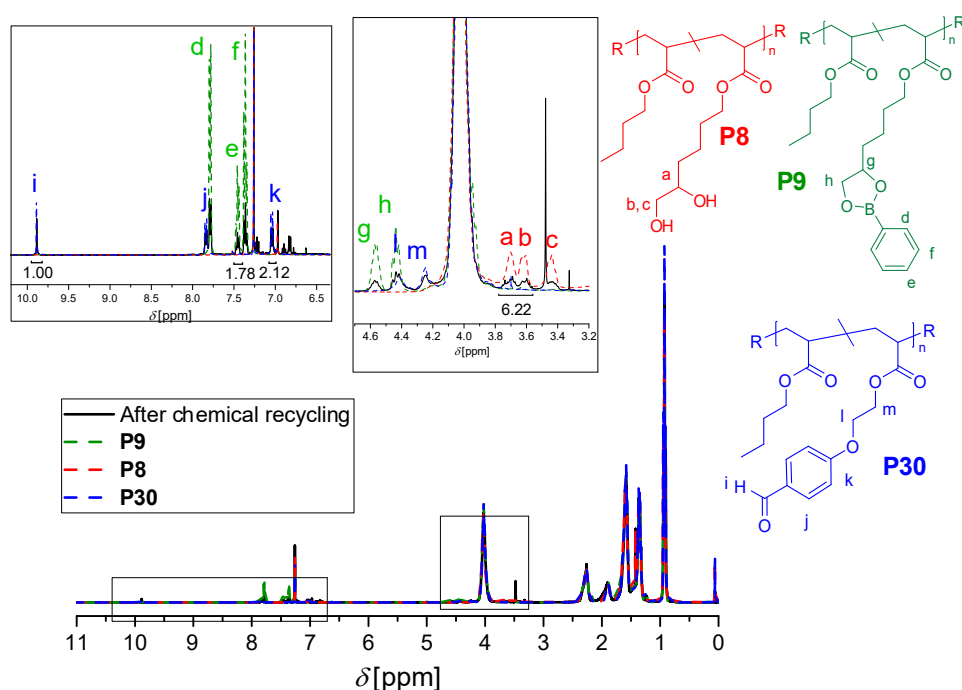
Figure 5.24: ^{1}H NMR spectra in CDCl$_3$ at 400 MHz of the obtained TPs after hydrolysis of **DN1-3c** (black) and the pristine TPs **P8** (diol, red), **P9** (dioxaborolane, green) and **P30** (aldehyde, blue).

The network can be thus easily retransferred to the respective TPs. The next step would be to esterify the diol groups with PBA and resynthesize the DN. It can also be envisioned to perform the cleavage in a one-pot reaction employing a small aldehyde and a boronic ester, followed by the precipitation to directly obtain the functional TPs **P9** and **P30**. However, the exchange reactions between boronic esters take significantly longer than the transesterifications between boronic esters and diols.

5.11.2 Separation of the Subnetworks

The orthogonality of the dynamic exchange reactions should allow to dissolve the individual subnetworks separately from each other. Thereby, it should be possible to recover the individual compounds of the DN. It was attempted to separate the imine-aldehyde network from the boronic ester network. In order to do so, the DN was swollen in THF and 1,2-propanediol was added as a small competitive monofunctional molecule. As already shown in Chapter 2.9.1, small diols are able to dissolve **Network 1** completely and recover the TP P9. In Chapter 4.9.2.2, it was demonstrated that **Network 3c** shows excellent structural stability in the presence of 1,2-propanediol and thus orthogonality to this compound. In the presence of an excess of the small molecule diol, the boronic ester subnetwork should be cleaved into the soluble diol functionalized TP **P8**, whereas the imine-aldehyde subnetworks remains intact (apart from its usual soluble fraction in THF) like displayed in Scheme 5.6. The imine-aldehyde network can be isolated by removing the soluble fraction. The thermoplastic precursor **P30** can then be reobtained by the hydrolysis of the insoluble fraction. The DN was immersed into a solution of 1,2-propandiol (500 eq / boronic ester crosslink) in THF. The soluble fraction, comprising **P8**, the excess of diol and the small boronic ester species, was removed after 72 h. The insoluble part was immersed two times for 2 h in THF as a washing step. Subsequently, the insoluble fraction was dried. The remaining insoluble fraction was 81 $\pm$ 6 % of the initial mass of the imine-aldehyde subnetwork. Only slightly lower than in pure THF (90 $\pm$ 1 %, compare Chapter 4.9.2.1). To recover the TP **P30**, the insoluble fraction was immersed into a THF/HCl$_{aq}$ (1M) (4 : 1) solution for hydrolysis like displayed in Scheme 5.7.
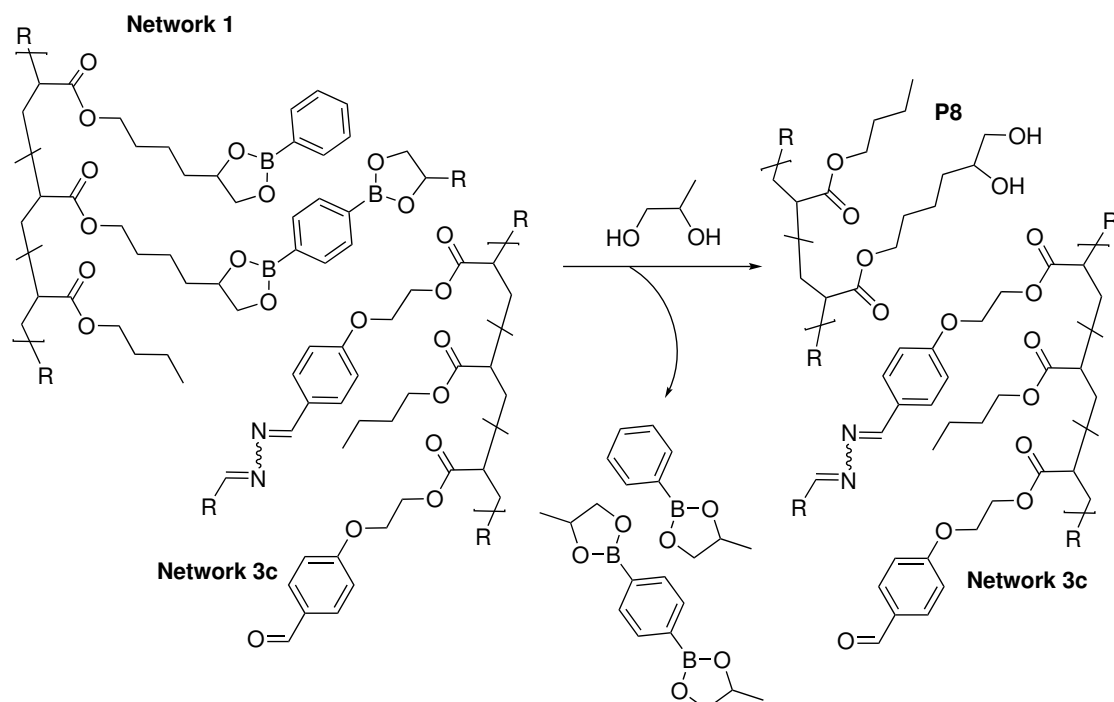
Scheme 5.6: Selective cleavage and separation of the boronic ester subnetwork from the imine-aldehyde subnetwork. An excess of 1,2-propanediol exchanges with the boronic ester moieties. The dioxaborolane crosslinks are cleaved and the soluble TP **P8** is obtained. The imine-aldehyde network stays intact due to its orthogonality to diols.
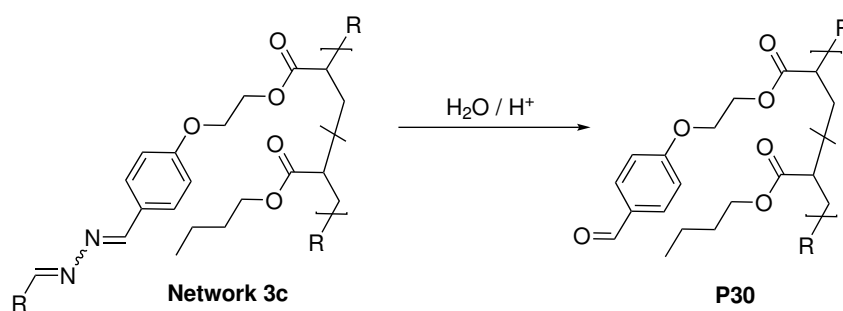
Scheme 5.7: Hydrolysis of the insoluble fraction after diolysis to recover TP **P30**.

After 24 h, the solution was concentrated and precipitated in MeOH. The NMR spectrum of the obtained polymer is displayed in Figure 5.25 (black).
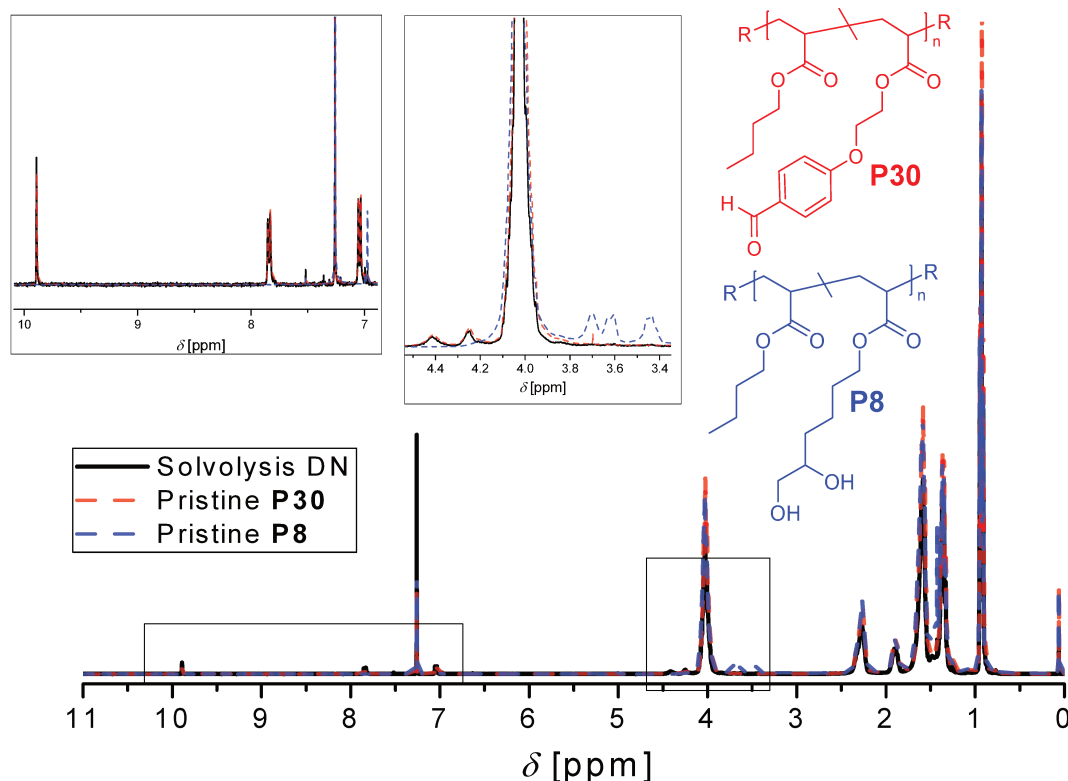
Figure 5.25: ^{1}H NMR spectrum in CDCl$_3$ at 400 MHz of the obtained TP (black) of the insoluble fraction after the chemical recycling with 1,2-propandiol and subsequent hydrolysis, compared to that of the pristine diol functionalized TP **P8** (blue) and aldehyde functionalized TP **P30** (red).

The NMR of the pristine diol functionalized TP **P8** (blue) and aldehyde functionalized TP **P30** (red) are superimposed. As can be seen, the TP P30 could be recovered pure. The boronic ester subnetwork was dissolved completely and separated from the imine-aldehyde network, since no traces of the diol TP were observed. The SEC analysis is shown in Figure 5.26. The curves of the TP after the hydrolysis and the pristine TP **P30** resemble each other in terms of *Đ*. However, there is a small shoulder towards higher molecular weights in the curve after the hydrolysis, which could indicate that the cleavage of the imine crosslinks was incomplete. However, the shoulder is not very pronounced and the sample was still completely soluble and easily filterable. It can thus be said that the imine-aldehyde network is very well chemically recyclable.
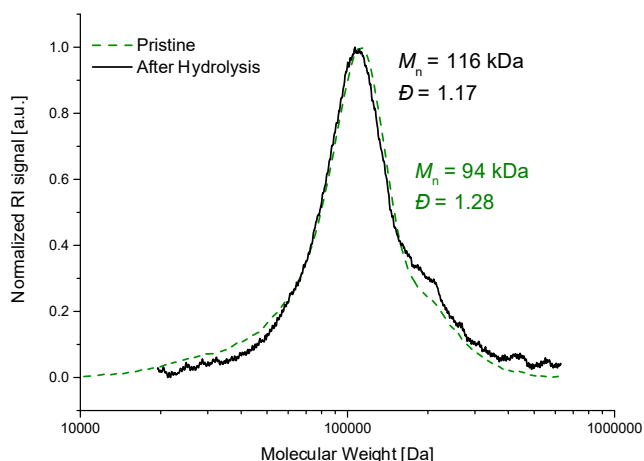
Figure 5.26: SEC trace in THF (PS calibration) of the obtained TP (red) of the insoluble fraction after the chemical recycling with 1,2-propandiol and subsequent hydrolysis compared to that of the aldehyde functionalized TP **P30** (black).

The soluble fraction obtained after the diolysis of the **DN1-3c** has been also analyzed. After it was removed from the insoluble network, some HCl_{aq} (1M) was added for hydrolysis. After 24 h, the solution was concentrated and precipitated into MeOH. The resulting NMR can be found in Figure 5.27. Two species could be identified: the diol functionalized TP **P8** (red), who still comprises some non-hydrolyzed boronic ester moieties (**P9** (green)), and the aldehyde functionalized TP **P30** (blue). The ratio of the compounds was calculated with the integration of peaks (c, f, and k) and normalized to the respective functionality of the chains. The obtained composition was **P8/9** : **P30** 0.71 : 0.29. A significant amount of aldehyde TP can be found in the soluble fraction. This was expected, since the **Network 3c** itself showed a soluble fraction of around 10 % in pure THF. In addition, the insoluble fraction of the imine-aldehyde subnetwork in the double network was also a little bit lower. Most part of the obtained material consists of cleaving products of the boronic ester network. Most of the boronic ester units have been cleaved off either by the propandiol or by the subsequent hydrolysis.

It was shown that it is possible to separate the imine-aldehyde subnetwork from the boronic ester one and recover the TP **P30** pure. However, it was not possible to reobtain the TP of the boronic ester subnetwork this way, since the soluble fraction of the imine-aldehyde subnetwork causes impurities. It is challenging to conduct chemical recycling on the boronic ester network. In theory, it would be possible to cleave the imine-aldehyde subnetwork by adding a competitive small molecule like benzaldehyde or n-butylamine that would cleave the imine crosslinks orthogonally. However, the boronic ester **Network**

1 showed limited stability in THF over longer periods (refer to Chapter 2.9.2), and the experimental conditions would necessitate some optimization.
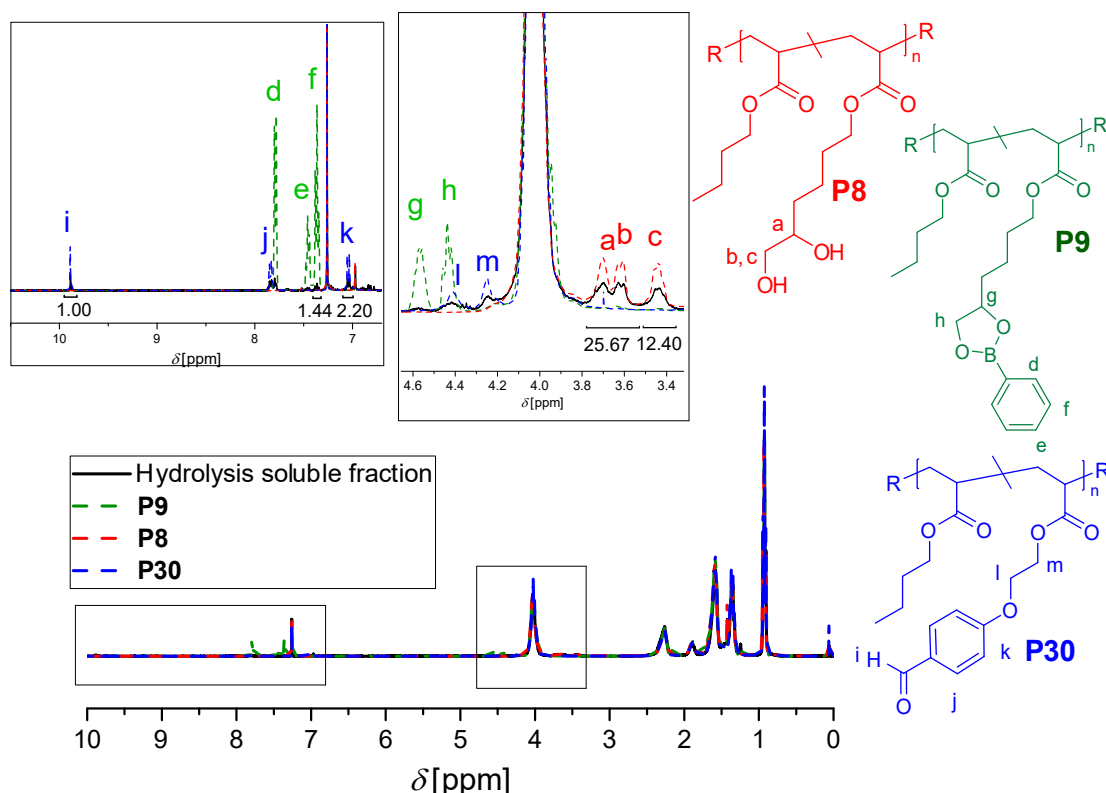
Figure 5.27: ^{1}H NMR spectrum in CDCl$_3$ at 400 MHz of the obtained soluble TP (black) after the selective diolysis of **DN1-3c** with 1,2-propandiol, compared to those of the pristine boronic ester functionalized TP **P8** (green), the diol functionalized TP **P8** (red) and the aldehyde functionalized TP **P30** (blue).

5.12 Conclusion

The aim of this chapter was to prepare and characterize a vitrimer DDN comprising two interpenetrated subnetworks based on a boronic ester exchange and an imine/aldehyde exchange, respectively. The individual subnetworks have been synthesized and characterized in Chapters 2 and 4. In this final chapter, it is evaluated if they can be united into a DDN. In order to do so, the individual components have been tested to guarantee their orthogonality to each other. It was shown that the boronic ester TP does react neither with the bis(imine) crosslinker nor with the aldehyde TP. Similarly, it was demonstrated that the aldehyde TP does not react with the bis(boronic ester) crosslinker nor with the

dioxaborolane TP. The subnetworks are thus perfectly orthogonal to each other and should not interfere during crosslinking.

The TPs were mixed in an equal ratio and crosslinked simultaneously to yield a ρ(CL) of 2.0 % for the boronic ester network and 0.5 % for the imine-aldehyde network. The DN was well processable via compression molding within 30 min at 110 °C with a pressure equivalent to 3 tons. A homogenous, slightly yellow elastomer was obtained that was subjected to a comparative study to the SNs. Solubility tests in THF showed that the DN features a similar connectivity than as single networks. Swelling tests showed that the DN has a swelling ratio between the both single networks. The more densely crosslinked subnetwork does not prevent the DN from swelling. This might be due to the fast rearrangements of the boronic ester bonds in combination with the swelling pressure of the loosely crosslinked subnetwork. The thermal stability of the DN was assessed with TGA. The degradation of the DN sets on about 70 °C above the degradation of the respective single networks. DSC analysis showed a broad glass transition that covers the entire transition region of both SNs. It is difficult to tell at this stage if the transition of the DN is in fact a composition of the two glass transitions of the subnetworks, or a broad single transition. During DMA, the DN shows an E' that is in between the moduli of the respective SNs. Also the T_g of the DN is in between the ones of the two subnetworks. Both phenomena can be explained by the overall lower crosslinking density of the double network, which allow the chains more degrees of freedom to move. However, the DN behaves more like the boronic ester subnetwork below 25 °C, above that temperature its behavior, as measured by DMA, resembles more closely the one of the imine-aldehyde network. The mechanical behavior of the DN was assessed by uniaxial tensile tests. One potential beneficial effect of the DN could have been to see strain hardening due to the energy dissipation of the dynamic network. However, the DN showed values in stress and strain at break in between the ones of the SNs. Its properties are mainly determined by the mix of the different crosslinking densities and no synergistic effects could be observed.

During frequency sweep experiments, the network exhibited a rubbery plateau over the entire measured temperature and frequency spectrum. Its G' was between the ones of the SNs, which can be explained by the difference in ρ(CL). In stress relaxation experiments, it could be observed that the short time stress relaxation featured by the imine-aldehyde SN is suppressed. Loose chain ends and free chains not attached to the network are prevented to relax in the DN. The DN relaxed about 80 % of its initial stress within 24 h. The relaxation process is much slower than in the boronic ester network, but much faster than in the imine-aldehyde network. It can be assumed that the relaxation in

the DN stems from the boronic ester exchange, which is now sterically more hindered and thus proceeds on slower time scales. During creep/recovery experiments, the elastic response, strain rate, viscosity and creep compliance of the DN ranged in between the ones of the SNs. However, when the stress was removed, the DN showed the largest elastic recovery and the lowest residual strain after 24 h with 0.6 % vs. 1.7 and 2.0 % for the **Networks 1 and 3c**, respectively. The interpenetrate structure of the DN restricts the ability of the subnetworks to reorganize themselves and therefore their ability to flow under stress. These results indicate that double network vitrimers hold great promises to improve simultaneously creep resistance and elongation at break of elastomeric vitrimers. These preliminary results will have to be confirmed, and the understanding of the different process at play deepened. Nonetheless, by playing on the functionality and M_n of the TP, as well as on the ρ(CL) and weight fractions of the subnetworks, materials with unique properties can be envisioned.

The vitrimer properties of both subnetworks allow the DN to be mechanically reprocessed in its crosslinked form. The DN was subjected to two recycling cycles and tested for its mechanical properties. The characteristics, such as stress and strain at break and Young's modulus, were not impacted. This proves the excellent mechanical recyclability under these conditions. The responsiveness of the exchanging groups to small competitive molecules gives the possibility to chemically recycle the TPs of the subnetworks. The orthogonality of the constituent exchange reactions allows even to separate the individual subnetworks from each other and recover the TPs. It was shown that the imine-aldehyde subnetwork can be isolated by dissolving the boronic ester network with small diols. The aldehyde TP could be recovered pure this way.

In this chapter, it was demonstrated that the boronic ester - imine/aldehyde system is a promising platform to create vitrimer DDNs. The TPs are easily adaptable in regards of functional group density and M_n as are the subnetworks in their ratio and crosslinking density. Both system showed excellent orthogonality to each other. The obtained DN showed mechanical and chemical recyclability and significant improvement as compared to the single networks with regards to some of its mechanical properties. The short time stress relaxation by loose chain ends from the imine-aldehyde subnetwork was suppressed and the DN showed superior creep recovery. The latter one is especially remarkable, regarding the lower average crosslinking density of the DDN as compared to the boronic ester network. The IPN structure provide thus the powerful mean to impart higher elongation at break while simultaneously enhancing creep resistance. The targeted strain hardening during tensile tests was not yet accomplished. The current composition of the dynamic network does not allow to dissipate energy under ambient conditions at the

applied rate of deformation. A perspective is now to adapt the DDN to feature the desired properties. This can be achieved in different ways. The default of the dynamic network to relax stress during the mechanical testing might have two reasons: either the ratio of the dynamic network in the DN was too high and its high crosslinking density limited the elastic properties of the DN. The other possibility is that the exchange reactions between the boronic esters are in general too slow and even more abated by the steric hindrance of the second subnetwork. It is possible to create new DDNs with an adapted ratio of the subnetworks (e.g. 1 : 2 or 1 : 3 boronic ester : aldehyde TP). In addition, the dynamics of the system can be easily adapted by the addition of free diols. In Chapter 2.17, it was demonstrated that the addition of free diols to the boronic ester network accelerates the exchange reaction by a factor of 25. The established systems offers multiple possibilities to be adapted, which holds the chance to influence the properties of future double dynamic systems via different parameters. The presented system shows thus great potential to further explore the promising prospects DDNs raise.

5.13 Experimental Part

5.13.1 Materials

All chemicals were purchased from Sigma Aldrich, Alfa Aesar, TCI, Acros Organics and Fischer. All starting materials and reagents were of analytic grade and used without further purification, if not stated otherwise.

5.13.2 Instrumental Data

NMR Spectroscopy

^{1}H NMR and ^{13}C NMR spectroscopy measurements were performed in oven dried NMR tubes on a Bruker Ultra Shield machine (400 MHz for ^{1}H NMR, 100 MHz for ^{13}C NMR) at ambient temperature. If not stated otherwise, samples of 10 mg for ^{1}H NMR and 30 mg for ^{13}C NMR were analyzed. CDCl$_3$ was employed as deuterated solvent. Chemical shifts are expressed in parts per million (ppm) and calibrated on characteristic solvent signals as internal standards (^{1}H NMR: CDCl$_3$: 7.26 ppm; ^{13}C NMR: CDCl$_3$: 77.16 ppm).

Size Exclusion Chromatography

The samples for SEC chromatography were prepared by dissolving the respective polymer in anhydrous THF to obtain a concentration of 1.0-1.2 mg/mL. A drop of toluene was added and the sample was passed through a 0.20 μm PTFE filter and placed in a Malvern GPC vial. SEC was performed on a Viscotek GPCmax/VE2001 connected to a Triple detection array (TDA 305) from Malvern. Obtained raw data were treated with a standard homopolymer calibration curve (PS).

DSC

DSC analyses were performed on TA DSC 250 apparatus. Two heating cycles, from -100 to 200 °C, were performed employing a heating rate of 10 °C min^{-1}. The values of T_g were determined with the data obtained on the second heating cycle.

TGA

TGA measurements were performed on a TG 209 F1 Libra from Netzsch. The samples were heated constantly with a rate of 10 °C min^{-1} from 30 to 600 °C. For isothermal treatment, the samples were heated with a constant rate of 10 °C min^{-1} from 30 to 150 °C, and kept at this temperature for 10 h.

DMA

DMA measurements were conducted on a TA Instruments Q800 in tension mode. Heating ramps were performed from -80 to 200 °C at a constant heating rate of 3 °C min^{-1} with a fixed frequency of 1 Hz and a maximum strain amplitude of 1 %. The T_g of the sample was determined at the maximum of the loss modulus function E".

Rheological Characterizations

All rheological characterizations were conducted on a Anton Paar MCR 501 rotational rheometer with a parallel plate geometry with a diameter of 25 mm. If not otherwise

stated, the experiments were run in a convection oven under nitrogen. For solid samples, a normal force of 0.4 N was employed.

Frequency sweeps were conducted at 1 % strain between 0.01 and 100 Hz log on a logarithmic ramp with 5 measuring points per decade (if not stated otherwise).

Stress relaxation was conducted applying 1 % strain for 24 h at 110°C. Before the experiment, samples were allowed to equilibrate for 5-6 h at 150°C. Before every stress relaxation a frequency sweep was conducted. The relaxation time τ was calculated from the obtained data using the KWW model after Equation 5.4 assuming total stress relaxation for $t \rightarrow \infty$. For the **Network 3c** the model was applied only to values >1 s.

$$\frac{G(t)}{G_0} = exp\left\{ -\left(\frac{t}{\tau}\right)^{\beta} \right\} \tag{5.4}$$

Creep experiments were conducted at 25 °C with a constant shear stress of σ = 2,500 Pa for 24 h. Subsequently, the sample rested at 0 shear stress at the same temperature for another 24 h. Before the experiment, samples were allowed to equilibrate for 5-6 h at 150 °C and a frequency sweep was conducted. The viscosity was calculated according to Equation 5.5. The strain rate was obtained via the slope of the strain as a function of time. The value over last 30 points was taken to calculate $\dot{\gamma}$.

$$\eta = \frac{\sigma}{\dot{\gamma}} \tag{5.5}$$

Creep compliance, J(t), creep recovery compliance J_r(t), and the true creep recovery compliance J_r^{true}(t) were calculated via Equations 5.6-5.8.[8]

$$J(t) = \gamma(t)/\sigma \tag{5.6}$$

$$J_r(t) = (\gamma_f - \gamma(t))/\sigma \tag{5.7}$$

$$J_r^{true}(t) = J_r(t) - \frac{dJ_r}{dt_r}t_r \tag{5.8}$$

Amplitude sweeps were conducted between 0.1-10 % strain on a logarithmic ramp with 5 measuring points per decade at a frequency of 1 Hz at 25 °C.

Tensile Tests

Uniaxial tensile tests were performed on dumbbell-shaped specimens (l x w x h = 13 x 1.6 x 2.1 mm) using an Instron 5564 tensile machine mounted with a 100 N transducer cell. The specimens were tested at a fixed cross-head speed of 10 mm/min. Testing was carried out at room temperature for all materials. Engineering stress-strain curves were obtained through measurements of the tensile force F and cross-head displacement Δl by defining the engineering stress as $\sigma = F/S_0$ and the strain as $\gamma = \Delta l/l_0$, where S_0 and l_0 are the initial cross section and gauge length of the specimens, respectively. The Young's modulus E was determined as the slope of the engineering stress-strain curves between 2-5 % strain.

Crosslinking

4.87 g of the dioxaborolane TP **P9** and 4.87 g of the aldehyde TP **P30** were introduced into a beaker and dissolved in 30 mL anhydrous THF. The solution was well stirred and 26.2 mg of the bis(imine) crosslinker **21** (89.6 μmol, 1.73 eq/**P30**) in THF solution were added, before the mixture was stirred again. Subsequently, 84.4 mg of the bis(boronic ester) crosslinker **10** (343 μmol, 7.03 eq/**P9**) in THF solution were added and the solution was stirred again. The beaker rested openly at ambient conditions. After 72 h, the solvent and volatile molecules were removed by drying under vacuum at 80 °C for 16 h.

Compression Molding

Compression molding was conducted using a hydraulic press applying a pressure equivalent to 3 tons. Dry samples were placed into a metal mold and pressed at 110 °C for 20-30 min.

Orthogonality Tests

- 500 mg of the dioxaborolane TP **P9** were dissolved in 2 mL of anhydrous THF, before 51.3 mg of the bis(imine) crosslinker **21** (175 μmol, 0.5 eq/functional group) were added in a THF solution.

- 550 mg of the aldehyde TP **P30** were dissolved in 2 mL of anhydrous THF, before 10.2 mg the bis(boronic ester) crosslinker **10** (41.2 μmol, 0.5 eq/functional group) were added in a THF solution.

- 200 mg of the dioxaborolane TP **P9** and 200 mg of the aldehyde TP **P30** were dissolved in 2 mL of anhydrous THF.

The mixture was stirred and rested openly for 72 h at ambient conditions, before it was dried under vacuum at 80 °C for 16 h. The still liquid mix was transferred into a PTFE mold and pressed at 110°C for 3 h. The sample was transferred into a vial and dissolved in CDCl$_3$ or anhydrous THF for NMR or SEC analysis, respectively.

Swelling and Solubility Experiments

The network was compression molded into disk like shapes and cut into parts of 200-300 mg (m(dry)). 20 mL of anhydrous THF were added and the sample was allowed to swell for 24 h. Subsequently, the excess of THF was removed with a syringe. The swelled samples were weighted (m(swollen)). The samples were dried under vacuum at elevated temperatures to remove the THF that was taken up. In the end, the mass of the dried sample was evaluated (m(dried)). The swelling ratio was determined via Equation 5.9, the insoluble fraction via Equation 5.10.

$$\text{Swelling ratio} = \frac{\text{m(swollen)} - \text{m(dried)}}{\text{m(dried)}} \tag{5.9}$$

$$\text{Insoluble fraction} = \frac{\text{m(dried)}}{\text{m(dry)}} \tag{5.10}$$

Chemical Recycling

- About 200-300 mg of the **DN1-3c** were immersed into 20 mL of a anhydrous THF: HCl$_{aq.}$ (1M) 4 : 1 solution. The sample rested 72 h at 30 °C before it was concentrated and precipitated in MeOH. The resulting polymer was dried with compressed air at ambient conditions and was subsequently analyzed by NMR.

- About 200-300 mg of the **DN1-3c** were immersed into 20 mL of anhydrous THF. 500 eq of 1,2 propandiol per boronic ester crosslink were added. After 72 h, the soluble fraction was removed and the insoluble fraction was immersed two times into 20 mL of anhydrous THF for 2 h. The insoluble fraction was dried and its value calculated with Equation 5.10, with m(dry) as half of the mass of the initial DN. The insoluble fraction was immersed into a THF/HCl$_{aq}$ (1M) (4 : 1) solution for hydrolysis. After 24 h the solution was concentrated and precipitated into MeOH. The resulting polymer was dried and analyzed via NMR spectrometry and SEC.

1 mL of HCl$_{aq}$ (1M) was added to the soluble fraction. After 24 h, the solution was concentrated and precipitated into methanol. The resulting polymer was dried and analyzed via NMR.

Bibliography

(1)   Gong, J. P. *Soft Matter* **2010**, *6*, 2583–2590.

(2)   Haque, M. A.; Kurokawa, T.; Gong, J. P. *Polymer (Guildf).* **2012**, *53*, 1805–1822.

(3)   Ducrot, E.; Chen, Y.; Bulters, M.; Sijbesma, R. P.; Creton, C. *Science.* **2014**, *344*, 186–189.

(4)   Neal, J. A.; Mozhdehi, D.; Guan, Z. *J. Am. Chem. Soc.* **2015**, *137*, 4846–4850.

(5)   Liu, Y.; Tang, Z.; Wu, S.; Guo, B. *ACS Macro Lett.* **2019**, *8*, 193–199.

(6)   Wang, S.; Ma, S.; Li, Q.; Xu, X.; Wang, B.; Huang, K.; Liu, Y.; Zhu, J. *Macro-molecules* **2020**, *53*, 2919–2931.

(7)   Chen, Y.; Tang, Z.; Liu, Y.; Wu, S.; Guo, B. *Macromolecules* **2019**, *52*, 3805–3812.

(8)   Ricarte, R. G.; Ois Tournilhac, F.; Cloître, M.; Leibler, L. *Macromolecules* **2020**, *53*, 1852–1866.

General Conclusion

In the here presented thesis, the concept of vitrimers has been successfully applied to create a dual dynamic network (DDN). Boronic ester metathesis and imine-aldehyde exchanges have been identified as orthogonal degenerate exchange reactions. Functional thermoplastic precursors (TPs) carrying the respective functional side-groups have been synthesized and crosslinked simultaneously with the corresponding complementary bifunctional crosslinkers. The orthogonal nature of the exchange reactions warrants the creation of an interpenetrated network containing two subnetworks that are interwoven, but chemically independent from each other.

To obtain and evaluate the final DDN, the respective subnetworks were synthesized and characterized as single networks (SNs) beforehand. The characteristics of the SNs were tailored individually to fulfill their specific needs in terms of dynamic behavior, processability and dimensional stability. These properties were adjusted by changing the molar mass of the thermoplastic precursors, their degree of functionality, their crosslinking density, or the lifetime of the dynamic bonds. Since previous studies suggested that the introduction of sacrificial bonds into a network can enhanced its mechanical properties, one of the subnetworks, the boronic ester network, was designed to be as dynamic as possible. The fast exchange reactions between the bonds are expected to dissipate energy and relax stress. However, elastomers that are dynamic under service conditions present limited to no creep resistance. Therefore, the second network, based on imine-aldehyde exchange, was designed to ideally non dynamic at service temperature, in order to act as the structural component.

The first part of the synthesis of the dynamic boronic ester subnetwork corresponds to the two-step synthesis of a functional acrylate monomer carrying a protected diol. This monomer was then copolymerized with nBA via RAFT polymerization to yield a well-defined copolymer, which was further treated to obtain the targeted TP with pendent dioxaborolane functions. The thermoplastic precursor was eventually crosslinked with a bifunctional boronic ester crosslinker to form the targeted SN. During stress relaxation experiments, complete stress relaxation was observed. The relaxation times followed the Arrhenius law, with an activation energy (E_a) of 73 kJ/mol. However, the relaxation times were relatively high, e.g., 2200 s at 110 °C. At ambient temperatures, the sample showed

only very slow dynamics. The T_V was extrapolated to be around 12 °C, close to ambient conditions, which is consistent with the limited dynamics observed at room temperature. In order to make the dioxaborolane exchange more dynamic, free diols were added to the sample. Stress relaxation experiments indicated that the addition of 10 mol% of diol, as compared to the boronic ester groups, allows decreasing the characteristic relaxation time of the material by a factor of 25.

Another possibility to tune the exchange rate of the dynamic crosslinks is to vary the structure of the boronic esters. Dioxaborinanes, 6-membered boronic esters, are thermodynamically more stable than dioxaborolanes, their corresponding five-membered analogs, due to the absence of ring strain in the 6-membered rings. It is thus anticipated to obtain a system with a different activation energy and thus different thermal dependency of the dynamic exchange. A dioxaborinane counterpart of the dioxaborolane network was prepared and the two model systems were compared. The network preparation followed the one of the dioxaborolane network. An acetal monomer was prepared in three steps and copolymerized via RAFT with *n*BA. After the polymerization, the thermoplastic was further treated to yield a dioxaborinane functionalized TP, which was subsequently crosslinked with a bis(boronic ester). The resulting dioxaborinane network presented the same to density of functional groups and crosslinks as the dioxaborolane network.

During the crosslinking and the processing, the dioxaborinane network showed a slightly slower exchange dynamic. The resulting network had a higher thermal stability than its dioxaborolane counterpart. In DSC, the dioxaborinane network featured next to the T_g, an exothermic transition at around 141 °C that was not observed with the dioxaborolane network. The transition was reversible and had an enthalpy of 0.16 J/g. Most likely, at this temperature the functional groups in the polymer chain form aggregates. Stress relaxation was conducted to assess the exchange dynamics of the dioxaborinane network. The determined E_a was calculated to be 97.4 kJ/mol vs. 72.8 kJ/mol for the dioxaborolane network. This is in accordance with small molecule exchange experiments, where dioxaborinanes also exhibited a higher E_a than their dioxaborolane counterparts. However, during the stress relaxation experiments, the network comprising the 6-membered rings showed next to the boronic ester exchange a second short time stress relaxation that became more pronounced with each relaxation experiment. Amplitude sweeps revealed that the material showed a significant higher brittleness than the 5-membered counterpart. The stress relaxation experiments might have conducted in the nonlinear regime. Network damages generated by the applied strain could be at the origin of the stress relaxation at short-times, thereby impacting the results. The peculiar behavior observed might be linked to the second thermal transition appearing in DSC. Formation of aggregates by the

functional groups might have led to the increase in modulus as well as the brittleness of the material. Additional experiments should allow to get further insights into the structural composition of this material.

The structural component of the DDN is a vitrimer network relying on imine-aldehyde exchange. This vitrimer was first characterized as a SN, to evaluate if it fulfills the requirement of dimensional stability and elasticity at ambient conditions, while presenting good processability and recyclability at elevated temperatures. An aldehyde acrylate monomer and a bis(imine) crosslinker were synthesized in two and one step, respectively. To obtain a slow exchange at room temperature, only a small amount of aldehyde groups was incorporated into the thermoplastic precursor. In a first attempt, a M_n of 500 kDa and a functionality of 0.5 % were targeted. The functional monomer was copolymerized with nBA via FRP and crosslinked with the bis(imine) to yield a soft elastomer with a ρ(CL) of 0.25 mol%. The material showed to be elastic at ambient conditions. However, it was not processable under the required conditions. Consequently, it was decided to make the material more dynamic by increasing the number of functional groups per chain. However, when attempting to prepare chains with a M_n of 500 kDa, parasitic crosslinking was observed. Several polymerization methods, such as RAFT, ATRP and FRP, were tested in an attempt to circumvent this issue. We hypothesize that the aldehyde functional monomer induces transfer, which results in crosslinking through subsequent radical termination by recombination. To limit if not avoid crosslinking, the chain length of the thermoplastics was reduced. The polymer could be synthesized successfully via RAFT copolymerization to yield a fully soluble thermoplastic with a M_n of 100 kDa and functionality of 2.0 %. A procedure to transform the RAFT end-groups without impacting the functional groups was elaborated. The thermoplastic precursors were crosslinked to yield elastomers with a ρ(CL) of 0.25 mol%. The samples were well processable via compression molding. However, small fluctuations in crosslinking density, which are unavoidable with the targeted very low concentration of dynamic crosslinks, had a significant impact on the properties of the material. It was hence decided to double the ρ(CL) to 0.5 %. This resulted in materials with reproducible crosslinking densities and consistent properties. The network showed good processability and was obtained as a homogeneous and stable material. The final imine vitrimer showed excellent dimensional stability at ambient conditions and was therefore chosen to be employed as structural subnetwork in the DDN.

Before combining the dioxaborolane and the imine-aldehyde vitrimers into a double network, orthogonality tests were conducted. It could be demonstrated that the boronic ester TP reacts neither with the bis(imine) crosslinker nor with the aldehyde TP. Likewise it was

demonstrated that the aldehyde TP does not react with the bis(boronic ester) crosslinker nor with the boronic ester TP. The subnetworks are thus orthogonal to each other and should not interfere during crosslinking. The thermoplastics have been combined in a 1 to 1 w/w ratio and crosslinked simultaneously. The DDN was obtained as a homogenous, slightly yellow elastomer, which was well processable via compression molding. This material was subjected to a comparative study with its two vitrimer SNs (Table C1).

Table C1: Comparative study of the boronic ester (BE) vitrimer, the imine-aldehyde (IA) vitrimer, and the DDN composed of this two-interpenetrated vitrimers.

Properties	Method	BE network	IA network	DDN
Insoluble fraction [%]	solubility test in THF (24 h)	98.5	90.3	95.2
Swelling ratio	solubility test in THF (24 h)	5.2	15.2	9.8
Degradation Temperature [°C]	TGA	264	261	336
T_g [°C]	DSC	-39.4	-47.1	-44.6
T_g [°C]	DMA	-25.0	-37.0	-31.9
E'(25 °C) [MPa]	DMA	0.491	0.191	0.403
E'(150 °C) [MPa]	DMA	0.587	0.083	0.337
Young's modulus [kPa]	tensile tests	505	66.1	218
Stress at break [kPa]	tensile tests	234	124	150
Strain at break [kPa]	tensile tests	114	377	180
Rubbery plateau G' (150 °C) [kPa]	oscillatory shear	140	15	50
Relaxation time τ (110 °C) [s]	rotational shear	2200	$1.10 \cdot 10^6$	32,000
Viscosity (25 °C) [GPa·s]	rotational shear	40.2	9.10	19.5
Residual strain (25 °C, 24 h, 2.5 kPa) [%]	rotational shear	1.7	2.0	0.6

Solubility tests in THF showed that the subnetworks in the DDN feature a chemical resistance similar to that of the single networks. Swelling tests showed that the DDN has a swelling ratio between the both single networks. The more densely crosslinked

subnetwork does not prevent the DDN from swelling. This might be due to the fast rearrangements of the boronic ester bonds under these conditions, in combination with the swelling pressure of the loosely crosslinked subnetwork. The DDN showed a significantly higher thermal stability than the SNs. It displays a broad glass transition that covers the entire transition region of both SNs. It is difficult to tell at this stage if the transition of the DN is a composition of the two glass transitions of the subnetworks or a broad single transition. The mechanical behavior of the DDN was assessed by uniaxial tensile tests. The ideal outcome would have been to see strain hardening due to the energy dissipation of the dynamic network. However, the DDN showed values in stress and strain at break in between the ones of the two SNs. Its properties are mainly determined by the mix of the different crosslinking densities and no synergistic effects were observed. The storage modulus of the DDN measured by rheometry is in between the moduli of the respective SNs. This is also a direct consequence of the ρ(CL). The loss modulus of the DDN seems to follow the behavior of the boronic ester subnetwork at low temperatures, while it is closer to that of the imine-aldehyde network at high temperatures.

Stress relaxation experiments showed that the short time stress relaxation caused by dangling chain ends and free chains featured in the imine-aldehyde SN is suppressed in the DDN. The interpenetrated structure seems to prevent these species to relax. The overall relaxation process in the DDN is much slower than in the boronic ester network, but much faster than in the imine-aldehyde network. It can be assumed that the relaxation in the DDN stems from the boronic ester exchange, which is the exchange working in the more crosslinked network. During creep/recovery experiments, the elastic response, strain rate, viscosity and creep compliance of the DDN ranged in between the ones of the SNs. However, when the stress was removed, the DDN showed the largest elastic recovery and the lowest residual strain after 24 h, which is even more remarkable regarding the lower average crosslinking density of the DDN. These results indicate that DDN vitrimers present a better creep resistance than single vitrimers. Consequently, when compared to the boronic ester vitrimer, the DDN allows increasing at the time creep resistance and elongation at break, which is really challenging to achieve, yet highly desirable for most elastomers. This unique behavior is likely a direct consequence of the structure of the interpenetrated network. The loosely crosslinked, slow dynamic imine-aldehyde vitrimer restricts the reshuffling of the dynamic crosslinks and the topology rearrangement of the more dynamic dioxaborolane network.

The vitrimer properties of both subnetworks allow the DDN to be mechanically repro-cessed in its crosslinked form. After several recycling cycles, the mechanical charac-teristics of the DDN were not impacted. The responsiveness of the exchanging groups

to small competitive molecules gives the possibility to chemically recycle the TPs of the subnetworks. The orthogonality of the dioxaborolane and imine-aldehyde exchange chemistries allows even to separate the individual subnetworks from each other, and regain the TPs. It was shown that the imine-aldehyde subnetwork can be isolated by dissolving the boronic ester network with small diols. The aldehyde TP could be reobtained pure after hydrolysis of the imine crosslinks.

It was demonstrated that the boronic ester - imine/aldehyde system is a very promising platform to create vitrimer DDNs, which allow an easy, precise and independent tuning of the functionality and crosslinking density of each subnetwork. Both systems showed excellent orthogonality to each other. The synthesized vitrimer DDN showed good mechanical and chemical recyclability and significant improvement towards the single networks in regards to creep resistance. The interpenetrated network structure provides thus a powerful mean to achieve higher elongation at break while simultaneously enhancing creep resistance, which is otherwise difficult to achieve. The targeted strain hardening during tensile tests was not yet accomplished. The current composition of the dynamic network does not allow to dissipate energy under ambient conditions at the applied rate of deformation. A perspective is now to adapt the DDN to feature specific advanced properties. One possibility is to address the dynamics of the exchange reaction, which can be easily tuned by the addition of free diols. Another possibility is to adapt the characteristics of the DDN by the variation of the ratio of the subnetworks. The approach to synthesize the DDN from thermoplastic precursors offers in addition the chance to influence the properties of future double dynamic systems via different parameters, such as the density of pendant groups and crosslinking points, the distribution (statistical, gradient or block-like) of the dynamic covalent bonds, as well as the composition and topology of each TP precursor. The presented system shows thus excellent perspectives in terms of creating a variety of DDNs with tunable properties.

Resumé

Les travaux de thèse présentés dans ce manuscrit ont permis d'étendre le concept de vitrimères à la synthèse et l'étude de doubles réseaux dynamiques (RDD). La métathèse des esters boroniques et les échanges imine-aldéhyde ont été identifiés comme des réactions d'échanges dégénérés orthogonales. Des précurseurs thermoplastiques (PT) portant des groupes latéraux dioxaborolane ou aldéhyde ont été synthétisés et réticulés séparément ou simultanément avec des agents de réticulation difonctionnels complémentaires, à savoir respectivement un bis(dioxaborolane) ou une bis(imine). Le caractère orthogonal des réactions d'échanges permet la création d'un réseau interpénétré contenant deux sous-réseaux entrelacés chimiquement indépendant l'un de l'autre (Figure C1).
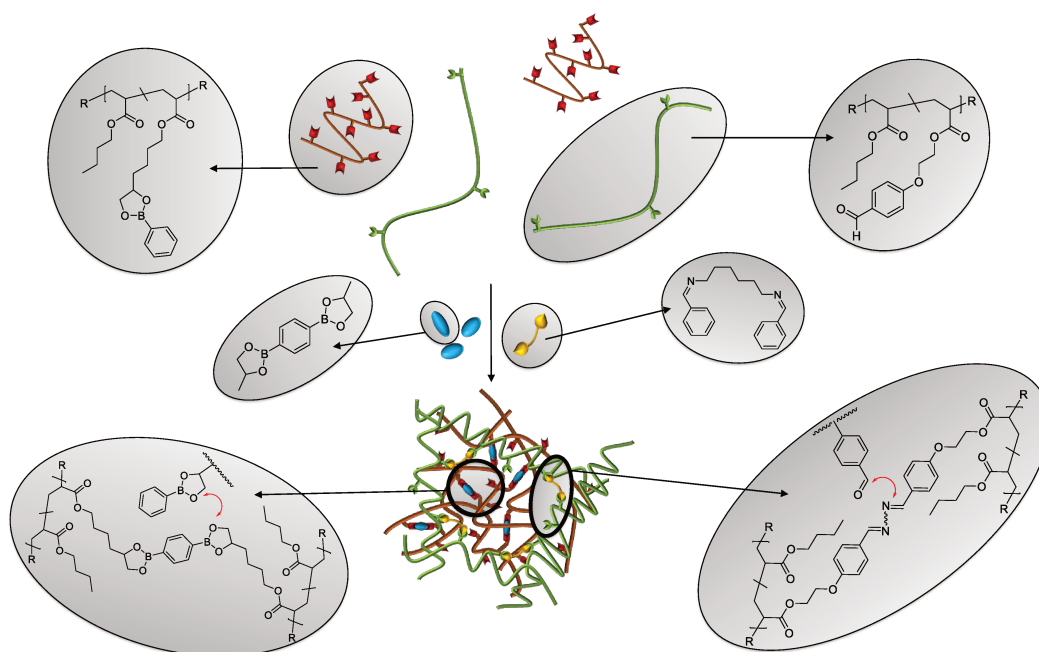
Figure C1: : Deux thermoplastiques fonctionnels sont réticulés simultanément et orthogonalement par métathèse des esters boroniques et échange imine-aldéhyde pour obtenir un RDD interpénétré.

Pour obtenir et évaluer le RDD final, les sous-réseaux respectifs ont été synthétisés et caractérisés au préalable en tant que réseaux simples (RS). Les caractéristiques des

réseaux simples ont été adaptés individuellement pour répondre aux besoins spécifiques en termes de dynamique, de mise en œuvre et de stabilité dimensionnelle. Ces propriétés ont été ajustées en modifiant la masse molaire des précurseurs thermoplastiques, leur taux de fonctionnalité, leur densité de réticulation ou le temps de vie des liens dynamiques. Des études précédentes avaient suggéré que l'introduction de liaisons sacrificielles dans un réseau peut conduire à une amélioration de certaines propriétés mécaniques. Par conséquent, un des sous-réseaux, le réseau à base d'esters boroniques, a été conçu pour être aussi dynamique que possible afin de dissiper l'énergie et relaxer les contraintes. Cependant, les élastomères dynamiques aux conditions d'usage présentent une résistance au fluage limitée, voire nulle. Par conséquent, le deuxième réseau, basé sur l'échange imine-aldéhyde, a été conçu pour être idéalement non dynamique à température ambiante, afin d'assurer la stabilité dimensionnelle du RDD.

La première partie de la synthèse du sous-réseau dynamique à base d'esters boroniques correspond à la synthèse en deux étapes d'un monomère acrylate fonctionnel porteur d'un diol protégé sous forme d'acétal. Ce monomère a ensuite été copolymérisé par RAFT avec du *n*BA. Le copolymère bien défini ainsi obtenu a finalement été modifié chimiquement pour obtenir un PT porteur de fonctions dioxaborolane pendantes. Le PT a finalement été réticulé avec un bis(dioxaborolane) pour former le RS ciblé (Schéma C1).
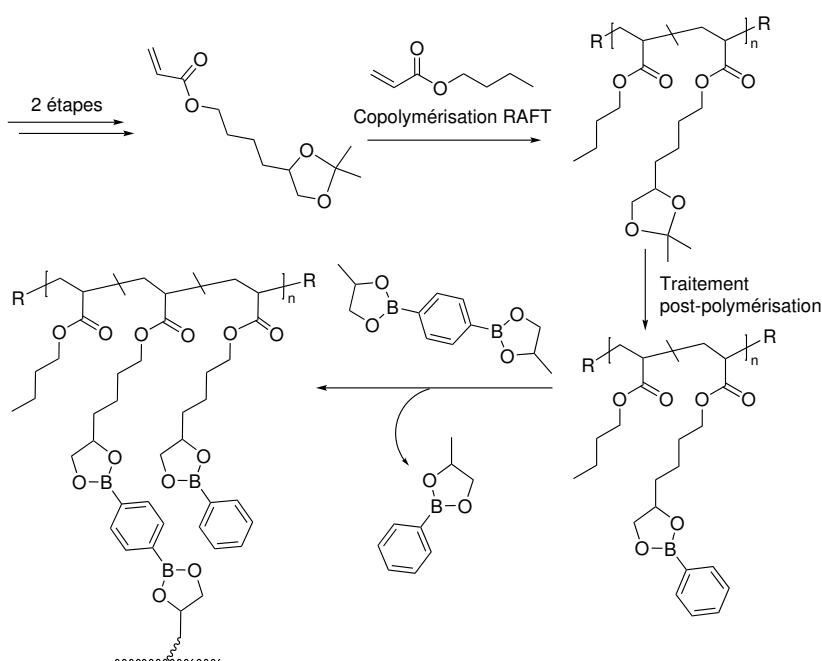
Scheme C1: Séquence réactionnelle suivie pour préparer le vitrimère ester boronique.

Au cours des expériences de relaxation de contraintes, une relaxation complète a été observée. Les temps de relaxation suivent la loi d'Arrhenius, avec une énergie d'activation de 73 kJ/mol. Cependant, les temps de relaxation sont relativement élevés, par exemple 2200 s à 110 °C. A température ambiante, l'échantillon n'a montré qu'une dynamique très lente. Une T_V de 12 °C environ a été déterminée par extrapolation, en bon accord avec la dynamique très lente observée à température ambiante. Afin d'accélérer l'échange entre dioxaborolanes, des diols-1,2 libres ont été ajoutés à l'échantillon. Des expériences de relaxation de contraintes ont confirmé que l'ajout de 10 % molaire de diols-1,2, par rapport aux groupes ester boronique, permet de diminuer le temps de relaxation caractéristique du matériau d'un facteur 25 (Figure C2).
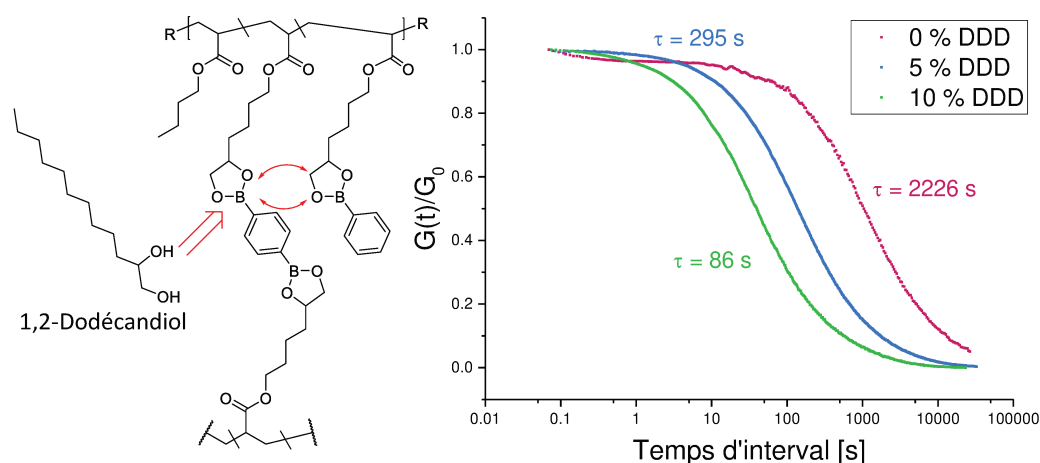
Figure C2: L'ajout d'un diol libre, tel que le 1,2-dodécandiol (DDD), permet de significativement réduire le temps de relaxation du réseau dioxaborolane.

Une autre possibilité pour ajuster la cinétique d'échange des réticulants dynamiques est de faire varier la structure des esters boroniques. Les dioxaborinanes, des esters boroniques hétérocycliques à 6 atomes, sont thermodynamiquement plus stables que les dioxaborolanes, leurs analogues hétérocycliques à 5 atomes, notamment en raison de l'absence de tension de cycle pour les dioxaborinanes. Il est ainsi envisageable de concevoir un vitrimère dont la réorganisation du réseau présente une énergie d'activation plus élevée, et par conséquence des propriétés d'écoulement plus fortement thermoactivées. Un réseau dioxaborinane analogue au réseau dioxaborolane a ainsi été préparé et les deux systèmes modèles ont été comparés (Schéma C2).
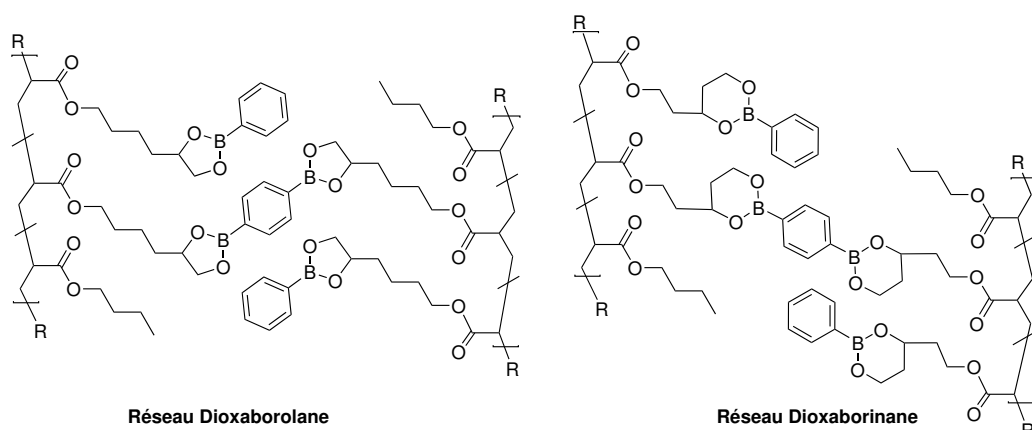
Scheme C2: Réseaux modèles ester boronique reposant sur des liaisons covalentes dynamiques dioxaborolane (gauche) et dioxaborinane (droite).

La synthèse du réseau dioxaborinane a été réalisée en suivant une approche similaire à celle suivie pour préparer le réseau dioxaborolane. Un monomère acétal a été préparé en trois étapes et copolymérisé par RAFT avec le *n*BA. Après la polymérisation, le copolymère a été traité pour obtenir un TP porteur de fonctions pendantes dioxaborinane. Ce dernier a ensuite été réticulé avec un bis(dioxaborolane). Un réseau dioxaborinane présentant la même densité de groupes fonctionnels et de points réticulations que le réseau de dioxaborolane a ainsi pu être préparé. Au cours de la réticulation et de la mise en œuvre, le réseau dioxaborinane a montré une dynamique d'échange légèrement plus lente et une stabilité thermique plus élevée que son homologue dioxaborolane. La caractérisation par DSC du réseau dioxaborinane a mis en évidence, en plus de la T_g, une transition exothermique vers 141 °C qui n'a pas été observée pour le réseau dioxaborolane. Cette transition est réversible et présente une enthalpie de 0,16 J/g. Cette seconde transition pourrait correspondre à un phénomène d'agrégation/dissociation des fonctions dioxaborinane latérales. Des expériences de relaxation de contraintes ont permis d'évaluer la dynamique d'échange du réseau dioxaborinane. Une E_a de 97,4 kJ/mol a été calculée, contre 72,8 kJ/mol pour le réseau dioxaborolane. Ces résultats sont conformes aux expériences d'échanges sur petites molécules, pour lesquels les dioxaborinanes présentent également une E_a plus élevée que leurs homologues dioxaborolane. Lors des expériences de relaxation de contraintes sur le réseau dioxaborinane, une seconde relaxation visible aux temps courts et s'accentuant au cours des expériences successives a été observée, en plus de la relaxation principale associée aux réaction d'échange entre ester boroniques. Les balayages en amplitude ont révélé que le matériau est nettement plus fragile que son homologue dioxaborolane. Les expériences

296

de relaxation de contraintes ont ainsi probablement été réalisées en dehors du domaine de déformation linéaire. Ces observations sont probablement liées à la deuxième transition thermique observée en DSC. La formation d'agrégats peut en effet conduire à une augmentation du module ainsi qu'à une plus grande fragilité du matériau. Des analyses structurales complémentaires du matériau devraient permettre de confirmer ou d'infirmer cette hypothèse.

La stabilité dimensionnelle du RDD doit être assurée par un réseau vitrimère reposant sur l'échange imine-aldéhyde. Ce vitrimère a d'abord été caractérisé en tant que RS pour évaluer sa dynamique d'échange. Ce réseau doit se comporter comme un solide élastique à température ambiante, tout en présentant une bonne aptitude à la mise en œuvre et à la recyclabilité à haute température. Un monomère acrylate portant une fonction benzaldéhyde et un agent de réticulation bis(imine) ont été respectivement synthétisés en deux et une étape. Afin d'obtenir un échange lent à température ambiante, une faible quantité de groupements aldéhyde a été incorporée dans le PT. Une M_n de 500 kDa et une fonctionnalité de 0,5 % ont été ciblées dans un premier temps. Le monomère fonctionnel a été copolymérisé avec le nBA par polymérisation radicalaire conventionnelle (FRP) et le copolymère ainsi obtenu a été réticulé avec la bis(imine) pour donner un élastomère avec une ρ(CL) de 0,25 % molaire. Le matériau s'est révélé élastique à température ambiante. Cependant, il n'était pas transformable dans les conditions visées (temps et température). Par conséquent, il a été décidé de concevoir un matériau plus dynamique en augmentant le nombre de groupes fonctionnels par chaîne. Cependant, en essayant de préparer des chaînes avec une M_n de 500 kDa, une réticulation parasite a été observée. Plusieurs méthodes de polymérisation, telles que la RAFT, l'ATRP et la FRP, ont été testées pour tenter de résoudre ce problème. Nous supposons que le monomère fonctionnel aldéhyde est à l'origine de réactions de transfert qui conduisent à une réticulation du polymère par réactions de terminaison radicalaire par recombinaison.

Pour limiter cette réticulation parasite, voire la supprimer, la longueur des chaînes polymères a été réduite. Un copolymère aldéhyde entièrement soluble présentant une M_n de 100 kDa et une fonctionnalité de 2,0 % a ainsi pu être synthétisé par polymérisation RAFT. Une procédure permettant de transformer les bouts de chaîne portant l'agent RAFT sans impacter les fonctions aldéhyde a été élaborée. Des élastomères vitrimères présentant une ρ(CL) de 0,25 % molaire ont ensuite été préparés par réticulation du copolymère aldéhyde (Schéma C3). Les matériaux ainsi obtenus peuvent être mis en forme par compression-moulage. Cependant, de faibles fluctuations de la densité de réticulation, inévitables du fait de la très faible réticulation visée, impactent fortement les

propriétés du matériau.
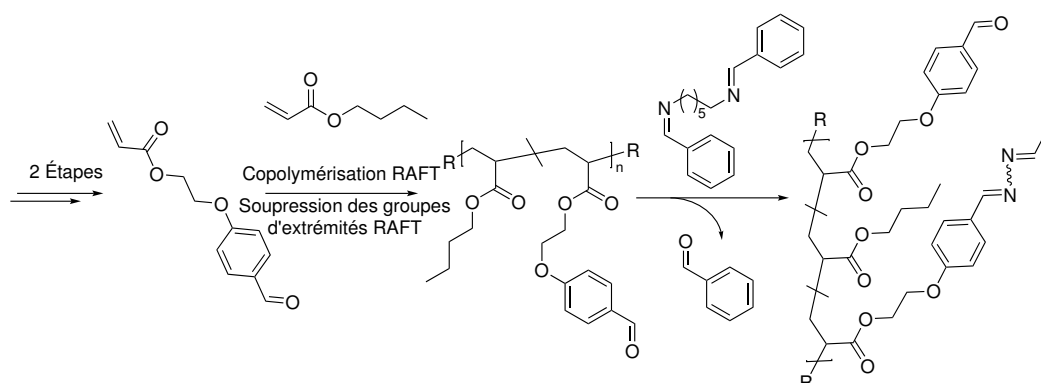
Scheme C3: Séquence réactionnelle suivie pour préparer le vitrimère imine-aldéhyde.

Il a donc été décidé de doubler la ρ(CL) à 0,5 % molaire. Des matériaux homogènes, avec des densités de réticulation et des propriétés reproductibles ont ainsi pu être préparés. Ce réseau imine-aldéhyde a également montré une bonne aptitude à la mise en œuvre. Le vitrimère imine final présente une excellente stabilité dimensionnelle à température ambiante. Il a donc été retenu comme sous-réseau structurel pour le RDD.

Avant de combiner les vitrimères dioxaborolane et imine-aldéhyde en un double réseau interpénétré, des tests d'orthogonalité ont été réalisés. Il a ainsi être démontré que PT ester boronique ne réagit ni avec l'agent de réticulation bis(imine), ni avec le PT aldéhyde. De même, il a été démontré que le PT aldéhyde ne réagit ni avec le réticulant bis(dioxaborolane), ni avec le PT ester boronique. Les sous-réseaux sont donc chimiquement orthogonaux entre eux, et ne devraient pas réagir ensemble lors de la réticulation. Les thermoplastiques ont été combinés dans un rapport massique de 1 pour 1 et réticulés simultanément. Le RDD a été obtenu sous la forme d'un élastomère homogène, légèrement jaune, pouvant être mis en forme par compression-moulage. Ce matériau a fait l'objet d'une étude comparative avec les deux RS vitrimères le constituant (Tableau C1). Des tests de solubilité dans le THF ont montré que les sous-réseaux du RRD présentent une résistance chimique similaire à celle des RS. Le taux de gonflement du RDD se situe entre ceux des deux réseaux simples. Le sous-réseau plus densément réticulé n'empêche donc pas le RDD de gonfler. Ce comportement reflète probablement le réarrangement rapide des liaisons dioxaborolane dans ces conditions, couplé à la pression de gonflement induite par le sous-réseau faiblement réticulé. Le RDD a montré une stabilité thermique significativement supérieure aux RS. Il présente transition vitreuse qui s'étale sur une fenêtre de températures qui englobe les transitions vitreuses des

deux RS. Il est difficile de dire en l'état si la transition du RDD est constituée des deux transitions vitreuses distinctes, associées à chaque sous-réseau, ou s'il s'agit d'une large transition unique.

Tableau C1: Etude comparative du vitrimère ester boronique (EB), du vitrimère imine-aldéhyde (IA) et du RDD composé de ces vitrimères interpénétrés.

Propriétés	Méthode	Réseau EB	Réseau IA	RDD
Fraction insoluble [%]	test de solubilité dans le THF (24 h)	98.5	90.3	95.2
Rapport de gonflement	test de solubilité dans le THF (24 h)	5.2	15.2	9.8
Température de dégradation [°C]	ATG	264	261	336
T_g [°C]	DSC	-39.4	-47.1	-44.6
T_g [°C]	AMD	-25.0	-37.0	-31.9
E'(25 °C) [MPa]	AMD	0.491	0.191	0.403
E'(150 °C) [MPa]	AMD	0.587	0.083	0.337
Module d'Young [kPa]	essai de traction	505	66.1	218
Stress à la rupture [kPa]	essai de traction	234	124	150
Tension à la rupture [kPa]	essai de traction	114	377	180
Plateau caoutchouteux G' (150 °C) [kPa]	cisaillement oscillatoire	140	15	50
Temps de relaxation τ (110 °C) [s]	cisaillement rotatif	2200	$1.10 \cdot 10^6$	32,000
Viscosité (25 °C) [GPa·s]	cisaillement rotatif	40.2	9.10	19.5
contrainte résiduelle (25 °C, 24 h, 2.5 kPa) [%]	cisaillement rotatif	1.7	2.0	0.6

Le comportement mécanique du RDD a été évalué par des essais de traction uniaxiale. Ces tests n'ont pas mis en évidence un durcissement sous contraintes résultant de la réorganisation du réseau dynamique fortement réticulé. Le RDD présente une contrainte

à la rupture et une déformation à la rupture comprises entre celles des deux RS. Ses propriétés sont principalement déterminées par le mélange des différentes densités de réticulation, et aucun effet de synergie n'a été observé dans ces conditions. Le module de conservation du RDD mesuré par rhéométrie se situe entre les modules des RS, ce qui s'explique de nouveau par la ρ(CL) intermédiaire du RDD. Le module de perte du RDD semble suivre le comportement du sous-réseau ester boronique à basse température, alors qu'il est plus proche de celui du réseau imine-aldéhyde à haute température.

Des expériences de relaxation de contraintes ont montré que la relaxation aux temps courts observée dans le RS imine-aldéhyde n'est pas présente dans le RDD. La structure interpénétrée du réseau semble supprimer ce mode de relaxation associé aux extrémités de chaîne et aux chaînes libres présentes dans le réseau imine-aldéhyde. Le processus global de relaxation dans le RDD est beaucoup plus lent que dans le vitrimère ester boronique, mais beaucoup plus rapide que dans le réseau simple imine-aldéhyde. On peut supposer que la relaxation dans le RDD repose sur la métathèse des esters boroniques, qui est entravée et donc ralentit dans le réseau interpénétré. Au cours des expériences de fluage/recouvrance, la réponse élastique, la vitesse de déformation, la viscosité et la conformité au fluage du RDD se situent entre celles des RS. Cependant, lorsque la contrainte est supprimée, le RDD présente la plus grande recouvrance élastique et la déformation résiduelle la plus faible après 24 h. Ce point est à souligner, sachant que la densité de réticulation du RDD est inférieure à celle du RS ester boronique. Ces résultats semblent donc indiquer que les vitrimères RDD présentent une meilleure résistance au fluage que les vitrimères simples. Par conséquent, le RDD présente à la fois une meilleure résistance au fluage et un allongement à la rupture plus important que le vitrimère ester boronique, une combinaison de propriétés recherchée pour la plupart des élastomères. Ce comportement est probablement une conséquence directe de la structure interpénétrée du double réseau dynamique. Le vitrimère imine-aldéhyde, faiblement réticulé et peu dynamique, ralentit les échanges entre points de réticulation dynamique et le réarrangement de la topologie du réseau dioxaborolane, plus dynamique. Les propriétés vitrimères des deux sous-réseaux permettent au RDD d'être recyclé mécaniquement. Après plusieurs cycles de recyclage, les caractéristiques mécaniques du RDD ne semblent pas être impactées. L'ajout de petites molécules compétitives monofonctionnelles pouvant s'échanger avec les ponts de réticulation dioxaborolane ou imine donne la possibilité de recycler chimiquement le RDD. L'orthogonalité des chimies d'échange dioxaborolane et imine-aldéhyde permet de séparer les sous-réseaux l'un de l'autre, et de récupérer les PT. Il a ainsi été montré que le sous-réseau imine-aldéhyde peut être isolé en dissolvant sélectivement le réseau ester boronique avec le propane-

1,2-diol. Le PT aldéhyde a ensuite pu être récupéré pur après hydrolyse des ponts de réticulation imines (Figure C3).
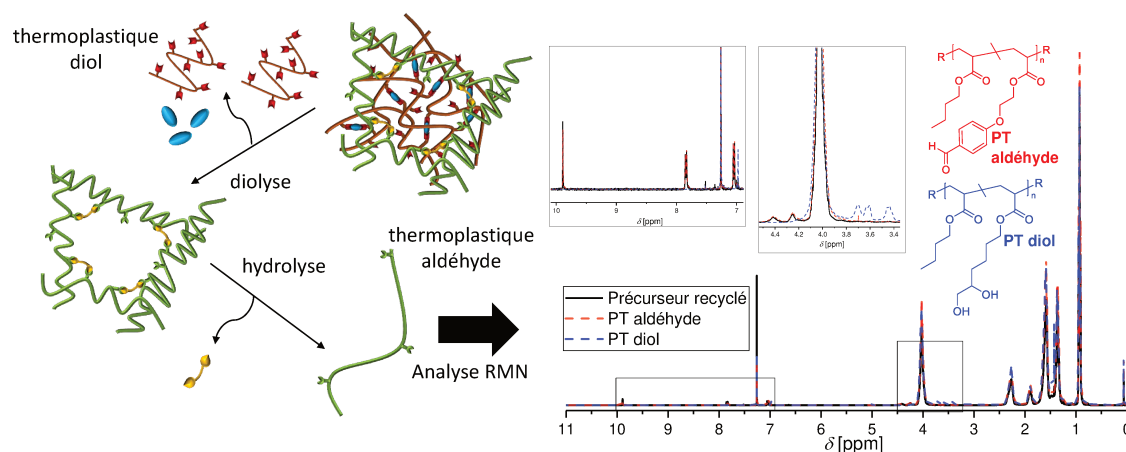
Figure C3: Le précurseur thermoplastique aldéhyde peut être récupéré pur par diolyse du RDD, suivie d'une hydrolyse du réseau imine-aldéhyde ainsi obtenu.

Il a été démontré au cours de ces travaux de thèse que le système ester boronique - imine/aldéhyde offre une plateforme extrêmement prometteuse pour concevoir des RDD vitrimères, dont la fonctionnalité et la densité de réticulation des sous-réseaux peuvent être facilement, précisément et indépendamment ajustées. Les deux sous-réseaux ont montré une excellente orthogonalité l'un par rapport à l'autre. Le RDD obtenu présente une excellente recyclabilité mécanique et chimique. Le vitrimère RDD présente une résistance au fluage nettement supérieure à celles des réseaux simples. La structure interpénétrée du réseau offre la possibilité d'augmenter l'allongement à la rupture tout en améliorant simultanément la résistance au fluage, propriétés qu'il est souvent difficile d'améliorer simultanément. Un durcissement sous contraintes du RDD n'a pas été observé lors des tests de traction uniaxiale. La composition actuelle du double réseau dynamique ne permet pas de dissiper l'énergie à température ambiante aux vitesses de déformation testées. Une perspective est maintenant d'adapter la conception des RDD pour qu'ils présentent des propriétés supérieures et spécifiques. Une possibilité, dans cette optique, est d'ajuster la dynamique de la réaction d'échange, par exemple par l'ajout de diols libres. Une autre possibilité est d'adapter les caractéristiques des RDD en variant leur teneur en chaque sous-réseaux, ainsi que la nature de ces derniers. La synthèse de RDD à partir de précurseurs thermoplastiques offre en effet de nombreux leviers pour moduler les propriétés des doubles réseaux dynamiques, telles que la densité de groupes fonctionnels pendants et de ponts de réticulation, la distribution (statistique, gradient ou

bloc) des liaisons covalentes dynamiques, ou encore la composition et la topologie de chaque PT. L'approche et les systèmes développés au cours de cette thèse offrent donc une plateforme modulable qui ouvre de très nombreuses perspectives pour la conception d'une large gamme de RDD présentant des propriétés ajustables.

List of Figures

List of Schemes

List of Tables

RÉSUMÉ

Les réseaux dynamiques doubles (RDD) sont des matériaux polymères qui combinent deux agents de réticulation distincts (ou plus) dans un seul système. En couplant différentes stratégies de réticulation, des matériaux sur mesure peuvent être conçus. Cette thèse explore la mise en œuvre du concept de vitrimère dans les RDD. Des élastomères vitrimères constitués de deux réseaux dynamiques interpénétrés reposant respectivement sur la métathèse des esters boroniques et sur l'échange imine-aldéhyde ont été conçus dans ce but. Les deux réactions procèdent selon un mécanisme dégénéré et sont orthogonales l'une à l'autre. Par l'utilisation de deux réticulations dynamiques différentes, deux dynamiques distinctes sont établies dans le réseau. Pour obtenir et évaluer le RDD final, les sous-réseaux respectifs ont été synthétisés au préalable et caractérisés en tant que réseaux simples. Les caractéristiques des réseaux simples ont été adaptés individuellement pour répondre à leurs besoins spécifiques en termes de comportement dynamique, de mise en œuvre et de stabilité dimensionnelle. Ces propriétés ont été ajustées en modifiant la masse molaire des précurseurs thermoplastiques, leur taux de fonctionnalité, leur densité de réticulation ou le temps de vie des liens dynamiques. Les deux réseaux ont été réunis avec succès en un RDD. Une étude comparative a permis de comprendre comment les sous-réseaux individuels contribuent aux propriétés du RDD, et si des effets synergiques sont obtenus. Dans les faits, la structure interpénétrée du vitrimère RDD permet d'augmenter à la fois la résistance au fluage et l'allongement à la rupture, ce qui est particulièrment difficile à réaliser, mais hautement souhaitable pour la plupart des élastomères. Au-delà, les matériaux obtenus ont montré un très fort potentiel pour le recyclage mécanique et chimique.

MOTS CLÉS

Réseaux Doubles, Réseaux Adaptables Covalents, Vitrimères, Recyclabilité, Polymères Réticulés

ABSTRACT

Dual dynamic networks (DDNs) are polymeric materials that combine two (or more) distinct crosslinkers in one system. By coupling different crosslinking strategies, precisely tailored materials can be designed. This thesis explores the implementation of the vitrimer concept into DDNs. Elastomeric vitrimers consisting of two interpenetrated dynamic networks that rely on boronic ester metathesis and on imine-aldehyde exchange, respectively, were designed to this aim. Both reactions proceed via a degenerate mechanism and are orthogonal to each other. By the engagement of two types of dynamic covalent crosslinks, two distinct dynamics are established in each subnetwork. To obtain and evaluate the final DDN, the respective subnetworks were synthesized beforehand, and characterized as single networks. The characteristics of the single networks were tailored individually to fulfill their specific needs in terms of dynamic behavior, processability and dimensional stability. These properties were adjusted by changing the molar mass of the thermoplastic precursors, their degree of functionality, their crosslinking density, or the lifetime of the dynamic bonds. The two networks were successfully united into a DDN. In a comparative study, insights were obtained how the individual subnetworks contribute to the DDN's properties, and whether synergetic effects arise. In fact, the interpenetrated nature of the vitrimer DDN allows increasing at the time creep resistance and elongation at break, which is really challenging to achieve, yet highly desirable for most elastomers. Over and beyond, the obtained materials show great potential for mechanical and chemical recycling.

KEYWORDS

Double Networks, Covalent Adaptable Networks, Vitrimers, Recyclability, Crosslinked Polymers